



B
A

newsletter

The official bi-monthly publication of Bhabha Atomic Research Centre

R
C

Materials
for
sustainable energy



Editor

Dr. S. Adhikari

Associate Editors

Dr. V. Sudarsan
Dr. Abhijit Ghosh
Dr. Pranesh Sengupta

Editorial Assistant

Shri Madhav N

Cover Page Concept & Illustration

Dr. Bitan Ghosh

Design & Creative Work

Shri Dinesh J. Vaidya
Shri Madhav N

Newsletter Committee

Chairman

Dr. A.P. Tiwari

Members

Dr. A.K. Nayak
Dr. G. Sugilal
Dr. V.H. Patankar
Dr. (Smt.) B.K. Sapra
Dr. L.M. Pant
Dr. Ranjan Mittal
Dr. (Smt.) S. Mukhopadhyay
Dr. K.P. Muthe
Dr. V. Sudarsan
Dr. A.V.S.S.N. Rao
Dr. S.R. Shimjith
Dr. Sandip Basu
Dr. Pranesh Sengupta
Dr. R. Tripathi

Member Secretary & Coordination

Shri Madhav N



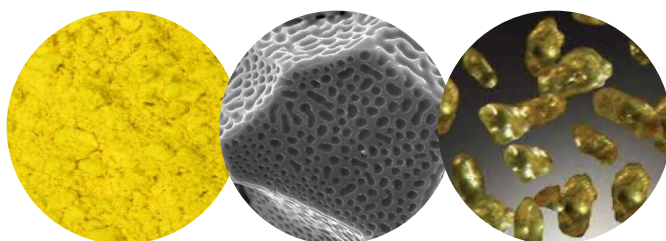
BARC Newsletter
September-October 2022
ISSN: 0976-2108



TECHNOLOGIES FOR
NEW INDIA @ 75
आज़ादी का अमृत महोत्सव

R&D *in*

pursuit of materials with
superior properties



Since inception, Materials Group has been contributing positively in realizing Departmental goals of clean energy on a wider scale to benefit large swathes of population in the country. Thanks to its dedicated human resource base, which is equipped with deep understanding of the subject and technical expertise in using sophisticated microscopic and spectroscopic instruments and interpreting the data, BARC Materials Group has overcome many technological challenges including ore dressing, extractive metallurgy, design and development of alloys and their performance assessments under simulated and after actual service conditions. Outcome of sustained high level R&D studies in nuclear material science vis-à-vis technology development has certainly placed our country in a prime position in the world in terms of fission and fusion reactor materials related program.

Besides its notable contributions in Nuclear Energy Program 'from Ore to Core', Materials Group has also been working on alternative energy materials like Fuel cells, Lithium ion batteries, Hydrogen storage materials and various other materials essential for societal and strategic applications. In that respect, the current issue of Newsletter on two interesting themes - Energy Storage Materials, and Advanced Inorganic and Non-metallic Materials is a well timed initiative. In each case, the scientists have been able to develop materials with superior properties for nuclear and specialized non-nuclear applications.

Under the theme Energy Storage Materials, research and developmental activities on energy storage materials giving special emphasis on new generation Lithium based materials have been discussed. Both experimental and simulation studies have been covered in this section. Apart from this, the issue also covers recent advancements in LaNi₅ alloy as a hydrogen storage material. A scientometric study on energy storage material related to publications from India has also been documented.

This issue of BARC Newsletter provides a glimpse of R&D work in development of advanced, efficient and economical energy storage materials for widespread applications in various clean energy programs of the Department of Atomic Energy. This includes recent advancements in inorganic and non-metallic materials for various societal applications like development of ceramics (hydroxyapatite), glass (yttrium alumina silicate) and glass-ceramics for bio-medical and micro device applications, development of new energy efficient materials for LED and others. Synthesis and applications of carbon based materials like carbon aerogel, silicon carbide fibre and particulates have also been covered. A special report on United Nations International Year of Glass – 2022 has also been included in this issue.

I hope this document would not only help the domain specialists but also those from other fields of expertise, especially the young researchers, to develop a brief idea about the front-end research activities in our department in the areas of 'Energy Storage Materials, and Advanced Inorganic and Non-Metallic Materials'.

Dr. Vivekanand Kain
Director, Materials Group

A *tryst* with clean energy & materials



It gives us immense pleasure to bring out this issue of BARC Newsletter issue on two interesting themes - Energy Storage Materials, and Advanced Inorganic and Non-metallic Materials. Towards successful implementation of Year 2030 Agenda for Sustainable Development, adopted in 2015 by all United Nations Member States, including India, DAE has been collaborating actively on programs associated with clean energy generation and distribution to ensure access to affordable and sustainable forms of energy. In this context, development of energy storage materials and devices indigenously with better service life has taken greater precedence.



Energy storage is considered critical for the sustainability of mankind. Batteries, capacitors, fuel cells and hydrogen storage materials are ideal candidates for energy storage applications. Amidst diversified forms of fuels globally, hydrogen has taken the centrestage and is touted as a prospective candidate for meeting the energy needs of this century. Hydrogen-fuelled cars have already become a reality. Development of efficient hydrogen storage materials is vital for developing deployable fuel cells for transport applications. Such technologies can help reduce carbon footprint as well as address the consequences of climate change.

Novel inorganic and non-metallic materials, including ceramics and carbon have gained extensive applications in various programs of DAE. Recent advancements in this domain are covered sufficiently in this issue of newsletter.



Finally, we would like to express our heartfelt appreciation to the authors for contributing articles to this thematic issue and also the reviewers, who have meticulously gone through the content to ensure they come out exceedingly well. We strongly feel the contents of this issue would ideally motivate young researchers of BARC to take up research activities in new exciting domains of science and technology in order to address the gap areas as well as come up with innovations that can contribute positively in department's efforts to enable access to clean and sustainable forms of energy.

V Sudarsan
Chemistry Division

Abhijit Ghosh
Glass & Advanced Materials Division

Pranesh Gengupta
Materials Science Division

3 FOREWORD: Dr. Vivekanand Kain

5 ASSOCIATE EDITORS' MESSAGE: Dr. V. Sudarsan, Dr. Abhijit Ghosh, Dr. Pranesh Sengupta

RESEARCH AND DEVELOPMENT: ENERGY STORAGE MATERIALS

9 Lithium-Sulfur Battery: Present Status and Future Direction

K. Sandeep Rao et al.

14 Development of NASICON based Solid State Electrolyte for Li-battery Application

Anurup Das et al.

19 First Principles based Atomistic Modeling of Lithium Ion Battery

Sk. Musharaf Ali et al.

25 Review on Electrochemical Capacitor Technology: Role of Transition Metal-based Oxides

Seemita Banerjee et al.

31 Influence of Transition Metals on Hydrogen Storage Properties of LaNi₅ Alloy

Asheesh Kumar et al.

SCIENTOMETRIC STUDY

36 Energy Storage Materials-A Scientometric Perspective of Indian Publications

E.R. Prakash et al.

POPULAR SCIENCE

41 Hydrogen Energy - Applications and Industry Decarbonization

Rupsha Bhattacharyya

BOOK REVIEW

45 Smarting Energy Management - A Computational Approach

Kumud Singh

INTERNATIONAL EVENTS

47 United Nations International Year of Glass - 2022

Madhumita Goswami

RESEARCH AND DEVELOPMENT: ADVANCED INORGANIC & NON-METALLIC MATERIALS

48 Development of Yttrium-Alumino-Silicate(YAS) Glass Microspheres for HCC Radiotherapy Application

Senthil Kumar et al.

54 Development of Hydroxyapatite Microspheres for Biomedical Applications

Rohini Garg et al.

59 Development of Ce: YAG Glass-ceramics Phosphor for White LED Application

P. Nandi et al.

63 Development of Ag-Ce Doped Photostructurable Glass Ceramics for Microdevice Application

Richa Mishra et al.

67 Development of Silicon Carbide Fibre through Pre ceramic Polymer Route

J. N. Sharma et al.

72 Synthesis of Silicon Carbide Particulate and Fibre by Reaction-Conversion Method

Abhijit Ghosh et al.

76 Carbon Nanotube Aerogel: Synthesis and Applications

Kinshuk Dasgupta et al.

81 Nanocomposite of Cement and Graphene Oxide: Impact on Strength Properties and Carbon Footprint

P. T. Rao et al.

SYNOPSIS OF DOCTORAL THESIS

87 Radiation Chemical Studies of Ionic Liquids...

Laboni Das

SCIENCE SIMPLIFIED

88 A Novel CO Laser

M. B. Sai Prasad et al.

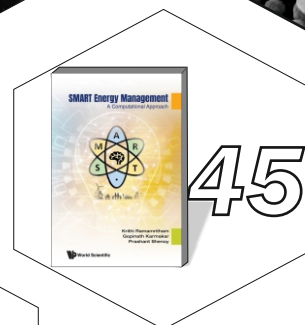
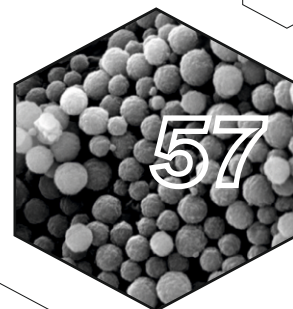
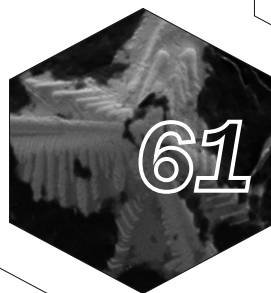
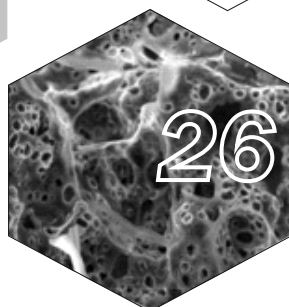
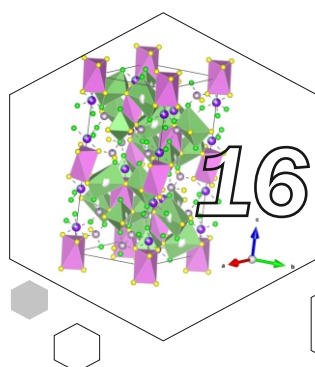
OFFICIAL LANGUAGE IMPLEMENTATION IN BARC

89 A Roundup of Activities for 2021-22

Hindi Cell & Newsletter Editorial Team

SCIENTIFIC SOCIAL RESPONSIBILITY IN DAE

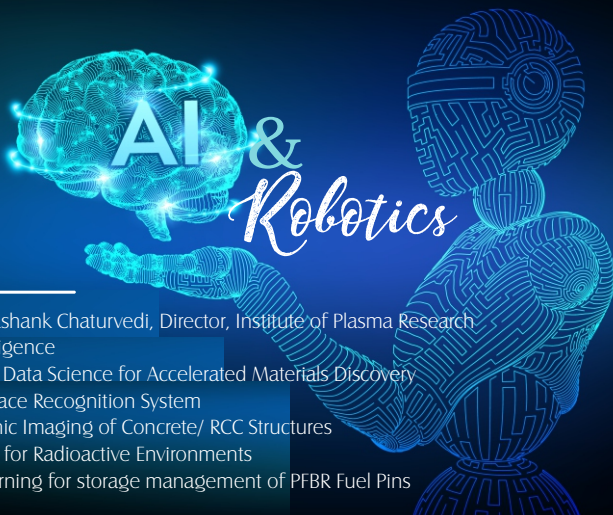
90 Glimpses of Parmanu Jyoti (August 2022)



CONTENTS



FORTHCOMING ISSUE



- Tete-a-Tete with Dr. Shashank Chaturvedi, Director, Institute of Plasma Research
- Life with Artificial Intelligence
- Machine Learning and Data Science for Accelerated Materials Discovery
- Deep learning based Face Recognition System
- Automation in Ultrasonic Imaging of Concrete/ RCC Structures
- Remote Handling Tools for Radioactive Environments
- Robotics and Deep learning for storage management of PFBR Fuel Pins

Background Image @freepik.com

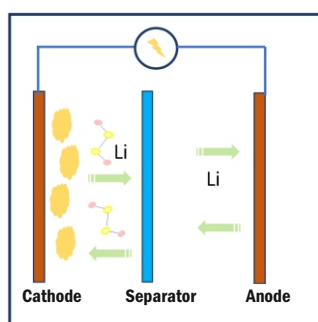
This page is intentionally left blank

Future Rechargeables

Lithium-Sulfur Battery: Present Status and Future Direction

K. Sandeep Rao, Dipa Dutta Pathak and Balaji P. Mandal*

Chemistry Division, Bhabha Atomic Research Centre, Mumbai 400085, INDIA



Li-S battery

ABSTRACT

Lithium-sulfur battery (LSB) is the future of rechargeable batteries as its theoretical specific capacity and theoretical energy density are much higher than those of conventional lithium ion battery (LIB). Another advantage of LSB is its relatively lower output voltage (2.1 V) which provides higher safety margin. However, life cycle, capacity fading and Coulombic efficiency are found to be serious problems for LSB. Several steps have been taken to improve the conductivity of sulfur cathode and to slow down the solubility of polysulfides in electrolyte. Mostly, the sulfur cathode has been encapsulated by different types of carbon to improve conductivity of the composite and to hinder dissolution of long chain polysulfides. At the same time, anode side also has been modified by suitable means like fabricating pre-lithiated carbon or Ge-C composite. Similarly, research work on electrolyte modification has also been discussed.

KEYWORDS: Energy density, Power density, Battery, Sulfur, Cycling, Electrode

Introduction

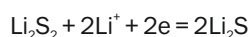
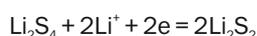
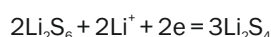
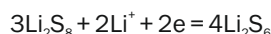
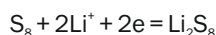
The ever-increasing demand to store electrochemical energy efficiently spurred the continued research interest in advanced batteries. The traditional lead acid or nickel cadmium batteries are found to be insufficient to cater the present needs due to lower energy density, power density, cycling etc of these batteries. On the other hand, lithium ion batteries (LIBs) have many superior attributes which make them a dominating player in battery market. In addition, conventional LIBs do not suffer from memory effect. The self-discharge rate of lithium ion battery is also very low for LIBs (~5% per month) in comparison to Ni-Cd or Ni-MH batteries. The global reserve of lithium in earth crust is around 20 ppm which is sufficient to build more than 12 billion electric vehicles[1]. Therefore, lithium based batteries have become the central focus of researchers globally. Even though Li-ion batteries have higher energy density than sodium ion battery still they are not very suitable to be installed in electric vehicles. The energy density of LIB can be 200-300 Wh/kg, which cannot satisfy all the requirements of upcoming applications like vehicle electrification or high end electronic application. These new demands have been prompting the researchers to work on other alternative rechargeable batteries with higher energy density and longer life cycle. Among other battery chemistries, Li-S is most important candidate due to its low cost, high theoretical capacity (1675 mAh g⁻¹) with a high theoretical specific energy of 2600 Wh kg⁻¹, on the presumption of the complete reaction of lithium with sulfur to form Li₂S[2,3].

The theoretical capacity of S is more than five times higher than that of traditional cathode materials based on transition metal oxides or phosphates. Another important aspect of Li-S battery is its low operating voltage (~ 2.1 V) which offer higher safety margin over the high-voltage oxide-

based cathodes (>4.3 V). It becomes more important in case large pouch cell configuration.

Working Principal of Li-S Battery

Like any other secondary cell, Li-S battery (LSB) also consists of cathode (where reduction takes place during discharge), anode (where oxidation takes place during discharge), electrolyte (through which ions migrates from one electrode to another internally) and a separator (to avoid physical contact between two electrodes). The working principle of a typical Li-S battery is slightly different from conventional lithium ion battery. In conventional LIBs, lithium ions move from lithium containing cathode to anode via electrolyte during charging process and in reverse direction during discharging process. However, in case of LSB, the cells are made in charged state and initially discharging is done. During discharging, lithium ion moves from lithium anode to sulfur (or sulfur composite) cathode via separator soaked in electrolyte and reduce S to Li₂S via a multi-step, multi-electron reduction process. In charging process, Li₂S gets oxidized to S and releases Li ions which migrate to lithium anode again via electrolyte. Interestingly, the reduction of sulfur (S₈) to Li₂S takes place in multiple steps.



Initially higher polysulfides (Li₂S_n, x=8, 6, 5 and 4) form on reaction between lithium and sulphur which on further lithiation results lower polysulfides (Li₂S_n, n=1,2). The higher polysulfide (Li₂S_n, x=8, 6, 5 and 4) are highly soluble in organic solvent (mostly 1,3-dioxolane and 1,2-dimethoxyethane are

*Author for Correspondence: Balaji P. Mandal
E-mail: bpmandal@barc.gov.in

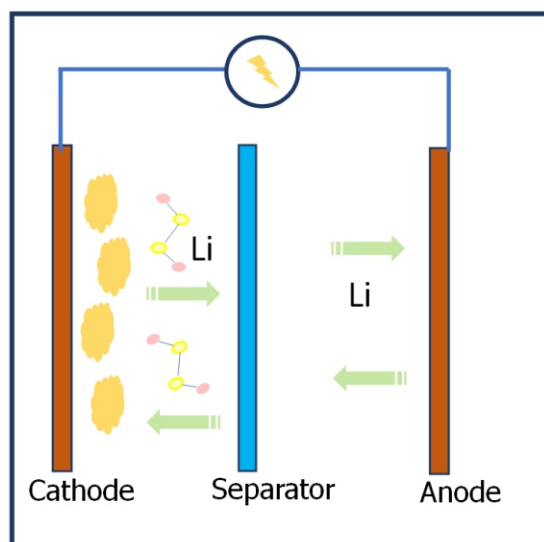


Fig.1: Schematic drawing of Li-S battery.

used as solvent) used as electrolyte in LIB. On the other hand, the lower polysulfides (Li_2S_x , $1 < x < 4$) are insoluble and hence remain in solid state. The rate of reaction is faster in initial phase of lithiation at the solid-liquid interface, however, it is slower in second step as lithiation takes place on solid Li_2S_2 . The voltage plateau for first reaction i.e. formation of S_4^{2-} from S_8 via above mentioned steps is observed around 2.3 V with corresponding capacity 418 mAhg^{-1} (~25% of total capacity). The lower discharge plateau occurs at 2.1 V (vs Li/Li^+) corresponding to subsequent reduction of Li_2S_4 to $\text{Li}_2\text{S}_2/\text{Li}_2\text{S}$, with a theoretical capacity of 1254 mAhg^{-1} (~75% of total capacity).

Challenges Ahead

Even though there are myriad of advantages of Li-S batteries, still the following challenges need to be addressed before its large-scale applications.

- (a) High Resistivity of Sulfur and Li_2S .
- (b) Shuttle Effect of Polysulfides.
- © Huge Volume Expansion/Contraction during Lithiation/Delithiation.
- (d) Use of Metallic Lithium Anode.

These problems are related to either electrodes or electrolyte and suitable modification of these components can improve the overall performance of Li-S battery. In the following sections highlight the important research on cathode, anode and electrolyte materials.

Research on Cathode Materials

Mostly, elemental sulfur is used as cathode material in Li-Sulfur battery. Sulfur has more than 30 allotropes and the most common and stable amongst them is cyclic octasulfur (S_8)[4]. The electronic conductivity of elemental sulfur is very low ($10^{-30} \text{ Scm}^{-1}$), therefore, it needs to be made composite with conducting material like carbon. Several methods have been adopted so far by different groups to make sulfur-carbon composites. Initially conventional carbons or carbon black were added with sulfur to make it conducting. These carbon blacks are mostly fabricated by thermal cracking or partial combustion of carbon precursors, such as natural gas, at elevated temperatures and in an inert atmosphere or an inadequate air supply. Graphite, bio-derived carbon are also

potential members in the list which can also increase the conductivity of the composite significantly. Typically, sulfur is vaporized in presence of these carbon hosts and then cooled down. Zhang *et al.* suggested to remove the sulfur on the outer surface in carbon host by heating it[5]. The loading of sulfur depends on porosity present in the matrix which in turn dictates the performance of the cathode. The optimal pore size required for excellent performance in Li-S batteries is not fully understood. However, a rough guideline might be deduced: (a) mesoporous and macroporous carbon (pore size more than 2 nm) are good in sulfur loading but poor in cycling stability; (b) small micropores (less than 0.5 nm) are advantageous in utilization of sulfur and good cycling stability but it has limitation in sulfur loading on it; (c) large micropores (i.e. 0.5 nm to 2 nm) are found to be non-suitable for designing the sulfur-carbon composite[6].

Another candidate with which composite can be made efficiently is carbon nanotubes (CNT). Cheng *et al.*[7] demonstrated loading of elemental sulfur on CNT by crushing the sulfur powder in ball mill along with CNT. The CNT bundles were acting as conducting medium in those heavily sulfur loaded CNTs. Since sulfur particles were on top of the nanotubes, cycleability of the composite was poor even though the interconnected CNTs provide a robust conductive network. The group observed a discharge capacity of around 560 mAhg^{-1} . Free standing 3D graphene were fabricated by Papandrea *et al.*[8] on which 90 wt% sulfur could be loaded. These interconnected graphene network ensured superior electronic conductivity and the pores therein allowed extra loading of sulfur. The electrolyte also could seep into the structure which helps in migration of Li ion. However, the structure could also trap the polysulfides form during lithiation reaction. This sulfur and 3D graphene composite is capable to deliver a high discharge capacity of 969 mAh g^{-1} . Lu and co-workers prepared a self-supported graphene sponges using hydrothermal reduction followed by freeze drying. The conductivity of 3D GO sponge is very high and the carbon network can support the conductivity whereas sulfur can be incorporated inside carbon pores. The pores present in GO sponge also ensure electrolyte percolation, which essentially improve sulfur utilization. Interestingly, the areal mass loading in this kind of structure is around $12 \text{ mg sulfur/cm}^2$ which is more than commercial requirement. In this case high aerial capacity of the cathode could be achieved. Moreover, the authors observed slow decay rate (0.08% per cycle at 0.1C) after 300 cycles. In addition to 3D graphene sponge researchers are also involved in development of interlayer of graphitic nitride coated on carbon fibre.

Thereafter, many researchers have reported engineering of structure of graphene for further improvisation of electrochemical properties of Li-S batteries. In this context, nitrogen doped 3D graphene has also been used as host matrix for sulfur[10]. In addition, to the modification of the cathode, attempts have also been made to trap lithium polysulfides (LiPS) on the interlayer of graphitic carbon nitride ($\text{g-C}_3\text{N}_4$) coated on carbon fiber paper (CFP). The resulting as-fabricated Li-S battery provided outstanding stability over 400 cycles with a reversible capacity of 1271 mAhg^{-1} at 0.1C. The capacity fading (only 0.068% per cycle) was found to be much lower than the self-supporting graphene sponges reported by Lu and co-workers[9].

Conducting polymers like polypyrrole (Ppy), polyaniline (PANI) are also widely used to fabricate yolk-shell type configuration. Conducting polymers helps to improve the electronic conductivity and also act as buffer to compensate the volume variation during charge-discharge[11].

Another approach at cathode side is insertion of graphene-based interlayer to reduce the dissolution of LiPS. Huge capacity retention could be observed in case of cells where interlayers have been introduced. It has been demonstrated by *Su et al.*[12] that sulfur cathode with high sulfur loading can show good cycling stability in presence of interlayers. Sulfur sandwiched between two graphene membrane is another suitable configuration. One graphene membrane with sulfur coating acts as current collector and other graphene layer was deposited on commercial separator. Sulfur loading on current collector graphene layer was around 70% of total weight. The cell with this configuration delivers specific capacity of 750 mAh/g at current density 6 A/g which is 50 times higher than that of cell using aluminium current collector and polymer separator[13]. It is important to mention that addition of conductive interlayer increases the overall performances of Li-S battery, however, the weight of the interlayer should be considered during calculation of weight of cathode. The dead mass of inactive component increases the overall weight of the cathode which leads to decreased sulfur content in the cathode. Hence, the dimension and density of the conductive interlayer should be selected judiciously.

Research on Cathode Materials

Mostly, researchers are involved in modification of cathode material with superior life cycle, higher capacity, higher loading of sulfur in lithium-sulfur battery. Relatively, lesser attention has been paid towards anode material of LSB. Metallic lithium is most suitable choice as anode material for LSB. However, the issues arising due to formation of dendrite, formation of SEI layer in first few cycles, volume variation, short cycle life etc. need to be addressed. There are three important aspects for stabilization of lithium anode: (1) stabilization of Li-electrolyte interface (2) a 3D lithium host (3) a lithiophilic lithium host. A brief introduction to other kind of anode, i.e. carbon and silicon has also been given.

The lithium anode reacts swiftly with organic electrolytes inside the cell, therefore, it needs to be passivated. In order to do that mostly research is done more extensively in electrolyte material. Most of the articles focus on variation of components of the electrolytes or addition of oxidizing agents like LiNO_3 in it[14–16].

In order to stabilize the interface between lithium anode and electrolyte, addition of lithium nitrate to ether-based electrolyte is found to be more effective in improving Coulombic efficiency and cycle life. LiNO_3 helps to form a passivation layer on the lithium anode, which prevents further reactions between lithium and polysulfides. However, addition of LiNO_3 does not have much effect in suppression of dendrite formation. Although it is very difficult to form sufficiently sturdy passivation layers on lithium anode in liquid electrolytes, a self-healing electrostatic shielding mechanism has been proposed by *Ding et al.* [17] In this work, additives like Cs/Rb has been used in the electrolyte which get easily reduced before Li ions get reduced to Li metal. These lead to lesser amount of dendrite formation during charge-discharge.

Another approach to modify the anode is introduction of mechanically stable artificial layers, such as polymer or solid-state blocking layers[18,19] to block the dendrite penetration. The interfacial layer suppresses the dendrite formation probability by reducing the activity of lithium anode. This also increases the coulombic efficiency. In this way, the dendrite is physically separated to avoid piercing the separator, however, the true nature of lithium anode could not be avoided.

Another approach is to use 3D lithium host instead of

planer lithium sheet. Generally, lithium dendrites grow on lithium surface due to inhomogeneous deposition of lithium ions on it. In this regard, 3D host copper is found to show promising behaviour in preventing dendrite growth[20].

Lithium anode undergoes volume variation due to lithium plating/stripping, and as a result of that the lithium surface gets pulverized after long cycling. SEI layer on the lithium surface can take care of the dimensional variation of the anode; however, during lithiation and delithiation the SEI layer breaks down which again form in the subsequent cycles. As a result of that electrolyte gets consumed continuously which also increases the possibility of dendrite growth. It would be beneficial to build a host matrix which has excellent lithium affinity (lithiophilicity) for metallic lithium. Lin et al. introduced molten lithium inside the rGO layers[21]. It has been observed that the surface of Li-rGO film does not change with lithium loading. The volume variation of the anode was also found to be relatively lower. They also observed that after long cycling, the cell with planer lithium anode shows a voltage drop due to short circuit whereas the cell with infused lithium in rGO shows better stability. Also, the voltage hysteresis arising in the cell where rGO-Li film has been used is found to be comparatively lower.

Several alternative anodes have been considered in recent past in place of pure lithium to reduce the activity of lithium. For example, *Brückner et al.*[22] demonstrated that a sufficiently stable Li-S cell could be fabricated using silicon-carbon (Si-C) composite as anode. It has been observed that when the cell is made with sulfur cathode and pristine lithium anode, the cell was able to achieve reversible cycling for 135 cycles at 167mA g^{-1} . However, when the same cathode could not be cycled at higher current density which might be due to rapid electrolyte depletion and formation of unstable SEI layers. On the other hand, the cell with sulfur cathode and pre-lithiated Si-C shows stability for more than 1300 reversible cycles with high Coulombic efficiency nearly 99%. Pre-lithiated carbon is also used as anode in some cells which shows excellent cycle ability for more than 500 cycles. However, the pre-lithiated carbon has higher potential compared to pure lithium which decreases with overall energy density.

Research on Electrolyte Materials

Electrolyte is a very important part of Li-S battery as carbonate-based solvent is found to be inferior in this case. However, carbonate base solvent does not cause much problems in case of short chain sulfur cathode. In case of Li-S battery, it is observed that ether-based solvents are superior to carbonate based solvent as dissolution and redeposition of polysulfides is faster in ether based solvent which enables better sulfur utilization. However, the formation of polysulfides cannot be restricted using these ether-based electrolytes. For optimum performance of LSB there are two important aspects viz. electrolyte concentration and electrolyte amount (Electrolyte/Sulfur ratio)

Electrolyte concentration

Dissolution of lithium polysulfides in electrolyte is a serious problem which not only decreases the specific capacity but also reduces the Coulombic efficiency. It is expected that the solubility of LiPS will decrease in presence of highly concentrated electrolyte due to common ion effect. A study has been carried out by *Suo et al.*[23] to investigate the impact of concentration of electrolyte on electrochemical performance of cells. In their experiment, they used highly concentrated (7 mol/l) electrolyte and found limited dissolution of LIPS which results enhanced cycling stability. Also, they observed poor

Coulombic efficiency of the cell with low concentration of electrolyte. It is established now that highly concentrated electrolyte is beneficial for electrochemical performance; however, it comes with its own set of drawbacks. Firstly, highly concentrated electrolyte leads to higher viscosity and as a result of that the cell exhibit lower output voltage. Secondly, higher concentration also means higher unwanted weight of electrolyte which ultimately decreases the overall energy density. Third disadvantage is that the higher electrolyte concentration is not cost effective.

Electrolyte amount

It is very important to use optimum amount of electrolyte to get higher energy density. Lower amount of electrolyte ensures relatively lesser dissolution of LiPS which increases the cycle-life. However, lower amount of electrolyte results in sluggish migration of lithium ion due to poor wetting of separator. On the other hand, cells with higher E:S (electrolyte and sulfur) ratio leads to lower gravimetric and volumetric energy densities. However, cells with excess electrolyte can improve the overall cycle life because the electrolyte will get depleted quickly as the depletion of electrolyte is one of the main reasons for failure of cell. It has been established by *Zheng et al.*[24] that E/S ratio should be 20 $\mu\text{l}/\text{mg}$ (electrolyte concentration 50 g/L).

Solid or polymeric gels are also found to be suitable option to be used as electrolyte. Solid electrolyte is superior to liquid counterpart with respect to LiPS dissolution, thermal stability, mechanical stability, non-flammability etc. Mostly, compositions from $\text{Li}_2\text{S-P}_2\text{S}_5$ solution are chosen as electrolyte in all solid-state Li-S battery. *Nagata et al.*[25] have reported that a cell comprised of carbon/S composite as cathode, Li-In alloy as anode and $\text{Li}_2\text{S-P}_2\text{S}_5$ solid solution as electrolyte could be cycled for more than 100 cycles with capacity 1600 mAhg^{-1} .

Summary

The issues with Li-S battery have been partially sorted out so far; however, lot of works needs to be done before this technology becomes viable for large-scale application. Most Li-S batteries reported sofar contains cathode with relatively lower sulfur loadings and excess electrolyte. This leads to cells having lower energy density and power density which cannot outperform the existing state-of-the-art LIBs.

Novel conducting materials need to be searched for better electrochemical performance. Also, the parameters like sulfur loading, electrolyte to sulfur ratio need to be optimized to realize higher energy density in LSB. The research on overall engineering of Li-S battery packaging needs to be emphasized. In the anode side, more work should be focused towards suppression of dendrite formation, stabilization of SEI layer and improvement of safety of lithium anode.

References

- [1] Grosjean, C.; Miranda, P. H.; Perrin, M.; Poggi, P. Assessment of World Lithium Resources and Consequences of Their Geographic Distribution on the Expected Development of the Electric Vehicle Industry. *Renew. Sustain. Energy Rev.*, 2012, 16 (3), 1735–1744.
- [2] Wang, L.; Zhao, Y.; Thomas, M. L.; Byon, H. R. In Situ Synthesis of Bipyramidal Sulfur with 3D Carbon Nanotube Framework for Lithium–Sulfur Batteries. *Adv. Funct. Mater.*, 2014, 24 (15), 2248–2252.
- [3] Sun, M.; Zhang, S.; Jiang, T.; Zhang, L.; Yu, J. Nano-Wire Networks of Sulfur–Polypyrrole Composite Cathode Materials for Rechargeable Lithium Batteries. *Electrochem. Commun.*, 2008, 10 (12), 1819–1822.
- [4] Greenwood, N. N.; Earnshaw, A. *Chemistry of the Elements*, Elsevier, 2012.
- [5] Zhang, B.; Lai, C.; Zhou, Z.; Gao, X. P. Preparation and Electrochemical Properties of Sulfur–Acetylene Black Composites as Cathode Materials. *Electrochimica Acta*, 2009, 54 (14), 3708–3713.
- [6] Liang, J.; Sun, Z.-H.; Li, F.; Cheng, H.-M. Carbon Materials for Li–S Batteries: Functional Evolution and Performance Improvement. *Energy Storage Mater.*, 2016, 2, 76–106.
- [7] Cheng, X.-B.; Huang, J.-Q.; Zhang, Q.; Peng, H.-J.; Zhao, M.-Q.; Wei, F. Aligned Carbon Nanotube/Sulfur Composite Cathodes with High Sulfur Content for Lithium–Sulfur Batteries. *Nano Energy*, 2014, 4, 65–72.
- [8] Papandrea, B.; Xu, X.; Xu, Y.; Chen, C.-Y.; Lin, Z.; Wang, G.; Luo, Y.; Liu, M.; Huang, Y.; Mai, L.; Duan, X. Three-Dimensional Graphene Framework with Ultra-High Sulfur Content for a Robust Lithium–Sulfur Battery. *Nano Res.*, 2016, 9 (1), 240–248.
- [9] Lu, S.; Chen, Y.; Wu, X.; Wang, Z.; Li, Y. Three-Dimensional Sulfur/Graphene Multifunctional Hybrid Sponges for Lithium-Sulfur Batteries with Large Areal Mass Loading. *Sci. Rep.*, 2014, 4 (1), 4629.
- [10] Wutthiprom, J.; Phattharasupakun, N.; Sawangphruk, M. Designing an Interlayer of Reduced Graphene Oxide Aerogel and Nitrogen-Rich Graphitic Carbon Nitride by a Layer-by-Layer Coating for High-Performance Lithium Sulfur Batteries. *Carbon*, 2018, 139, 945–953.
- [11] Dutta Pathak, D.; Mandal, B. P.; Tyagi, A. K. A New Strategic Approach to Modify Electrode and Electrolyte for High Performance Li–S Battery. *J. Power Sources*, 2021, 488, 229456.
- [12] Su, Y.-S.; Manthiram, A. Lithium–Sulphur Batteries with a Microporous Carbon Paper as a Bifunctional Interlayer. *Nat. Commun.*, 2012, 3 (1), 1166.
- [13] Zhou, G.; Pei, S.; Li, L.; Wang, D.-W.; Wang, S.; Huang, K.; Yin, L.-C.; Li, F.; Cheng, H.-M. A Graphene–Pure-Sulfur Sandwich Structure for Ultrafast, Long-Life Lithium–Sulfur Batteries. *Adv. Mater.*, 2014, 26 (4), 625–631.
- [14] Weng, W.; Pol, V. G.; Amine, K. Ultrasound Assisted Design of Sulfur/Carbon Cathodes with Partially Fluorinated Ether Electrolytes for Highly Efficient Li/S Batteries. *Adv. Mater.*, 2013, 25 (11), 1608–1615.
- [15] Li, W.; Yao, H.; Yan, K.; Zheng, G.; Liang, Z.; Chiang, Y.-M.; Cui, Y. The Synergetic Effect of Lithium Polysulfide and Lithium Nitrate to Prevent Lithium Dendrite Growth. *Nat. Commun.*, 2015, 6 (1), 7436.
- [16] Qian, J.; Henderson, W. A.; Xu, W.; Bhattacharya, P.; Engelhard, M.; Borodin, O.; Zhang, J.-G. High Rate and Stable Cycling of Lithium Metal Anode. *Nat. Commun.*, 2015, 6 (1), 6362.
- [17] Ding, F.; Xu, W.; Graff, G. L.; Zhang, J.; Sushko, M. L.; Chen, X.; Shao, Y.; Engelhard, M. H.; Nie, Z.; Xiao, J.; Liu, X.; Sushko, P. V.; Liu, J.; Zhang, J.-G. Dendrite-Free Lithium Deposition via Self-Healing Electrostatic Shield Mechanism. *J. Am. Chem. Soc.*, 2013, 135 (11), 4450–4456.
- [18] Kang, I. S.; Lee, Y.-S.; Kim, D.-W. Improved Cycling Stability of Lithium Electrodes in Rechargeable Lithium Batteries. *J. Electrochem. Soc.*, 2013, 161 (1), A53.
- [19] Zheng, G.; Lee, S. W.; Liang, Z.; Lee, H.-W.; Yan, K.; Yao, H.; Wang, H.; Li, W.; Chu, S.; Cui, Y. Interconnected Hollow Carbon Nanospheres for Stable Lithium Metal Anodes. *Nat. Nanotechnol.*, 2014, 9 (8), 618–623.
- [20] Yang, C.-P.; Yin, Y.-X.; Zhang, S.-F.; Li, N.-W.; Guo, Y.-G. Accommodating Lithium into 3D Current Collectors with a Submicron Skeleton towards Long-Life Lithium Metal Anodes. *Nat. Commun.*, 2015, 6 (1), 8058.

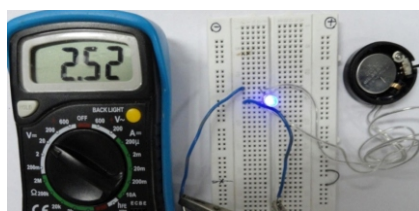
- [21] Lin, D.; Liu, Y.; Liang, Z.; Lee, H.-W.; Sun, J.; Wang, H.; Yan, K.; Xie, J.; Cui, Y. Layered Reduced Graphene Oxide with Nanoscale Interlayer Gaps as a Stable Host for Lithium Metal Anodes. *Nat. Nanotechnol.* 2016, 11 (7), 626–632.
- [22] Brückner, J.; Thieme, S.; Böttger-Hiller, F.; Bauer, I.; Grossmann, H. T.; Strubel, P.; Althues, H.; Spange, S.; Kaskel, S. Carbon-Based Anodes for Lithium Sulfur Full Cells with High Cycle Stability. *Adv. Funct. Mater.* 2014, 24 (9), 1284–1289.
- [23] L. Suo, Y. S. Hu, H. Li, M. Armand, L. Chen, *Nat. Commun.* 2013, 4, 1481
- [24] Zheng, J.; Lv, D.; Gu, M.; Wang, C.; Zhang, J.-G.; Liu, J.; Xiao, J. How to Obtain Reproducible Results for Lithium Sulfur Batteries? *J. Electrochem. Soc.* 2013, 160 (11), A2288.
- [25] Nagata, H.; Chikusa, Y. A Lithium Sulfur Battery with High Power Density. *J. Power Sources* 2014, 264, 206–210.

Solid State Lithium Cell

Development of NASICON based Solid State Electrolyte for Li-battery Application

Anurup Das*, Madhumita Goswami and Ashok Arya

Glass & Advanced Material Division, Bhabha Atomic Research Centre, Mumbai 400085, INDIA



Demonstration of coin-type solid state lithium cell using synthesized LAGP glass ceramics.

ABSTRACT

All-Solid-State-Lithium Batteries (ASSLBs) are getting attentions because of their promising high energy density and safety characteristics. These batteries can provide better safety by preventing the internal short-circuit as compared to currently used liquid electrolyte in commercial batteries. Among others, inorganic oxide Solid State Electrolyte (SSE), such as, NASICON based $\text{Li}_2\text{O-Al}_2\text{O}_3\text{-GeO}_2\text{-P}_2\text{O}_5$ (LAGP) has certain advantages over others for use in ASSLBs. In this work LAGP glass was prepared using melt-quench technique and converted into glass-ceramics by controlled heat treatment. Phase formation was confirmed using XRD (X-ray diffraction) and ND (Neutron diffraction). Rietveld refinement analysis was used for structural analysis using both ND and XRD data. Bottleneck for Li^+ ion conduction found to increase on substitution of Al^{3+} making an easier path for Li^+ migration. Impedance spectroscopy was used to evaluate the d.c. ionic conductivity and the value found was $2.48 \times 10^{-4} \text{Scm}^{-1}$ at room temperature. Cells were fabricated with LiFePO_4 (LFP) as cathode and Li metal as anode. The cell operated successfully giving capacity of 130mAhg^{-1} with coulombic efficiency of 99% at 0.05C ($1\text{C}=170 \text{mAhg}^{-1}$) at the initial stage of Li-cells fabrication.

KEYWORDS: Solid state electrolyte, NASICON, Li-ion solid state battery

Introduction

Lithium ion batteries (LIBs) play important role in recent years for their applications as energy storage device in various electronic gadgets. However, LIBs suffer with various shortcomings: (a) internal short circuit (b) fire or explosion at high temperature because of the uses of the flammable liquid electrolyte etc[1]. To avoid all these issues pertaining to conventional LIBs, ASSLBs are considered as the safest alternative[2]. ASSLBs have mainly three components: cathode, anode and solid-state-electrolyte (SSE). The charging and discharging mechanism is same as LIBs. During the charging, lithium ion transferred from cathode to anode through SSE and during the discharge process exactly reverse phenomenon takes place[3]. SSEs are mainly two types: organic and inorganic. Despite of several advantages of organic SSE, it has few drawbacks like narrow temperature range and poor structural stability, whereas inorganic SSEs can have improved stability and safety over wide temperature range. A promising SSE should have high ionic conductivity, thermal and electrochemical stability. Lithium ions hop from one stable position to another inside the SSE. Therefore, the ion diffusion mainly related to the crystal lattice of the SSE. The ion migration channel can be widened by doping. Among other inorganic SSEs, oxide SSEs are more environment friendly and have ease of processing. These kind of materials are mainly polycrystalline, where the lithium ion migrates through two regions: grain and grain boundary. The movement is slow inside grain boundary as compared to the grain. Therefore, the oxide SSEs should have large and dense grains[4]. Among other oxides (i.e. perovskite, garnet etc.) Li-based NASICON

(**NaSuper-Ionic Conductor**) type materials ($\text{LiM}^{(IV)}_2(\text{PO}_4)_3$, $\text{M}^{(IV)}$: Ge, Ti, Zr etc.) show high ionic transport properties and find a potential application in ASSLBs as SSE[5]. In this work we report synthesis of $\text{Li}_2\text{O-Al}_2\text{O}_3\text{-GeO}_2\text{-P}_2\text{O}_5$ (LAGP) glass ceramics with right amount of required phases and electrical conductivity value. The process parameters were optimised for synthesis of the LAGP glass ceramics and characterised for thermal, structural and electrical properties for use in Li battery.

Synthesis of Glass/Glass Ceramics

Glass sample with composition of $\text{Li}_{1.5}\text{Al}_{0.5}\text{Ge}_{1.5}\text{P}_{2.9}\text{Si}_{0.1}\text{O}_{12}$ (LAGP) was prepared by standard melt-quench technique. Each batch of 100g weight was prepared by taking initial constituents (Li_2CO_3 , Al_2O_3 , GeO_2 , SiO_2 , $\text{NH}_4\text{H}_2\text{PO}_4$), in the form of carbonate and di-ammonium hydrogen phosphate proportionately. The charge was calcined by holding the batch at decomposition temperature of each initial constituent for sufficient time. The calcination process was repeated to ensure complete decomposition after through mixing & grinding. The calcined charge was mixed and ground properly and melted in a Pt-Rh crucible at around 1450-1550°C. The melt was held at the melting temperature for 1-2 hrs for homogenization and poured on a metal plate. The glass was annealed at around 400-450°C for 4-6 hrs and cooled down to room temperature slowly.

Characterization

The annealed glasses were powdered, and differential thermal analysis measurements were carried out using a TGA/DTA instrument. Solid glass samples were taken for the DTA scan to avoid the dependency of crystallization on the particle size distribution. DTA scans were recorded at the

*Author for Correspondence: Anurup Das
E-mail: anurup@barc.gov.in

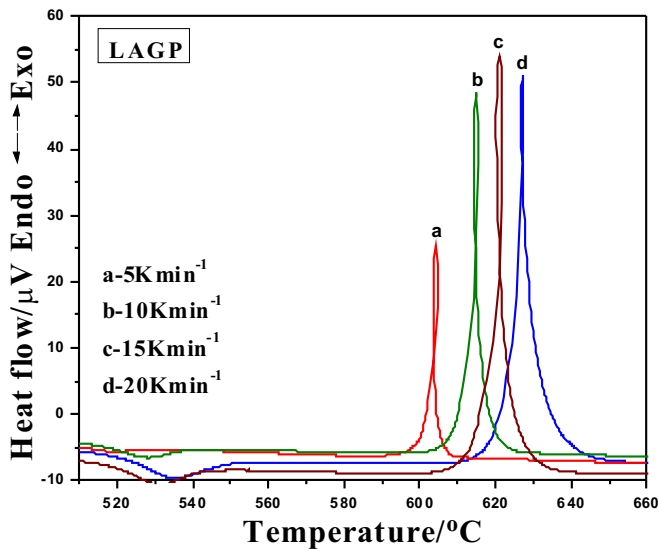


Fig.1: DTA scans for LAGP glass sample at different heating rates.

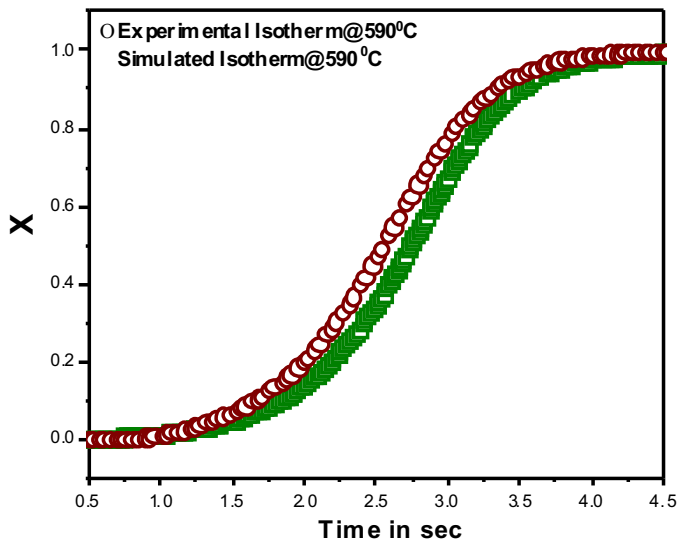


Fig.2: Simulated and experimental isotherms at 590°C.

heating rates of 5, 10, 15, 20 and 25K min⁻¹. The samples were scanned up to maximum 900°C. Based on the DTA data, the glass samples were heated at different temperatures: 600, 650, 700, 750 and 800°C for one hour to convert into glass-ceramics. Nature of glassy and crystalline phases formed in the base glass and glass ceramics (GC) samples were identified using powder X-ray diffractometric technique (XRD) with Cu K_α was used as radiation source. The impedance measurements were carried out in the frequency range of 1-10⁶Hz at room temperature. Conductivity studies showed that the sample heat treated at 700°C for one hour, exhibited highest value of d.c. ionic conductivity at room temperature among others. Therefore, further characterizations and cell testing were carried out on this sample only. For the detailed structural characterization, neutron diffraction data was collected with the linear 5-PSD based powder diffractometer at 100MW Dhruva Research Reactor in BARC Trombay in the two-theta range of 8–135°. Galvanostatic charge/discharge experiment was performed using automatic battery analyzer.

Results and Discussion

DTA analysis

Fig.1 shows the DTA scans of LAGP glass sample for different heating rate. Figure shows onset of a broad

endotherm at around 520°C indicating the glass transition temperature (T_g). The endotherm is followed by a sharp and intense exothermic peak called peak crystallization temperature (T_p) at around 600°C for 5Kmin⁻¹. In addition, a small loop was observed at the middle of the exothermic peak in the DTA scan which suggests a certain ‘self-feeding’ reaction, in this system. It suggests existence of some endothermic reaction along with the crystallization process[6]. Using the model free kinetics analysis an isotherm at 590°C was simulated using AKTS software and compared with the experimental data. Fig.2 shows the crystallized volume fraction (x) versus time (t) plot of the simulated and experimental isotherms. Simulated data obtained almost follow the experimental data within error.

Joint Rietveld Refinement

Joint Rietveld refinement was carried out with the collected XRD and ND data using Full Prof software. This gives us a structural model agreeing with both XRD and ND data giving us high confidence in the obtained model. Joint Rietveld refinement was carried out with the model based on the typical NASICON structure: space group R-3c and unit cell parameters given in ICSD file of pure LiGe₂(PO₄)₃. The observed and calculated neutron and X-ray diffraction patterns are shown in Fig.3 and Fig.4.

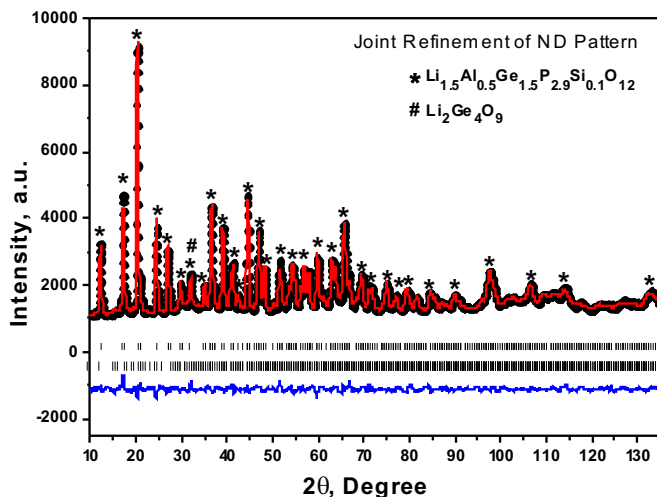


Fig.3: Experimental (+) and calculated (-) neutron diffraction pattern. The difference profile is given at bottom. The Bragg positions are indicated by vertical marker below the observed pattern.

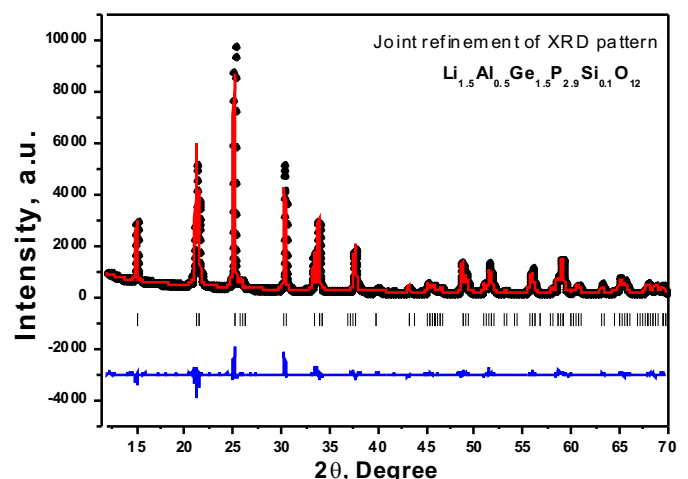


Fig.4: . Experimental (+) and calculated (-) X-ray diffraction pattern. The difference profile is given at bottom. The Bragg positions are indicated by vertical marker below the observed pattern.

Table 1

| Joint Refinement of ND and XRD | |
|--------------------------------|---|
| Molecular formula | $\text{Li}_{1.5}\text{Al}_{0.5}\text{Ge}_{1.5}\text{P}_{2.9}\text{Si}_{0.1}\text{O}_{12}$ |
| Molecular weight | 417.47u |
| Spacegroup | R-3c |
| Unit cell parameters | |
| a | 8.2682(9) Å |
| b | 8.2682(9) Å |
| c | 20.668(3) Å |
| Volume (unit cell) and Z | 1412.14 Å ³ , 6 |
| Density (Calculated) | 3.42 gm/cc |
| Profile | Pseudo-Voigt |
| Goodness of fit (χ^2) | 1.87 |
| R_{wp}, R_{exp} | ND: 3.35%, 2.45% XRD: 8.56%, 4.41% |

The details of various profile parameters and structural parameters obtained are shown in Table 1. A minor amount (0.63 wt%) of $\text{Li}_2\text{Ge}_4\text{O}_9$ impurity phase was detected in ND pattern only during the refinement, along with the major NASICON phase of 99.37% weight fraction. Simulated NASICON unit cell and its projection on b-c plane, using the joint Rietveld refinement, are shown in Fig.5(a) and Fig.5(b). Here GeO_6 octahedra and PO_4 tetrahedra are linked to each other [7]. Li^+ ions reside in two positions: M1 (0,0,0) site (6-fold co-ordination), which is directly located between two GeO_6 octahedra and M2 (0.07, 0.34, 0.08) site (8-fold co-ordination), which is located between two columns of GeO_6 .

Ionic Conductivity Studies

Fig.6 shows the variation of electrical conductivity with frequency at room temperature. From the figure, it is observed that the a.c. conductivity value varies with frequency in three

different regimes. At lower frequency region, conductivity value is quite low and there is a gradual increase in conductivity value with frequency up to the order of 104Hz. Above this region the conductivity value is almost constant with frequency up to 106Hz. This frequency independent conductivity may be thought to be due to the long-range transport of existing mobile Li^+ ion, and contributed as d.c. conductivity of the sample. In this region the conductivity is contributed primarily from the potential relaxation of ion, when the Li^+ ion hops from one equilibrium position to a new position [8].

Further, at higher frequency regime, above 106Hz, there is a dispersion and the conductivity again increases rather sharply with increase in frequency. In this region conductivity roughly increases in a power law fashion and eventually become almost linear at even higher frequencies. In low frequency region due to the accumulation of highly mobile lithium ions at the electrode surfaces, the conductivity is comparatively low. Considering the electrode polarization at low frequency region, the a.c. conductivity ($\sigma(\omega)$) can be expressed as [9]:

$$\sigma(\omega) = \sigma_{dc} - \frac{\sigma_{dc} - \sigma_0}{1 + (i\frac{\omega}{\omega_0})^\alpha} + B\omega \tag{1}$$

The real part of the above equation is:

$$\sigma'(\omega) = \sigma_{dc} - (\sigma_{dc} - \sigma_0) \frac{1 + (\frac{\omega}{\omega_0})^\alpha \cos(\frac{\alpha\pi}{2})}{1 + 2(\frac{\omega}{\omega_0})^\alpha \cos(\frac{\alpha\pi}{2}) + (\frac{\omega}{\omega_0})^{2\alpha}} + B\omega \tag{2}$$

Where, σ_{dc} is d.c. ionic conductivity, $\sigma_0 = \sigma(0)$, ω_0 is the frequency at which full development of polarization occurs, α , B are constants. Experimental conductivity data was fitted with equation (2) and shown in Fig.6. The values of the different parameters, after fitting, are given in Table 2. The value of σ_{dc} is found $2.48 \times 10^{-4} \text{ Scm}^{-1}$ which is higher as compared to other SSE.

Table 2

| σ_{dc} in Scm^{-1} | σ_0 in Scm^{-1} | ω_0 in Hz | α | B in $\frac{\text{S}}{\text{cm.Hz}}$ |
|------------------------------------|---------------------------------|--------------------|----------|--------------------------------------|
| 2.48×10^{-4} | 2.09×10^{-5} | 3.03×10^3 | 0.066 | 4.07×10^{11} |

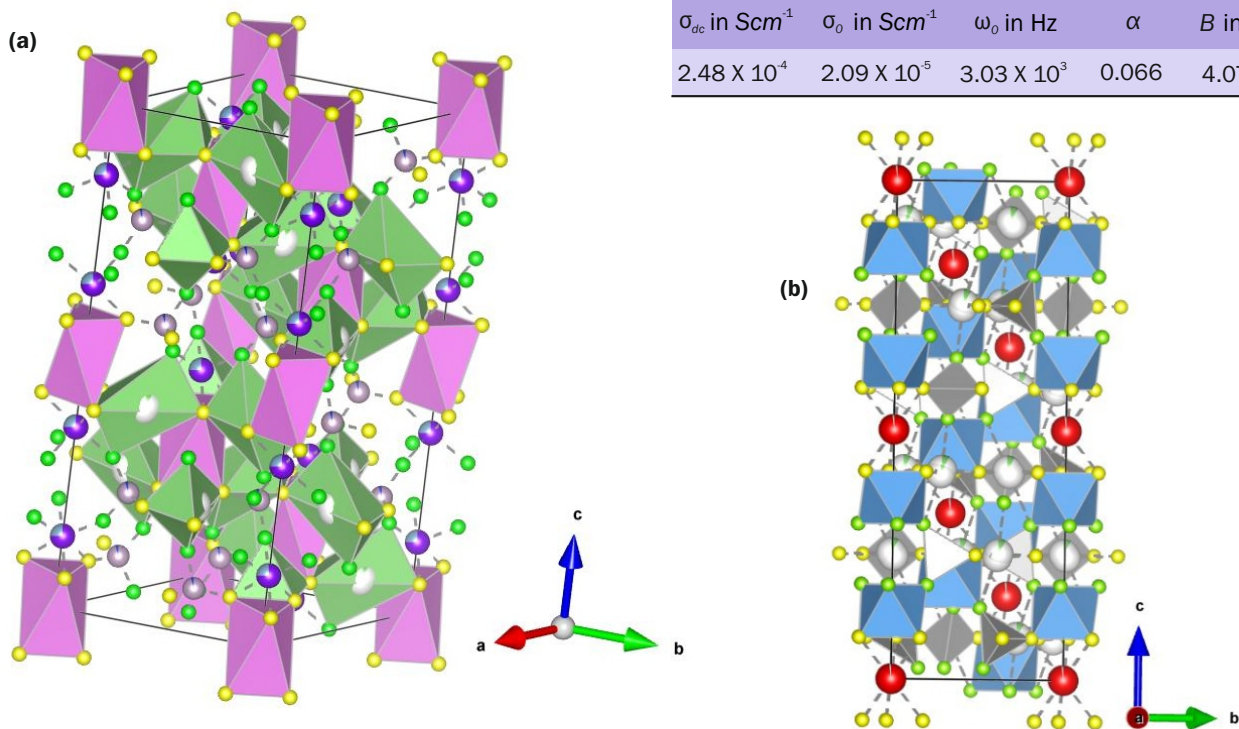


Fig.5: (a) Unit cell obtained from joint Rietveld refinement of ND and XRD for LAGP. Li1 atoms reside at the center of the pink polyhedral which is also known as trigonal antiprism and Li2 atoms situated at the center of the green polyhedra. Blue, violet, green and yellow atoms are Ge, P, O1 and O2 respectively. (b) Projection of the unit cell on bc plane. GeO_6 -octahedra and PO_4 -tetrahedra are shown in blue and grey colour respectively. Red, white, green and yellow atoms are Li1, Li2, O1 and O2 respectively.

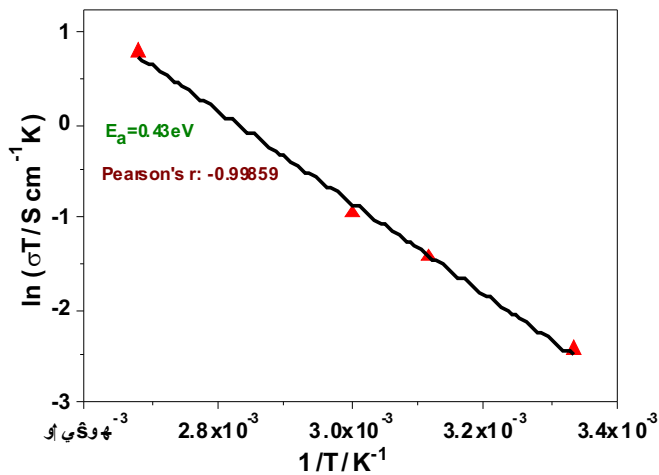


Fig.6: Variation of A.C. electrical conductivity (σ') with frequency at room temperature.

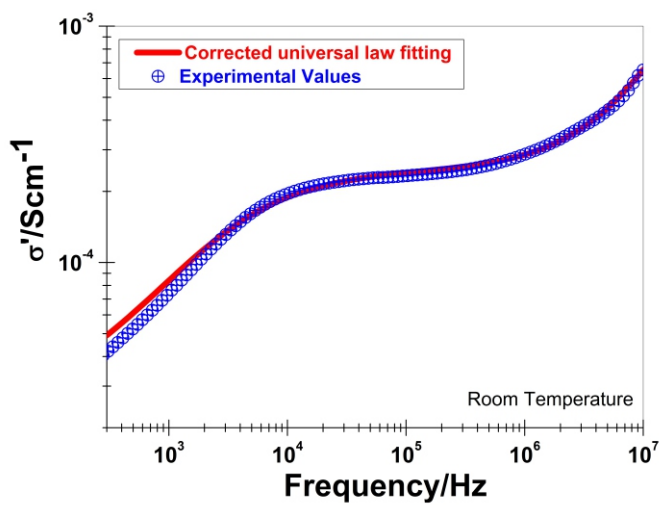


Fig.7: $\ln(\sigma T)$ versus $1/T$ plot.

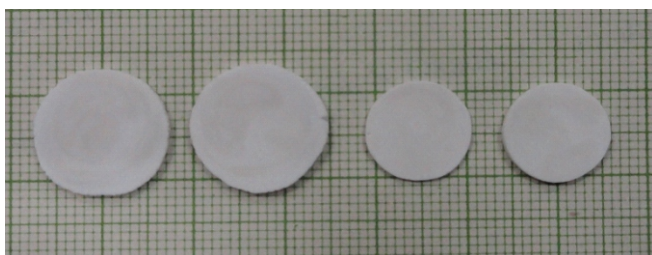


Fig.8: LAGP glass ceramics disks of various dimensions (Diameter: 12mm, Thickness: 0.7mm).

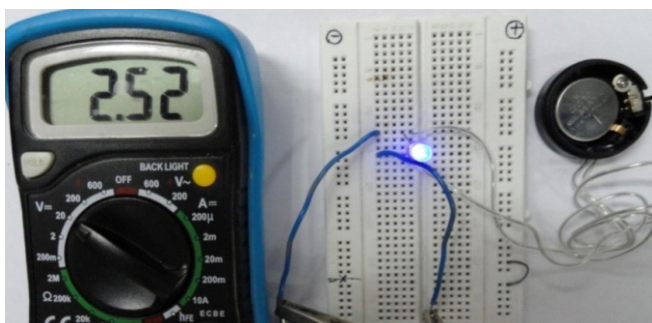


Fig.9: Demonstration of coin-type solid state lithium cell using synthesised LAGP glass ceramics.

The d.c. ionic conductivities at different temperatures were also measured to evaluate the activation energy of ionic conduction (E_a). The temperature was varied from 300K to 373K. The relation between σ_{dc} and E_a is given below:

$$\sigma_{dc}(T) = \frac{A}{T} \exp\left(-\frac{E_a}{kT}\right) \quad (3)$$

Where, A is the pre-exponential factor and k is the Boltzmann constant. From the slope of $\ln(\sigma_{dc}T)$ versus $1/T$ plot the value of E_a (see Fig.7) was calculated.

Cell Fabrication and Testing

Coil cell was fabricated using LiFePO_4 as cathode and lithium metal as anode. The loading of the active material on cathode was 9.47mgcm^{-2} . LFP/LAGP/Li cell was assembled with 2032-coin cell inside argon filled glove-box. Fig.8 shows the photographic image of the LAGP SSEs in disc forms. The demonstration of cell testing using blue LED light is shown in Fig.9 in which the voltage shown in the multimeter is the 'closed circuit voltage' in Volt unit.

Fig.10 shows first three cycles of galvanostatic charge-discharge profiles of LFP/LAGP/Li cell in the voltage range of 2.6 to 4.0V at a constant current rate of 0.05C. The voltage plateau is nearly at 3.63V for charging and at 3.21V for discharging of the first cycle at 0.05C.

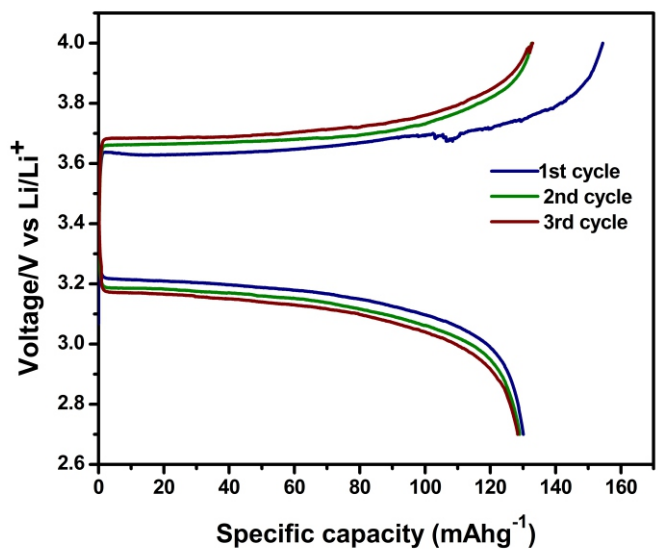


Fig.10: The galvanostatic charge and discharge curves of LFP/LAGP/Li cell at 0.05C at room temperature.

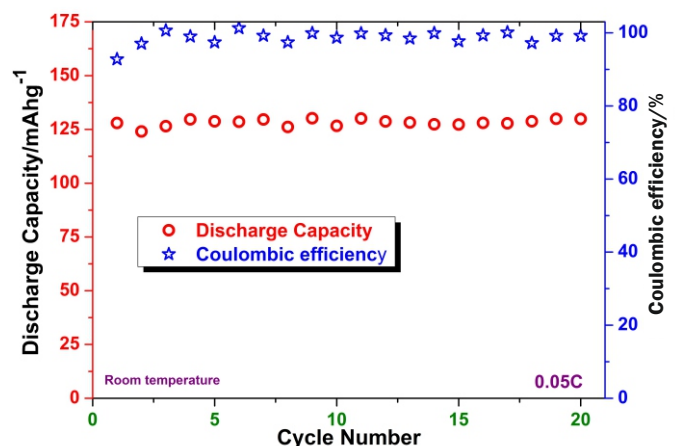


Fig.11: Cyclic performance of specific discharge capacity and coulombic efficiency of the cell at 0.05C at room temperature.

At the first charging cycle, the specific capacity calculated is 154mAhg^{-1} which is approximately 90% of the theoretical capacity (170mAhg^{-1}) and after that the charge and discharge capacities are almost fixed at nearly 130mAhg^{-1} (approximately 76% of theoretical capacity). Fig.11 depicts the values of discharge capacity and coulombic efficiency at different cycles. The capacity retention up to 20th cycle is almost 100% which reveals that LAGP can be used in solid state Lithium ion batteries.

Conclusion

DTA study was used to predict the process parameters for conversion of glass to glass ceramics. Model free crystallization kinetics was performed to simulate isotherm of LAGP glass. This simulated isotherm almost matches with the experimental one. XRD and ND confirm the formation of Lithium Germanium Phosphate (LGP), NASICON phase in the Glass ceramic system. Joint Rietveld refinement of ND and XRD shows quite accurate structure of the crystal. The predicted amount of NASICON phase was 99.37% obtained from the refinement. For its higher ionic conductivity ($2.48 \times 10^{-4}\text{Scm}^{-1}$), it can be used as SSE in ASSLBs. The value of activation energy of ionic conduction (E_a) obtained is 0.43eV which is small enough to provide high ionic conduction in LAGP SSE. Performance of the solid state cell exhibited a good capacity retention (almost 100%) and coulombic efficiency. The cell showed a stable voltage of 3.42V.

Acknowledgements

Authors wish to thank PSR Krishna of Solid State Physics Division, BARC, for providing neutron diffraction facility. Technical help from Anupam Dixit and Radhakrishnan Nair, Glass & Advanced Material Division, BARC is gratefully acknowledged.

References

- [1] N. Kamaya, K. Homma, Y. Yamakawa, M. Hirayama, R. Kanno, M. Yonemura, T. Kamiyama, Y. Kato, S. Hama, K. Kawamoto, A. Mitsui, *Nat Mater*, 2011, 10, 682.
- [2] M. Tatsumisago, M. Nagao, A. Hayashi, *J. Asian Ceram. Soc.*, 2013, 1, 17.
- [3] B. Scrosati, G. Jürgen, *Lithium batteries: status, prospects and future*, *J. Power Sources*, 2010, 195, 2419–2430.
- [4] X. Yao, B. Huang, J. Yin, G. Peng, X. Xu, *All-solid-state lithium batteries with inorganic solid electrolytes: review of fundamental science*, *Chin. Phys. B*, 2016, 25, 018802.
- [5] L. Shi-Chun, L. Zu-Xiang, *Solid State Ion.*, 1983, 10, 835.
- [6] Speyer RF. *Kinetics of phase transformations in amorphous materials by DSC. Part I. Thermochim Acta.*, 1988, 131, 211.
- [7] H.Y.P. Hong, *Mater. Res. Bull.*, 1976, 11, 173-182.
- [8] K. Funke, R. Hoppe, *Jump-relaxation model yields Kohlrausch-Williams-Watts behaviour*, *Solid State Ion.*, 1990, 40–41, 200–204.

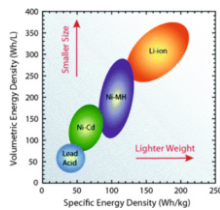
Density Functional Theory

First Principles Based Atomistic Modeling of Lithium Ion Battery

Sk. Musharaf Ali^{*1,2}, Reman Rana², Anil Boda¹, and Dilip K. Maity²

¹Chemical Engineering Division, Bhabha Atomic Research Centre, Mumbai 400085, INDIA

²Homi Bhabha National Institute, Anushaktinagar, Mumbai-400094, INDIA



Specific energy density and volumetric energy density illustrates that Li-ion batteries are ahead of most other battery types

ABSTRACT

The present article reports a review on the key materials used for making lithium ion battery. Five decades of research findings confirm that first principle based density functional theory (DFT) and classical molecular (CMD) dynamics simulations can play a decisive role for screening and design of cathodes, anodes and electrolytes. DFT and CMD simulations in conjunction with machine learning will further boost in the identification and design of next generation battery which will not be confined to only lithium but to sodium, calcium, zinc and others ions and thus offers ample scope for future research.

KEYWORDS: Energy density, Power density, Battery, Sulfur, Cycling, Electrode

Introduction

Lithium, the lightest metal, has many technological applications but one of the most commendables is as a constituent of high energy-density rechargeable Li-ion battery which was understandably awarded with Noble prize in 2019[1]. The need of rechargeable lithium-ion battery is further increased to reduce the global warming due to CO₂ generated from the burning of fossil fuels as well as to the large-scale implementation of intermittent renewable energy conversion devices like wind turbines and photovoltaics. Li metal may become even more important in large batteries for powering all-electric and hybrid vehicles which will generate huge requirement for this metal. The concept of intercalation electrodes was first discovered by Whittingham in the 1970s, who invented the first rechargeable Li-ion battery (LIB) using a Li-Al anode and titanium disulfide cathode[2] and further extended using lithium cobalt oxide as a cathode by Goodenough in 1980[3]. Subsequently, a prototype LIB was developed by Yoshino in 1985 based on the findings of Whittingham, Goodenough and Yazami[4] followed by a commercial LIB by a team led by Nishi in 1991. LIBs are commonly used for portable electronics and electric vehicles and are increasing in popularity for military and aerospace applications.

The chemistry, performance, safety and cost vary across different types of LIBs. Handheld electronics mostly use Li ion polymer batteries, LiCoO₂ cathode, and a graphite anode, which together offer a high energy density[5]. LiFePO₄, LiMn₂O₄ spinel, or Li₂MnO₃ based Li rich layered materials, LMR-NMC, and LiNiMnCoO₂ or NMC may offer longer lives and may have improved rate capability and are widely used for electric tools, medical equipment, and many others.

Working Principle of LIB

A LIB works on an advanced principle where Li ions are used as a key charge carriers (Fig.1). Li atoms in the anode are

ionized and separated from their electrons during discharge of the battery. The Li ions move from anode and pass through the electrolyte to reach the cathode, where they recombine with electrons and become electrically neutral.

Li ions are small enough to be able to move through a micro-permeable separator between cathode and anode and thus LIBs are capable of displaying a very high voltage and charge storage per unit mass and unit volume. LIBs can use a number of different materials as electrodes and typically ether as an electrolyte. LIBs have many advantages over nickel-cadmium (Ni-Cd) or nickel-metal-hydride (NiMH) rechargeable battery (Fig.2) and most prominent is the highest energy density (100-265 Wh/kg or 250-670 Wh/L) than any other battery. Also, LIB can deliver up to 3.6 V, 3 times higher than that of Ni-Cd or Ni-MH and can generate high current for high-power applications with relatively low maintenance. LIBs are not affected by memory effect, a detrimental process where repeated discharge/charge normally cause a battery to

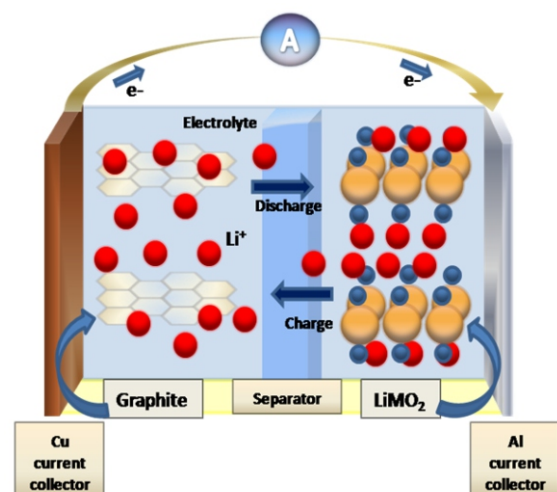


Fig.1: Schematic of Li-ion battery.

*Author for Correspondence: Sk. Musharaf Ali
E-mail: musharaf@barc.gov.in

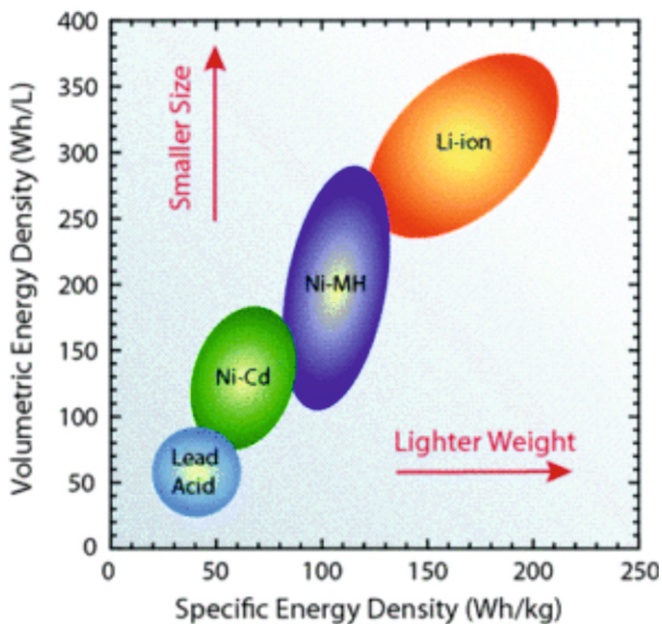


Fig.2: Specific energy density and volumetric energy density illustrates that Li-ion batteries are ahead of most other battery types.

‘remember’ a lower capacity and thus offers an advantage over both Ni-Cd and Ni-MH. LIBs also have low self-discharge rate of ~ 1.5-2% per month and easier to dispose than Ni-Cd batteries due to non-presence of toxic Cd. Owing to these advantages, LIBs not only have become the market leader in portable electronic over Ni-Cd batteries but are also used for some aerospace applications, notable in the new and more environmental friendly Boeing 787, where weight is a significant cost factor. From a clean energy perspective, much of the promise of Li-ion technology comes from their potential applications in battery-powered cars. Now, the best selling electric cars, Nissan Leaf and Tesla Model S, both use LIBs as primary fuel source.

The major research topics for LIBs include extending lifetime, increasing energy density and charging speed, improving safety, and reducing cost[6]. Extensive research are being carried out in the area of non-flammable electrolytes to avoid the flammability and volatility of the organic solvents used in the typical electrolyte that comprise aqueous LIBs, solid electrolytes, polymer electrolytes, ionic liquids, and heavily fluorinated systems.

Extensive experiments were performed and are being performed to have a superior battery than the existing one. First-principles simulations were also performed to understand the structural, dynamical and thermodynamical behaviour of various constituents of the LIB.

Key Battery Properties from Simulations

Atomistic simulations can be used to simulate the structures and properties of less understood battery materials, offering deep insight into fundamental processes that are otherwise difficult to access, such as ion diffusion and electronic structure effects. Simulations can also predict the state of charge, state of health, and cycle life of batteries, coupled with experimental measurements for real-time evaluation of battery performance. This provides a precise quantitative assessment about absolute limits for performance, such as the remaining useful life, optimal fast charging rate, and risk of short circuits/premature failures, etc.

The voltage[7], band gap[8], diffusivity[9] and ionic conductivity[10] are the major properties that are likely to decide the best battery materials and hence are used to screen the components of LIB.

Computational Protocols

Theoretical and computational modeling enables us to fundamentally understand the chemistry and physics of the components of the lithium ion battery. Primarily, atomistic models based on DFT[11], molecular dynamics (MD)[12] and continuum models[13] are being applied. These models can be used to study a wide variety of battery processes occurring at different length and time scales, including Li ion diffusion, dendrite growth, solid electrolyte interphase (SEI) formation/growth and phase separation. In this article, we discuss atomistic view of Li ion battery using DFT and MD simulations.

First-principles calculations have proven to be quite successful in predicting and elucidating qualitative trends and behavior of materials and in some cases have been able to predict chemical and physical properties to a high degree of accuracy. The multi-electron Schrodinger equation and the associated electronic wave functions of a collection of atoms provide the basic properties such as the equilibrium structure and total energy. DFT is the most widely studied approach for solving the multi-electron Schrodinger equation[14].

The electron density, for any molecular system, is a function of only three spatial coordinates (for a given set of nuclear positions). The first Hohenberg and Kohn (H-K) theorem states that the ground state energy of an N-electron system in an external potential $v(r)$ is a unique functional of its ground state electron density $\rho(r)$.

$$\rho(r_1)=N \int |\Psi(\vec{x}_1, \vec{x}_2, \dots, \vec{x}_N; \vec{R}_1, \dots, \vec{R}_N)|^2 d\sigma, d\vec{x}_2, \dots, d\vec{x}_N \quad (1)$$

The integral of the density over all space equals N. The total energy can be written as

$$E[\rho] = T[\rho] + V_{ee}[\rho] + \int \rho(\vec{r}^-) V(\vec{r}^-) d\vec{r}^- \quad (2)$$

In 1965, Kohn and Sham formulated an indirect way of evaluating the kinetic energy functional thus making the DFT an efficient method for carrying out rigorous calculations. The KS method relies on the introduction of a fictitious reference system of non-interacting electrons that is constructed to have the same electron density as the system of interest. These electrons must move in a complex potential that takes into account the actual forms of electron correlation and the difference between kinetic energy functional of the reference system and the real system. The reference system of fictitious non-interacting particles has a rigorous solution in terms of single electron wave functions, or molecular orbitals (K-S orbitals). One can express the kinetic energy exactly for the reference system as the sum of the expectation value of the Laplacian for each “electron”.

$$T_s[\rho_s] = -\frac{1}{2} \sum_{j=1}^N \langle x_j | \nabla_j^2 | x_j \rangle \quad (3)$$

Provided that the density of the real system,

$$\rho = \rho_s \sum \sum |x_j(\vec{r}, \sigma)|^2$$

Then, the energy functional of the real system is written as:

$$E[\rho] = T_s[\rho] + J[\rho] + V_{en}[\rho] + Exc[\rho] \quad (4)$$

with exchange correlation energy,

$$E_{xc}[\rho] = T[\rho] + T_s[\rho] + E_{ee}[\rho] - J[\rho] \quad (5)$$

The exchange-correlation energy includes the error in the kinetic energy, the correlation effects, and also the correction for the self-interaction of the electron that has been included

in the classical Coulomb integral (J). The main challenge in implementing DFT is to find a good approximation to $E_{xc}[\rho]$. There are various approximations to calculate $E_{xc}[\rho]$, such as Local Density Approximation (LDA), Generalized Gradient Approximation (GGA) and hybrid functionals[15]. The well-known limitation of LDA and GGA functionals is that they significantly underestimate redox potentials due to the incomplete cancellation of electron self-interaction errors[16]. Hence, accurate calculations of the voltages of transition metal oxide electrodes are usually performed using the Hubbard U extension to DFT, where the U parameter is determined either self-consistently or by fitting to experimental oxidation energies[17]. Heyd–Scuseria–Erzern (HSE) functional was reported to generate acceptable redox potentials without variable parameters, although at higher computational cost[18].

Components of Battery: Present Status

Cathode Materials

Extensive atomistic simulations were carried out by Ceder group on electrode materials[19], specially on cathode. They reported intercalation voltage for LiCoO_2 , LiNiO_2 , LiTiO_2 , LiVO_2 , LiMnO_2 and LiZnO_2 compounds and concluded that metal cation, anion, and structure affect the intercalation voltage which in turn influence the ultimate voltage considerably. Later, the calculations were extended to various lithium-metal oxides, sulfides, and selenides. Further, few compounds were identified by replacing non-transition metals with transition metals based on the understanding that oxygen, rather than transition-metal ions, functions as the electron acceptor upon incorporation of Li ion as observed in $\text{Li}(\text{Co,Al})\text{O}_2$, where the cell voltage was reported to be increased while decreasing both the density of the material and its cost due to replacement of Al. They have shown by ab-initio calculations that Li ion diffusion in layered Li_xCoO_2 occurs via a divacancy mechanism. Ceder *et al* further demonstrated that LDA/GGA methods were not suitable for the determination of density of states and band gap in LiFePO_4 and LiMnPO_4 and recommended for use of GGA+U instead. Similarly, the Li ion intercalation potential of LiNiPO_4 , LiMnSiO_4 , LiFeSiO_4 , LiCoSiO_4 and LiNiSiO_4 in the olivine structure, layered Li_xMO_2 (M = Co, Ni) and spinel-like $\text{Li}_x\text{M}_2\text{O}_4$ (M = Mn, Co) materials with GGA+U method was predicted to be more accurate than LDA/GGA methods when compared with experimental results. A high-throughput ab initio analysis of phosphates as cathode materials was screened by calculating capacity, voltage, energy density, and thermal stability using Perdew-Burke and Ernzerhof (PBE) functional with GGA. Using DFT under GGA+U approach they further showed that $\text{Li}_9\text{M}_3(\text{P}_2\text{O}_7)_3(\text{PO}_4)_2$ (M=V, Mo)

could potentially generate a specific energy which is higher by 10% over LiFePO_4 . The performance of $\text{Li}_{1.211}\text{Mo}_{0.467}\text{Cr}_{0.3}\text{O}_2$ was evaluated by studying Li ion diffusion in order to design disordered-electrode with high energy density and capacity[20]. DFT calculations were performed to explore the thermodynamics of fluorination in transition metal oxide cathodes[21] that provide higher capacity than conventional layered oxides. Starting from fundamental thermodynamics and phenomenological equations, rigorously derived theoretical relationships for key battery properties, such as voltage, capacity, ion diffusivity, and other relevant parameters were reported. The Li ion diffusion in LiFePO_4 was found to be one dimensional[22] (Fig.3). The delithiation performance of disordered-rocksalt Li-Mn-V-O-F was investigated with PBE and Hubbard U correction[23] using a combination of low-valence transition metal redox and a high-valence redox active charge compensator along with fluorine replacement for oxygen to attain high energy density, capacity and good reversibility.

The vacancy order-disorder, intercalation voltage profiles, and voltage-temperature phase diagrams of electrode materials were conducted employing linearized augmented plane wave (LAPW) method with the exchange correlation of Ceperley and Alder[24]. The Li ion migration in Li_xTiS_2 using a mixed-basis cluster expansion approach was predicted to occur between adjoining octahedral voids bypassing a nearby tetrahedral void. The diffusion barriers for Li ion were seen to be very sensitive to the local structure with lower diffusion barriers into a divacancy over an isolated Li ion vacancy[25]. The structural changes and voltages of LiMn_2O_4 spinel as a function of Li content were investigated with DFT-GGA+U[26].

DFT was used to determine the electronic, structural and electrochemical properties of $\text{LiM}_{1/2}\text{Mn}_{3/2}\text{O}_4$ (M=Ti, V, Cr, Fe, Co, Ni, and Cu)[27]. The inductive effect of different polyoxianions $(\text{XO}_4)_n$ (X = Ge, Si, Sb, As, P) on the Li ion deintercalation voltage of olivine- $\text{LiCo} + 2\text{XO}_4$, $\text{Li}_y\text{V} + 4\text{XO}_4$ and $\text{Li}_y\text{M} + 2\text{XO}_4$ (M= Mn, Fe, Co, Ni) within structure of $\text{Li}_2\text{FeSiO}_4$ was reported. Additionally, a correlation between the Li ion deintercalation voltage and the Mulliken electronegativity X at the GGA+U level was drawn which displayed a linear dependence for each structural type/redox couple[28]. Li-ion and ion-vacancy migration barriers were evaluated to elucidate the Li/Fe site-mixing during electrochemical cycling of $\text{Li}_2\text{FeSiO}_4$ and its effect in cell performance[29]. DFT findings on the polymorphs of $\text{Li}_2\text{FeSiO}_4$ and its delithiated products indicate a structural transformation from the pristine structure to cycled polymorph and confirmed that ~ 1.5 Li ions could be extracted from $\text{Li}_2\text{FeSiO}_4$, representing two redox reactions resulting to high experimental capacity of over 200 mAh/g, recorded in experiments[30].

The doping performance, defect chemistry and Li ion migration in $\text{Li}_2\text{MnSiO}_4$ were explored by advanced modeling and has shown that the most favorable intrinsic defect type was cation anti-site defect, in which Li and Mn ions swap positions which affects the intrinsic Li ion mobility and thus the rate of recharging ability[31]. A DFT study for predictions of voltages of the Li ion intercalated LiMSO_4F and deintercalated MSO_4F systems (M = Fe, Co and Ni) and Bader's topological analysis of the electron density was also earlier reported[32].

Anode Materials

Generally, various forms of carbon or alloys were used as anode materials. For understanding anode chemistry, first principles computations were also used extensively. Typically graphite materials with a layered crystal structure made of graphene sheets were reported to be the best due to easy

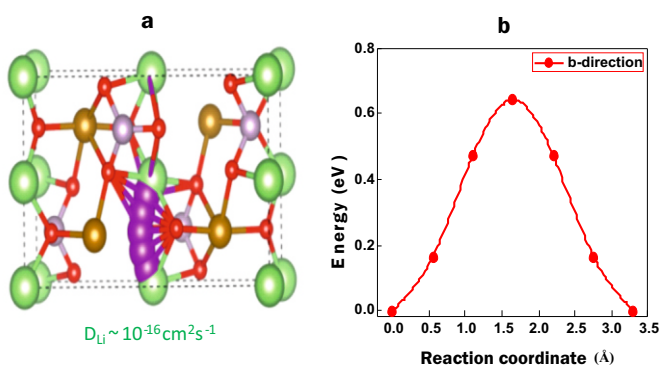


Fig.3: (a) One dimensional diffusion of Li ion in LiFePO_4 (Li:green, Fe:brown, P:silver, O:red) and (b) migration barrier for Li ion using NEB method.

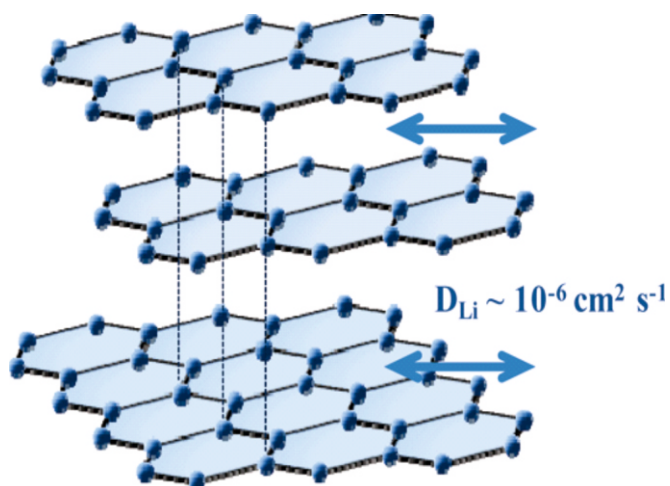


Fig.4: Diffusion of Li ion within graphite anode.

intercalation with Li ion and therefore used in the batteries[4]. The thermodynamics and kinetics of Li_xC_6 were investigated by dispersion corrected DFT[33] and shown that the interlayer interactions are dominated by van der Waals forces. The structural parameters for graphite intercalated Li compounds predicted with LDA were found to be well matched with the experimental results[34]. Energetic evaluation of stacking structures of Li-graphite intercalation compounds (Li-GICs) using LDA/GGA was shown to well reproduce the stability of the structures[35]. Li diffusion in a stage-1 structure of LiC_6 was investigated from first principles and transition state theory[36]. Mulliken population analysis were done to explain that the interlayer state of LiC_6 contains significant amount of 2s character of Li[37]. Ab initio computations were conducted to evaluate the electronic structure of graphite and LiC_6 and quantify the mechanism of Li ion diffusion (Fig.4) in highly oriented pyrolytic graphite[38].

The most common commercially used anode material for LIBs is graphite, which only has an ideal capacity of 372mAh/g limiting the energy density of the battery. To increase the capacity, Li alloys including Si, Sn, Al, Sb, Pb, In, Zn, and Ge have been considered as possible anodes owing to their low operating voltage, high volume energy density, and high theoretical capacity. Among which, the Ge-Li system has a high theoretical capacity of 1600 mAh/g by forming $\text{Li}_{22}\text{Ge}_5$ and relatively high Li ion diffusivity at room temperature[19].

Electrolytes

The electrolyte is normally an organic solvent (e.g., carbonates or ethers) comprising Li salt[39] which only allows the migration of Li^+ ions but prevents the passage of electrons. Li salts in the electrolyte is added so that individual Li ions don't have to make the complete journey from the anode to the cathode to complete the circuit. As ions are kicked out from the anode, other Li ions in the electrolyte, near the electrode surface, can easily be intercalated into the cathode. The reverse happens during recharging. The electrolyte solution must have a high ionic conductivity (at least 0.1 mS/cm with >1 mS/cm) coupled with low electronic conductivity. The electrolyte is subject to both low and high extrema in alkali chemical potential, being in contact with both cathode and anode at the same time. The nature of electrified electrode/electrolyte interfaces, i.e., the existence of any reactions, the products formed, and ionic transport across interface has been the focus of major studies.

The most common electrolytes are solutions of Li salts (LiPF_6 , LiClO_4 and Lithium bis (trifluoromethanesulfonyl) imide,

LiTFSI) in a mixture of solvents such as 1:1 ethylene carbonate (EC): dimethyl carbonate (DMC) which usually exhibit high Li^+ ion conductivities ($\sim 1\text{--}10$ mS/cm) with good electrochemical stability up to 4.5 V. The types of electrolytes can be liquid, polymers, amorphous or crystals and can be divided into two broad classes: "liquid electrolytes", which encompasses liquid and polymer, and "solid electrolytes", which encompasses amorphous and crystalline phases. First-principles computational techniques have been used heavily to the study of electrolytes.

Liquid Electrolytes

Computational studies of liquid electrolytes have focused on electrochemical stability and the reactions that occur at the electrode/electrolyte interface. The existence of strong ion-solvent interactions means that the electrochemical window of the electrolyte is not simply determined by the highest occupied molecular orbital (HOMO) and lowest unoccupied molecular orbital (LUMO) energy levels for isolated components[40] although it was a frequently used approximation for high-throughput screening[41]. Explicit modeling of the Li salt and solvent mixture demands simulation boxes containing thousands of atoms. Hence, MD simulations using atomistic force fields are often used to obtain realistic liquid structures mostly for the commonly used EC/DMC solvent with or without LiPF_6 salt[42].

Recently, super-concentrated aqueous electrolyte solutions, known as the "water-in-salt" (WIS) electrolytes[43] are emerged to mitigate the solvent decomposition by controlling the free water molecules. It was shown that a $\text{LiTFSI}(\text{H}_2\text{O})_2$ WIS electrolyte was stable up to 3.0 V, well beyond the oxidation potential of water. DFT calculations reported that the $\text{Li}_2(\text{TFSI})(\text{H}_2\text{O})_x$ aggregates become unstable at a much higher potential (2.9V versus Li ion) compared to an isolated TFSI anion (1.4V)[43]. Ong *et al*[44] investigated the electrochemical stability window for room temperature ionic liquids (RTILs) using a combination of classical MD and DFT simulations. Besides finding that explicit modeling of the RTIL structure yields much better agreement with experimentally measured electrochemical windows compared to simplified gas phase or polarizable continuum model calculations. The computed equilibrium structure of Li-TF2N system and diffusion of Li ion using molecular dynamics simulations are displayed in Fig.5.

Many computational studies have focused on poly(ethylene oxide) (PEO) and related polymers blended with Li salts, but the performance of such electrolytes are generally limited by poor low-temperature conductivity due to the unfulfilled requirement of segmental chain motion for ion transport[45].

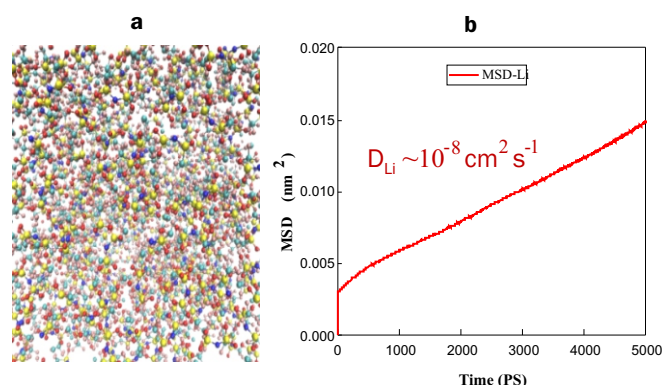


Fig.5: (a) Snapshot of Li ion- TF_2N system that acts as electrolyte in Li ion battery and (b) Mean square displacement of Li ion using CMD.

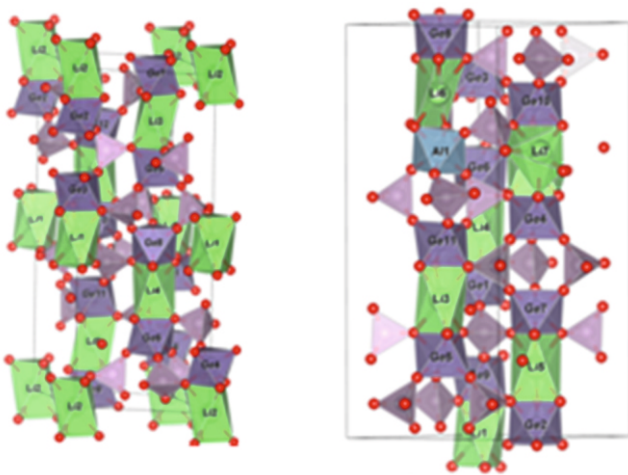


Fig.6: Relaxed structure of a) $\text{LiGe}_2(\text{PO}_4)_3$ and b) $\text{LiAlGe}_2(\text{PO}_4)_3$.

Solid Electrolytes

Although solid electrolytes have been known for decades, they have enjoyed a resurgence of interest during the past decade with an increased emphasis on thermal safety as alkali-ion batteries move beyond consumer electronics to automotive and grid energy storage applications.

There are different types which include Li super ionic conductor (LISICON) type $\text{Li}_{1-x}\text{Zn}_x(\text{GeO}_4)_4$ [46], perovskite-type $\text{Li}_x\text{La}_{2/3-x}\text{TiO}_3$ (LLTO)[47] and Li garnets, $\text{Li}_x\text{Ln}_3\text{M}_2\text{O}_{12}$ ($x = 5-7$, $\text{M} = \text{Te}, \text{W}, \text{Zr}$; $\text{Ln} = \text{lanthanides}$)[48]. Among sulfides, thio-LISICON LGPS family $\text{Li}_{4-x}\text{M}_{1-x}\text{P}_x\text{S}_4$ ($0 < x < 1$; $\text{M} = \text{Si}, \text{Ge}, \text{Sn}$)[49], and Na_3PS_4 [50] and its analogues were reported. Extensive computational studies have been reported on the sulfide solid electrolyte because ionic conductivity of the sulfides tends to be higher than the oxides indicates adequate diffusion statistics can be accessed within reasonable AIMD simulation time[51]. Further, the recent explosion in the number of newly discovered crystalline sulfide superionic conductors in both Li-ion and Na-ion chemistries have given rise to many computationally driven discovery and optimization efforts. Among the most promising SEs to emerge in recent years is the $\text{Li}_{10}\text{GeP}_2\text{S}_{12}$ (LGPS) family of superionic conductors with ionic conductivities exceeding 10 mS/cm. Shortly after its reported discovery by Kamaya *et al* [49] computational works by Mo, Ong, and Ceder provided much needed insights into the diffusion mechanisms and electrochemical stability of the LGPS superionic conductor as well as potential avenues for further optimization. The high conductivity of the LGPS family, as well as $\text{Li}_7\text{P}_3\text{S}_{11}$ glass-ceramic has been attributed to their body-centered cubic-like anion framework, which allows direct hopping of Li ion between adjacent tetrahedral sites with low activation barrier. Using this design principle, Richards *et al.* identified a new lithium superionic conductor $\text{Li}_2\text{Zn}_{1-x}\text{P}_x\text{S}_4$ ($x = 0-0.75$) with room temperature Li^+ -conductivity predicted to be $>10 \text{ mS cm}^{-1}$ [52]. However, the LGPS was observed to produce toxic H_2S gas when in contact with water which prompted the use of NASICON-type materials ($\text{LiM}_2(\text{PO}_4)_3$). $\text{LiGe}_2(\text{PO}_4)_3$ and $\text{LiAlGe}_2(\text{PO}_4)_3$ are such materials and thus optimized using DFT (Fig.6).

Summary and Future Directions

First principles atomistic simulations along with simple and at the same time powerful, phenomenological models could be useful to complement experimentally measurable thermodynamic and kinetic parameters. The electrochemical processes of Li ion batteries are in general thermally activated

and thus inclusion of temperature and entropy is very crucial. Therefore, any first principle-based approach that links to phenomenological models have to integrate statistical mechanics. These computational protocols have proven to be an important complement to experimental studies in gaining fundamental insights of battery materials. The properties of battery materials that can be computed from first-principles, is still incomplete. There are many phenomena where the connection between electronic structure and the macroscopic parameters is not well understood. Possibly, least understood are the atomic and electronic processes that take place at the electrode–electrolyte interfaces of Li ion batteries. Combined in situ experiments and multiscale modeling with electronic and atomic-level resolution are needed to decode the structure of the interface and associated kinetic processes.

It is known that charging and discharging of battery depends on the diffusional motion of Li ion. The Li ion with mass 6 is known to have higher diffusion than mass 7 and hence it will be of great academic and technological importance to explore the isotope effect on diffusion and ionic conductivity in Li ion battery. A critical gap remains in our ability to simulate materials with chemical accuracy at the meso-/micro-scales. This is particularly relevant to the understanding of chemical reactions and transport at the electrode–electrolyte interfaces as well as within the electrodes and electrolytes themselves. While recent developments in machine learning interatomic potentials show promise in relatively simple chemistries, methodological developments that enable universal application to complex chemistries and bonding types, especially electron transfer, are truly needed. In the development of anode side, silicon is being investigated as an anode material because it can form a 3D cage that has more capacity to absorb lithium ion.

References

- [1] <https://www.nobelprize.org/prizes/chemistry/2019/press-release/>. 2019.
- [2] M.S. Whittingham, 1976, 192, 1126–1127.
- [3] K. Mizushima, P.C. Jones, P.J. Wiseman, J.B. Goodenough, Mater. Res. Bull., 1980, 15, 783–799.
- [4] R. Yazami, Y.F. Reynier, Electrochimica Acta, 2002, 47, 1217–1223.
- [5] A. Mauger, C.M. Julien, Ionics. 2017, 23, 1933–1947.
- [6] E. Ali, ACS Sustainable Chemistry & Engineering. 2018, 5, 2799–2816.
- [7] M.K. Aydinol, A.F. Kohan, G. Ceder, K. Cho, J. Joannopoulos. Physical Review B, 1997, 56, 1354-1365.
- [8] A.I. Liechtenstein, V.I. Anisimov, J. Zaanen, Phys. Rev., B, 52, 1995, R5467.
- [9] M.P. Allen, D.J. Tildesley, Computer Simulation of Liquids, Clarendon Press, Oxford University, 2017.
- [10] J. Kang, H. Chung, C. Doh, B. Kang, B. Han, J. Power Sources, 2015, 293, 11–16.
- [11] T. Baba, K. Sodeyama, Y. Kawamura, Y. Tateyama, Phys. Chem. Chem. Phys., 2020, 22, 10764–10774.
- [12] M. Z. Bazant, Faraday Discuss., 2017, 199, 423–463.
- [13] J. M. Reniers, G. Mulder, D. A. Howey, J. Electrochem. Soc., 2019, 166, A3189–A3200.
- [14] Kohn, W.; Sham, L. J. Phys. Rev., 1965, 140, A1133.
- [15] C. Lee, W. Yang, R.G. Parr, Phys. Rev., B, 1988, 37 785-789.

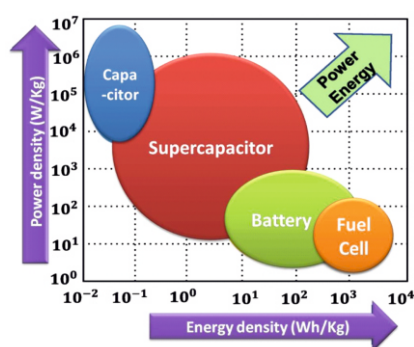
- [16] F. Zhou, M. Cococcioni, C.A. Marianetti, D. Morgan, G. Ceder, *Phys. Rev. B: Condens. Matter Mater. Phys.*, 2004, 70, 235121.
- [17] L. Wang, T. Maxisch, G. Ceder, *Phys. Rev., B: Condens. Matter Mater. Phys.*, 2006, 73, 195107.
- [18] J. Heyd, G.e. Scuseria, M. Ernzerhof, *J. Chem. Phys.*, 2003, 118, 8207.
- [19] Y. Tian, G. Zeng, A. Rutt, T. Shi, H. Kim, J. Wang, J. Koettgen, Y. Sun, B. Ouyang, T. Chen, Z. Lun, Z. Rong, K. Persson, G. Ceder, *Chem. Rev.*, 2021, 121, 3, 1623–1669.
- [20] J. Lee, A. Urban, X. Li, D. Su, G. Hautier, G. Ceder, *Science* 2014, 343, 519–522.
- [21] W.D. Richards, S.T. Dacek, D.A. Kitchaev, G. Ceder, *Adv. Energy Mater.*, 2018, 8, 1701533.
- [22] J. Yang, J.S. Tse, *J. Phys. Chem., A*, 2011, 115, 13045–13049.
- [23] D.A. Kitchaev, Z. Lun, W.D. Richards, H. Ji, R.J. Clement, M. Balasubramanian, D-H. Kwon, K. Dai, J.K. Papp, T. Lei, B. D. McCloskey, W. Yang, J. Lee, G. Ceder, *Energy Environ. Sci.*, 2018, 11, 2159.
- [24] C. Wolverton, A. Zunge, *Phys. Rev. Lett.*, 1998, 81, 606.
- [25] A. Van der Ven, J.C. Thomas, X. Xu, B. Swoboda, D. Morgan, *Phys. Rev. B: Condens. Matter Phys.*, 2008, 78, 104306.
- [26] B. Xu, Y.S. Meng, *J. Power Sources* 2010, 195, 4971–4976.
- [27] M.C. Yang, B. Xu, J.H. Cheng, C.J. Pan, B. J. Hwang, Y.S. Meng, *Chem. Mater.*, 2011, 23, 2832–2841.
- [28] M.E. Arroyo-de Dompablo, M. Armand, J.M. Tarascon, U. Amador, *Electrochem. Commun.*, 2006, 8, 1292–1298.
- [29] A. Liivat, J.O. Thomas, *J. O. Solid State Ionics* 2011, 192, 58–64.
- [30] P. Zhang, Y. Zheng, S. Yu, S.Q. Wu, Y.H. Wen, Z.Z. Zhu, Y. Yang, *Electrochimica Acta*, 2013, 111, 172–178.
- [31] N. Kuganathan and M. S. Islam, *Chem. Mater.*, 2009, 21, 5196–5202.
- [32] C. Frayret, A. Villesuzanne, N. Spaldin, E. Bousquet, J.N. Chotard, N. Recham, J. M. Tarascon, *Phys. Chem. Chem. Phys.*, 2010, 12, 15512–15522.
- [33] K. Persson, Y. Hinuma, Y.S. Meng, A. Van der Ven, G. Ceder, *Phys. Rev. B: Condens. Matter Mater. Phys.*, 2010, 82, 125416.
- [34] J.-S. Filhol, C. Combelles, R. Yazami, and M.-L. Doublet, *J. Phys. Chem., C*, 2008, 112, 3982.
- [35] Y. Imai and A. Watanabe, *J. Alloys Compd.*, 2007, 439, 258.
- [36] K. Toyoura, Y. Koyoma, A. Kuwabara, and I. Tanaka *J. Phys. Chem., C*, 2010, 114, 2375.
- [37] N. A. W. Holzwarth, S. G. Louie, and S. Rabii, *Phys. Rev., B*, 1984, 30, 2219.
- [38] K. Persson, V.A. Sethuraman, L.J. Hardwick, Y. Hinuma, Y.S. Meng, A. van der Ven, V. Srinivasan, R. Kostecki, G. Ceder, *J. Phys. Chem. Lett.*, 2010, 1, 1176–1180.
- [39] K. Xu, *Chem. Rev.*, 2004, 104, 4303–4418.
- [40] J.B. Goodenough, Y. Kim, *Chem. Mater.*, 2010, 22, 587–603.
- [41] L. Cheng, R.S. Assary, X. Qu, A. Jain, S.P. Ong, N.N. Rajput, K. Persson, L.A. Curtiss, *J. Phys. Chem. Lett.*, 2015, 6, 283–291.
- [42] Y. Li, K. Leung, Y. Qi, *Acc. Chem. Res.*, 2016, 49, 2363–2370.
- [43] L. Suo, O. Borodin, W. Sun, X. Fan, C. Yang, F. Wang, T. Gao, Z. Ma, M. Schroeder, A. vonCresce, S.M. Russell, M. Armand, A. Angell, K. Xu, C. Wang, *Angew. Chem., Int. Ed.* 2016, 55, 7136–7141.
- [44] S.P. Ong, O. Andreussi, Y. Wu, N. Marzari, G. Ceder, *Chem. Mater.*, 2011, 23, 2979–2986.
- [45] O. Borodin, G.D. Smith, *Macromolecules* 2006, 39, 1620–1629.
- [46] H.Y.P. Hong, *Mater. Res. Bull.*, 1978, 13, 117–124.
- [47] Y. Inaguma, C. Liqun, M. Itoh, T. Nakamura, T. Uchida, H. Ikuta, M. Wakihara, *Solid State Commun.*, 1993, 86, 689–693.
- [48] V. Thangadurai, S. Narayanan, D. Pinzaru, *Chem. Soc. Rev.*, 2014, 43, 4714.
- [49] N. Kamaya, K. Homma, Y. Yamakawa, M. Hirayama, R. Kanno, M. Yonemura, T. Kamiyama, Y. Kato, S. Hama, K. Kawamoto, A. Mitsui, *Nat. Mater.*, 2011, 10, 682–686.
- [50] A. Hayashi, K. Noi, A. Sakuda, M. Tatsumisago, *Nat. Commun.*, 2012, 3, 856.
- [51] X. He, Y. Zhu, A. Epstein, Y. Mo, *npj Comput. Mater.*, 2018, 4, 18.
- [52] W.D. Richards, Y. Wang, L.J. Miara, J.C. Kim, G. Ceder, *Energy Environ. Sci.*, 2016, 9, 3272–3278.

Super Capacitors

Review on Electrochemical Capacitor Technology: Role of Transition Metal-based Oxides

Seemita Banerjee and Vinita Grover*

Chemistry Division, Bhabha Atomic Research Centre, Mumbai-400085, INDIA
Homi Bhabha National Institute, Anushaktinagar, Mumbai-400094, INDIA



Ragone Plot: Power vs Energy Density.

ABSTRACT

Electrochemical capacitors constitute an important class of energy storage devices that has been on the forefront of research in materials science in the last decade. The article presents the overview of recent progress in the field of supercapacitor materials with special emphasis on electrode materials. Even though the commercial supercapacitors presently available in market are based on carbon materials, there is a huge impetus on research on other materials including transition metal-based oxides, hydroxides and polymers to obtain better energy density. The charge storage mechanisms of different kind of electrodes along with their advantages and disadvantages and the strategies that are adopted to improve the capacitive performance have also been discussed. The article provides the synthesis challenges of the electrode materials with better electrochemical performance using environmental friendly, facile and low-cost methods for development of efficient and cost-effective electrochemical capacitors for energy storage applications.

KEYWORDS: Energy storage, Supercapacitor, Electrode, Carbon, Transition metal oxide, Layered double hydroxide

Introduction

The development of mankind is intrinsically related to energy supply and demand[1]. With continuous increase in technological growth, there has been unprecedented increase in energy demand as well. This calls for developing efficient, clean and sustainable sources of energy production, storage and conversion given the state of non-renewable fossil fuels which are still the primary energy providers worldwide. This has prompted the scientific and technical community to focus its research in the areas of solar, nuclear, hydrogen and other renewable and sustainable energy forms. However, for the intermittent nature of energy sources like solar energy there is a necessity for developing inexpensive and efficient energy storage and conversion devices. In fact, these devices shall become absolutely necessary as these renewable energy technologies become more widespread, and are integrated into the electrical grid. Among different energy storage technologies, the role of those based on electrochemical techniques such as batteries and electrochemical supercapacitors has been considered paramount in overcoming fossil fuel exhaustion[2]. Common features among these two are that the underlying chemical processes take place at the interface of electrode/electrolyte and the electron and ion transport occur through different routes. However, there are certain differences in the charge storage mechanisms of batteries and supercapacitors that bestows them with different features and makes them useful for different purposes. Batteries, like Li-ion batteries were introduced in 1990 by Sony, following pioneering work by Whittingham, Scrosati and Armand. They are excellent in terms of performance, with energy densities up to 180 watt hours/Kg but they suffer from slow power delivery or uptake (power

densities), and hence are not much helpful when faster and higher-power energy storage systems are needed. This is where the electrochemical capacitors fill in the bridge as they can be fully charged or discharged in seconds. As a result, their energy density (about 5 Wh kg⁻¹) is lower than batteries, but they deliver such higher power delivery or uptake (power density ~ 10 kW kg⁻¹) and that can be achieved in very short durations (a few seconds). Hence, they could play an important role in complementing batteries in the energy storage applications, such as back-up power supplies to protect against power disruption and load-leveiling. Due to features such as fast charging, long charge-discharge cycles, and broad operating temperature ranges, electrochemical supercapacitors find widespread applications in hybrid/electric vehicles, electronics, and smart grids. Fig.1 gives the plots of specific energy vs specific power for various electrical energy storage devices. The specific power shows how fast one can go, and the specific energy shows how far one can go on a single charge.

Strictly speaking, depending on working mechanism, electrochemical capacitors may be classified as (1) Electrical Double layer Capacitor (EDLC or supercapacitor) and (2) Pseudocapacitors. While EDLCs depend on formation of an ionic double layer at the electrode-electrolyte interface for electrical energy storage, pseudocapacitors store energy due to reversible redox reactions based on Faradaic charge transfer, in which the concentration of redox sites on the surface of electrodes is a governing factor of the specific capacitance. Supercapacitors or EDLCs are cheap and widely available but suffer from low E density. On the other hand, pseudocapacitors are costly but provide better energy and power density. From the materials point of view, the materials used/researched for supercapacitor applications fall in three main categories: a) Carbon-based materials for electric double-

*Author for Correspondence: Vinita Grover
E-mail: vinita@barc.gov.in

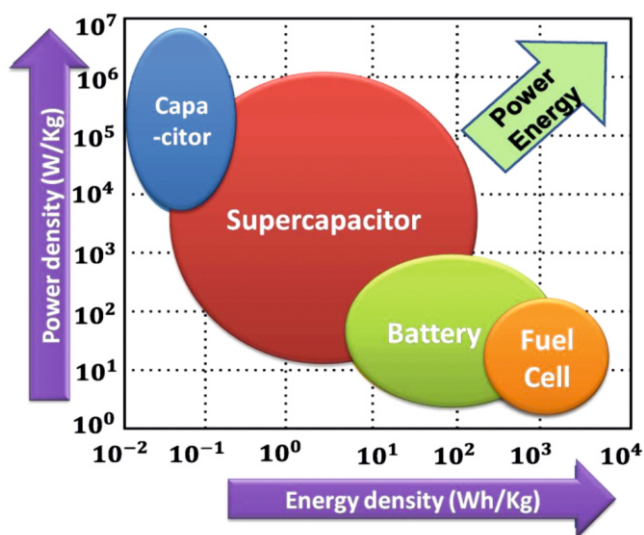


Fig.1: Ragone Plot: Power vs Energy Density of different electrochemical energy storage devices.

Carbon based Supercapacitors

Carbon-based materials are well documented as efficient electrode materials for supercapacitor applications and till now all the commercial supercapacitors available in market are based on carbon materials only. The major advantages of carbon based supercapacitors are possibility of larger surface area and higher conductivity of carbon based material apart from their low cost and easy processibility[4]. The major challenge of carbon based super capacitor research is to increase the energy density keeping the total cost comparable with the existing one. For that numerous strategies have been adopted, such as, increase in surface area, optimization of pore size of carbon electrode materials and increase of operating voltage by using different electrolyte materials[5]. It has been reported that the co-existence of micro and meso pores facilitate the mobility of ions within the electrode materials because of superior inter pores connectivity. In recent times, several carbon structures with interconnected hierarchical pores were synthesized, which show better electrochemical performances due to high surface area and optimized diffusion pathway for easy conduction or movement of ions[6].

layer capacitors (EDLCs): For this class of materials, the charge storage is due to the electrostatic separation between the ions of the electrolyte and the high-surface area electrodes; b) Electronically conducting polymers: These materials store energy through fast reversible doping/de-doping processes; c) pseudocapacitive transition-metal-based oxides/hydroxides: These materials store energy by virtue of fast reversible multi-electron surface redox Faradaic reactions. This is in addition to the double layer capacitance that is due to high surface area of the electrode material. This particular class include materials that mostly belong to oxides and hydroxides based on transition-metal, such as MnO_2 , NiO , CoO_x , $Co(OH)_2$, and $Ni(OH)_2$ [3]. They exhibit rich redox states, which can provide considerably improved specific capacitance than typical carbon-based EDLCs. Some of the materials that find application in electrochemical capacitors based on carbon, transition metal oxides and hydroxides are discussed in details in the following sections.

Doping of carbon materials with boron (B), nitrogen (N), oxygen (O), sulfur (S) and phosphorus (P) have tremendous effect on the supercapacitive properties by increasing the energy density of carbon based EDLCs[7]. Nitrogen is the most accepted doping element because of its greater electronegativity, similar size and easy synthesis methodology. Primarily, two different synthesis strategies have been adopted for nitrogen containing porous carbons, viz. (a) post-treatment of pre-synthesized carbons in nitrogen atmosphere, like ammonia or urea and (b) pyrolysis of nitrogen-containing precursors, namely polyaniline, polypyrrole, polyimide, melamine, polyvinyl pyridine etc for in-situ nitrogen doping[8]. We have synthesized nitrogen doped porous carbon with hierarchical interconnected pore structure by single step annealing of EDTA precursor, where the nitrogen doping and pore diameter were varied by changing the annealing temperature [Fig. 2]. The optimized sample can provide high energy density of 9.5 Whkg^{-1} at a power density of 64.5 Wkg^{-1}

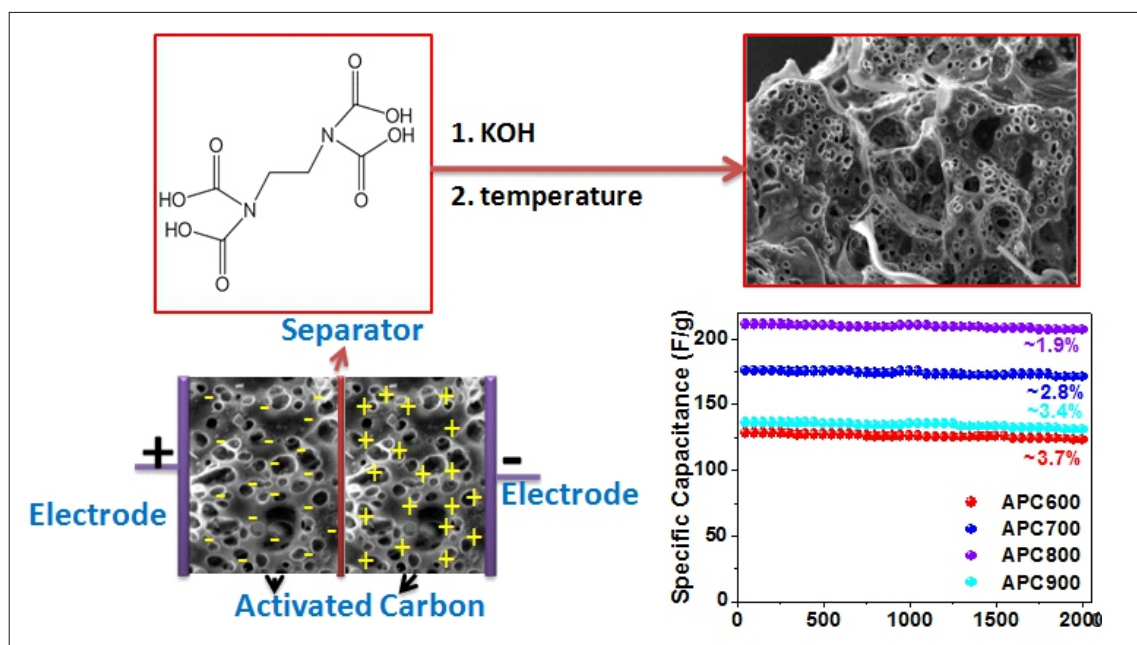


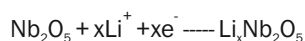
Fig.2: N-doped porous carbon prepared from the pyrolysis of EDTA.

within a voltage window of 1.0 V with very high capacity retention[9]. Similarly, Kang *et. al.* has synthesized hierarchical interconnected carbon which demonstrated high capacitance of 268.4 Fg^{-1} confirming the increased ions transport in presence of interconnected larger micropores and mesopores[10].

Transition Metal Oxides-based Supercapacitors

The significance of transition metal based supercapacitor rely on the fact that, due to the existence of variable oxidation states, they can store more amount of charge by reversible Faradic reaction near the surface of the active material, leading to more energy density compared to the traditional carbon based supercapacitor. The main difference from the battery material is that in pseudo capacitor, the change in the oxidation state does not led to the phase change of the material. The initial reports on the pseudocapacitor behaviour of transition metal based system are mostly on ruthenium oxide (RuO_2) which exhibits high theoretical specific capacitance value around $1300\text{-}2200 \text{ Fg}^{-1}$. Due to the high cost of RuO_2 afterwards different systems were studied and reported including other transition metal oxides, hydroxides, and doubled layer hydroxides. Apart from that, recently several derivatives were also studied such as sulfides, and selenides for their supercapacitive application[11]. The main research objective of transition metal based supercapacitor study is the optimisation of synthesis procedure to get better electrochemical performance by varying the composition, morphology and structural parameters by using different synthetic methodologies. The main advantage here is that the TM based supercapacitors can be combined with carbon based supercapacitor to make a hybrid capacitor, which ultimately leads to both higher specific and current density along with the long term cyclic stability.

The major charge storage mechanism of the pseudocapacitor can be divided in two major categories, the redox based pseudo capacitance and intercalation based pseudocapacitance[12]. In the redox based pseudocapacitor redox reactions typically take place at the surface and near surface region and the GCD (galvanostatic charge discharge) curve exhibit triangular shape similar to the EDLC. Typical electrodes, where these types of mechanisms are seen are RuO_2 and MnO_2 . Here during the charging process the electrolyte gets absorbed on the electrode and the metal ions get oxidised to their higher oxidation states. For example, in acidic medium the Ru(II) gets converted to Ru(IV), where as Mn(III) gets oxidised to Mn(IV). During the discharging the reverse process occurs. In the intercalation based pseudo capacitance the electrolyte goes into the voids and also in the interlayer spacing of the electrode materials and gets intercalated. A very well known example for that is hexagonal $\text{T-Nb}_2\text{O}_5$ oxide, which in virtue of its layer structure allow Li^+ ion to transport within it without any activation barrier [13]. The reaction occurs during the charging process is given by



The major benefits for these kinds of systems are very high specific capacitance and energy density due to the utilisation of the complete bulk material but the application is limited by poor cyclic stability. Another major drawback is the poor conductivity of the electrode material where improvement has been achieved by making composite with carbon. Jiawen *et al.* demonstrated that Nb_2O_5 @mesoporous carbon hollow core-shell nanostructures exhibits an initial reversible specific capacity of 410 Cg^{-1} at 1 Ag^{-1} with rate capability of 173 Cg^{-1} at 50 Ag^{-1} [14]. Apart from the cation intercalation (Li^+ , Na^+), perovskite oxide anionic intercalated supercapacitors are also

reported, where O^{2-} ions gets intercalated. It can be easily achieved in the aqueous medium and due to higher charge storage capacity of O^{2-} ions, these kinds of supercapacitors show higher charge density[15].

RuO_2 is considered as the ideal pseudocapacitor material due to its good electrical conductivity and high power and energy density. In spite of its excellent electrochemical properties the material has been rarely used due to its toxic nature, low abundance and high cost. Apart from that, there are issues regarding the agglomerations of RuO_2 nanoparticles which lead to the decrease in energy and power density of the system. This problem can be taken care by dispersing RuO_2 nanoparticles on carbon surface. Different carbon materials have been studied for this purpose and it has been found that the presence of carbon support does not only prevent the agglomeration of the nanoparticles, but also provides more active sites by increasing the surface area of the electrode material and reduces the overall cost. For example, RuO_2 and electrospun carbon composite, with very low RuO_2 loading concentration, shows excellent pseudo capacitance performances with high energy density of $22\text{-}15 \text{ W h kg}^{-1}$ in the power density range of $400\text{-}4000 \text{ W kg}^{-1}$ [16]. Han *et al.* also established that a solid-state supercapacitors with RuO_2 /Vertical Graphene hybrids and polymer gel electrolyte shows excellent capacitance retention with at least 10,000 cycles[17]. Flexible supercapacitor synthesized by homogeneously dispersing RuO_2 nanoparticles on carbon nano anion (CNO) support by sol gel route shows a high energy and charge density of 10.62 Whkg^{-1} and 4.456 kWkg^{-1} with excellent cyclic stability, where CNO acts both as the electrical conducting material as well as the support for the oxide nanoparticles[18].

Though there is commanding advancement on the supercapacitor work of RuO_2 , still the toxicity and cost of the material are found to be the limiting parameters. Development of cheaper and environmental friendly counter parts with comparable supercapacitive behaviour with RuO_2 is in progress and the most potential material till now is MnO_2 , due to its low cost, high theoretical capacitance. The major issue in the phase pure MnO_2 is its very poor thermal conductivity. Change in the morphology and structural parameters and making nanocomposite with other metal oxides and conducting carbons are some of the routes for the improvements of their supercapacitive performances. For example, to obtain nanosize and high surface area materials, Xiao *et al.* had implemented salt-templated approach for synthesis of 2D- MnO_2 sheets[19].

Mixed Transition Metal Oxide

Mixed transition metal oxides have obtained enormous significance for pseudocapacitor applications[20]. In the mixed transition metal oxide the synergistic effect by different metal ions play a vital role to increase the electron transportation, which finally leads to higher specific capacity and conductance.

One of the very interesting and widely explored mixed oxides of Ni and Co is NiCo_2O_4 , where contribution of redox properties of both Ni and Co ions, giving rise to excellent electrochemical behaviour. Different morphological structures have been synthesized for NiCo_2O_4 and depending on the morphology vast difference in the supercapacitive performance are reported. NiCo_2O_4 nanosheets and nanowires with oxygen vacancy on the surface promote specific capacitance by facilitation the absorption of OH^- ion and are reported to have high specific capacitance (1590 and 1280 Fg^{-1}) at current density of 1 Ag^{-1} [21]. It is important to note that

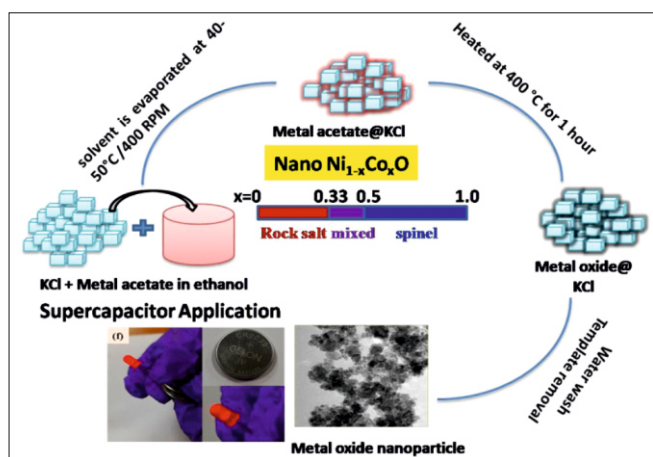


Fig.3: Synthesis and supercapacitor application of $Ni_{1-x}Co_xO$ ($0.0 \leq x \leq 1.0$) oxide.

NiO adopts rock salt structure whereas Co_3O_4 crystallizes in a spinel structure. The structure of the mixed oxide depends on their calcinations temperature as well as their preparation method. In general in very low Co content the mixed oxide stabilizes in the rock salt structure but with increase in the Co content it forms spinel or inverse spinel structure. In our recent study we have seen that $Ni_{1-x}Co_xO$ ($0.0 \leq x \leq 1.0$) system synthesized by salt templated route, formed a biphasic mixture of fcc and spinel-type phases upon 33 mol% of cobalt-substitution, but gets converted to single-phasic spinel-type phase field which continued up to 100 mol% Co_3O_4 [22]. [Fig.3] Among the range of composition it has been found that due to the combined effect of both Ni and Co ions, the $Ni_{0.5}Co_{0.5}O_x$ exhibits highest specific capacitance of 146 F g^{-1} at 1 A g^{-1} with 97% retention up to 1000 cycles[22].

Apart from the mixed Ni-Co oxides, zinc cobaltites and copper cobaltites[23] are two emerging electrode materials for supercapacitor application. The major advantage of zinc cobaltite ($ZnCo_2O_4$) is that it possesses good redox activity and conductivity along with high theoretical specific capacitance of 2650 F g^{-1} . Electrode made with urchin-like $ZnCo_2O_4$ microspheres prepared by Jadav *et al.* shows a high specific capacitance of 677 F g^{-1} at 1 A/g current density[24]. $ZnCo_2O_4$ nanorods deposited on Nickel-foam via co-precipitation method exhibits a specific capacitance value of 604.52 F/g [25]. Binder free $ZnCo_2O_4$ deposited on stainless steel prepared by the hydrothermal method was reported to exhibit a specific capacitance value of 593 F/g at 10 mV/s .

$CuCo_2O_4$ (CCO) also has emerged as one of the potential materials for supercapacitor application as it possesses inherently high specific capacity. But the semiconducting nature of the $CuCo_2O_4$ materials is the major hindrance to its electrochemical application. So for the practical application, composite with other conductive material or introduction of conductive skeleton in the structure is needed. Aliovalent metal ion doping has also been reported to increase the conductivity by introduction of oxygen vacancy in the structure. An electrode prepared by core shell nanocomposite of CCO@CuO synthesized by hydrothermal method and deposited on flexible stainless steel mesh substrate exhibited a high specific capacitance of 713 F g^{-1} at a current density of 11 mA cm^{-2} , which was higher than that of the individual components[26].

Layered Double Hydroxides as Supercapacitors

Layered double hydroxides (LDHs) multi-metal clay materials that consist of layers of metal cations (mostly

transition metal ions) that octahedrally surrounded by hydroxyls forming $M(OH)_6$ ($M: M^{2+}/M^{3+}/M^{4+}$) octahedra[27]. The layers are positively charged and are held together by charge balancing negative ions and many a times neutral species like water molecules. A considerable amount of research is being dedicated towards LDH materials as pseudocapacitors because of the following factors:

- (1) High redox activities, green and environmentally-friendly nature and efficient utilization of transition metal atoms that are dispersed homogeneously in LDH structure.
- (2) Easy tunability of cations in the host layers of LDH and possibility of anion exchange without altering the crystal structure.
- (3) Easy and facile exfoliation of LDH structure into monolayer nanosheets and possibility of chemical modification.

Plenty of research studies have been carried out on the electrochemical behaviors of LDHs in recent years. Most of these studies focus on the effect composition, structure design and device assembly[14–19].

The general formula of LDH compounds is $[M_{1-x}^{2+}M_x^{3+}(OH)_2]A_{x/n}^{n-} \cdot nH_2O$. There is wide variety of interlayer anions present in the LDH. The wide tunability option available for tuning M^{2+}/M^{3+} in addition to choosing the interlayer anion, yields a range of host-guest combinations and nano-architecture and this provides a huge data set for electrochemical properties. Thus, there is a lot of scope for varying the electrical behaviour of these materials by varying any of the above parameters and hence in the recent years a tremendous amount of research has been dedicated to this area. The open two-dimensional structure of transition metal based LDHs enables highly efficient Faradaic redox reactions at the near-surface transition metal sites with fast kinetics.

LDH based on Ni and Co ions have been widely explored due to their high theoretical specific capacitance of more than 2000 F g^{-1} [28]. Electrochemical behavior of Ni, Al and Co, Al-based LDH have also been widely explored. In case of Ni-Al-LDH, two redox peaks were observed in the cyclic voltammetry (CV) curves, as represented by the following reaction:



The charge transport inside the material is due to electron hopping along the layers and “proton transfer” from hydroxyl attached to Ni^{2+} ions from host layers to electrolyte solution when the anodic potential is applied. Co-Al-LDH however shows different behaviour[29]. In order to understand the effect of M^{2+}/M^{3+} ratio on structural and energy storage response, several studies have tried to adjust the amount of Al^{3+} in Co-Al-LDH. It has been observed that etching the Co-Al-LDH with KOH leads to loss of non-electroactive Al^{3+} and results in porous morphology that enhances the capacitive performance[30]. In fact, the synthesis routes are being modified and controlled to obtain monometallic LDH by making use of different oxidation states of Ni (Ni^{2+} - Ni^{3+} - LDH) and Cobalt (Co^{2+} - Co^{3+} - LDH)[31].

It is understandable that LDH containing different electroactive ions within a single double hydroxide structure shows better capacitive performance owing to wider inter layer space and reduced mechanical stress during the charge/discharge process. Many dually active metal-based LDHs (e.g. NiMn-LDHs, CoMn-LDHs and CoFe-LDHs)[32] have also been studied for electrode application of pseudo-supercapacitors owing to redox activity of both the ions within the same structure. In such cases, the capacitive performance

parameters such as specific capacitance, rate performance and cycling stability are affected by a variety of factors. The atomic ratio of the cations is one of the biggest influencing factors that controls not just the crystal phase but also the morphology, structure and capacitive behaviour. Several studies have shown the effect of Ni/Co ratio on the morphology of the Ni-Co LDH [33]. In addition, the content of Co makes the nanostructures thicker. The thickness has an adverse effect on capacitive behaviour as larger thickness would limit their surface area, make lesser surface sites accessible and affect surface-dependent redox reactions. The ratio of Ni and Co ions also affect the electrochemical behaviour as this determines the position of redox peaks. In addition, the presence of Co increases the electronic conductivity because of conversion of $\text{Co}(\text{OH})_2$ to CoOOH which is more conductive and hence aids the e^- transfer during electrochemical process[34]. However, higher Ni amounts leads to better specific capacitance. Thus, an optimal ratio of Ni and Co ions is required for designing efficient layered double hydroxide for this application. Similarly, a lot of studies have been reported on LDH containing other electrochemically active ions such as Fe and Mn[35]. Other than manipulating the cations and their ratio in LDH structures, tuning the anions present in the interlayer gallery of LDH is also a strategy employed for designing materials with enhanced electrochemical behaviour. The ionic movement of OH^- ions (from electrolyte) inside the layers of LDH is hindered that leads to increase in resistance. In order to circumvent this, many organic anions (sodium dodecyl sulfate) can be exchanged with inorganic anions such as CO_3^{2-} , NO_3^- etc. usually present in the interlayers of LDH leading to increase in the gallery height that promotes ionic diffusion and lesser ohmic resistance resulting in superior electrochemical behaviour such as better specific capacitance and rate capabilities[36]. Sometimes the neutral organic moieties such as ethylene glycol, glucose etc. are also used for this purpose that have yielded encouraging results[37]. LDHs belongs to one of the most technologically promising structural families for application as electrode materials for electrochemical capacitors owing to their low cost, facile synthesis and high theoretical specific capacitance. Due to their inherently layered structure, possibility of choosing a wide variety of host metal ions and the ease of exchange of interlayer anions, they have tremendous potential in energy storage applications.

Conclusion and Prospects

Transition metal-based oxides have been frontrunners for oxides for energy storage applications. The advantages are higher relative natural abundance, low production cost, higher specific capacitance as compared to other candidates such as carbon-based materials and conductive polymers. There has been a lot of research in tuning the composition and concomitant structure to optimise the electrochemical behaviour. This has direct bearing on redox behaviour exhibited by the material. In case of layered materials, the interlayer spacing of the material provides an additional parameter to control the electrochemistry. Control on nanoarchitecture aids in improving the capacitive performance as it enhances the utilization of active sites and promotes fast ion transport. The biggest roadblock in their large scale application is that they possess relatively low electrical conductivity which restricts the charge/ discharge kinetics. A multi-pronged approach is followed to overcome this problem, which includes synthesis of electrode materials with nanostructure possessing larger active surface area, combining with conductive materials (i.e., conducting polymers and carbon materials) as well as employing multiple metals composite with synergistic effect. Despite a lot of research being carried out in all the aspects of

developing viable electrochemical capacitors, their practical capacitance and energy densities leave scope for exploration. The synthesis of electrode materials with good electrochemical performance by an environmentally friendly, facile and low-cost method is need of the day for developing efficient and cost-effective electrochemical capacitors for energy storage applications.

References

- [1] F. Wang, X. Wu, X. Yuan, Z. Liu, Y. Zhang, L. Fu, Y. Zhu, Q. Zhou, Y. Wu and W. Huang, *Chem. Soc. Rev.*, 2017, 46, 6816.
- [2] [(a) C. Zhong, Y. Deng, W. Hu, J. Qiao, L. Zhang and J. Zhang, *Chem. Soc. Rev.*, 2015, 44, 7484–7539; (b) W. Tang, Y. Zhu, Y. Hou, L. Liu, Y. Wu, K. P. Loh, H. Zhang and K. Zhu, *Energy Environ. Sci.*, 2013, 6, 2093–2104; (c) F. Wang, X. Wu, C. Li, Y. Zhu, L. Fu, Y. Wu and X. Liu, *Energy Environ. Sci.*, 2016, 9, 3570–3611; (d) R. Li, Z. Lin, X. Ba, Y. Li, R. Ding and J. Liu, *Nanoscale Horiz.*, 2016, 1, 150–155.
- [3] Y. Wang, J. Guo, T. Wang, J. Shao, D. Wang and Y.-W. Yang, *Nanomaterials*, 2015, 5, 1667-1689.
- [4] Ling Miao, Ziyang Song, Dazhang Zhu, Liangchun Li, Lihua Gan and Mingxian Liu, *Mater. Adv.*, 2020, 1, 945-966.
- [5] S. Kondrat, C. R. Pérez, V. Presser, Y. Gogotsi and A. A. Kornyshev, *Energy Environ. Sci.*, 2012, 5, 6474-6479.
- [6] Ruben Heimböckel, Frank Hoffmann and Michael Fröba, *Phys. Chem. Chem. Phys.*, 2019, 21, 3122-3133.
- [7] Lijing Xie, Fangyuan Su, Longfei Xie, Xiaoqian Guo, Zhenbing Wang, Qingqiang Kong, Guohua Sun, Aziz Ahmad, Xiaoming Li, Zonglin Yi and Chengmeng Chen, *Mater. Chem. Front.*, 2020, 4, 2610-2634.
- [8] Polyacrylonitrile/polyvinyl alcohol-based porous carbon nanofiber electrodes for supercapacitor applications, Yasin Altin, Ayse Celik Bedeloglu, *Int. J. of Energy Research*.
- [9] Das TK, Banerjee S, Sharma P, Sudarsan V, Sastry PU. *Int J Hydrogen Energy*, 2018, 43, 8385–94.
- [10] Min Seok Kang, Incheol Heo, Kyung Gook Cho, Hyuna Kyung, Hee Soo Kim, Keun Hyung Lee, Won Cheol Yoo, 2022, 45, 380-388.
- [11] Cong Wang Zehao Song Houzhao Wan, Xu Chena, Qiuyang Tan, Yi Gan, Pei Liang, Jun Zhang, Hanbin Wang, Yi Wang, Xiaoni Peng, Peter A. van, Akenb Hao Wang, *Chemical Engineering Journal*, 2022, 400, 125955.
- [12] (a) Yuqi Jiang, Jinping Liu, *Energy and environmental materials*, 2019; 2:30-37. (b) Y. Liu, S. P. Jiang, Z. Shao, *Materials Today Advances*, 2020, 7, 100072.
- [13] (a) J. W. Kim, V. Augustyn, B. Dunn *Adv. The effect of crystallinity on the rapid pseudocapacitive response of Nb2O5 Energy Mater.*, 2012, 2, 141; (b) V. Augustyn, J. Come, M. A. Lowe, J. W. Kim, P. L. Taberna, S. H. Tolbert, B. Dunn, *Nat. Mater.*, 2013, 12, 518.
- [14] Songmin Zhang, Jiawen Wu, Jitong Wang, Wenming Qiao, Donghui Long, Licheng Ling, *Journal of Power Sources*, 2018, 396, 88-94.
- [15] L. Zhu, Y. Liu, C. Su, W. Zhou, M. Liu, Z. Shao, *Angew. Chem.*, 2016, 128, 9728-9731.
- [16] Sohyun Jeon, Ji Hwan Jeong, Hyomin Yoo, Hak Ki Yu, Bo-Hye Kim*, and Myung Hwa Kim, *ACS Appl. Nano Mater.*, 2020, 3, 3847–3858.
- [17] Zhao Jun Han, Shafique Pineda, Adrian T. Murdock, Dong Han Seo, Kostya (Ken) Ostrikov, Avi Bendavid, *J. Mater. Chem. A*, 2017, 5, 17293-17301.
- [18] VEDIKUYIL AZHAGAN MUNIRAJ, CHAITANYA KRISHNA KAMAJA, and MANJUSHA V. SHELKE, *ACS Sustainable Chem. Eng.* 2016, 4,

2528–2534.

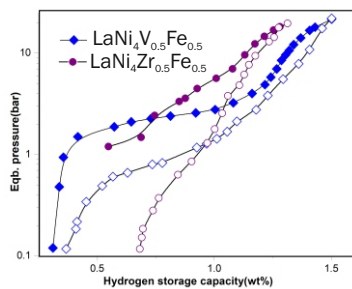
- [19] X. Xiao, H Song, S. Lin, *et al.* Nature Communications, 2016, 7, 11296.
- [20] (a) T.-Y. Wei, C.-H. Chen, H.-C. Chien, S.-Y. Lu, C.-C. Hu, *Adv. Mater.*, 2010, 22, 347–351; (b) P.F. Teh, Y. Sharma, S.S. Pramana, M. Srinivasan, *J. Mater. Chem.*, 2011, 21, 14999–15008.
- [21] D. Yan, W. Wang, X. Luo, C. Chen, Y. Zeng, Z. Zhu, *Chem. Eng. J.*, 2018, 334, 864–872.
- [22] S. Banerjee, A. Chowdhury, A. Chandra, V. Grover, *Mat. Chemi. and Physics*, 2022, 286, 126202.
- [23] S. Vijayakumar, S.-H. Lee, K.-S. Ryu, *Electrochim. Acta*, 2015, 182, 979–986.
- [24] H. Chen, J. Wang, X. Han, F. Liao, Y. Zhang, X. Han, C. Xu, *Ceram. Int.*, 2019, 45, 4059–4066.
- [25] T. Huang, C. Zhao, R. Zheng, Y. Zhang, Z. Hu, *Ionics (Kiel)*, 2015, 21, 3109–3115.
- [26] Gokul P. Kamble, Akash S. Rasal, Samadhan B. Gaikwad, Vivek S. Gurav, Jia-Yaw Chang, Sanjay S. Kolekar, Yong-Chien Ling, and Anil V. Ghule, *ACS Appl. Nano Mater.* 2021; 4: 12702–12711.
- [27] J. Zhao, J. Chen, S. Xu, M. Shao, D. Yan, M. Wei, D. G. Evans and X. Duan, *J. Mater. Chem. A*, 2013, 1, 8836.
- [28] (a) Z. Lu, Z. Chang, W. Zhu and X. Sun, *Chem. Comm.*, 2011, 47, 9651–9653; (b) H. Chen, J. Jiang, Y. Zhao, L. Zhang, D. Guo and D. Xia, *J. Mater. Chem. A*, 2015, 3, 428–437.
- [29] X. Li, D. Du, Y. Zhang, W. Xing, Q. Xue and Z. Yan *J. Mater. Chem. A*, 2017, 5, 15460.
- [30] (a) Z. Lu, W. Zhu, X. Lei, G. R. Williams, D. O'Hare, Z. Chang, X. Sun and X. Duan, *Nanoscale*, 2012, 4, 3640–3643; (b) Y. Wang, W. Yang, C. Chen and D. G. Evans, *J. Power Sources*, 2008, 184, 682–690; (c) N. Abushrenta, X. Wu, J. Wang, J. Liu and X. Sun, *Sci. Rep.*, 2015, 5, 13082.
- [31] (a) F. Gu, X. Cheng, S. Wang, X. Wang and P. S. Lee, *Small*, 2015, 11, 2044–2050; (b) P. Vialat, C. Mousty, C. Taviot-Gueho, G. Renaudin, H. Martinez, J. C. Dupin, E. Elkaim, F. Leroux, *Adv. Funct. Mater.*, 2014, 24, 4831–4842.
- [32] (a) H. Chen, F. Cai, Y. Kang, S. Zeng, M. Chen and Q. Li, *ACS Appl. Mater. Interfaces*, 2014, 6, 19630–19637; (b) J. Zhao, J. Chen, S. Xu, M. Shao, Q. Zhang, F. Wei, J. Ma, M. Wei, D. G. Evans and X. Duan, *Adv. Funct. Mater.*, 2014, 24, 2938–2946.
- [33] (a) J. Yang, C. Yu, X. Fan and J. Qiu, *Adv. Energy Mater.*, 2014, 4, 1400761; (b) X. Sun, G. Wang, H. Sun, F. Lu, M. Yu and J. Lian, *J. Power Sources*, 2013, 238, 150–156.
- [34] (a) X. Zheng, Z. Gu, Q. Hu, B. Geng and X. Zhang, *RSC Adv.*, 2015, 5, 17007–17013; (b) Y. Cheng, H. Zhang, C. V. Varanasi and J. Liu, *Energy Environ. Sci.*, 2013, 6, 3314–3321.
- [35] (a) K. Y. Ma, J. P. Cheng, J. Zhang, M. Li, F. Liu and X. B. Zhang, *Electrochim. Acta*, 2016, 198, 231–240; (b) A. D. Jagadale, G. Q. Guan, X. M. Li, X. Du, X. L. Ma, X. G. Hao and A. Abudula, *J. Power Sources*, 2016, 306, 526–534.
- [36] X. Wu, L. Jiang, C. Long, T. Wei and Z. Fan, *Adv. Funct. Mater.*, 2015, 25, 1648–1655.
- [37] (a) C. Wang, X. Zhang, Z. Xu, X. Sun and Y. Ma, *ACS Appl. Mater. Interfaces*, 2015, 7: 19601–19610; (b) L. Lv, K. Xu, C. D. Wang, H. Z. Wan, Y. J. Ruan, J. Liu, R. J. Zou, L. Miao, K. Ostrikov, Y. C. Lan and J. J. Jiang, *Electrochim. Acta*, 2016, 216, 35–43.

Hydrogen Storage Materials

Influence of Transition Metals on Hydrogen Storage Properties of LaNi₅ Alloy

Asheesh Kumar*, Seemita Banerjee, Priyanka Ruz and V. Sudarsan

Chemistry Division, Bhabha Atomic Research Centre, Mumbai 400085, INDIA



The pressure-composition isotherm

ABSTRACT

LaNi₅Fe alloy is found to have good hydrogen storage capacity among studied AB₅ alloy at room temperature. Effect of partial substitution of Fe by Zr and V in LaNi₄Fe alloy on its hydrogen storage properties has been investigated in detail. Alloys with composition LaNi₄Zr_{0.5}Fe_{0.5} and LaNi₄V_{0.5}Fe_{0.5} were prepared by arc melting method and the phase formation was confirmed by X-ray diffraction (XRD) technique. Hexagonal structure of the parent alloy is found to be retained even after substitution. Hydrogen absorption-desorption properties of these alloys as well as the kinetics involved in hydrogen absorption-desorption process were studied in detail using a Sievert's type set-up. LaNi₄Zr_{0.5}Fe_{0.5} and LaNi₄V_{0.5}Fe_{0.5} are found to absorb a maximum of 1.3 wt. % and 1.5 wt. % hydrogen respectively at room temperature. The substituted alloy shows improved kinetics than LaNi₅ alloy at room temperature.

KEYWORDS: Solid state electrolyte, NASICON, Li-ion solid state battery

Introduction

In recent years many hydrogen storage materials such as carbon nanotubes, porous metal-organic frameworks, complex hydrides, alanates, intermetallic compounds etc., have been explored extensively[1-2]. However, hydrides of alloys and intermetallic compounds continue to be the most promising materials for practical applications[3]. Among intermetallic compounds the AB₅ type are well known for their excellent hydrogen storage properties like easy activation, fast kinetics, cyclic stability and moderate plateau pressure[4-5]. LaNi₅ is one of the extensively studied systems among AB₅ alloys with a storage capacity of 1.5 wt%. This alloy absorbs hydrogen rapidly at room temperature without rigorous activation of surface at high pressure and temperature[6-7]. Besides hydrogen storage application, this alloy shows excellent catalytic properties.

Many researchers reported CO₂ methanation using LaNi₅ alloys. The ball-milling of LaNi₅ powder in a mixture of CO₂ and H₂ gases was found to successfully result in CH₄ generation[8]. LaNi₅ type alloys are commercially used as negative electrode in Ni-MH rechargeable batteries.

The hydrogen storage properties such as reversibility, desorption capacity, hydrogen storage capacity, and desorption temperature of the alloys can be further improved by changing their composition [9] or by elemental modification. The elemental modification by suitable substitution at La/Ni sites is expected to tune the hydrogen storage properties of LaNi₅ alloy. Researchers have tried partial substitution of elements like Ce, Zr, Mg, Co, Fe, Mn, Al, Cu and Sn in place of both elements and investigated the hydrogen storage properties in detail [10-11]. The partial substitution of Co, Fe, Al and Sn in place of Ni in this alloy is found to improve the hydrogen storage properties of the parent alloy. For example,

Sn substitution for Ni in LaNi₅ alloy enhances the long-term hydrogen storage stability, and the hydrogen storage capacity of the alloy reduced only 1.2 % in 1000 cycles[12]. It is inferred from the studies that hydrogen storage properties and cyclic stability improved significantly upon elemental modification [13].

Though it is reported that substitution of Fe for Ni is found to increase the storage capacity of LaNi₄Fe to 2.2 wt%[14], several other studies reported storage capacities in the range of 1 to 1.25 wt.% at room temperature[15-16].

In general, hydrogen absorption capacity of LaNi₄Fe alloy can be enhanced by the substitution of Fe with elements having higher electron affinity and bigger size than that of Ni. Substitution of bigger size element increases the c/a ratio of the hexagonal lattice, and larger value of c/a ratio decreases the diffusion path length of hydrogen atoms into the unit cell and reduces the micro strain.

With this background, in the present study elemental substitution of Fe in LaNi₄Fe alloy has been carried out with bigger atomic size element such as Zr and V, with a view to improve the hydrogen storage properties of the alloy.

In the present manuscript effect of partial substitution of Fe by Zr and V in LaNi₄Fe alloy on its hydrogen storage properties have been discussed. The alloys LaNi₄Zr_{0.5}Fe_{0.5} and LaNi₄V_{0.5}Fe_{0.5} were synthesized by arc melting of the constituent elements. The structure of the alloy and their hydrogen absorption properties have been studied in detail.

Experimental

The studied LaNi₄Zr_{0.5}Fe_{0.5} and LaNi₄V_{0.5}Fe_{0.5} alloys were prepared by arc melting high purity constituent elements in a water-cooled copper hearth under argon atmosphere. For achieving the homogeneity, the alloy button was turned over and re-melted 4 times. The crystal structure of the as-cast alloy was examined by X-ray diffraction (XRD) technique using

*Author for Correspondence: Asheesh Kumar
E-mail: asheeshk@barc.gov.in

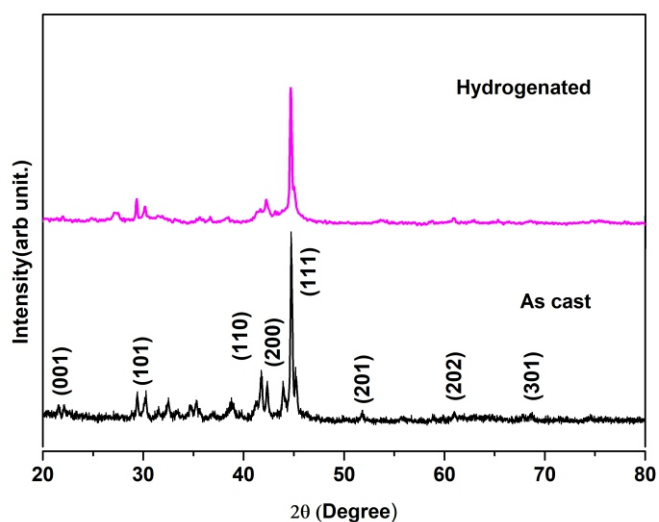


Fig.1a: XRD pattern of $\text{LaNi}_4\text{V}_{0.5}\text{Fe}_{0.5}$ alloy as cast and after hydrogenation.

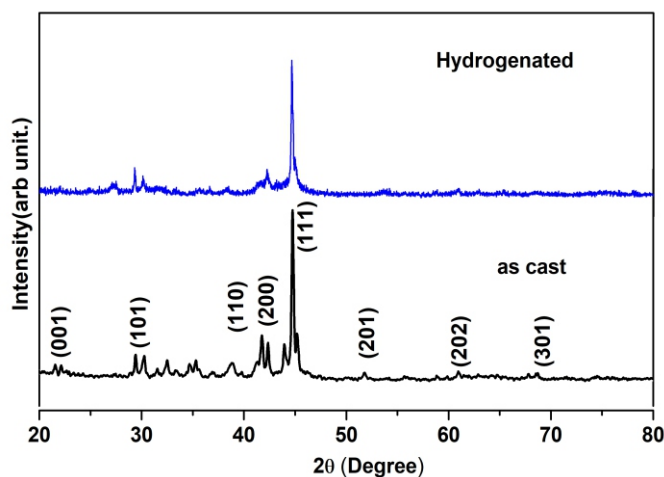


Fig.1b: XRD pattern of $\text{LaNi}_4\text{Zr}_{0.5}\text{Fe}_{0.5}$ alloy, as cast and after hydrogenation.

monochromatic Cu K α radiation. Hydrogen absorption and desorption studies were done using a Sievert's type set up described in our earlier studies[17].

The activation procedure involved heating of the alloy under vacuum (10^{-6} mbar) for 2 hours at 673 K. Pressure-composition isotherms were studied at room temperature and up to a hydrogen pressure of 2 MPa. Kinetic study was done at room temperature and hydrogen pressure of 2 MPa after one absorption-desorption cycle. The amount of total hydrogen in the hydrides was estimated by monitoring change in the hydrogen pressure during the absorption process. The hydride sample was surface poisoned before being taken out. Hydrogen content of the saturated hydride sample was estimated by complete decomposition of a small amount of the hydride sample in a pre-calibrated evacuated quartz chamber described in our earlier studies [17].

Results and Discussion

Crystal structure

Fig.1 (a and b) show the XRD patterns of $\text{LaNi}_4\text{Zr}_{0.5}\text{Fe}_{0.5}$ and $\text{LaNi}_4\text{V}_{0.5}\text{Fe}_{0.5}$ alloys, before and after hydrogen absorption. The data confirmed that all the samples are single phase, and crystallized in the hexagonal CaCu_5 type structure, (space group P6/mmm), the same structure as of prototype LaNi_5 .

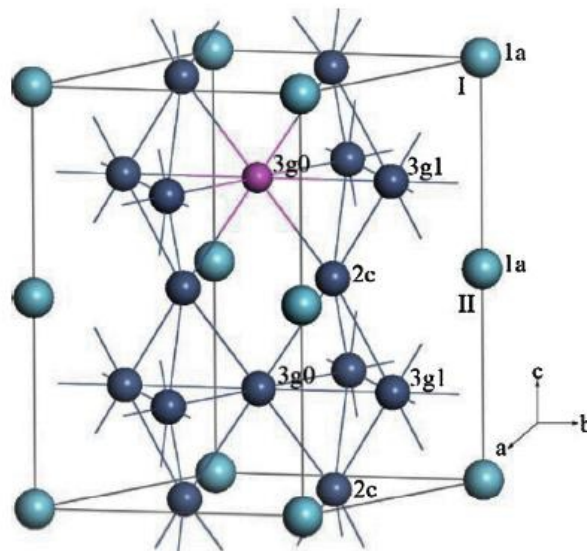


Fig.2: Crystallographic arrangements of LaNi_5 unit cell adopted from Ref [18].

The unit cell lattice parameters were obtained by least square fitting. The lattice parameters of both the alloys are given in Table 1. It can be seen that with the substitution of V in the alloy, the lattice parameters "a" and "c" as well as the cell volume increases. The observation is in line with the expectation as V (134 pm) has higher atomic size compared to both Ni (124 pm) and Fe (126 pm). The increase in the lattice parameter suggests that V preferentially gets substituted in the lattice position of Ni. It can also be observed that there is an increase in the c/a ratio of the hexagonal unit cell after V substitution.

In Fig. 2, the structure of LaNi_5 with two different layers of atoms is shown. The basal plane contains both La and Ni atoms at the 1a and 2c sites, respectively. The intermediate layer consists of only Ni atoms in 2c sites. After the substitution of V in the structure, there is an increase in the c/a ratio indicating that the substituent elements preferentially goes in the intermediate layer and replace Ni atoms in the structure. The situation is slightly different for Zr substitution. With Zr substitution, the c/a ratio remains almost same and it is obvious that in the latter system the basal or both available nickel crystallographic positions are involved in the substitution process. It is also clear from the XRD patterns of both the alloys that the peaks are similar in as cast and hydrogenated alloys with minor change in peak positions, which indicates that the hydrides are of the same structure as the parent alloy with change in lattice parameters.

During the formation of hydrides the hydrogen atoms go into the interstitial position of the alloy, increasing the lattice parameter slightly. The strain created during hydride formation leads to broadening in the X-ray diffraction peaks. As peak become broader merging take place, leading to removal of necks.

Hydrogen Absorption Study

The hydrogen absorption and desorption properties of the alloys were studied at room temperature using a Sievert's type set up. For the construction of pressure-composition isotherms at a temperature, certain pressure of hydrogen is introduced in the reaction chamber and the hydrogen absorption was monitored with pressure drop. After complete absorption at that dose pressure, same procedure was repeated until the equilibrium pressure reaches 20 atm.

Table 1: Hydrogen storage capacity, lattice parameter and unit cell volume of the studied alloy.

| S.N. | Alloy | a(Å) | c(Å) | Unit cell volume | c/a ratio | Rate of H ₂ uptake (cc/g/min) | Hydrogen storage capacity (H/M) |
|------|--|-------|-------|------------------|-----------|--|---------------------------------|
| 1. | LaNi ₅ | 5.017 | 3.986 | 86.2 | 0.7945 | 22 | 6 |
| 2. | LaNi ₄ Fe | 5.049 | 4.015 | 88.02 | 0.7952 | 19 | 5.4 [15] |
| 4. | LaNi ₄ V _{0.5} Fe _{0.5} | 5.052 | 4.022 | 88.28 | 0.7961 | 28 | 6.5 |
| 5. | LaNi ₄ V _{0.5} Fe _{0.5} | 5.049 | 4.014 | 88.00 | 0.7950 | 23 | 5.9 |

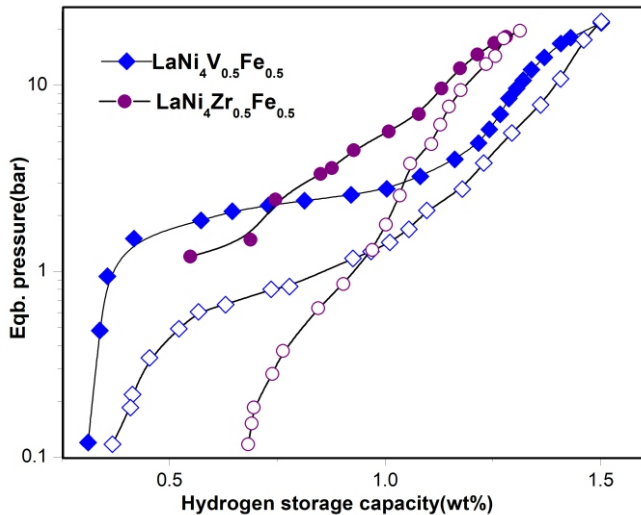


Fig.3: The pressure-composition isotherm of LaNi₄Zr_{0.5}Fe_{0.5} and LaNi₄V_{0.5}Fe_{0.5} alloys.

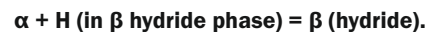
Fig.3 shows the room temperature pressure-composition isotherms of LaNi₄Zr_{0.5}Fe_{0.5} and LaNi₄V_{0.5}Fe_{0.5} alloys. As shown in Fig.3, alloys LaNi₄Zr_{0.5}Fe_{0.5} and LaNi₄V_{0.5}Fe_{0.5} are found to absorb maximum of 5.9 H/formula unit and 6.5 H/formula unit respectively at room temperature. The absorption in LaNi₄Zr_{0.5}Fe_{0.5} is close to the hydrogen storage capacity of LaNi₅ alloy. In AB₅ type alloy total 34 tetrahedral holes are available for hydrogen storage. But all the holes cannot be occupied simultaneously due to stability consideration. As per Switendic Criterion, minimum distance between two H atoms is 2.1 Å and this controls the hydrogen occupancy in holes. Hydrogen storage capacities of both the alloys are listed in Table 1. The probable cause for reduction in hydrogen storage capacity of the studied alloys may be unavailability of suitable interstitial site. Pressure composition isotherm studies show change in plateau pressure for both the alloys at room temperature. The plateau region, in the absorption isotherm of vanadium substituted alloy is found nearly flat and slightly above 1 bar pressure which actually suggest that at room temperature around 1 bar hydrogen pressure will be generated to from the

alloy and at a particular temperature with small change in the equilibrium pressure hydrogen absorption and desorption can be carried out. On the other hand, Zr substitution in place of Fe increased the plateau pressure drastically and LaNi₄Zr_{0.5}Fe_{0.5} alloy shows sloping plateau at higher pressure. Unlike the earlier case, the hydride LaNi₄Zr_{0.5}Fe_{0.5}H_{5.9} is quite unstable at room temperature and is not suitable for room temperature applications. Thus, from the above discussion it can be concluded that change in chemical composition of LaNi₅ alloy affect the thermodynamic stability of the alloy remarkably, which may or may not be beneficial for the practical application.

It is also expected that change in chemical composition would affect the kinetics of hydrogen absorption-desorption. The hydrogenation reaction of metal/alloy/intermetallic compound comprises following steps[19]

- 1. Physisorption of H₂ molecules on the surface of alloy/intermetallic compound.
- 2. Dissociation of H₂ molecules into H atoms.
- 3. Penetration of H atoms from surface into bulk followed by chemisorption.
- 4. Diffusion of H atoms through the hydride layer.
- 5. Hydride formation at the metal/hydride interface.

Among the above mentioned processes, the slowest one would govern the overall reaction kinetics, thus considered as rate determining step of the hydrogen absorption reaction. When the H atoms reach the interface (step 5) of metal/alloy/intermetallic compound (α phase) and hydrides (β phase), a fast reaction happens leading to the formation of growing hydride layer.



The hydrogen desorption reaction follows the above mentioned steps in a reverse order. Extensive studies have been carried out on the hydrogenation-dehydrogenation kinetics of LaNi₅ alloy by different researchers[20-22]. The activation energy of hydrogen absorption-desorption of LaNi₅ alloy can be tuned by changing the reaction conditions as well as by chemical modifications. Some of the examples are listed in Table 2. It is

Table 2: Reported kinetic details of LaNi₅ alloy in different study.

| Alloy | Operating condition | Kinetic model | Activation Energy | Ref. |
|-------------------|---------------------|---------------------------|------------------------|------|
| LaNi ₅ | 25- 40 °C | JMA 1 st order | 30 (abs), 40 (des) | 20 |
| LaNi ₅ | 20- 50 °C | Shrinking Core Model | 19.65 (abs) | 21 |
| LaNi ₅ | 40- 70 °C | JMA 1 st order | 19.5 (abs) | 9 |
| LaNi ₅ | 20- 40 °C | Pressure dependent model | 26.4 (abs), 39.8 (des) | 22 |

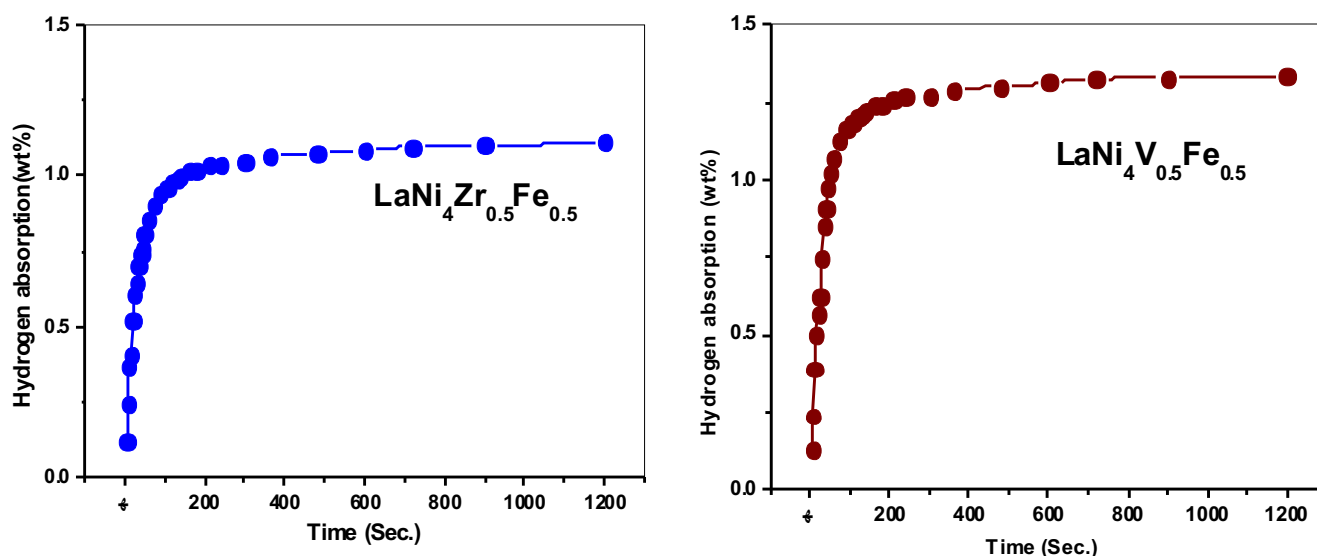


Fig.4: The hydrogen absorption kinetics of $\text{LaNi}_4\text{Zr}_{0.5}\text{Fe}_{0.5}$ and $\text{LaNi}_4\text{V}_{0.5}\text{Fe}_{0.5}$ alloys.

found from the literature survey that different types of kinetic models have been used by researchers to describe the hydrogenation-dehydrogenation kinetics of LaNi_5 alloy. These kinetic models are used to determine the rate constants of hydrogenation-dehydrogenation reactions from experimentally obtained kinetic data at different temperatures (T). Finally activation energy is obtained from the Arrhenius plot of rate constant vs $(1/T)$.

Like the thermodynamic parameters, the derived activation energy plays an important role during the engineering design of metal-hydride systems for different applications. Hence in the present study, kinetics of hydrogen absorption for Zr and V substituted LaNi_5 alloys have also been investigated. The hydrogenation kinetics for $\text{LaNi}_4\text{Zr}_{0.5}\text{Fe}_{0.5}$ and $\text{LaNi}_4\text{V}_{0.5}\text{Fe}_{0.5}$ alloys have been studied after one absorption desorption cycle. The hydrogen absorption kinetics of both the alloys is shown in Fig.3. It is found that hydrogen absorption is fast and it reaches near saturation value very fast. There is no incubation period before absorption as clear from the figure.

The alloy $\text{LaNi}_4\text{Zr}_{0.5}\text{Fe}_{0.5}$ absorbs maximum 93% of its total hydrogen storage capacity within 5 minutes and $\text{LaNi}_4\text{V}_{0.5}\text{Fe}_{0.5}$ alloy absorbs 95% of total hydrogen absorption within same time period. As mentioned in Table 1 the rate of hydrogen absorption for V and Zr substituted alloy is faster than the parent alloy. Hence, it is inferred that hydrogen absorption kinetics of V substituted alloy is better than that of Zr substituted alloy.

Conclusions

Hydrogen absorption-desorption properties of $\text{LaNi}_4\text{Zr}_{0.5}\text{Fe}_{0.5}$ and $\text{LaNi}_4\text{V}_{0.5}\text{Fe}_{0.5}$ alloys have been studied. The maximum storage capacities of 1.3 and 1.5 wt. % are found for $\text{LaNi}_4\text{Zr}_{0.5}\text{Fe}_{0.5}$ and $\text{LaNi}_4\text{V}_{0.5}\text{Fe}_{0.5}$ alloys, respectively. The pressure composition isotherm studies show the change in plateau pressure for both the alloys at room temperature. The plateau region, in the absorption isotherm of vanadium substituted alloy is found nearly flat and slightly above 1 bar pressure, whereas, $\text{LaNi}_4\text{Zr}_{0.5}\text{Fe}_{0.5}$ alloy shows sloping plateau at higher pressure. Hydride of $\text{LaNi}_4\text{V}_{0.5}\text{Fe}_{0.5}$ alloy is more stable than $\text{LaNi}_4\text{Zr}_{0.5}\text{Fe}_{0.5}$ hydride under similar conditions. Hydrogen absorption kinetics of both ($\text{LaNi}_4\text{V}_{0.5}\text{Fe}_{0.5}$ and $\text{LaNi}_4\text{Zr}_{0.5}\text{Fe}_{0.5}$) alloys are found to be faster than that of parent alloy. Crystal structure of the alloy remains unaffected with hydrogen

absorption and desorption. The $\text{LaNi}_4\text{V}_{0.5}\text{Fe}_{0.5}$ alloy may desorb hydrogen easily at ambient condition as plateau pressure of the alloy is above 1bar.

References

- [1] Zuttel A, Sudan P, Mauron Ph, Kiyobayashi T, Emmenegger Ch, Schlabach L. Hydrogen storage in carbon nanostructures, Int J Hydrogen Energy, 2002, 27, 203-204.
- [2] Zaluski L, Zaluska A and Ström-Olsen JO. Nanocrystalline metal hydrides, J Alloys Compd 1997; 253–254, 70–9.
- [3] Sakintuna B, Farida LD, Michael H. Metal hydride materials for solid hydrogen storage: a review, Int. J. Hydrogen Energy 2007, 32, 1121–40.
- [4] Jain RK, Jain A, Agarwal S, Lalla NP, Ganesan V, Phase DM, Jain IP. Characterization and hydrogenation of $\text{CeNi}_{5-x}\text{Cr}_x$ ($x = 0, 1, 2$) alloys, J. Alloys Compd. 2007, 430, 165-169.
- [5] Yamagishi R, Kojima T, Kameoka S, Okuyama D, Sato TJ, Nishimura C, Tsai AP. Creating the hydrogen absorption capability of CeNi_5 through the addition of Al, Int. J. Hydrogen Energy 2017, 42, 21832-21840.
- [6] Joubert JM, Paul-Boncour V, Cuevas F, Zhang J, Latroche M. LaNi_5 related AB_5 compounds: structure, properties and applications, J Alloys Compd 2021, 862, 158163.
- [7] Yatagai K, Shishido Y, Gemma R, Boll T, Uchida HH, Oguri K. Mechanochemical CO_2 methanation over LaNi -based alloys, Int. J. Hydrogen Energy 2020, 45, 5264-5275.
- [8] Sawahara K, Gemma R. In-situ monitoring of CO_2 methanatic pressure change upon ball-milling of LaNi_5 under CO_2 and H_2 , J. Ac Sci, 2021, 33, 33107.
- [9] Zhang W, Cimato J, Goudy AJ. The hydriding and dehydriding kinetics of some $\text{LaNi}_{5-x}\text{Al}_x$ alloys, J Alloys Compd., 1993, 201, 175-17
- [10] Chen XY, Xu J, Zhang WR, Zhu S, Zhang N, Ke DD, Liu JJ, Yan Cheng HH. Effect of Mn on the long-term cycling performance of AE type hydrogen storage alloy, Int. J. Hydrogen Energy, 2021, 46, 21973-21983.
- [11] Msika E, Latroche M, Cuevas F, Percheron-Guégan A. Zr-substitution in LaNi_5 -type hydride compound by room temperature ball milling, Materials Science and Engineering: B, 2004, 108, 91-95.
- [12] Laurencelle F, Dehouche Z, Goyett J. Hydrogen sorption cycling

performance of $\text{LaNi}_{4.8}\text{Sn}_{0.2}$, *J Alloys Compd.*, 2006, 424, 266-271.

[13] Hu WK, Kim DM, Jang KJ, Lee JY., Studies on Co-free rare-earth-based hydrogen storage alloys, *J. Alloys Compd.*, 1998, 269, 254-258.

[14] Pandey SK, Srivastava A, Srivastava ON. Improvement in hydrogen storage capacity in LaNi_5 through substitution of Ni by Fe, *Int. J. Hydrogen Energy*, 2007, 32, 2461-2465.

[15] Lamloumi J, Percheron-Guegan A, Lartigue C, Achard JC, Jehannoc G. Thermodynamic, structural and magnetic properties of $\text{LaNi}_{5-x}\text{Fe}_x$ hydrides, *J. Less-common Met.*, 1987, 130, 111-122.

[16] Misawa T, Sugawara H. Acoustic emission and exoelectron emission characteristics during disintegration process with hydrogen absorption in LaNi_4Fe and CaNi_5 , *J. Less-common Met.*, 1983, 89, 19-25.

[17] Seemita Banerjee Ph.D thesis (2013)
<http://hdl.handle.net/10603/11613>.

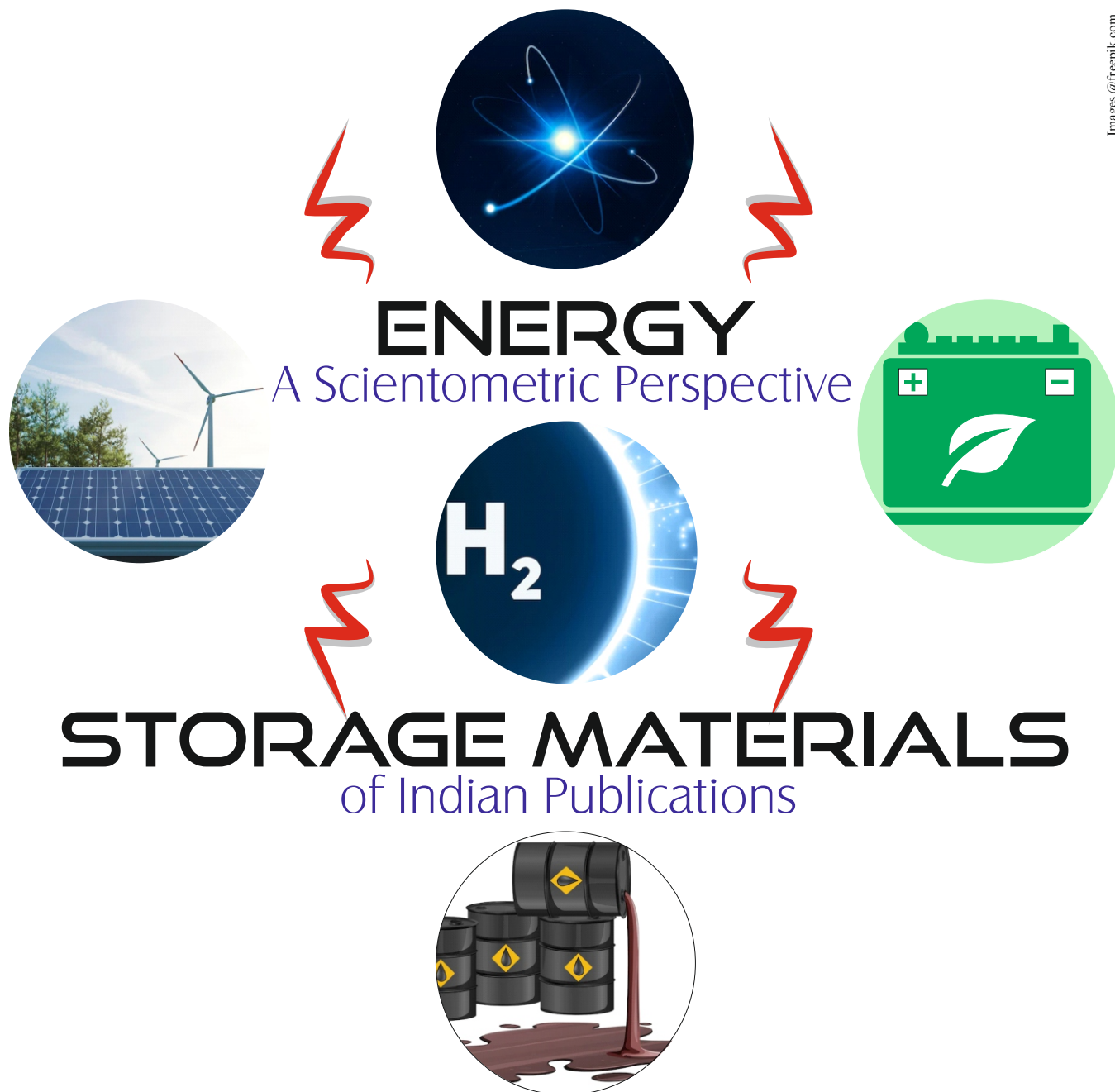
[18] Liu G, Chen D, Wang Y, Yang K. Experimental and computational investigations of $\text{LaNi}_{5-x}\text{Al}_x$ ($x=0, 0.25, 0.5, 0.75$ and 1.0) tritium-storage alloys, *Journal of Materials Science & Technology*, 2018, 34, 1699-1712.

[19] Martin M, Gommel C, Borkhart C, Fromm E. Absorption and desorption kinetics of hydrogen storage alloys *J. Alloys Compd.*, 1993, 201, 193-201.

[20] Zarynow A, Goudy AJ, Schweibenz RG, Clay KR. The effect of the partial replacement of nickel in LaNi_5 hydride with iron, cobalt and copper on absorption desorption kinetics, *J. Less-common Met.*, 1991, 172, 1009-17.

[21] Nahma KS, Kima WY, Honga SP Lee WY. The reaction kinetics of hydrogen storage in LaNi_5 , *Int. J. of Hydrogen Energy*, 1992, 17-5, 333-338.

[22] Dhaoua H, Askria F, Ben Salaha M, Jemnia A, Ben Nasrallah S, Lamloumib J. Measurement and modelling of kinetics of hydrogen sorption by LaNi_5 and two related pseudo binary compounds, *Int. J. of Hydrogen Energy*, 2007, 32, 576-87.



E. R. Prakash*, Ganesh Surwase, Madhav N, Pranesh Sengupta

Introduction

Energy is captured and stored in devices known as accumulator or battery for all kinds of potential use. Energy manifests itself in several forms, including chemical energy, potential energy, heat from burning of fossil fuels etc. The development of energy storage technologies has become a thrust area for scientists, researchers and engineers, globally. Efforts are underway for identifying highly promising energy storage materials from a range of potential combinations. Importantly, the stored energy should ideally be accessible on a larger scale and also available easily at the point-of-use[1-4]. In the present study, we have applied the popular Scientometrics approach to analyze both quantitatively and qualitatively a range of scientific publications and citations to understand the structural aspects and growth of scientific research in energy storage materials at global level;

performance of countries; performance of institutions; and also understand the eminence of scientists working in this domain. The study also helped ascertain the information seeking behavior of scientists, researchers and engineers by way of identifying the platforms across which scholarly work is mostly published and the data cited usually in these works[5-6].

Globally, China, the United States, South Korea, and Japan lead the list of countries in terms of scientific research on energy storage materials. As per Scopus database, India is placed fifth in terms of number of publications, and several prominent Indian institutions are involved in high quality R&D on energy storage materials. The present study aims to scientometrically analyze the Indian journal articles published during the last 20 years in this interesting field of science and technology.

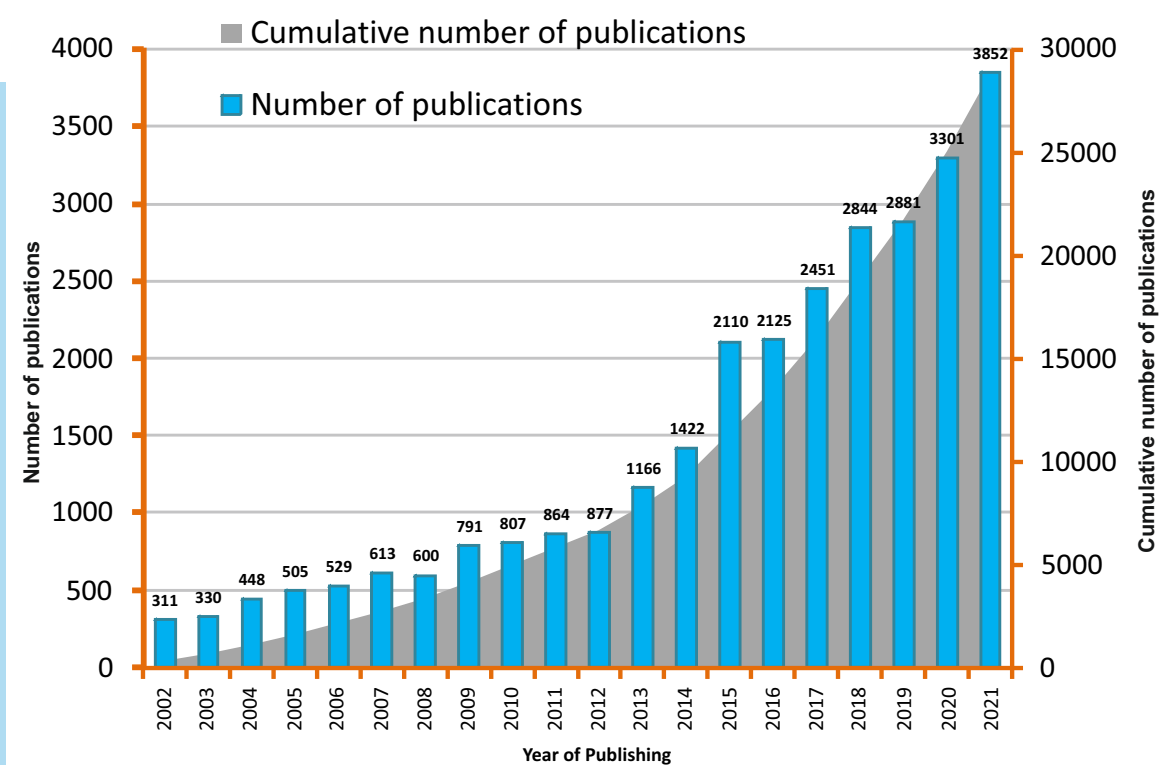
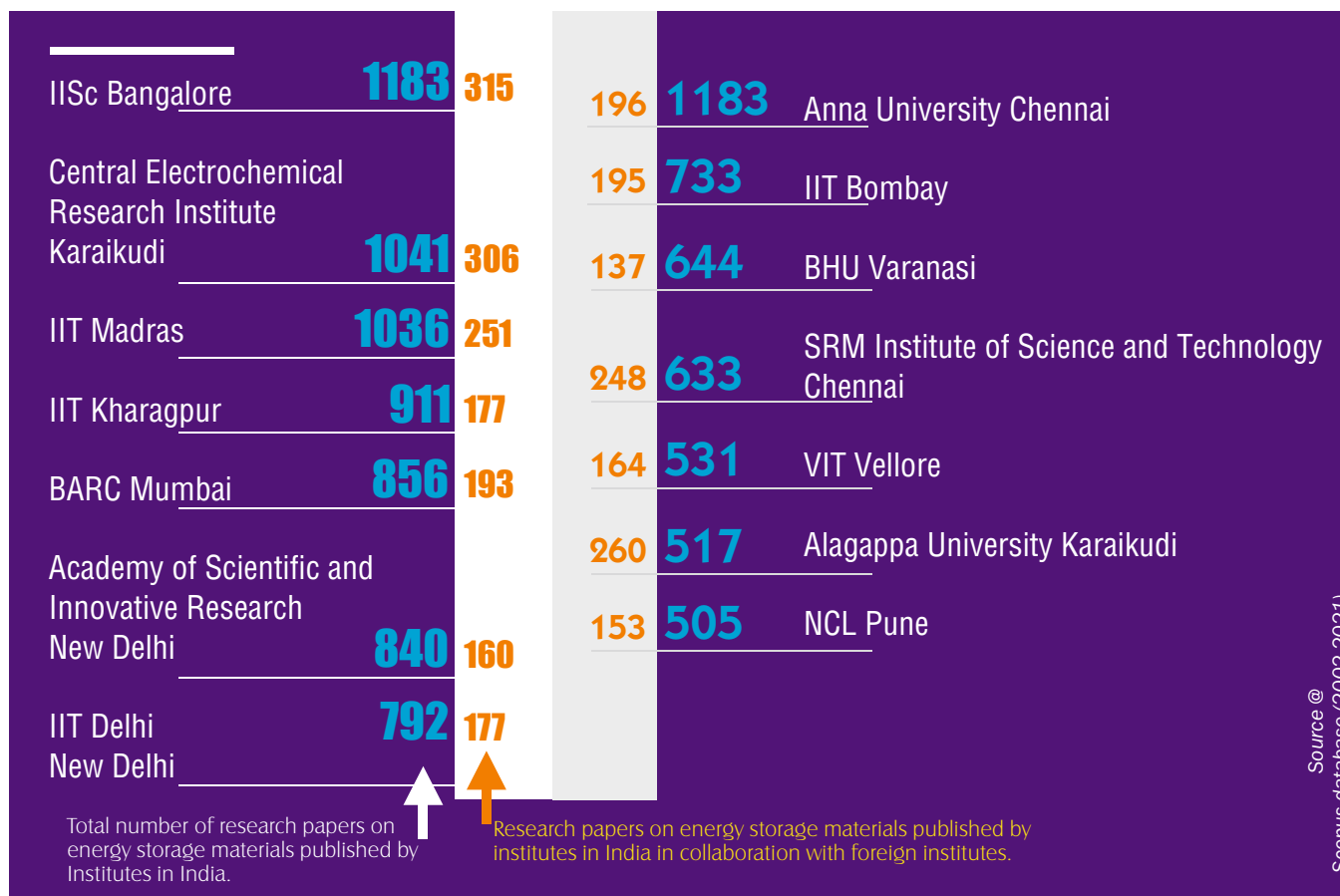


Fig.1: Year-wise distribution of Indian research papers on energy storage materials.

Research Method and Data Collection

The ‘Secondary Research’ method was adopted in the present study. Scopus, an international bibliographical database of references to scientific and research articles with citation data, was used for eliciting publication records pertaining to ‘energy storage materials’ published by Indian

scientists during 2002 to 2021. The study is restricted to only journal articles and a total of 28,827 research papers are found in the Scopus database and these were subjected to scientometric analysis as per the objectives of the study.

Results and Discussion

Year-wise Trend of Publications: As per Scopus database, a

| | | | | | |
|--|------|-------|-----------------|-----|--|
| International Journal of Hydrogen Energy | 1017 | 5.816 | 2.478 | 561 | Journal of Materials Science: Materials in Electronics |
| Journal of Alloys and Compounds | 699 | 5.316 | 9.127 | 528 | Journal of Power Sources |
| Electrochimica Acta | 680 | 6.901 | NA [#] | 392 | International Journal of Applied Engineering Research |
| RSC Advances | 654 | 3.361 | 6.583 | 377 | Journal of Energy Storage |
| Ionics | 584 | 2.817 | 5.742 | 377 | Solar Energy |

Total number of research articles on energy storage materials published by Indian scientists in popular journals.

Impact factor of the journals in which these articles have been published

Impact factor not available

Source @ Scopus database (2002-2021)

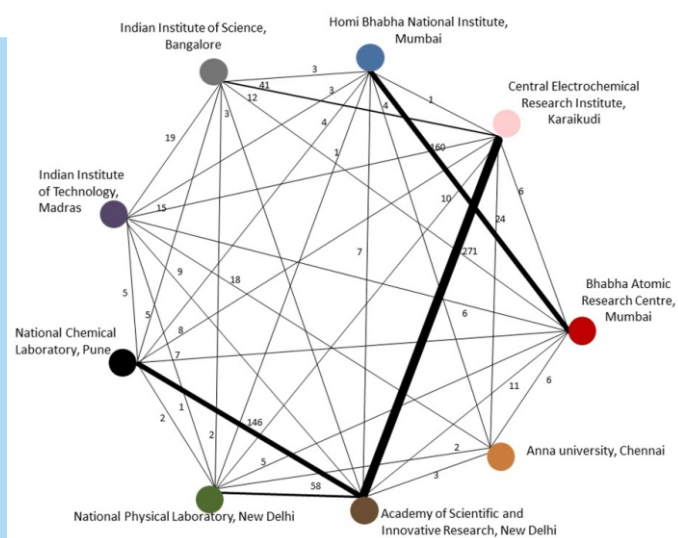


Fig.2: Collaboration network of highly-collaborated Indian Institutes involved in research on energy storage materials.

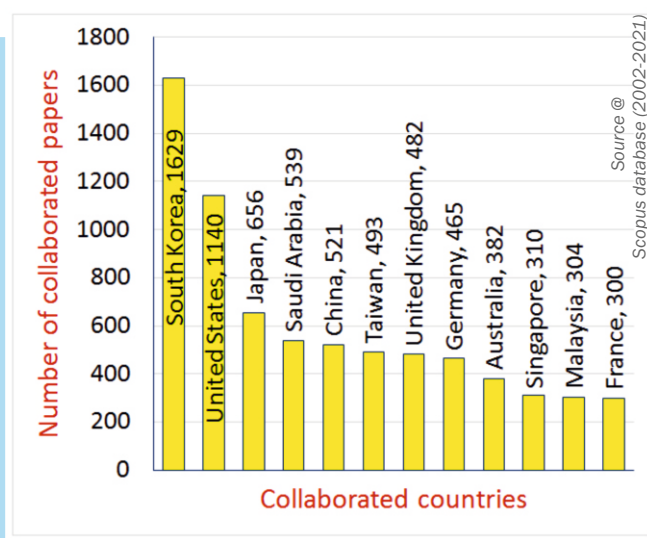


Fig.3: Highly collaborated countries with Indian research institutes involved in research on energy storage materials.

total of 4,42,452 publications were published during 2002 to 2022 on 'energy storage materials'. China is placed at the top amongst the countries with the highest number of research papers followed by the United States, South Korea and Japan. India occupied fifth position with a total of 28,827 research papers published during this period. Chronological distribution of these papers is depicted in Fig.1. The citations to these papers have been analyzed and it has been found that the average to maximum citations is 40 and 3,806 (in case of review paper).

Indian Research Institutes and Collaboration: Research papers originating from India on 'energy storage materials' is predominantly on account of joint collaboration between several research institutes based within the country. Institutes in India with over 500 research papers published on energy storage materials are listed in the Table 1.

The Scopus records were carefully analyzed to understand the nature of collaboration between the leading research institutes and various other institutes within the country as well as with the foreign institutes in the common domain of energy storage materials. Results showed that

3,527 (12.24%) publications out of the total of 28,827 publications have been as a result of joint collaboration between research institutes situated within the country whereas 7,579 (26.29%) resulted from international collaboration.

The collaboration network of few leading Indian institutes is portrayed in Fig.2. Our analysis showed that the foreign institutes with which Indian institutes collaborated in a large way (most-collaborated) are South Korea, the United States, Japan, Saudi Arabia and China. The number of papers published jointly with these most-collaborated countries is presented in the form of a bar graph in Fig.3.

The chronological trend of collaboration among research institutes situated in India and also with the foreign institutes are depicted in Fig.4. A linear growth has been observed in the rate of collaboration among the Indian research institutes and with the foreign institutes during 2002 to 2021. Average citations received for internationally collaborated papers is 34 and for non-collaborated papers it is 25. The average Impact Factor of the journals publishing internationally collaborated papers is 5.56 whereas for non-collaborated papers it is 4.41.

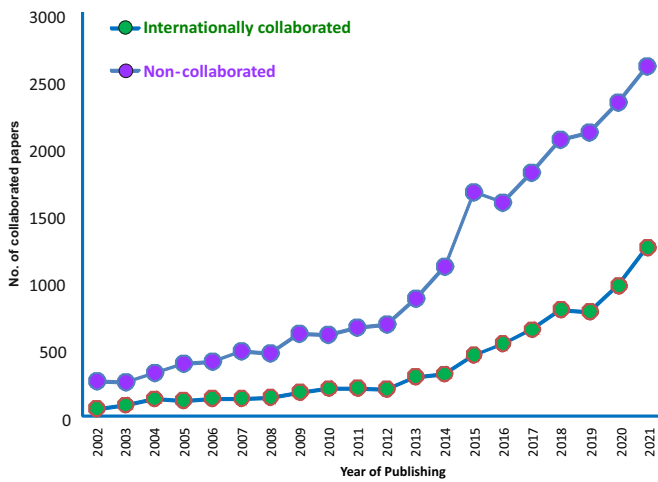


Fig.4: Year-wise distribution of Indian research papers on energy storage materials.

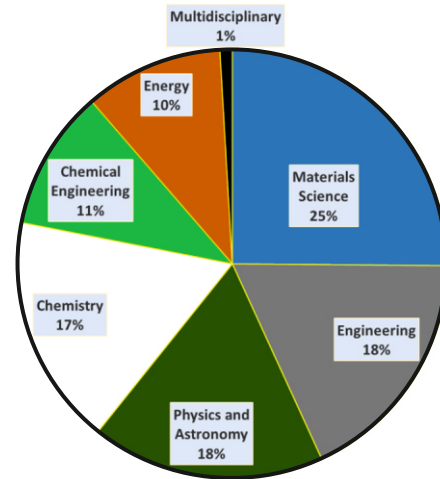


Fig.5: Subject-wise distribution of journals in which scholarly work on energy storage materials are published by Indian scientists & engineers.

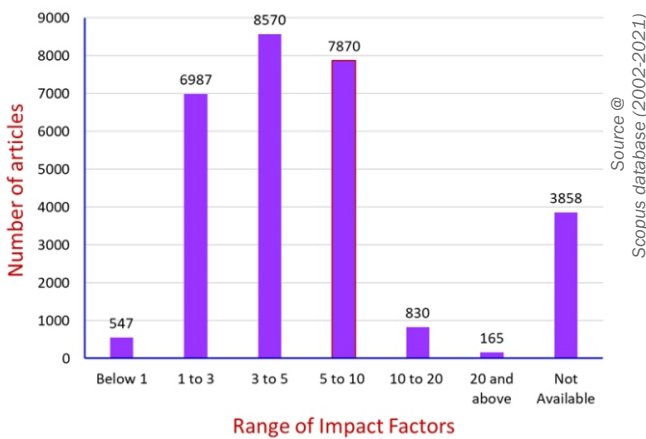


Fig.7: Indian publications in energy storage materials in different impact factor ranges.

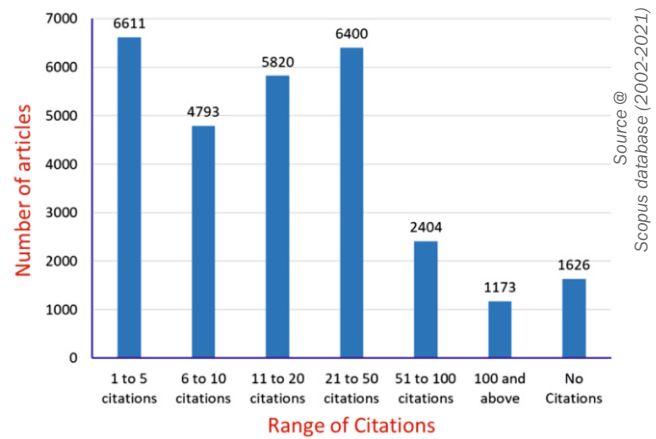


Fig.6: Indian publications in energy storage materials in different citations ranges.

Published Journals: The study has identified journals preferred by Indian scientists & engineers to publish their articles on ‘energy storage materials’. The papers are published in 1,391 distinct journals and top ten journals are listed in Table 2 with number of articles published in them and impact factors. The average Impact Factor of journals publishing articles on energy storage materials was 4.73.

By analyzing the subject categories of journals, it was found that, maximum number of research papers on energy storage materials are published in journals categorized as materials science (25%), followed by engineering, physics and astronomy 18% each (Fig.5).

Citations and Impact Factors: Citations indicate the impact of individual publications and impact factor suggests the quality of journals in which articles are published when the quality (impact) of published articles are considered. The present study has analyzed citations of individual articles and impact factors of the published journals. The citations impact factors in different ranges are presented in Fig.6 and Fig.7.

Conclusion

The results of the scientometric analyses on ‘energy storage materials’ provide valuable insights ranging from the nature and the extent of collaboration amongst the leading Indian institutes and inter-institutional collaboration globally, etc. This study may be useful to researchers, science administrators and policy makers. The extent of collaboration by Indian scientists & engineers in the field indicates the societal commitment of them as well as the willingness to share the models and technology in the field.

A detailed study on contributions of other countries in the field and a comparison with Indian publications is suggested. The scope of journals in which articles related to energy storage materials are published varied from materials science to engineering, physics and astronomy, chemistry, chemical engineering, energy indicates the usage of knowledge base from various subjects for the development of energy storage materials.

Acknowledgement

Authors are highly grateful to S. Adhikari, Head, Scientific Information Resource Division for the valuable guidance and suggestions, which helped in improving the study. Authors are thankful to their colleagues Balram Meena and Ujwala Aroskar for extending their technical assistance in compiling this manuscript.

References

- [1] Liu, C., Li, F., Lai-Peng, M., Cheng, H.-M., Advanced materials for energy storage. *Advanced Materials*, 2010, 22(8), E28-E62.
- [2] Simon, P., Gogotsi, Y., Materials for electrochemical capacitors. *Nature Materials*, 2008, 7(11), 845-854.
- [3] Baughman, R.H., Zakhidov, A.A., De Heer, W.A., Carbon Nanotubes-the Route Toward Applications. *Science*, 2002, 297(5582), 787-792.
- [4] Miller, J.R., Simon, P., Materials science: Electrochemical capacitors for energy management. *Science*, 2008, 321(5889), 651-652.
- [5] Song, M., Long, Y., Scientometric review of transition metal oxides for hydrogen energy production. *Energy Sources-A*, 2022, 44(2), 3720-3734.
- [6] Chanchetti, L.F., Leiva, D.R., Lopes de Faria, L.I., Ishikawa, T.T., A scientometric review of research in hydrogen storage materials. *International Journal of Hydrogen Energy*, 2020, 45(8), 5356-5366.

**Author for Correspondence: E.R. Prakash
E-mail: prak@barc.gov.in*



Rupsha Bhattacharyya

The latest series (released in 2021-2022) of the Assessment Reports (ARs) from the three Working Groups (WGs) of the Intergovernmental Panel on Climate Change (IPCC) has established without doubt the role of greenhouse gas (GHG) emissions in human induced climate change[1]. Carbon dioxide emissions reduction across all sectors of the economy and management of residual and unavoidable emissions from the hard-to-abate sectors through technological and nature-based means is the most critical need of the hour in our attempts at climate change mitigation.

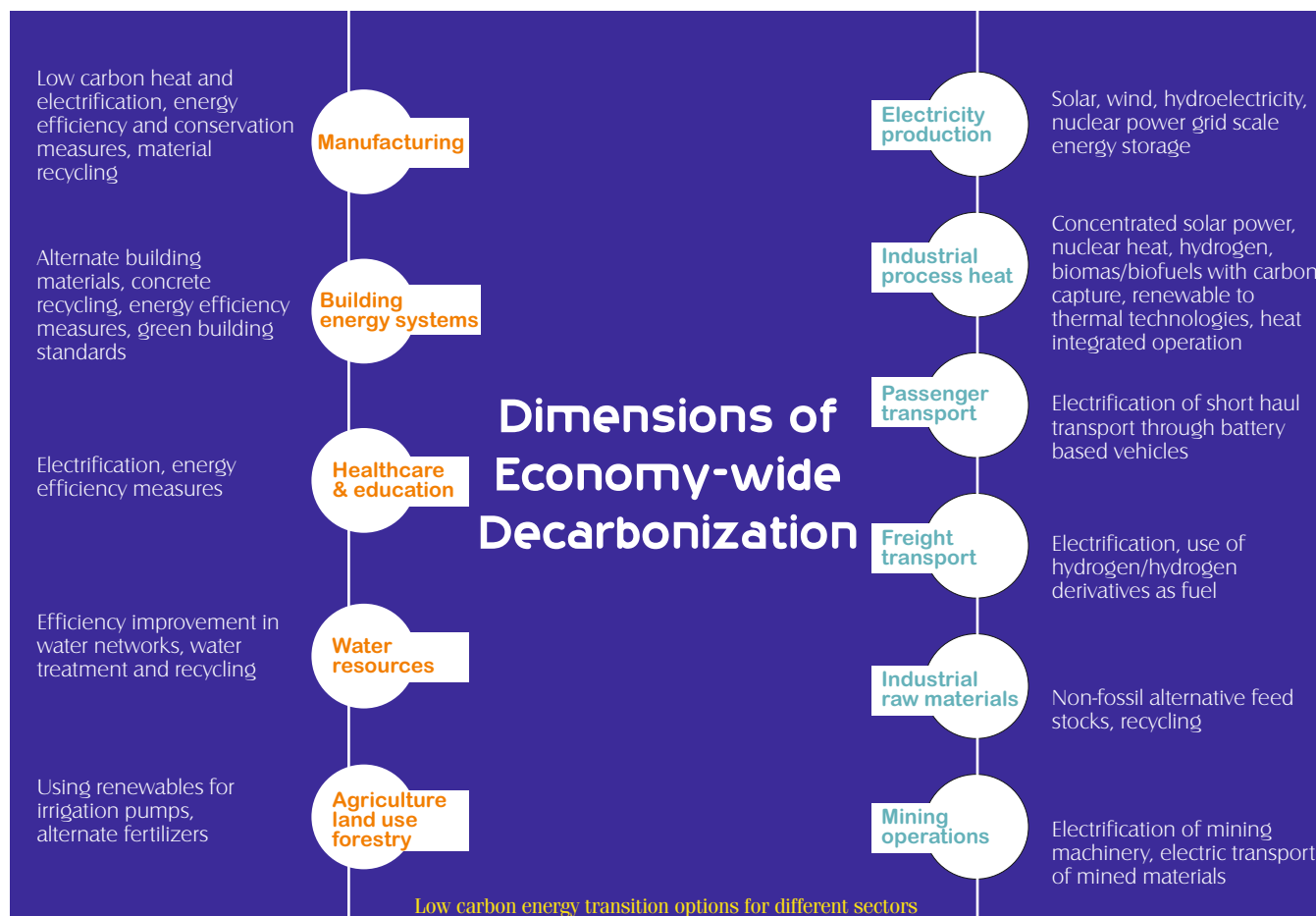
Most emissions today arise from fossil energy use and industrial processes; therefore, these sectors are the focal points for practically all emissions reductions initiatives round the world. So, what are the options for sectoral decarbonization? The illustration presented in the following page tries to highlight some of the mature and near-mature alternatives as applicable to different sectors. It shows that for the electric power sector, energy transition means switching to clean/emissions-free sources of electricity generation including renewable resources, hydro-electricity and nuclear power from the current thermal power generation stations based on coal, natural gas etc, unless the emissions from the thermal power plants are fully captured and permanently stored away. For passenger transport (which is a mobile source of carbon emissions), this implies making use of clean electricity in the shift to electric vehicles from the current dependence on liquid fossil fuels like petrol and diesel.

For many other sectors, the answers are not so straight forward yet. The difficulty lies in decarbonizing certain sectors such as heavy transport, chemical synthesis industries (such as ammonia, methanol, etc production), metallurgical processes (such as steel production), glass and cement production. This is because not only do these sectors depend on fossil fuels for energy, but very often they make use of fossil fuel derived compounds as a raw material or feed stock to the process.

Therefore, electricity alone will not decarbonize these sectors, low carbon electricity must be used to produce low or zero carbon materials/energy vectors which can then contribute to decarbonization of these sectors. One such vector is clean hydrogen (produced by using clean electricity from renewable and nuclear sources and/ or heat using a carbon free feed material such as water), that has gained massive momentum all over the world. This form of hydrogen is often described as green hydrogen.

The most developed technique for green hydrogen production today is the electrolysis of water in alkaline water electrolyzers or proton exchange membrane electrolyzers, which can make use of any low carbon electricity source to split water into its constituent elements oxygen and hydrogen.





Energy Considerations in Hydrogen Production and Utilisation

Unlike primary energy sources like coal, crude oil, natural gas which may be designated as fuels, hydrogen does not occur freely in nature. It is a secondary energy form that has to be produced by using some primary energy form. Thus it is best designated as an energy vector or carrier and not a fuel. Let us look at the energy considerations surrounding hydrogen production by electrochemical water splitting and its uses for different applications[2]. This becomes an important decision criterion governing the ultimate applications of hydrogen for decarbonization.

The water splitting reaction producing hydrogen and oxygen may be written as follows:



It indicates that the thermodynamic minimum amount of energy required to completely split 1 mol of water to produce 1 mol of hydrogen is about 285 kJ (all products and reactants being at 298 K, 1 atm pressure). It also indicates that if 1 mol of hydrogen is burnt with the stoichiometric minimum amount of oxygen (i.e., 0.5 mol of O₂), the maximum heat that may be released is 285 kJ (this is also called the calorific value of hydrogen). These figures pertain to ideal processes of production or combustion which have infinitesimally slow rates and are therefore considered ideal.

It is thus evident that in any real system where finite rates of hydrogen production and utilization have to be accomplished, additional energy greater than 285 kJ would be needed to split a mole of water and energy less than 285 kJ would be obtained from combustion of a mol of hydrogen in oxygen. How much more or less depends on the system efficiencies and various losses and irreversibilities occurring during the process. For example, a typical industrial scale water electrolyser has an electricity-to-hydrogen production efficiency of 70 to 75%.

Thus to split water by electrolysis, one needs to spend between 285/0.75 to 285/0.7 kJ (or 380 to 407 kJ of electric energy) per mol of water split. Then, if one were to burn this hydrogen in a typical fuel cell of 60% efficiency, one would recover a maximum of 285*0.6 = 171 kJ electricity per mol of H₂ burnt. If hydrogen is burnt and used to produce electricity in a gas turbine power plant, even less electricity would be produced since these plants may have efficiencies of about 45 to 50%.

Thus, the net energy return from hydrogen applications on the energy used for producing hydrogen is always less than one. Because of these factors, hydrogen is at best an energy carrier or converter and not a fuel. So, its first uses need to be in non-energy applications and then only energy related applications of hydrogen for decarbonization should be considered.



Essential

Ammonia/Fertilizers

Food processing

Iron, steel, other metallurgical uses

Hydro-treatment/hydro-processing applications in refineries

Methanol synthesis; semiconductors

Shipping/aviation/long distance/heavy transport

Conditional

Long Distance Rail Transport

River/lake based local water transportation

Industrial heating/thermal applications

Autonomous power systems in remote areas/islands

Avoidable

Renewable Energy long duration storage/transportation

Buses, cars and other modes of urban transport

Domestic heating, cooking and other energy services

Grid balancing/flexibility/reliability services

Classification of the uses of low carbon hydrogen [based on the conceptual framework in [3] and [4]

Decarbonization – Role of Hydrogen

Once it is established that hydrogen is a crucial component of the decarbonization journey of a nation, one needs to consider the best uses of hydrogen (based on thorough evaluation and comparison of possible alternatives) and thereby identify the priority sectors to be decarbonized by hydrogen. On the basis of alternatives available for specific sectors and their relative techno-commercial maturity levels today, these uses may be classified as 'Essential', 'Conditional', and 'Avoidable', as shown in the illustration presented above. The rationale for such categorization is provided next.

a) Under the 'Essential' category in the above illustration, many of the listed applications such as ammonia production and chemical synthesis, semiconductor and food processing industries already make use of hydrogen derived from fossil fuels (e.g. by steam reforming technology using natural gas as the feed stock). Therefore in the hierarchy of uses of hydrogen, these automatically occupy the top places, since they must mandatorily replace fossil hydrogen in their approach to full decarbonization. Low carbon hydrogen is therefore a direct or drop-in substitute for fossil hydrogen in these industrial applications. These sectors must be supported by adequate policies and incentives related to hydrogen use in the near term.

The technological alternate for these sectors is to use carbon capture technologies at the point of fossil hydrogen production so that the emissions intensity is greatly reduced. Such hydrogen is often designated as 'blue hydrogen'. But given the fact that carbon capture technologies still need to prove their techno-commercial viability at scale (vis-à-vis the maturity level already attained by electrolytic hydrogen technologies), this 'blue hydrogen' route is very likely to slow down the net zero carbon emissions journey of these sectors, not to mention keeping the end user sectors exposed to natural gas price volatility and supply security concerns (given the geo-political situation and natural gas related energy crisis already facing many countries today).

Therefore electrolytic hydrogen has a very good business case in these sectors already. The challenge would be to produce and dispatch the renewable or nuclear hydrogen to these end users, because not all these industries will be able to produce their required quantities of hydrogen at their site itself (which has usually been the case when using fossil hydrogen – the methane reformers are installed close to the ammonia plant or chemicals complex, thereby obviating the need for bulk storage or transport of hydrogen).

b) For the sectors under the 'Conditional' category in the above illustration, one needs to be cautiously optimistic about the use of hydrogen. This is because not only will adequate amounts of hydrogen have to be generated and transported, one would also need additional demand-side hardware (such as hydrogen storage and fuel cell systems or hydrogen based reduction furnaces for iron ore reduction in steel production) in order to let these industries make use of hydrogen. For example, in countries (such as India) where the railway system is already



electrified, the dedicated production and use of hydrogen (which is ultimately used to generate electricity itself via fuel cells) is not advised, since it merely serves to introduce additional conversion steps and the associated inefficiencies in the overall process, along with the need for massive new infrastructure build out. Use of clean electricity is the most direct route to their decarbonization. In other applications such as small scale distributed power systems or micro grids, the use of renewable electricity and battery based electricity storage system is a techno-economically better alternative than the system. In many industrial heat applications, use of renewable electricity based heat and thermal storage in suitable media may prove to be adequate, without requiring hydrogen combustion. But in high temperature applications, in the absence of high temperature heat sources hydrogen as a zero carbon fuel may turn out to be the only viable option. But this too would need some modification in the hardware, for example in the burners or furnaces which have so far worked on natural gas or fuel oil as the heating media. Biofuels to substitute fossil fuels has been considered but unless carbon capture is also deployed alongside, the process will not be entirely carbon neutral.

c) The sectors placed under the 'Avoidable' category are currently the least attractive use cases for hydrogen utilization, given the still high hardware or capital costs for hydrogen production vis-à-vis that of battery based electricity storage for urban mobility and grid scale energy storage. The relevant alternatives are building hydrogen fuelling stations versus electric vehicle chargers and currently electric chargers are somewhat more accessible than hydrogen stations, thereby favouring direct electrification versus use of hydrogen in some transport applications.

Another such area is the use of electricity driven heat pumps for building heating applications rather than replacing previously installed oil or gas fired boilers by hydrogen fired ones. Thermodynamically, heat pumps make much more sense in most geographies with moderate to even severe winters than hydrogen boilers, due to greater number of conversion steps and corresponding losses at each level, as discussed earlier. Depending on size of the grid and any potential imbalance, the need for energy reserves can be very different. If hydrogen is used for grid balancing and long duration energy storage, very large hydrogen storage would be needed in many areas. And these areas may not have access to underground caverns, etc which have been proposed to be used for large scale hydrogen storage.

Concluding Remarks

The discussion in the above sections drives home the point that use of hydrogen should not be considered as the panacea for all the ills of a fossil fuel driven world! There are specific sectors where the use of hydrogen is mandatory for net zero emissions targets to be achieved, but there are many more sectors which are better served by direct electrification and electricity storage compared to the alternate hydrogen-hydrogen storage-fuel cell route. In many of these applications, not only must the supply side of hydrogen be taken care of, substantial revamps and retrofits on the hydrogen use or demand side will also be required if hydrogen truly has to play a part in their decarbonization. The maturity of carbon capture technologies may also make some potential hydrogen applications redundant. In any case, the major prerequisite in both cases is that only low carbon energy forms be used to harness the electricity and heat that will ultimately go into the production of the hydrogen or for carbon capture process plants. Use case selection is a very important part of a successful hydrogen economy! That must be supported by rigorous analysis that looks at near and long term considerations holistically.

References

- [1] IPCC (2021). Climate Change 2021: The Physical Science Basis. Contribution of Working Group I to the Sixth Assessment Report of the Intergovernmental Panel on Climate Change [Masson-Delmotte, V., P. Zhai, A. Pirani, S. L. Connors, C. Péan, S. Berger, N. Caud, Y. Chen, L. Goldfarb, M. I. Gomis, M. Huang, K. Leitzell, E. Lonnoy, J.B.R. Matthews, T. K. Maycock, T. Waterfield, O. Yelekçi, R. Yu and B. Zhou (eds.)]. Cambridge University Press. In Press. Available at <https://www.ipcc.ch/report/ar6/wg1/#SPM> (Last accessed on 11.8.2022).
- [2] Bhattacharyya R, Singh K.K., Grover R.B., Bhanja K., Estimating Minimum Energy Requirements for Transitioning to a Net-Zero, Developed India in 2070, Current Science, 2022, 122(5), 517-527.
- [3] Liebreich M (2021). The Clean Hydrogen Ladder: An Introduction, Version 4.1, 15th August, 2021.
- [4] Bhattacharyya R, Singh K.K., Bhanja K., Grover R.B., Leveraging Nuclear Power-to-Green Hydrogen Production Potential in India: A Country Perspective, International Journal of Energy Research, 2022, DOI:10.1002/er.8348.



Ms. Rupsha Bhattacharyya is currently working as a Scientific Officer at Upgrading Plant Design & Fabrication Section, Chemical Engineering Group, BARC. She has 11 years' experience in nuclear chemical engineering with focus on hydrogen isotope separation and heavy water management technologies for nuclear power and research reactors, energy economics studies, techno-commercial analyses and optimization of nuclear and renewables assisted hydrogen production, purification and storage systems. She is also a doctoral candidate at the Homi Bhabha National Institute, Mumbai, working on assessment of the extended role of nuclear power in deep decarbonization and net zero strategies of industrial sectors beyond power and energy.

SMART ENERGY MANAGEMENT

A Computational Approach

By Kumud Singh

Energy management from the point of view of power generation and distribution has been driving the power sector till last decade. However, with gears shifted towards efforts to enhance energy efficiency by incorporating advanced measurement tools, optimization algorithms and control, SMART energy Management is an emerging and intriguing field for Electrical engineers. And the Authors of this book introduce a fairly new branch of electrical engineering in a most simplistic manner supported by case studies to bring out the practical aspects. The focus of the book is on computational approach to the problem of energy efficiency enhancement, and it traverses through the topic by espousing data driven approach & in-network processing for some of the critical energy saving requisites. The harmonious amalgamation of Electrical engineering concepts & Computational Science methodologies sets it as interesting read for the target audience.

Chapter 1 of the book introduces the concept of smart buildings and smart grid and familiarizes the reader to computational techniques in energy management. This establishes a platform and motivates the reader to delve deeper into the field of Smart energy management.

Chapter 2 confers time-criticality and latency requirement for critical real-time monitoring of Smart Electrical grid by data dissemination and processing. It also provides ephemeral background information on electrical grid, power flow and grid stability so as the readers belonging to branch other than Electrical Engineering do not feel left out in distinctly understanding the goals of energy management. Case study on data dissemination for Bus angle monitoring for Indian Electrical grid further allows the reader to understand optimization with data driven approach for meeting Quality of Service (QoS) requirements in a better way.

Chapter 3 is dedicated to energy management systems for modern buildings with a case study discussing the hardware architecture design, characterization of building loads, communication protocols and algorithms for inferring the state of building and responding using hybrid sensing.

Chapter 4 explicates solutions and methodologies for achieving thermal comfort in buildings following a smart cycle of energy management. It elaborates the thermal conditioning requirements, thermal conditioning resources, challenges for providing thermal comfort and different ways to approach thermal modeling and thermal characteristics of modern buildings/ building materials. It presents an adaptive hybrid approach in thermal modeling of spaces and schemes to adapt to changes in ambient temperature, peak demand and occupancy levels for small, medium and large building spaces.

Chapter 5 elucidates techniques for the learning based sequencing systems in which occupancy data can be embedded in schedule based HVAC control systems to derive optimal schedules and dynamically adapt the learned schedules to serve as energy efficient systems for smart buildings.

Chapter 6 addresses the need for judicious exploitation of renewable energy resources, in particular from Solar Energy perspective and methodologies for deriving its full generation potential. Authors suggest a hybrid approach utilizing Dynamic array reconfiguration as well as Current injection for full generation potential. Authors present the advantages of the suggested approach with an example and results of an experimental validation on a prototype system. This makes it easier for the reader to comprehend the challenges for deriving maximum potential of solar energy under partial shading and varying insolation conditions.

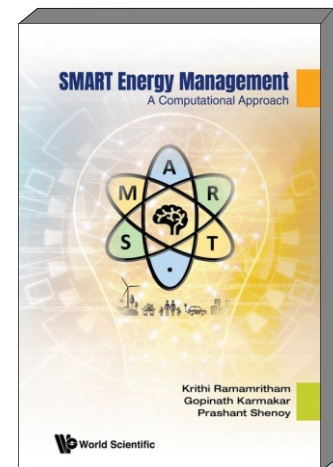
The last chapter of the book, **Chapter 7** discusses energy management during power deficit. It drives home the point of smarter ways to prevent complete blackouts. Controlled distribution of power, its frame work, optimization formulation and solution strategies are discussed. The chapter also discussed Non-intrusive load monitoring for evaluating energy conservation options and influencing the consumer's to be energy conscious and grid friendly.

The book takes a pragmatic approach to address key areas in energy management. Some of the figures and tables may be enlarged to make it more comprehensible in future editions. Being an emerging field, it is no easy task to cover an ocean of interesting problems of smart energy management, however authors remains faithful in explaining the issues and methodologies to deal with few captivating energy issues in the present world scenario. Relevant background material is exquisitely merged in the form for appendices.

I would recommend this book for practicing engineers working in the field of energy management, researchers focusing on research trends and optimization algorithms for increasing energy efficiency and moreover to all electrical engineering graduates who want to learn and enter the field of Smart energy management being touted as the future of power sector.

Smart Energy Management – A Computational Approach

By Krithi Ramamritham,
Gopinath Karmakar and
Prashant Shenoy
World Scientific Publishing Co. Pte Ltd.,
Singapore



Kumud Singh, Scientific Officer/F in Electromagnetic Applications & Instrumentation Division of BARC, works in the field of electromagnetic & accelerator technology. Her research interests include magnetic sensors and devices, superconducting devices and particle accelerator technology. She has over 20 publications in reputed international journals and conferences and is a recipient of DAE Young Applied Scientist/Technologist Award.

This page is intentionally left blank

YEAR OF GLASS

On 18th of May 2021, the UN General Council announced that the year 2022 shall be marked as the International Year of Glass. The prime objective behind this promising move was to highlight the overarching role of glass on modern science and technology landscape and its future prospects in mankind's pursuit towards environment-friendly materials for achieving sustained economic progress.

Glass and glass-based materials played a significant part in scientific and technical breakthroughs in recent times due to its versatility and technical attributes. Right from the early Bronze era, glass has been an integral part of art, architecture and culture. In the historical perspective, glass accounted for a major role in packaging industry by virtue of its inherent chemical inertness, allowing for storage of chemicals without alternation in quality for longer durations coupled with several other positive attributes.

Of late, technological advancements helped to enhance the properties of glass viz., surface treatment/ modification in order to impart promising characteristics such as self-cleaning, chemical resistance, controlled optical and heat transmission, electrical behaviour, and mechanical properties.

In Information & Communication Technology arena, a vital sector of present times, glass is considered as the backbone, strengthened by a number of innovations, including glass based optical fibres and photonic components. Thinner and highly toughened crack-resistant glasses have become an unassailable part of touch screen feature of electronic gadgets, including mobile phones.

The development of high quality optical mirrors and lenses brought about a transformational change in the field of astronomy where it aided researchers' efforts to explore the universe more accurately.

The photovoltaics (PVs) and concentrated solar power applications cannot be realized without the development of suitable glasses. New advancements in glass would contribute immensely to the development of systems for energy generation to energy storage.

In the highly vibrant domain of nuclear energy, glass continues to be the most appropriate medium for containment and disposal of diversified forms of radioactive wastes.

Corrosion-resistant borosilicate glasses are the material of choice for making of COVID-19 vaccine vials. In medical science, bioglass/ glass ceramics are being used increasingly because of their ability to integrate with human bone mass resulting in healing of wounds considerably. In tissue engineering, bioglass has found enough applications to address bone and skull related issues, etc. Development of glass micro/ nanosphere would aid efforts to produce highly efficient life-saving drugs in radiation therapy.

In a nutshell, Glass is one of the most recyclable materials and is suitably poised to address greenhouse gas emissions to enable a cleaner and better world for future generations of mankind.

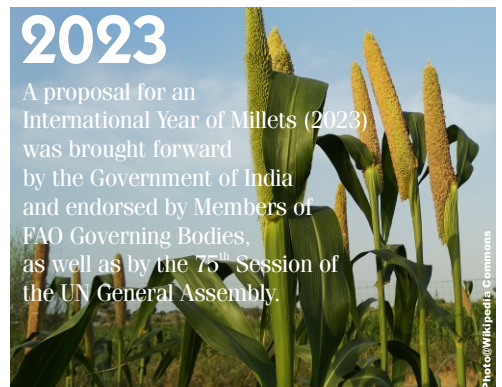
▶▶▶ Madhumita Goswami
Materials Group, BARC

UN International

2022

2023

A proposal for an International Year of Millets (2023) was brought forward by the Government of India and endorsed by Members of FAO Governing Bodies, as well as by the 75th Session of the UN General Assembly.

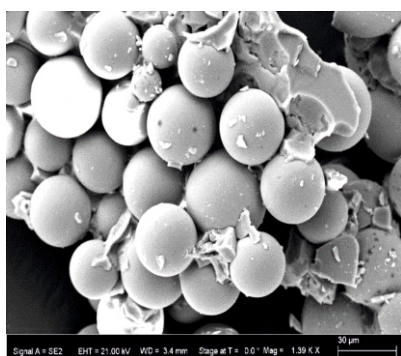


Glass for Affordable Radiotherapy

Development of Yttrium-Alumino-Silicate Glass Microspheres for HCC Radiotherapy Application

Senthil Kumar, R. S. Nair, A. Dixit, M. G. Sawant, P. Mollick, M. Goswami*, Ashok K. Arya

Glass & Advanced Materials Division, Bhabha Atomic Research Centre, Mumbai 400085, INDIA



SEM image of YAS glass microspheres

ABSTRACT

^{90}Y -loaded glass microspheres are one of the potential candidate for selective internal radiotherapy treatment (SIRT) for Hepatocellular carcinoma (HCC). We report here the indigenous development of the Yttria loaded alumina silicate (YAS) glass microsphere of controlled size for Hepatocellular carcinoma radiotherapy using Oxy-hydrogen flame ($\text{H}_2\text{-O}_2$) spheroidization process. The complete flow chart has been formulated by optimising different process steps for obtaining the YAS glass microsphere of 20-35 μm sizes and with 100% sphericity. Initial study for optimisation of base glass composition was carried out for optimum yttria loading and highly leach resistance glass. Efforts were made to set up a complete facility for flame spheroidization process for synthesis of YAS glass microsphere of controlled size. For optimised parameters the maximum conversion efficiency obtained was >99% for Oxy-Hydrogen flame spheroidization process. Additionally to address the issue of H_2 gas dependency in flame spheroidization process, Ar-plasma gun for synthesis of YAS glass was conceptualized, designed and fabricated. The process also shown encouraging results.

KEYWORDS: YAS glass microsphere, Yttria loaded glass microsphere, HCC radiotherapy

Introduction

Currently, Hepatocellular carcinoma (HCC) is one of the most pervasive causes of cancer related deaths worldwide. Selective internal radiation therapy (SIRT) using a suitable β -emitting radionuclide is one of the most promising treatment modality for primary and metastatic hepatic malignancies. Among other treatments, ^{90}Y -labelled glass microsphere is most extensively used radiotherapeutics agent for SIRT. Once administered in the hepatic artery, the microspheres preferentially lodge in the vasculature of the malignant hepatic cells and the dose of ionizing radiation get deposited from ^{90}Y [$T_{1/2} = 64.1\text{h}$, $E_{\beta}(\text{max}) = 2.28\text{ MeV}$] without damaging nearby healthy tissues (maximum penetration length of beta radiation from ^{90}Y is 11mm with mean length 2.5mm). As per reported data, the life expectancy of a Hepato-cellular carcinoma (HCC) patient is normally in the range of 2 months to 2 years, which can be enhanced from one to 5 years by a treatment of 100mg of labelled YAS glass microspheres. Alumino silicate glass matrix was chosen because of its higher yttria loading, glass stability and good chemical resistance. In addition, the constituents of glass matrix are stable under neutron irradiation and do not show any additional radioactive emission. Commercially, ^{90}Y loaded microspheres are available in two different forms, i.e. ^{90}Y -resin microsphere (SIR-sphere, SIRTEX Australia) and ^{90}Y -Glass microsphere (Therasphere, Nordon, Canada). The loading of ^{90}Y is comparatively higher in case of glass microspheres with additional advantages higher of chemical stability. ^{90}Y -labelled glass microsphere (TherasphereR) is approved by FDA, USA for the treatment of liver cancer and is available commercially. However, the prohibitively high cost of commercially available ^{90}Y -labelled glass microspheres severely restricts its utility in countries like

India. Glass and Advanced Materials Division (G&AMD), MG, BARC, initiated the indigenous development of Yttria loaded alumina-silicate glass microsphere with required clinical characteristic with an economical price. Synthesized ^{90}Y -glass microsphere showed characteristics equivalent/better compared to imported TherasphereR. The materials has been successfully characterised after neutron irradiation in collaboration with Radio Pharmaceuticals Division, BARC and a limited clinical trial has been taken up in collaboration with Tata Memorial Hospital, Mumbai. Preliminary results were quite satisfactory.

Synthesis of YAS Glass Microsphere

Glass preparation

The glass composition based on $\text{Al}_2\text{O}_3\text{-SiO}_2\text{-Y}_2\text{O}_3$ system was chosen from glass forming region of the $\text{Al}_2\text{O}_3\text{-SiO}_2\text{-Y}_2\text{O}_3$ phase diagram (Fig.1) with a criteria of maximum Y_2O_3 loading and good thermal and chemical resistance glass. Glasses of optimised composition 40 $\text{Y}_2\text{O}_3\text{-20Al}_2\text{O}_3\text{-40SiO}_2$ (wt.%) were prepared by taking high purity initial chemical constituents in the form of oxides of Al_2O_3 (99.9% purity New Met), SiO_2 (99.5% purity, Leico) and Y_2O_3 (99.9% purity, Otto Kemi). The weighing of each oxide was done with utmost accuracy of $\pm 0.002\text{gm}$. Precaution were taken to avoid any cross contamination during preparation process. The glass was prepared using standard melt-quench technique. All constituents were mixed and ground thoroughly and kept overnight at 110 $^\circ\text{C}$ for removal of any moisture absorbed during mixing and grinding process. The batch was heated in a Pt-Rh crucible at 1650 $^\circ\text{C}$ in an electrically heated Raising-Lowering (R-L) melt furnace. The melt was stirred and held for sufficient time at melting temperature for homogeneous mixing and to remove all air bubbles to obtain a clear melt. Afterwards, the melt was removed from the furnace and quenched with an optimum

*Author for Correspondence: Madhumita Goswami
E-mail: mgoswami@barc.gov.in

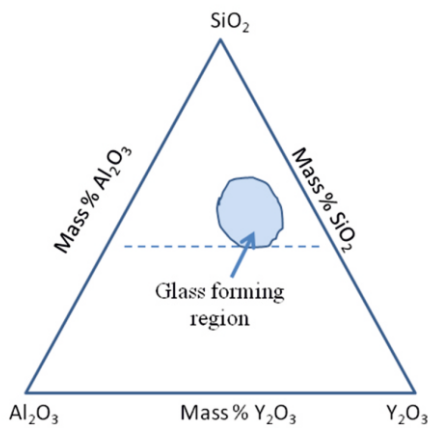


Fig.1: Glass forming region of $Y_2O_3-Al_2O_3-SiO_2$ (YAS) glass system.

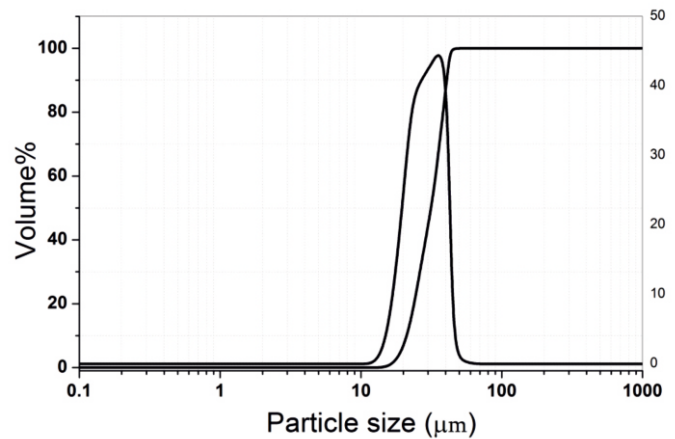


Fig.2: Particle size analysis of glass feed particles using laser scattering method.

condition to obtain cracked small pieces of glasses. The density of the glass was measured using Archimedes principle with distilled water as solvent. The density value obtained is 3.42 g/cm^3 .

Feed particle preparation

The glass frits were ground in a planetary ball milling machine followed by a mortar pestle and transferred into a series of sieves with lid and collection pan. The sieving and crushing process are carried out with at most care to avoid generation of very fine particles and reduce the efficiency. Manual sieving were done by gentle tapping from top and side of the sieved frame. Crushing and sieving were done continuously to collect sufficient feed particles in the required range. The collection was done for the glass particles in the range between $20-37 \mu\text{m}$. To speed up the sieving process, an automated Shieve Shaker unit equipped with 5-6 stacks was used. Final cleaning of dust particles from the sieved particle are done using a airjet sieving machine. The feed particles were pre-heated for sufficient time to remove moisture before flame spheroidization process.

Particle size analysis of feed particles

Size distribution analysis of feed articles was done using particle size analyser (Model: ZEPHYR OcchioSA, Belgium) based on laser scattering technique. About $100-150 \text{ mg}$ of particles were taken in water and the solution was agitate to make the colloidal solution. The particle size distribution was obtained by diffracting the laser light on these feed particles. Fig.2 shows the size distribution of the particles. Approximately 85% of particles are in the range of $15-40 \mu\text{m}$.

Spheroidization of glass particles

The feed particles were converted into glass microsphere by two process (i) Flame spheroidization (ii) Plasma gun spheroidization. Details of both these processes are discussed below.

Flame spheroidization using oxy-hydrogen torch (H_2-O_2 Torch): The schematic of a Flame spheroidization unit is seen in Fig.3. In this process, the glassy feed particles are converted into glass microsphere by introducing them into an oxy-hydrogen (O_2-H_2) flame. Before passing through the flame glass powder was heated to remove any moisture and agglomeration and make them free flowing through the feeder. The vertically placed glass feeder was mounted with two layer of mesh of size $40-50 \mu\text{m}$ to control the flow of particles and directed into the flame. The flame was conditioned by passing $H_2:O_2$ ratio 2:1. The glass particles exposed to the flame melts and spheroidizes due to surface tension and cooled rapidly to

maintain the sphericity. The flame is directed into a quartz chamber of approximately one meter long and 100 mm dia, which collects the glass microspheres after expelled from the flame. Conversion of feed particle into microsphere is $>99\%$ and sphericity is almost 100%. Fig.4(a) shows the optical image of the feed particles used in spheroidization and glass microsphere in Fig.4(b) obtained from flame spheroidization process using the optical microscope (BX60MF5,60M model, Olympus). The sphericity of the particles is confirmed from particle size analyser (Model: ZEPHYR OcchioSA, Belgium) and optical microscope.

Plasma spheroidization using argon-plasma spray gun:

To reduce the dependency of O_2-H_2 flame which has lots of safety issue because of handling of hydrogen gases, spheroidization using plasma gun has been conceptualized, designed, fabricated and commissioned. Argon plasma was generated using microwave power source with a rated capacity of 2 kW . The maximum temperature of the said plasma flame could achieve 2200°C . The design criteria for the temperature of the plasma and its flame length has been obtained using Finite Element Method (FEM) simulation using COMSOL Multiphysics software (Version 5.6, Year 2000). Simulation was performed to process the glass particle of cubic shape to convert it to spherical shape when falling through the plasma flame under gravity. Based on the simulation results, it takes about 300 milliseconds to travel through the plasma flame up to an about $100 \mu\text{m}$ to get it spheroidized, if the temperature of the plasma flame is 2200°C .

The unit has a unique design of gas outlet nozzle through which argon is passed to develop plasma flame at the tip of the nozzle. A fluidized bed system attached with this facility fluidizes non-spherical glass particles which is further being sucked through an ejector to enter into the plasma flame along

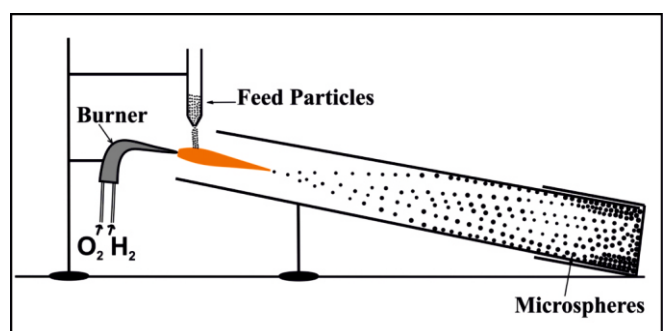


Fig.3: Schematic of flame spheroidization process.

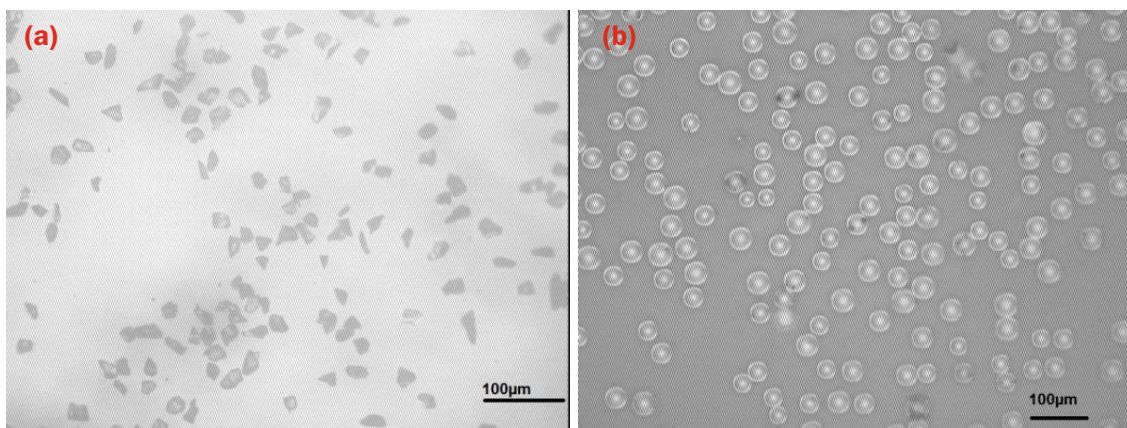


Fig.4: Optical images of (a) feed particles and (b) glass microsphere synthesised by flame spheroidization process.

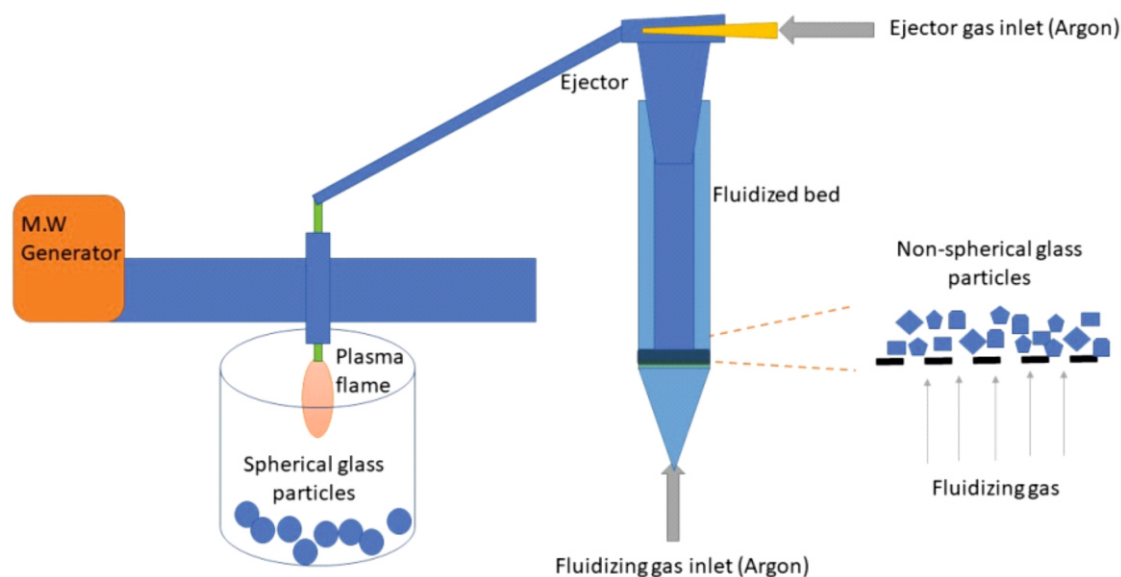


Fig.5: A simplified schematic of the plasma processing facility attached with fluidized bed and ejector.

with the argon gas as shown in schematic Fig.5. As a result, the non-spherical glass particles of typical size 20 to 35µm gets spheroidized upon melting (melting point ~1650 °C) followed by droplet formation due to surface tension. Once the particle leaves the plasma flame after a travel length of 30mm, it starts cooling and thus solidified and collected as spherical glass microspheres. Fig.6 shows a photograph of the commissioned plasma processing facility in G&AMD.

After several trials experiments, the facility has been optimized for maximum conversion of feed particle to glass microsphere. With present facility, conversion efficiency achieved has been >90% and sphericity >99%. Further modification are in the process to increase the conversion efficiency of the process. Fig.6 shows Scanning Electron Microscopy (SEM) image of the YAS feed particles and the plasma spheroidized YAS particles captured using SEM instrument, Model Table Top Mini SEM, Korea.

Post synthesis treatment

After spherodization, the glass microspheres were collected from the quartz chamber and seen under microscope for checking any unmelted microspheres. Then the microspheres were sorted by sieving to obtain desired size range of microspheres. Further, the microspheres are screened using sedimentation technique with a suitable solvent to remove microspheres with air bubbles/defects. The glass microspheres are then heated in a furnace to remove

organic impurities and then cleaned with acetone and dried. In final stage, microspheres were cleaned in a cold plasma furnace. Microspheres sphere was observed under SEM and optical microscope to check for sphericity, size and visible defects. Size distribution measurement was carried out using optical image analysis process.

Characterisation of Glass Microsphere

X-Ray Diffractometer study of YAS glass microsphere

Fig.8(a) shows the X-ray diffraction pattern of synthesised glass microspheres measured using powder X-ray diffractometric (XRD) technique (Model Bruker 8 tools) with Cu Kα as radiation source the XRD pattern of synthesised glass microspheres. Lack of sharp reflection peaks confirm typical glassy nature of prepared glass microspheres samples. The characterisation has been repeated for 6 batches to see the reproducibility of the synthesis process. Fig.8(b) shows the DTA(Differential thermal Analysis) plot of the glass microsphere measured using TG/DTA Labsys 1600 instrument, M/s. Setaram. The endothermic shift at 876 °C conform the glass transition temperature and glassy nature of glass microspheres.

Chemical analysis

To see the intact of glass composition before and after microsphere synthesis, chemical analysis of six different bathes of YAS glass microspheres are carried out and results

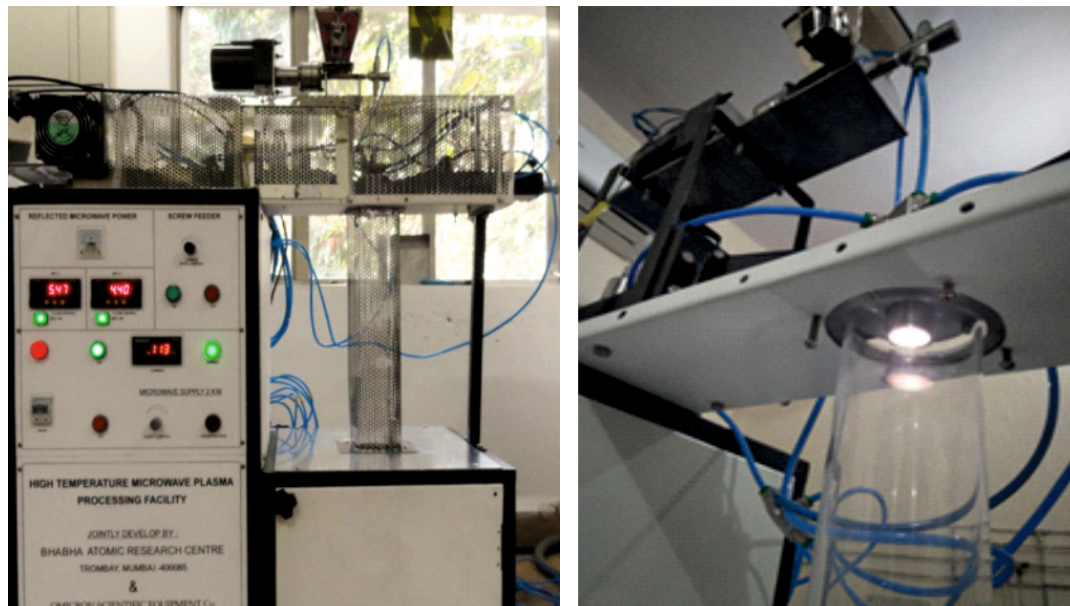


Fig.6: Plasma processing setup facility in BARC.

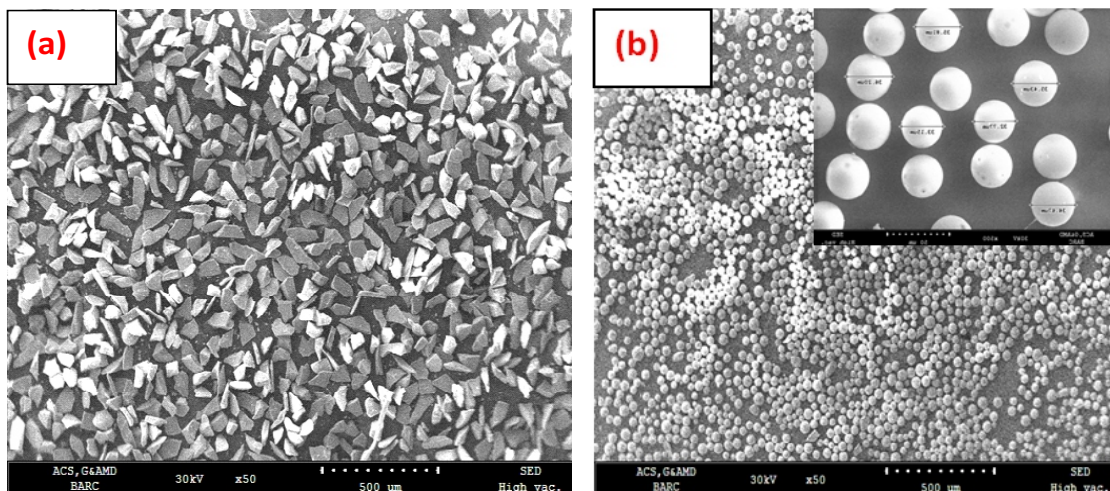


Fig. 7: SEM image of (a) feed YAS particles and (b) plasma spherodized YAS particles (inset with higher magnification).

are summarized in Table 1. Analysis was done by ED-XRF technique (EDXRF spectrometer EX 3600 M, Xenometrix Israel), having Rh-anode X-ray tube and in-built acquisition and analysis software. Results showed no significant changes in composition of the glass microsphere compared to the base glass.

Table 1: Compositional analysis of $40Y_2O_3-20Al_2O_3-40SiO_2$ glass microspheres (wt. %)

| | Y_2O_3 | Al_2O_3 | SiO_2 |
|------------------|------------|-------------|-------------|
| Batch I | 40.1 ± 2.6 | 19.4 ± 1.3 | 40.4 ± 1.1 |
| Batch II | 43.2 ± 3.0 | 18.0 ± 1.6 | 39.3 ± 1.4 |
| Batch III | 38.1 ± 2 | 20.54 ± 1.3 | 40.77 ± 1.5 |
| Batch IV | 40.3 ± 1.6 | 21.5 ± 1.3 | 41 ± 1.6 |
| Batch V | 42.1 ± 2 | 19.1 ± 1.2 | 40.5 ± 2.3 |
| Batch VI | 38.5 ± 1.5 | 19.5 ± 1.2 | 39.7 ± 2.3 |

Size analysis of glass microsphere

As laser scattering process required higher amount (>0.1gm) of sample to see the particle size distribution, size distribution of sorted glass microsphere was carried out using optical image analysis process. Optical images were taken on six different batches of glass microspheres and images were processed suitably to get maximum number of well separated particle (Fig.9). Image J analysis software (v1.3.0.x, 2006) was used for determination of particle size distribution. Statistics of particle size distributions were shown in Fig.10. More than 96% of glass microspheres are within the range of 20-35mm with mean diameter of 32.43µm.

Chemical stability study of YAS glass microsphere

The chemical stability/leaching study of sorted glass microspheres was carried out in aqueous (distilled water) as well as saline medium at RT per the ASTM standard method. These medium were chosen as the glass microsphere will be stored in distilled water and delivered along with saline water. The ratio of the weight of leachant (distilled/ saline water) and glass microsphere was fixed at 100:1. The experiments were carried out in a closed vessel to avoid any loss of water. At regular intervals, the weight of exposed glass microspheres

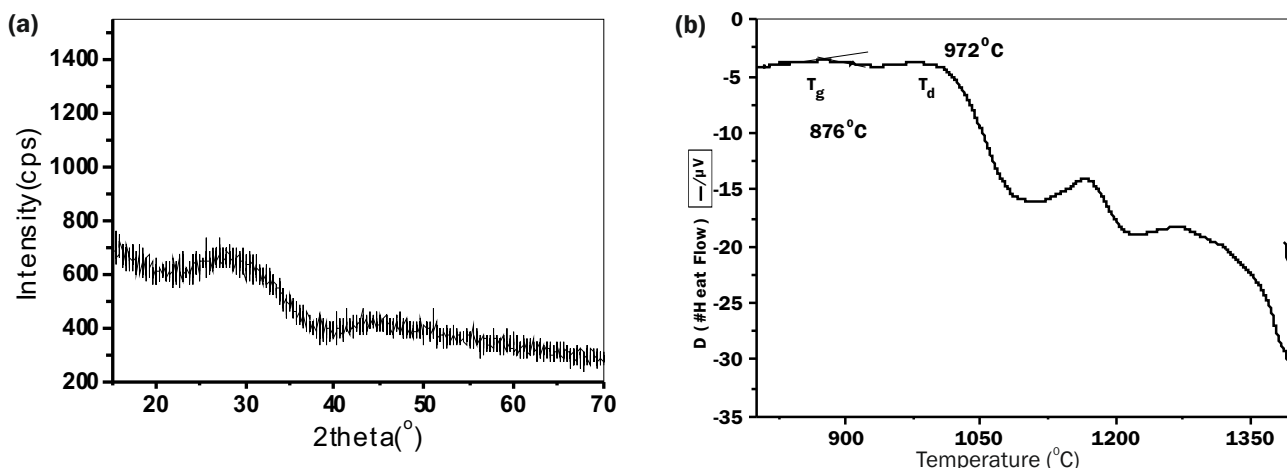


Fig.8: (a) XRD pattern of glass microspheres. (b) DTA plot of glass microspheres.

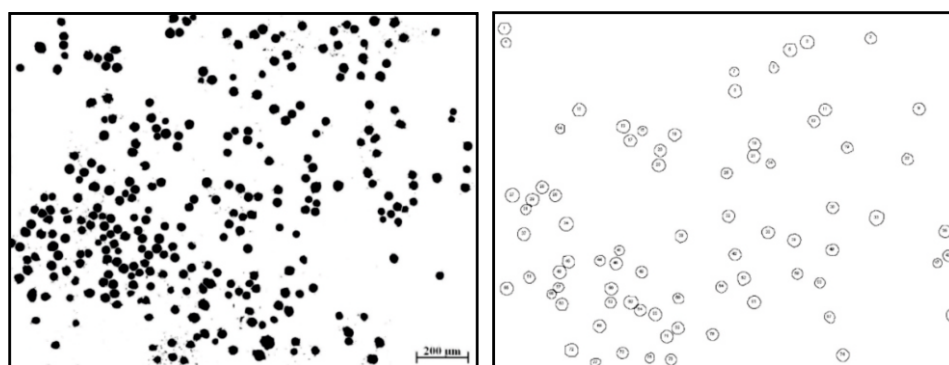


Fig.9: Images processed using analysis software for particle size analysis.

were recorded and weight change was calculated. Small amount of glass microspheres and leaching solution were taken out from the vessels after each interval for different characterizations. The experiments in aqueous medium were carried out for a maximum of 30 days ($> 10 t_{1/2}$ of yttrium) and in saline water for a maximum of 7 days.

There was very minimal or no loss in weight was observed from the glass microspheres after the leaching experiments

Table 2: Weight loss (gm, ± 0.002) of YAS glass microsphere with time in aqueous medium.

| Sample | Initial weight | Final weight | Weight loss |
|------------------|----------------|--------------|-------------|
| Batch 1 (24hr) | 0.502 | 0.501 | 0.001 |
| Batch 2 (3 days) | 0.455 | 0.452 | 0.003 |
| Batch 3 (7days) | 0.416 | 0.411 | 0.005 |
| Batch 4 (3 days) | 0.385 | 0.373 | 0.012 |
| Batch 5 (7days) | 0.350 | 0.335 | 0.015 |

Table 3: Weight loss (gm, ± 0.002) of YAS glass microsphere with time in saline medium.

| Sample | Initial weight | Final weight | Weight loss |
|------------------|----------------|--------------|-------------|
| Batch 1 (24hr) | 0.105 | 0.103 | 0.002 |
| Batch 2 (3 days) | 0.742 | 0.730 | 0.012 |
| Batch 3 (7days) | 0.053 | 0.035 | 0.018 |

carried out in both aqueous and saline medium. To see any changes in the surface morphology of the glass microsphere such as formation pores and their size distribution if any, SAXS study was carried out on these microsphere. SAXS experiments was performed using a laboratory based SAXS instrument (x-ray wavelength $\lambda=0.154\text{nm}$). The sample to detector distance was $\sim 1\text{m}$. Radial averaged scattered intensities, $I(q)$ from each of the samples were recorded as a function of q (wave vector transfer $q=4\pi\sin\theta/\lambda$, where 2θ represents the scattering angle).

SAXS result showed scattering from the surface in nanometric scale, and no internal scattering from the samples, indicates no pores on the surface of the sample. Fig.11(a) shows no changes in SAXS pattern. This indicates both the sample have smooth surface with almost no pores/defects even after leaching study was done on these samples for 30 days. SEM images of glass microsphere after leaching study is shown in Fig.11(b). No changes in surface of the spheres also confirm the chemical stability of the glass microspheres after leaching study in aqueous medium.

The irradiation study of the glass microspheres were carried in Druva reactor in collaboration with RPhD, BARC. The glass microsphere showed required radionuclide purity, specific activity and chemical stability. The in-vivo study carried out in wistar showed complete emobilization of activity in the liver cell. Trial clinical runs were carried out by doctors (Tata Memorial Centre, Mumbai), confirm efficacy of the material for HCC radiotherapy.

Conclusion

Composition and glass synthesis process of Ytria loaded alumino silicate (YAS) glass microsphere has been optimized

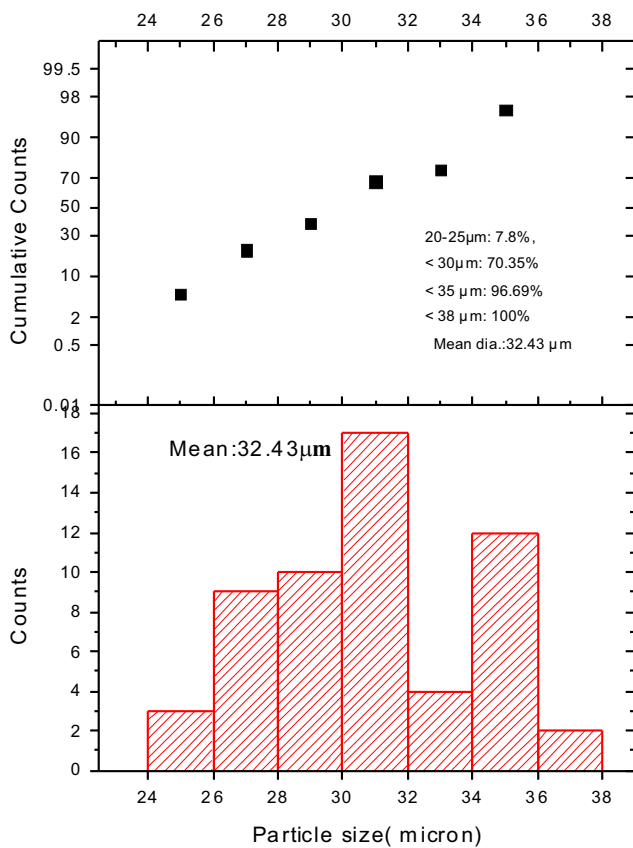


Fig.10: Statistics of particle size distribution obtained from image analysis process.

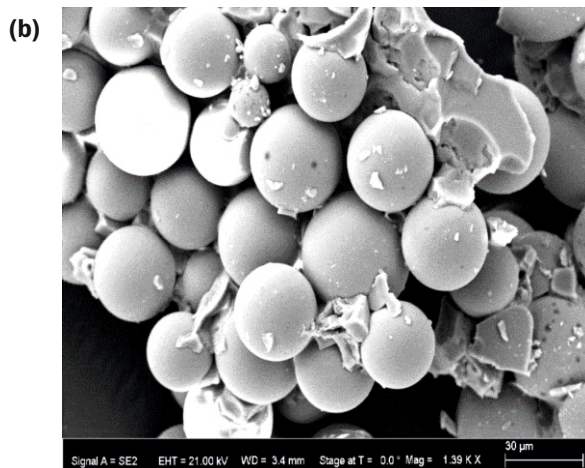
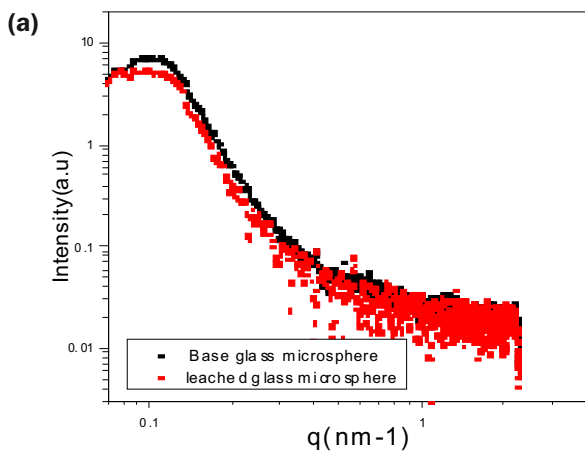


Fig.11: (a) SAXS plots for glass microspheres before & after leaching study. (b) SEM image of glass microspheres after leaching study (intact in size and shape).

with a maximum Yttria loading and optimum chemical stability. The spheroidization process was fine tuned for 100% conversion of feed particle to glass microspheres and sphericity. Glass microsphere of size 20-35µm were sorted with successive sieving. Glassy phase and chemical stability was found intact after spheroidization. The materials shows equivalent physical and chemical characteristic as imported Therasphere material. Irradiation study showed acceptable clinical characteristics and initial clinical trials carried out by Doctors showed encouraging result.

Acknowledgement

Authors thank M Krishnan, Former Director, Materials Group, BARC for initiation, conceptualization and guidance for this work. Thanks to P.K. Pujari, Former Director, Radiochemistry & Isotope Group, BARC for his guidance and support in facilitating clinical study at TMC, Mumbai. We extend our thanks to V. Kain, Director, Materials Group, BARC for his encouragement and support. Authors are thankful to S. Chakraborty, Radio Pharmaceuticals Division, BARC for carrying out irradiation study on glass microsphere and V. Rangarajan, TMC, Mumbai for his role during clinical trials of indigenously developed material. Authors also thank D. Sen of Solid State Physics Division, BARC for his assistance in SAXS analysis.

Bibliography

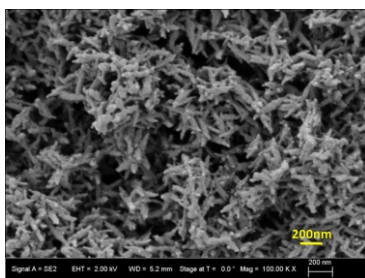
- [1] The development, commercialization, and clinical context of yttrium-90 radiolabeled resin and glass microspheres, A. Mark. M.D. Westcott, M. Douglas, M.D. Coldwell, David M.M.D Liu, F Joseph. M.D. Zikria, *Advances in Radiation Oncology*, 2016, 1, 351-364.
- [2] Glass Microspheres, Delbert E. Day, Rolla Gary, J. Ehrhardt, United States Patent: 673,123, 73.
- [3] Radioembolization using 90Y resin micropsheres for patients with advanced hepatocellular carcinoma. Bruno Sangro, J.I. Bilbao, J. 3oan, Antonio Martinez-Cuesta, Alberto Benito, Javier Rodriguez, Nagel Panizo, Belen Gil, M. Inarrairaegui, Ignacio Herrero, Jorge Quiroga, Jesus Prieto, *Int. J. Radiation Oncology Biol. Phys.*, 2006, 36(3), 792-800.
- [4] Yttrium-90 radioembolization is safe and effective treatment for unresectable hepatocellular carcinoma: A single center experience of 45 consecutive patients, Akshat Saxena, Baerbel Meteling, Jada Kapoor, Sanjeev Golani, Mark Danat, David L Morris, Lourens Bester, *International Journal of Surgery*, 2014, 12, 1403-1408.
- [5] Y90 radioembolization dosimetry using a simple semi quantitative method in intrahepatic cholangiocarcinoma: Glass vs resin microspheres, N Nezami, Nima Kokabi, J.C. Camacho, David M Schuster, M Xing, Hyun S Kim, *Int. J. Radiation Oncology Biol. Phys.*, 2008, 71(1), S147-S151.
- [6] Preparation of glasses for radiotherapy by ion implantation, M Kawashita, T Yao, F. Miyaji, T. Kokubo, G H Takaoka and I. Yamada, *Radiat. Phys. Chem.*, 1995, 46(2), 269-274.
- [7] Production and quality control of radioactive yttrium micropsheres for medical applications, M.R. Ghahramani, A.A Garibov, T.N. Agayev, *Applied Radiation and Isotopes*, 2014, 85, 87-91.
- [8] Phase evaluation during high temperature long heat treatment in Y₂O₃-Al₂O₃-SiO₂ system, S. Ahmad, T. Ludwig, M. Herrmann, M.M. Mahmoud, W. Lippmann, H.J. Seifert, *Journal of the European Ceramic Society*, 2014, 34, 3835-3840.
- [9] Preparation and characterization of composite micropsheres for brachtherapy and hyperthermia treatment of cancer, Di Zhao, Wenhai Haung, Mohamed N Rehaman, D.E. Day, Deping Wang, Yifei Gu, *Materials Science and Engineering C*, 2012, 32, 276-281.

Efficient Drug Delivery

Development of Hydroxyapatite Microspheres for Biomedical Applications

Rohini Garg*, Ashok Kumar Sahu, Abhijit Ghosh and Ashok Kumar Arya

Glass and Advanced Materials Division, Bhabha Atomic Research Centre, Mumbai 400085, INDIA



SEM micrograph of as-synthesized hydroxyapatite nano-particles

ABSTRACT

Porous biocompatible microspheres of hydroxyapatite (HAp), are potential candidates for various bio-medical applications including drug delivery and bone tissue engineering. We have synthesized porous HAp microspheres with diameter ranging 3-5 μ m consist of needle/rod shape HAp nanoparticles with an average length of 200nm using spray drying technique. We have shown that solely by controlling the spray drying temperature the outer shape of the microspheres can be tuned from spherical to doughnut. Their phase structure and outer morphology has been studied using X-ray diffraction and scanning electron microscopy. The absorption of bovine serum albumin protein by the synthesized granules has been tested as a potential application.

KEYWORDS: Hydroxyapatite, Biomaterials, Microspheres, Spray drying, XRD, SEM, Nanoparticles

Introduction

Hydroxyapatite (HAp, $\text{Ca}_{10}(\text{PO}_4)_6(\text{OH})_2$), major mineral component of human bones and teeth plays an important role in bone tissue engineering such as implant coatings and bone substitutes and variety of bio-medical industrial applications including matrices for drug release control etc[1,2]. The close chemical similarity between HAp and mineralized bone of human tissue has led to extensive research efforts in synthetic HAp and based ceramic. These materials have excellent biocompatibility, osteoconductivity, and osteotransductivity. To meet the needs of different applications, HAp based bone graft substitutes are being used in the form of powders, microspheres, sintered porous blocks, cements, putties and sponge/foams and as a coating over metallic implants. Among various morphologies, especially HAp granules has been proven to be ideal vehicles for drug delivery or scaffold for cell delivery[3] due to their relatively low cost, broad availability, good biological properties.

The pore size distribution and porosity of spherical granules is of major importance for drug delivery and for orthopedic and dental applications. The main focus is on the space between the particles. Most granular CaP bone graft substitutes have a diameter in the range of 0.5 to 5 mm because blood vessels and cells should be able to invade the space in between the particles to promote ceramic resorption and bone formation throughout the defect. Drug delivery is usually controlled by dissolution, diffusion and surface interaction, hence precipitated HAp crystals become promising due to its very large specific surface areas (typically above $50\text{m}^2/\text{g}$)[2].

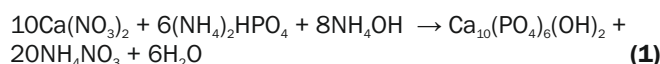
There have been several methods reported in literature for preparation of HAp microspheres such as microwave assisted hydrothermal route[4], ion-assisted mineralization method[5], biopolymer assisted assembly from HAp nano

rods[6] and glass conversion method[7]. However, these methods require numerous processing steps and are time consuming and complicated in nature. On the other hand, spray drying method[8] offers the inherent flexibility in operation and allows modification of process parameters which makes it possible to engineer the powder properties to predefined specifications, such as microsphere size, morphology and density. There have been few reports of HAp microspheres prepared by spray drying[8,9] in literature.

The main objective of this study is to synthesize HAp microspheres by modifying the spray drying process parameter i.e. temperature and evaluate the effect of drying temperature on the outer morphology of dried microspheres. The protein adsorption by HAp microspheres is investigated using model protein Bovine Serum Albumin (BSA), which was chosen as a test protein because of its better stability and availability at high purity. Details of this work can be obtained from reference [10].

Method

HAp nanoparticles were prepared by precipitation method according to the reaction described as follows:



Under continuous stirring aqueous solutions of 0.2M calcium nitrate ($\text{Ca}(\text{NO}_3)_2$) was gradually added into 0.2M ammonium hydrophosphate ($(\text{NH}_4)_2\text{HPO}_4$) solution. Their stoichiometric ratio Ca/P was kept at ~ 1.67 . Temperature of the water bath was adjusted at 55°C and pH of solution was maintained at 10 till complete precipitation. The experimental steps were shown in the flow sheet given in Fig.1. The HAp nanoparticles were subsequently characterized for phase purity, size and shape.

HAp microspheres were obtained by drying the HAp colloidal dispersion solution using LU 228 (M/s. LABULTIMA, India) spray dryer. The stability of feed mixture was determined

*Author for Correspondence: Rohini Garg
E-mail: rohinig@barc.gov.in

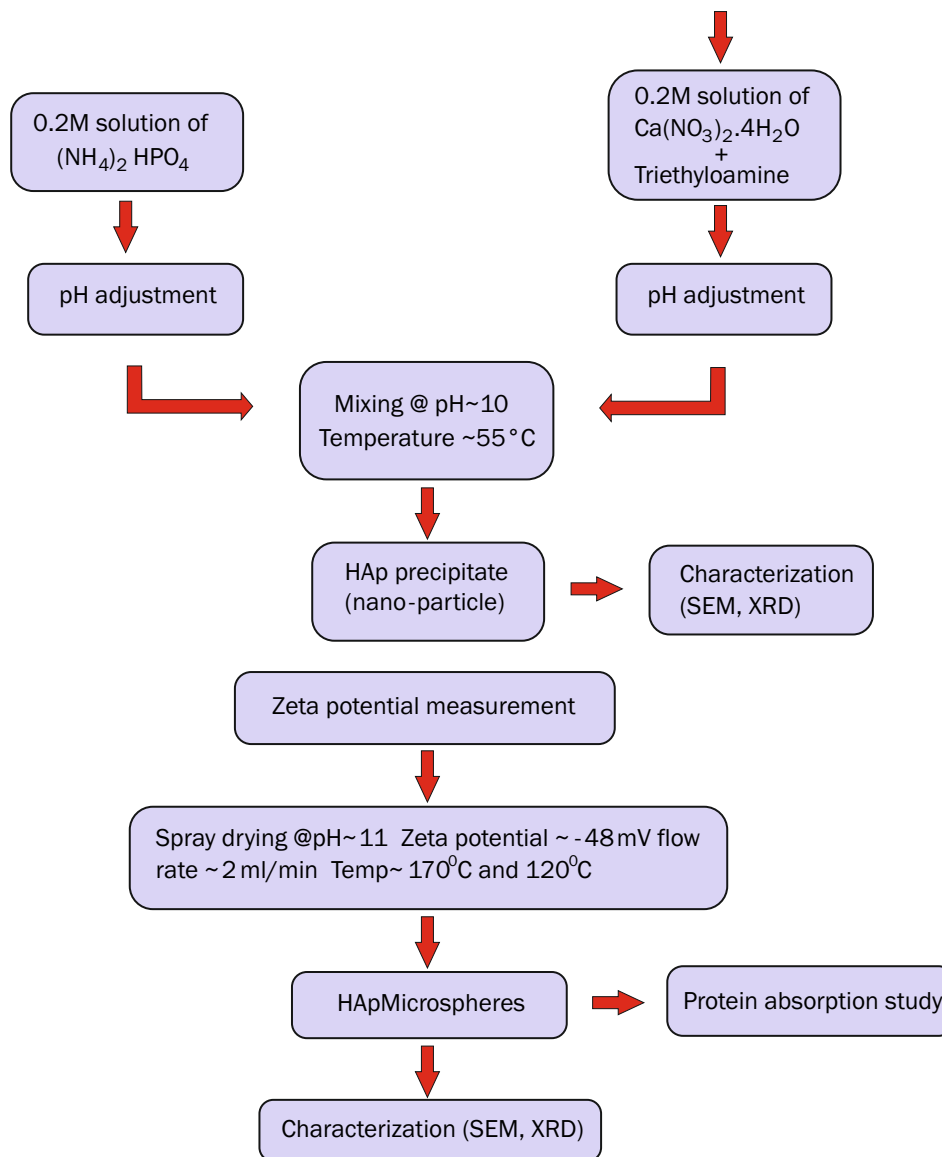


Fig.1: Flow sheet of experiments.

prior to spray drying by measuring zeta potential (ζ) and maintained at $\zeta \sim -49$ mV at pH ~ 11 . Spray drying was carried out with compressed air at selected air pressure of 2 kg/cm^2 during atomization and flow rate was kept 2 ml/min . The aspiration rate was kept fixed at $50 \text{ m}^3/\text{h}$. The final values of these parameters were obtained after series of experimental trials. In the initial trial of spray drying it has been observed that large volume of power was not converted into microsphere and it remained in the form of agglomerated powder chunks. In the further trials by changing initial slurry concentration and flow rate of feed, microspheres could be formed but there was huge agglomeration of microspheres. After various trials spray drying parameters were optimized for disperse microspheres in the size range of $3\text{--}5 \mu\text{m}$. Later on, in spray drying experiment inlet temperature was varied at 120°C and 170°C , respectively to understand the effect of drying temperature on the morphology of dried granules.

The phase analysis of HAp nanoparticles was carried out using x-ray diffractometer (D8 discover, Bruker) using Cu K_α radiation ($\lambda = 0.15406 \text{ nm}$). Rietveld analysis of XRD pattern was done using "Fullprof" software for crystal structural analysis. The morphology of HAp nanoparticles and microstructure of external surface of spray dried HAp

microspheres was examined using Carl Zeiss Auriga FE-SEM.

Crystallized and lyophilized BSA (Grade A9418, Sigma Chemical Co.,) protein with molecular weight of 69 kDa and iso-electric point ~ 4.74 was used for the protein adsorption study. Initially, 300 mg Hap granule (S1 sample) was added in 10 ml BSA with concentration of 25 mg/ml and incubated at 37°C for different time schedule from 3 h to 96 h . The supernatant solutions were collected for each conjugate after centrifugation at 800 rpm and kept at temperature 4°C . UV-vis spectroscopy (Perkin Elmer Lambda 35) at 562 nm was used to characterize the absorbance peaks and BSA concentration was quantified through the use of a pre-determined standard concentration-intensity calibration curve. The amount of adsorbed protein was calculated from solution depletion.

Results and Discussion

Phase analysis

XRD patterns of as-synthesized Hap nano-particles (Fig.2a) shows broad and overlapped diffraction peaks which indicate low crystallinity and small crystallite size of nano-particles. However, broadening and overlapping of Bragg peaks is significantly reduced after calcination at 800°C .

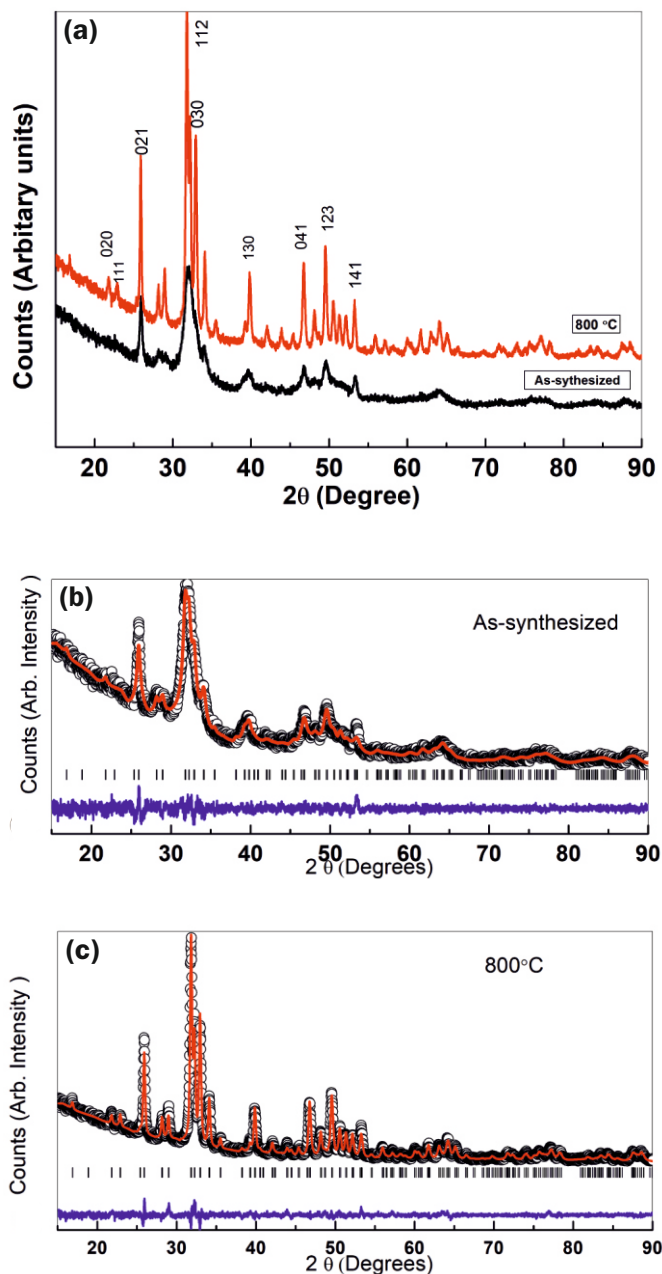


Fig.2: (a) XRD pattern of as-precipitated and after calcination at 800°C. Rietveld refinement plots of x-ray diffraction data of HAp nano-particles (b) as-synthesized dried (c) after calcination at 800°C. Experimental data, simulated data and difference plots are represented as open circles, continuous line (red) and continuous line (blue) respectively. Vertical bar symbol represents Bragg peak positions.

Calcined XRD pattern is determined to be pure HAp phase by comparing it with standard JCPDS card (09-432). The average crystallographic data was determined by Rietveld refinement of XRD data. Starting unit cell and structural parameters came from the refinement performed with neutron data by Kay *et al.*, [11] for HAp phase. First, scale factor, background, peak profile (pseudo-voigt function) and lattice parameters were simultaneously refined, later atomic positions and isotropic displacement parameters were refined one by one for each atom. Fig.2 shows the Rietveld plot of HAp powder obtained by refinement with space group P63/m. The refined lattice parameters and volume for as-synthesized powder are: $a=b=9.4279(31)$, $c=6.8683(25)$, $V=528.70(31)$, and for calcined HAp powder $a=b=9.4128(2)$, $c=6.8755(2)$ and

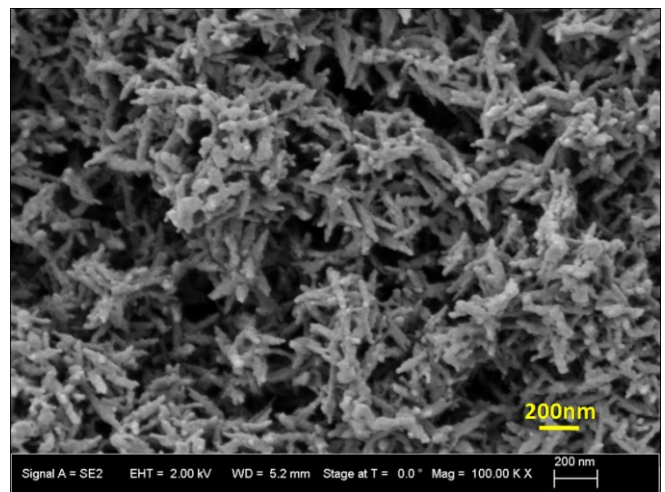


Fig.3: SEM micrograph of as-synthesized hydroxyapatite nano-particles.

$V=527.56(2)$ respectively. Error associated with refined parameters is much higher for as-synthesized powder due to its low counting rate and presence of nano scale crystallite size.

Microstructural characterization

SEM micrograph of as-synthesized HAp nano-particles (Fig.3) suggests that nano-particles have reasonably small polydisparsity as most of the nano-particles have similar size and shapes. They exhibit ellipsoidal morphology with $\sim 200\text{nm}$ length and aspect ratio of ~ 0.3 . The nanometer size of HAp as-synthesized particles easily explain the presence of broad and overlapping peaks in XRD pattern shown in Fig.2. It is observed from the figure that these nano-particles are soft agglomerates which can be easily dispersible and friable. Fig.4 shows the SEM micrographs of HAp granules prepared by spray drying at 120°C (a-b) and 170°C (c) respectively with diameter 3-5 μm . HAp granules have spherical morphology when spray drying is performed at temperature 120°C and doughnut-like morphology for spray drying temperature of 170°C (Fig.4c).

At lower drying temperature, HAp nano-particles with in a droplet have sufficient time to redistribute themselves by diffusion throughout evaporating droplet and yields in a final arrangement inside an assembled granule corresponding to a packing due to random jamming of the constitute particles. Fig.5 shows schematically the possible mechanisms for the dense homogeneous sphere. On the other hand, higher drying temperature accelerates the droplet evaporation and water (solvent) on the surface runs away quickly. HAp nano-particles have insufficient time to diffuse from surface to the center of the droplet and instead accumulate near the drying front of the droplet and dimpled or doughnut shaped morphology forms (schematic Fig.5).

BSA protein adsorption on HAp microspheres

Fig.6 exhibits the BSA protein adsorption on HAp granules at different time interval. It is clearly visible that with increasing time the concentration of adsorbed BSA is increasing. Their mutual interaction and adsorption behavior is dependent upon hydrophobicity of individual HAp and BSA molecule [12].

Conclusions

HAp microspheres of diameter ranging 3-5 μm were synthesized using precipitation method followed by spray

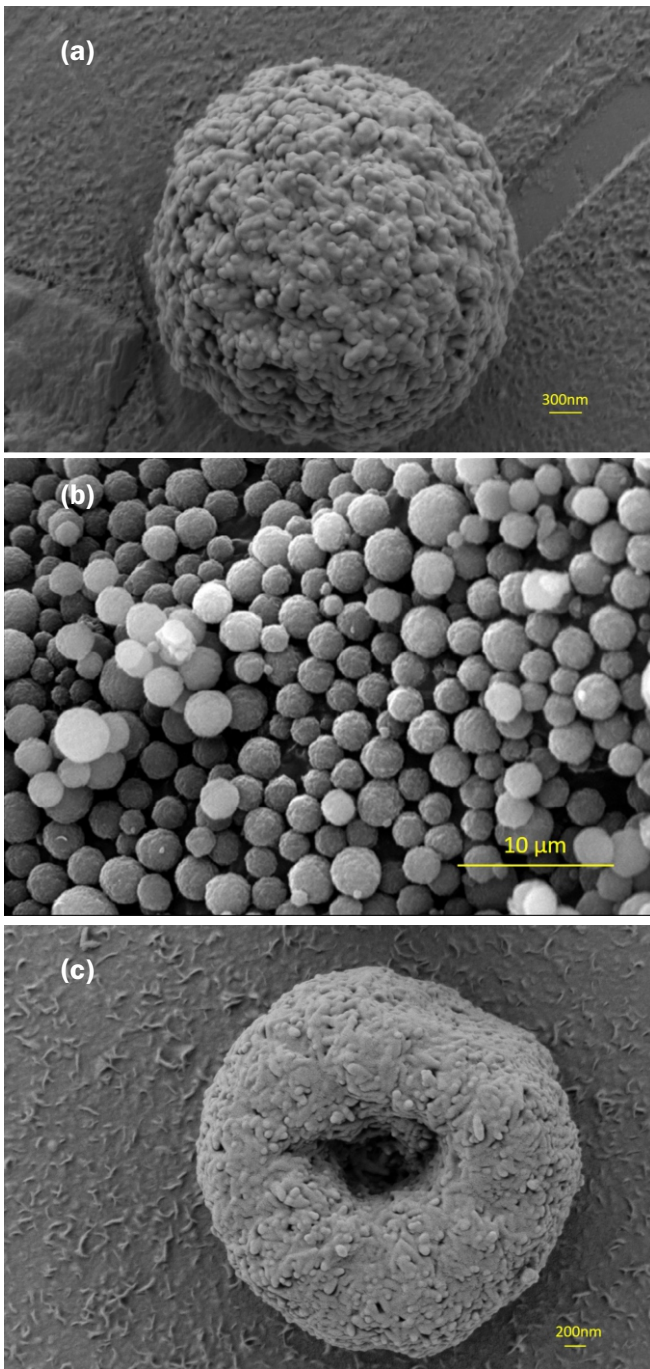


Fig.4: SEM micrographs of spray dried HAp microspheres dried at drying temperature (a)-(b) 120°C and (c) 170°C.

drying of aqueous solution of precipitate. These microspheres were consisted of needle/rod shape HAp nano particle of 200nm length. XRD results reveal that as-precipitated HAp powder was amorphous and calcination at 800°C transformed it to phase pure HAp with crystalline nature.

It has been shown that morphology of spray dried HAp microspheres can be simply tuned from spherical to doughnut-like by solely changing the drying temperature. Adsorption of BSA protein on spray dried HAp granules is also demonstrated as a potent application.

Acknowledgement

Authors would like to thank Debasis Sen, Solid State Physics Division, BARC for providing spray drying facility and for helping in carrying out spray drying experiments. Technical

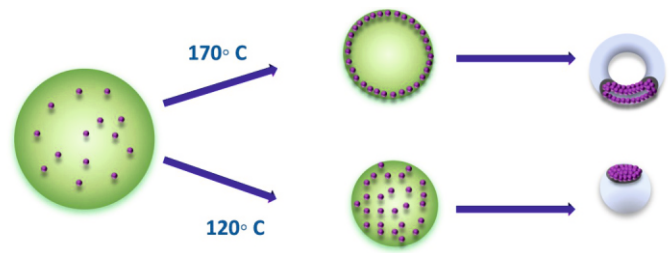


Fig.5: The schematic diagram of the granule morphology in two extreme cases (at 120°C and 170°C).

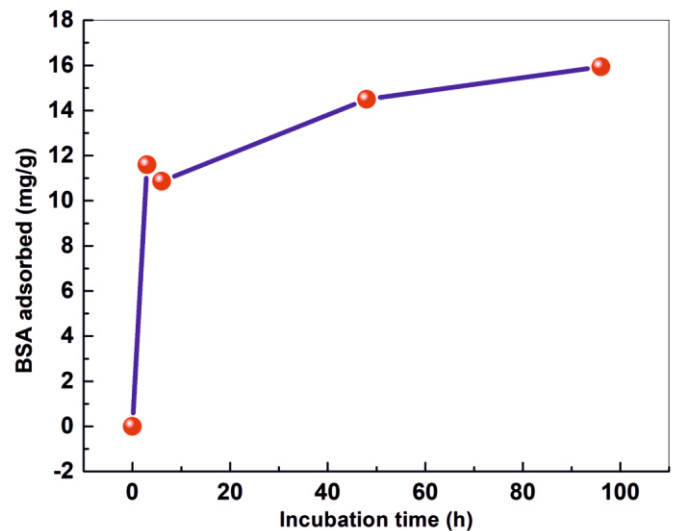


Fig.6: BSA adsorption by HAp granule at different incubation time.

assistance by Shoeb K Hashmi during synthesis of HAp particles is highly acknowledged.

References

- [1] L.L. Hench, Bioceramics: from concept to clinic, Journal of the American Ceramic Society, 1991, 74, 1487-1510.
- [2] M. Bohner, S. Tadier, N. van Garderen, A. de Gasparo, N. Do`belin, G. Baroud, Synthesis of spherical calcium phosphate particles for dental and orthopedic applications, Biomatter, 2013, 3(2), e25103.
- [3] H.-H. Lee, S.-J. Hong, C.-H. Kim, E.-C. Kim, J.-H. Jang, H.-I. Shin, H.-W. Kim, Preparation of hydroxyapatite spheres with an internal cavity as a scaffold for hard tissue regeneration, Journal of Materials Science: Materials in Medicine, 2008, 19, 3029-3034.
- [4] K.W. Wang, Y.J. Zhu, X.Y. Chen, W.Y. Zhai, Q. Wang, F. Chen, J. Chang, Y.R. Duan, Flower-Like Hierarchically Nanostructured Hydroxyapatite Hollow Spheres: Facile Preparation and Application in Anticancer Drug Cellular Delivery, Chemistry-An Asian Journal, 2010, 5, 2477-2482.
- [5] W. Xia, K. Grandfield, A. Schwenke, H. Engqvist, Synthesis and release of trace elements from hollow and porous hydroxyapatite spheres, Nanotechnology, 2011, 22, 305610.
- [6] S.D. Jiang, Q.-Z. Yao, G.-T. Zhou, S.-Q. Fu, Fabrication of hydroxyapatite hierarchical hollow microspheres and potential application in water treatment, The Journal of Physical Chemistry C, 2012, 116, 4484-4492.
- [7] W. Xiao, H. Fu, M.N. Rahaman, Y. Liu, B.S. Bal, Hollow hydroxyapatite microspheres: A novel bioactive and osteoconductive

carrier for controlled release of bone morphogenetic protein-2 in bone regeneration, *Acta biomaterialia*, 2013, 9, 8374-8383.

[8] R. Sun, Y. Lu, K. Chen, Preparation and characterization of hollow hydroxyapatite microspheres by spray drying method, *Materials Science and Engineering: C*, 2009, 29, 1088-1092.

[9] P. Luo, T. Nieh, Synthesis of ultrafine hydroxyapatite particles by a spray dry method, *Materials Science and Engineering: C-Biomimetic Materials Sensors and Systems*, 1995, 3, 75-78.

[10] R. Garg, D. Sen, A. Sahu, K. Madangopal, Morphological Tuning of Nanostructured Hydroxyapatite (HAp) Porous Microgranules by Evaporation-Induced Assembly, *Journal of Nanoscience and Nanotechnology*, 2020, 20, 1631-1642.

[11] M.I. Kay, R. Young, A. Posner, Crystal structure of hydroxyapatite, *Nature*, 1964, 204, 1050.

[12] K. Kandori, M. Mukai, A. Fujiwara, A. Yasukawa, T. Ishikawa, Adsorption of bovine serum albumin and lysozyme on hydrophobic calcium hydroxyapatites, *Journal of Colloid and Interface Science*, 1999, 212, 600-603.

Glass-ceramics Phosphor

Development of Ce:YAG Glass-ceramics Phosphor for White LED Application

P. Nandi*, M. Goswami, Ashok K. Arya

Glass & Advanced Materials Division, Bhabha Atomic Research Centre, Mumbai 400085, INDIA



Demonstration of white light generation using Ce:YAG glass-ceramics phosphor

ABSTRACT

We report here successful synthesis of Ce:YAG glass-ceramic phosphor with improved thermal characteristics compared to polymer based phosphor used in conventional white LEDs. Composition of the base glass and subsequent heating schedule were fine tuned for optimum concentration of Ce:YAG phosphors with proper microstructure and optical properties. Understanding the crystal growth kinetics in the glass was essential to predict the time-temperature parameters for the required phase concentration. Isothermal predictions were derived and then applied to convert the glass to glass-ceramics by thermal activation. XRD analysis confirmed the development of single phase Ce:YAG phosphor crystals in glass-ceramics powder samples. Surface crystallization of $\sim 50\mu\text{m}$ of phosphor layer was observed from the Scanning electron microscopy (SEM) study. Glass-ceramics disk with desired optical quality was prepared to demonstrate generation of the white light.

KEYWORDS: Glass, Glass-ceramics, Phosphors, White LED

Introduction

Conventional white LED devices has Ce:YAG ($\text{Y}_3\text{Al}_5\text{O}_{12}$) phosphor crystals dispersed in polymer matrix, and placed in front of a blue LED source. The blue light is partially absorbed by microscopic Ce:YAG phosphors and converted to yellow light which additively mix up with unabsorbed blue to generate white light. The working principle is shown schematically in Fig.1. The drawback of polymer matrix is that they degrade due to junction temperature of the semiconducting light emitting diode during continuous operation and thermal cycles, thus the performance quality decrease over time and usage. An improved thermal stability using Ce:YAG glass-ceramics phosphors were proposed in the literature[1-4]. Glass-ceramics is a material having crystalline phase embedded in a glass matrix. Starting from Ceria doped Ytria-Alumina-Silica (YAS) base glass one can derive the Ce:YAG glass-ceramics phosphor with suitable heat treatment. The advantage is they are thermally stable and have almost no degradation upon thermal cycles. There are reports about compositional dependence, structure property correlations, microstructure evolution and luminescent properties of Ce:YAG phosphor crystals in YAS glasses[1-4]. Crystallization kinetics of YAS glass compositions and evolution of mixed crystalline phases like Mullite ($\text{Al}_6\text{Si}_2\text{O}_{13}$), Crystoballite and Y-disilicate ($\text{Y}_2\text{Si}_2\text{O}_7$) are reported in literature[5-7].

In this work, we focused on fabrication and characterization of a glass compositions which can be devitrified into a single phase Ce:YAG glass-ceramics phosphor. Further, to optimize the white light generation, we systematically studied the phosphor crystal growth kinetics, microstructure and photoluminescence spectra. Knowledge of crystallization kinetics is important for controlled devitrification, which was extracted from non-isothermal DTA

data. Crystallization kinetics and isothermal predictions were simulated for YAS glass using non-isothermal data and AKTS software. This study helped us to develop the Ce:YAG glass-ceramics phosphor with required concentration, microstructure and photoluminescence for the demonstration of a white LED.

Glass Synthesis

CeO_2 doped Y_2O_3 - Al_2O_3 - SiO_2 glasses were prepared with varying compositions. The aim was to derive the desired Ce:YAG phosphor phase in the glass matrix. Most of the time there were mixed phases like $\text{Y}_2\text{Si}_2\text{O}_7$, $\text{Al}_6\text{Si}_2\text{O}_{13}$ and $\text{Y}_3\text{Al}_5\text{O}_{12}$ in the glass-ceramics depending on the initial glass composition and heat treatment schedule. After several iterations glass composition 45.1 Y_2O_3 - 31.8 Al_2O_3 - 21.4 SiO_2 - 1.7 CeO_2 (wt %) suitable for the glass-ceramics phosphor was optimised. To prepare the glass, constituent oxides were weighed and mixed thoroughly. Each batch were melted in Pt-Rh crucibles at

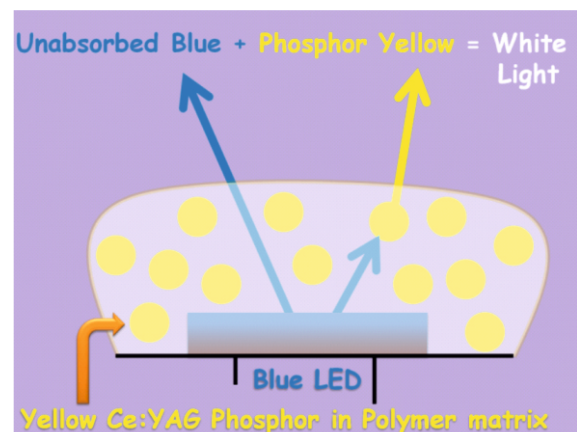


Fig.1: Schematic highlighting the working principle of white LED.

*Author for Correspondence: P. Nandi
E-mail: pnandi@barc.gov.in

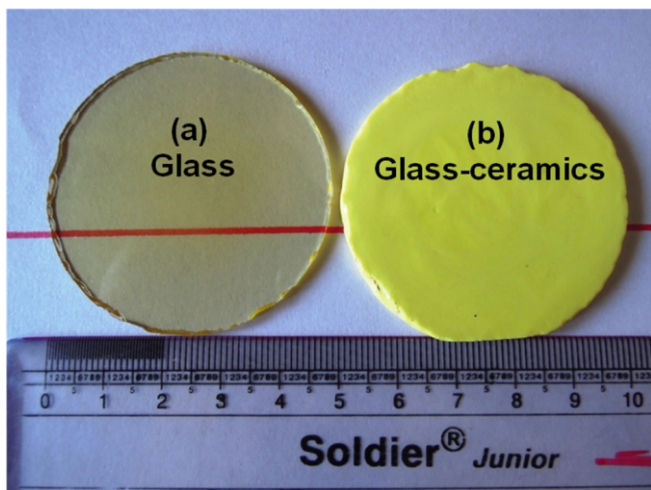


Fig.2: Polished YAS glass disk(a) and glass-ceramics phosphor(b).

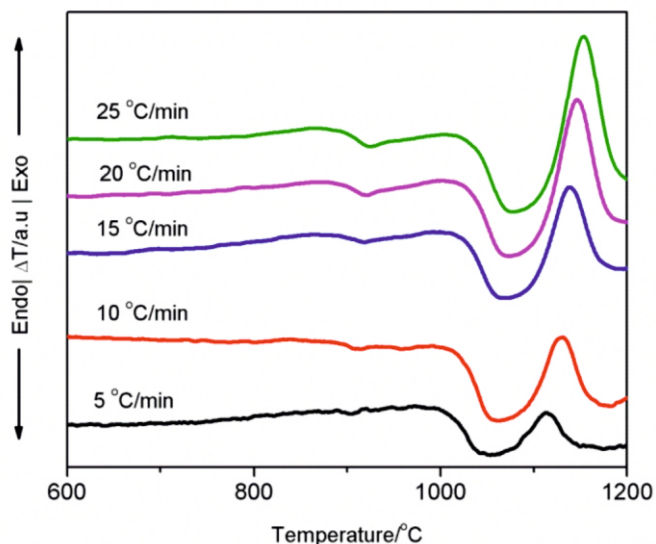


Fig.3: DTA plot of YAS glass powder at five different rates of heating.

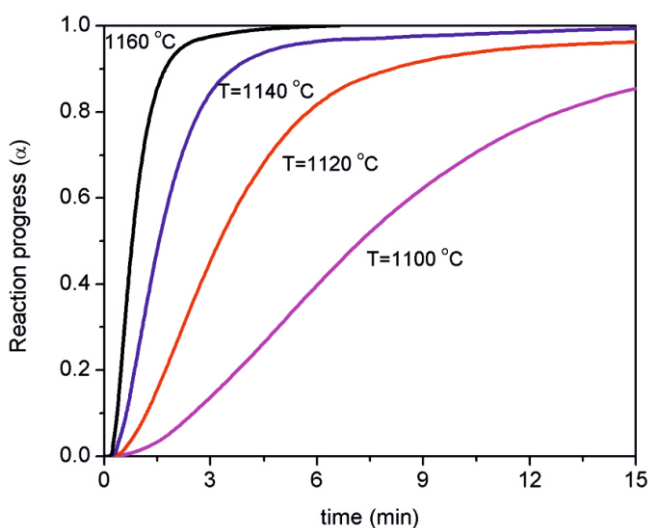


Fig.4: Isothermal predictions of the reaction progress(α) with time(min) at four temperatures (T °C).

~1650°C and held for two hours for homogeneous mixing before quenching the melt into a cylindrical mold. The same composition of the glass was prepared several times to check the repeatability and also to prepare glass cylinders in diameter range 10mm to 50mm. Prepared glasses were annealed at appropriate temperature to remove the thermal stresses. The glasses were cut into disks and polished before crystallization. Photographs of transparent and bubble free glass disk (left) and the yellow glass-ceramics (right) after suitable isothermal heat treatment are shown in Fig.2.

Thermal analysis

The differential thermal analysis (Labsys-SETARAM) was used to record the thermal changes of glass powder for five different heating rates: 5, 10, 15, 20 and 25°C per min shown in Fig.3. The data shows the glass transition (T_g) at around 875°C followed by exothermic peak in the temperature range of 1050-1200°C, indicating crystallization of glass. Because of high T_g, the glass-ceramics phosphors are thermal stable and not degrading as compared to polymer based phosphors at LED working temperature. The DTA data was used to derive the crystallization kinetics parameters by isoconversional method as reported elsewhere[8].

The isoconventional principle is that reaction rate (dα/dt) at a constant reaction progress (α) is only a function of temperature (T). The activation energy E(α) was calculated without any particular form of the reaction model f(α). That is the reason it is also called ‘model free’ kinetics principle. Activation energy (E) of crystallization at reaction progress (α = 0.5) estimated 659 kJmol⁻¹. No specification of the reaction model f(α) is necessary for the kinetic prediction since the product term {A(α) f(α)} considered constant, which was also experimentally extracted along with E(α) from the isoconventional data analysis. Then it is possible to simulate kinetic predictions at isothermal temperature (T) as given below.

$$t_{\alpha} = \int_{\alpha_0}^{\alpha} \frac{d\alpha}{\{A(\alpha) f(\alpha)\} e^{-\frac{E(\alpha)}{RT}}}$$

Four isothermal predictions of our interest simulated from above equation shown in fig.4. For fixed conversion α = 0.8, calculated time prediction for isothermals at 1160°C, 1140°C, 1120°C and 1100°C are approximately 1.4, 2.7, 5.7, and 12.9 min, respectively. Accordingly the glass samples were baked at isotherms for different holding times, for different fraction of crystalline phase. The yellow colored glass-ceramics disk (Fig.2) was obtained by isothermal heating at 1120°C for ~ 5 min.

Glassy/ Crystalline phase and microstructure analysis

X-ray diffraction of base glass and glass-ceramics powder are given in Fig.5. The characteristic broad hump confirms the amorphous nature of the glass sample. The diffraction pattern of glass-ceramics shows the crystalline peaks and a broad hump in the background at around 25–35 degrees indicating the residual glass. All the crystalline peaks can be attributed to cubic YAG as compared to JCPDS card #33-0040. Thus it confirms that single phase Ce:YAG phosphors present in the glass-ceramics sample.

The microstructure of glass-ceramics surface as observed under scanning electron microscope. Dendrite like crystal growth was observed on the glass-ceramics surface shown in Fig.6. These microscopic dendrites grew uniformly in glass matrix acting as yellow phosphors. Polishing quality of the

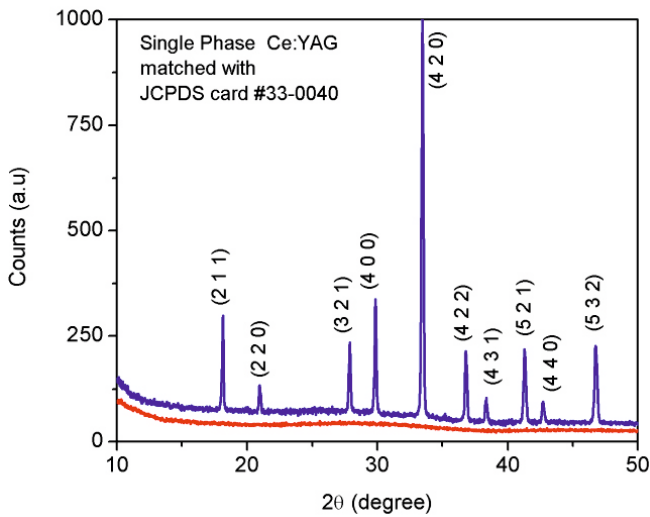


Fig.5: XRD pattern of as prepared YAS glass(red) and glass-ceramics phosphor(blue).



Fig.6: Micrograph of Ce:YAG dendrite at glass-ceramics surface.

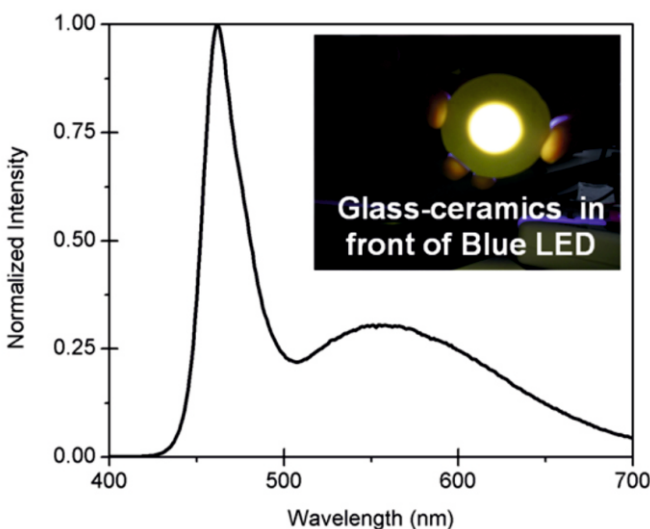


Fig.7: The illuminated glass-ceramics(inset) and the white light spectra as recorded by the PL spectrometer.



Fig.8: White light dispersed by a compact disk grating to create the rainbow.

surface before crystallization was important parameter to control the microstructures. Fine polished surface has less nucleation, hence shows less number of dendrite compared to the rough polished surface. Surface nucleation was particularly helpful to control the crystal growth only on the surface, therefore their optical properties suitable for generation of white light.

Optical properties of glass-ceramics phosphors

The photoluminescence experiments were done to test the optical quality of the material. The glass-ceramics sample shown in Fig.7 was illuminated against a blue LED. The spectrum was recorded in spectrometer (FLS 980-Edinburgh Instruments) using the remote fibre optic probe, and PMT detector. Two peaks are observed, one is the unabsorbed blue peaked at 465 nm and the other one is broad band Ce:YAG yellow fluorescence, ranging from 500 to 700 nm with a peak maximum at 570 nm as shown in Fig.7. The color co-ordinates of the spectrum found at (0.37, 0.39) which is nearest among the prepared samples to the theoretical white point at (0.33, 0.33). It was evident from the study that using appropriate heating schedule one can fine-tune the phosphor concentration, thickness and color of the resultant spectra. A device was assembled for white light generation using a commercially available blue light source and our laboratory made Ce:YAG glass-ceramics phosphor. The white light was again diffracted by a CD grating to disperse the light into rainbow colors shown in the Fig.8. This confirms the presence of red, green, and blue colors primarily required for white light spectrum.

Conclusions

We have developed a unique glass composition that can be converted to single phase Ce:YAG glass-ceramics phosphor. Processing parameters like, time and temperature dependent crystallization rate, polishing quality, microstructure and thickness of evolving phosphor layer are optimized to generate the white light. Isothermal predictions were used to crystallize the glass. Ce:YAG glass-ceramics with conversion factor (~ 0.75) was obtained by isothermal heating at 1120°C for ~5 min, found to generate the desired optical properties. XRD analysis of glass-ceramics confirms the evolution of Ce:YAG phase. Microstructure evolution showed surface nucleation and dendrite like growth of phosphor crystals, making ~50 μm thick phosphor layer. A device was setup using blue LED to demonstrate the white light generation using our laboratory made glass-ceramics phosphor.

Acknowledgements

Authors thank Madangopal Krishnan, Former Director, Materials Group, BARC for his role in conceiving and guiding the team of scientists involved in this work. We acknowledge thankfully Senthil Kumar, Yogesh Shirkar and P. A. Wagh for rendering technical assistance during preparation of glass and glass-based ceramics. Thanks to Abhijit Ghosh for carrying out FESEM experiments as part of this study.

References

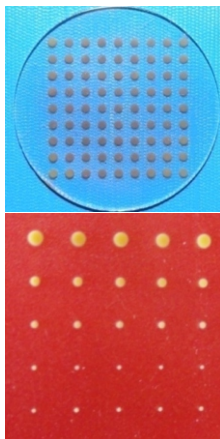
- [1] S. Fujita, S. Tanabe, Glass-Ceramics and Solid-State Lighting, *International Journal of Applied Glass Science*, 2015, 6, 356-363.
- [2] S. Fujita, A. Sakamoto, S. Tanabe, Luminescence characteristics of YAG glass-ceramic phosphor for white LED, *IEEE Journal of Selected Topics in Quantum Electronics*, 2008, 14, 1387–1391.
- [3] D. Chen, Xiang W, Liang X, Zhong J, Yu H, Ding M, Lu H, Z. Ji, Advances in transparent glass ceramics phosphors for white light emitting diode- A review, *Journal of the European Ceramic Society*, 2015, 35, 859–869.
- [4] A. Keshavari, W. Wisniewski, R. Kloe, C. Russel, Surface Crystallization of yttrium aluminum garnet from a silicate glass, *Crystal Engineering Communication*, 2013, 15, 5425-5433.
- [5] S. Ahmad, T. Ludwig, M. Herrmann, M. Mahmoud, W. Lippmann, H. Seifert, Phase evaluation during high temperature long heat treatments in the $Y_2O_3 - Al_2O_3 - SiO_2$ system, *Journal of the European Ceramic Society*, 2014, 34, 3835–3840.
- [6] B. Roudit, W. Dermaut, A. Lunghi, P. Folly, B. Berger, A. Sarbach, Advanced Kinetics based simulation of time to maximum rate under adiabatic conditions, *Journal of Thermal Analysis and Calorimetry*, 2008, 93, 163–173.
- [7] R. Muller, E. D. Zanotto, V. M. Fokin, Surface crystallization of silicate glasses: nucleation sites and kinetics, *Journal of Non-Crystalline Solids*, 2000, 274, 208-231.
- [8] P. Nandi, M. Goswami, A. Arya, M. Krishnan, Study of crystallization kinetics, microstructure and optical properties of Ce: YAG glass-ceramics for white LED applications; *Journal of Thermal Analysis and Calorimetry*. 2021. <https://doi.org/10.1007/s10973-021-10690-w>.

Photostructurable Glass for Microdevices

Development of Ag-Ce Doped Photostructurable Glass Ceramics for Microdevice Application

Richa Mishra*, M. Goswami, Ashok K. Arya

Glass and Advanced Materials Division, Bhabha Atomic Research Centre, Mumbai 400085, INDIA



Glass Discs after UV Exposure and Heat Treatment
(Scale: 0.2 to 1 mm diameter of holes)

ABSTRACT

In recent years glassy materials for micro devices fabrication are acquiring much attention over other materials for its excellent properties such as optical transparency, chemical inertness, thermal and electrical insulation, biocompatibility as well as ease of manufacturing. In this work we have utilized photolithography for micro structuring of glass. Ag and Ce doped Lithium Alumino Silicate glasses of composition (wt%): $74\text{SiO}_2\text{-}6\text{Al}_2\text{O}_3\text{-}15\text{Li}_2\text{O-}5\text{X}$ (X=other additives) were prepared by melt quench technique and exposed to UV light for conversion of Ce^{3+} to Ce^{4+} and Ag^+ into Ag^0 metallic state for preferential nucleation/growth of metasilicate phase. XRD was used for phase identification in the heat treated glasses. DTA data revealed a lower crystallization temperature (T_p) at around 610°C for UV exposed glass as compared to unexposed base glass which is at around 627°C . UV Visible spectra confirm conversion of Ce^{3+} to Ce^{4+} ions in exposed glass samples. In the samples heat treated at nucleation temperature Ag agglomeration was confirmed from the band position at around 430nm . Heat schedule was optimized for the crystallization of Lithium metasilicate phase on UV-exposed glass. Activation energy calculation showed lower value after exposure under UV-light. The developed metasilicate phase was selectively etched in dil. HF for fabrication of micro devices. Different micro-patterns up to 200μ could be successfully prepared.

KEYWORDS: Photostructurable glass ceramic, Microdevice, LAS glass ceramics, Crystallization kinetics

Introduction

Microfluidic devices find wide spread applications in various fields in the form of micro reactors, micro needles, micro sensors etc. These provide better thermal hydraulic and fluidic properties due to their large surface area to volume ratio than conventional devices[1]. They also provide large catalytic surface area and uniform temperature distribution which is most valuable for a number of reactions. Surface to volume ratio is key requirement in various applications and varies inversely with characteristic length. As characteristic length reduces surface to volume ratio increases and at micron size domain this value is significantly high owing to very small characteristic length. Small size of devices makes it portable and hazardous intermediates can be prepared insitu rather than storing them at isolated places. These can be fabricated using variety of materials such as metals, semiconductors, polymers, glasses, ceramics, etc[2]. Glass based micro devices have certain advantage over semiconductors and metals, thanks to its high/beneficial transparency in visible range, better thermal and electrical insulation, good corrosion resistance, biocompatibility[3]. As compared to polymer based micro devices the glass based devices are much more thermally stable and corrosion resistance and can withstand at higher pressures. In many places these materials are used as alternate to silicon based micro devices. Since glasses are isotropic in nature which makes these suitable for microstructuring in any direction in comparison to semiconductor such as Silicon. Different methods are reported

for manufacturing of microdevices with complex shapes such as wet etching, dry etching, laser fabrication, sand blasting, mechanical machining, etc. Preparation of complex microstructures with high aspect ratio using mechanical methods is comparatively difficult due to poor machinability of glasses[4]. Photolithography is one of the popular and simplest methods for preparation of complex and high aspect ratio micro structures in glasses. Photostructurable glasses based on ternary Lithiumalumino silicate (LAS) system with small amount of Ag and Ce can be patterned with micrometer accuracy over large areas without use of photoresist[5].

In this study we report, fabrication of micropatterns/microstructures on the glass by using photolithography. Ag and Ce doped Lithium alumino silicate glasses were prepared and characterized for selective growth of metasilicate phase. This phase has higher solubility in dil. HF than the base glass making them suitable for micro structuring. In this composition, Cerium is added to increase the glass photosensitivity and silver oxide to enhance the crystallization of the glass[6,7]. Micropatterning down to 200 micron scale were carried out on these glasses using this process.

Methodology/ Synthesis

Ag and Ce-doped LAS glasses of composition (wt.%): $74\text{SiO}_2\text{-}6\text{Al}_2\text{O}_3\text{-}15\text{Li}_2\text{O-}5\text{X}$ (X=other additives) were prepared by melt-quench technique. Melting was carried in the temperature range of $1550\text{-}1600^\circ\text{C}$ followed by annealing to remove thermal stresses. Cerium was used to provide the glass photosensitivity and silver oxide addition enhanced the photosensitivity of glass. All prepared glasses were

*Author for Correspondence: Richa Mishra
E-mail: richa@barc.gov.in

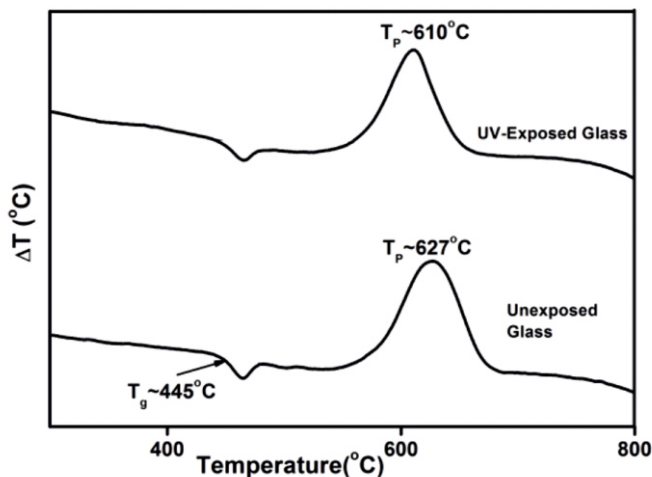


Fig.1: Merged DTA plots of unexposed and UV exposed Glasses.

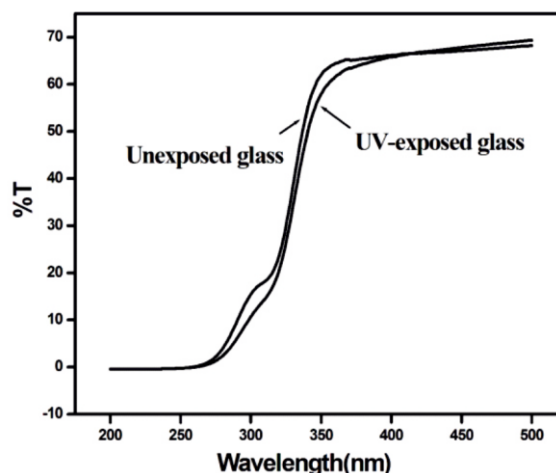


Fig.3: UV-Vis transmission spectra of unexposed and exposed Glasses.

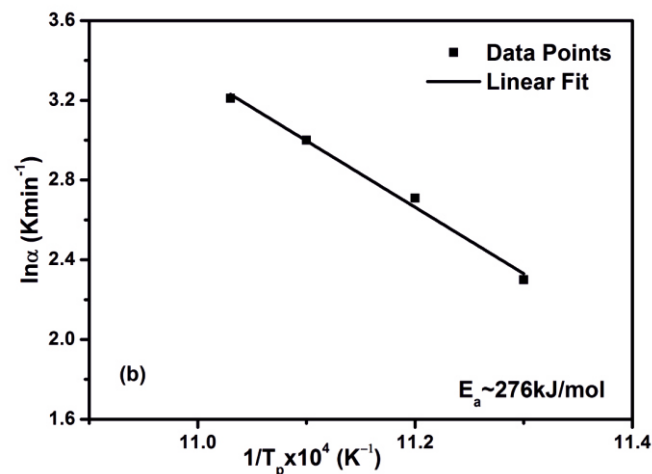
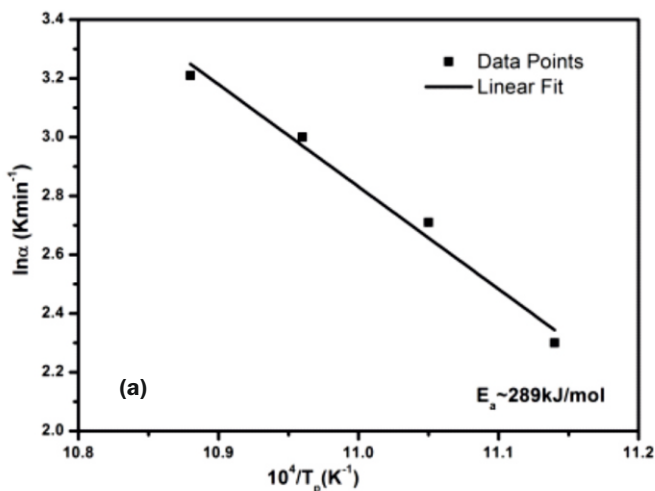


Fig.2: Marotta plot for activation energy of LASK (a) Unexposed (b) UV exposed glass.

transparent and bubble free. The glass samples were cut into thin pieces, polished and exposed under UV light at wavelength around 312nm (corresponding to Ce^{3+} absorption) for varying time periods (5 min to 4h). Based on the information by DTA data, heat treatment schedule optimization was carried for selective crystallization of Lithium metasilicate (Li_2SiO_3) phase. A two stage heat treatment was carried out on these polished and exposed glasses. In the first stage, sample was heat treated at nucleation temperature (in the range of 470-480°C)

in which formation of silver agglomerates is expected. In the second stage, sample was heat treated in the temperature range 500-550°C for required time period, for growth of Lithium metasilicate phase on silver agglomerates. To prepare pattern, glass piece was masked with a metal having desired pattern, UV exposed for pattern transfer, and then heat treated for Ag agglomeration and growth of Li_2SiO_3 phase. Finally this phase was preferentially dissolved in the 5-10% HF acid to leave the patterned glass.

Characterization

Differential thermal measurements (DTA) were performed on unexposed and exposed glass powder to determine glass transition temperature and shift in peak crystallization temperature using TG/DTA apparatus (Model: LABSYS). DTA experiments with varying rates of heating (10-25Kpm) were carried for activation energy calculations. XRD measurements were carried out to confirm the amorphous nature of the annealed glasses and to identify the crystalline phases in the exposed and heat treated glasses using Bruker D8 X-Ray Diffractometer.

UV-VIS spectrophotometer (Model V-670, M/s. JASCO, Japan) was used for absorption studies on unexposed and exposed glass samples, and on exposed and nucleated glass samples. Exposed and heat treated glasses were etched in dil. HF acid of different concentrations to dissolve metasilicate phase for time period in the range of 60-125 minutes.

Results/Discussion

Fig.1 depicts the DTA plots of unexposed and UV-exposed glasses with heating rate of 10 Kmin⁻¹. Both the glasses show broad endotherm at around 445°C indicating glass transition temperature (T_g). Data shows a lower exothermic peak temperature (T_p) at around temperature 610°C for UV-exposed samples as compared to unexposed base glass with peak temperature at around temperature 627°C. Non isothermal crystallization kinetics was carried on exposed and unexposed glasses by recording the DTA plots for different heating rates (10-25Kpm). Activation energy was calculated using Marotta equation which is as follows,

$$\ln(\alpha) = -\frac{E}{RT_p} + Constant$$

Here, E is the activation energy for crystallization, R is the gas constant, T_p is the peak of crystallization temperature, α is the heating rate (K min⁻¹).

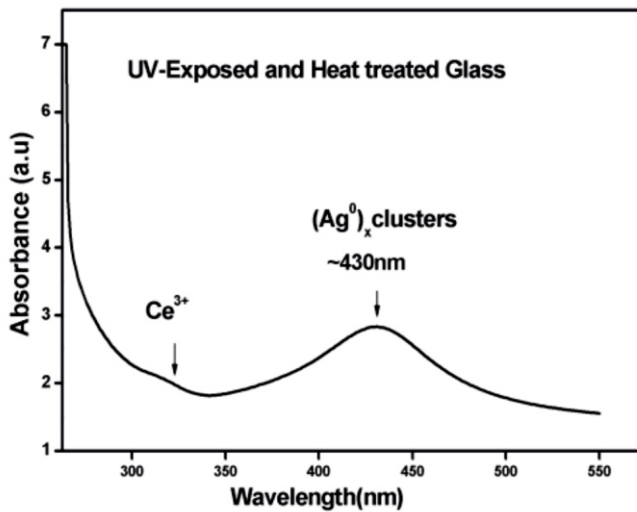


Fig.4: UV-Vis Absorption spectra of UV exposed and heat treated glass.

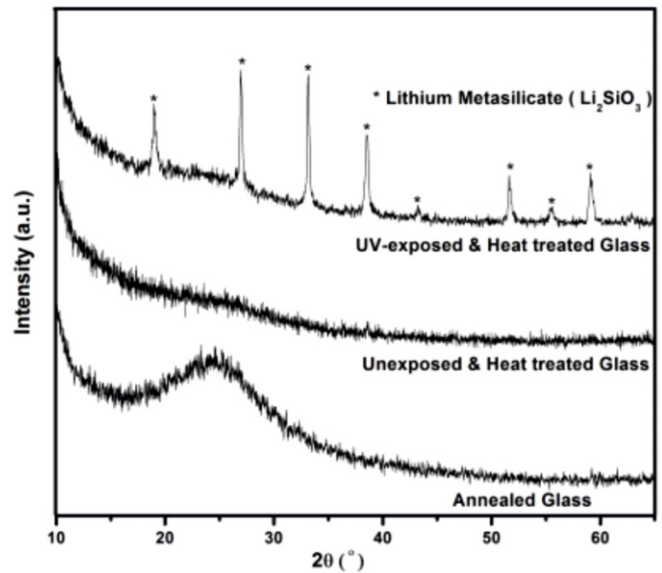


Fig.5: Merged XRD plots of heat treated, unexposed and UV exposed glasses.

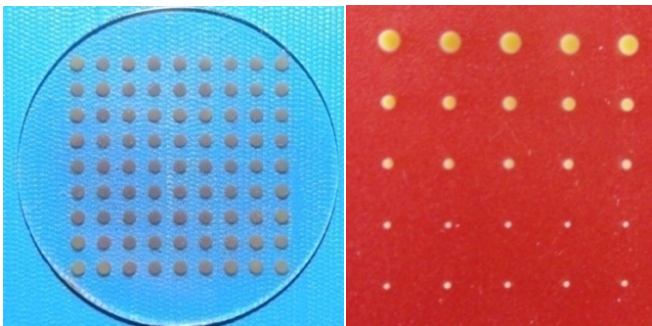


Fig.6: (a). Glass Discs after UV Exposure and Heat Treatment (Scale: 0.2 to 1 mm diameter of holes).

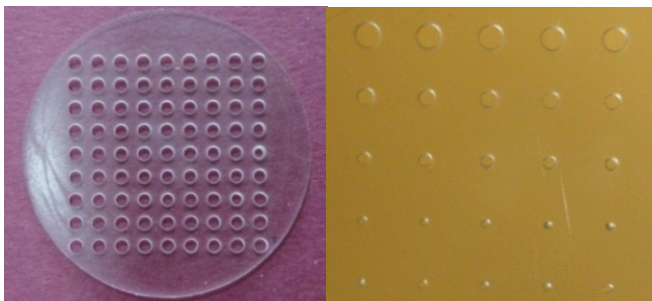


Fig.6: (b). Glass Discs after UV Exposure, HT and Etching in dil. HF (0.2 to 1 mm diameter of holes).

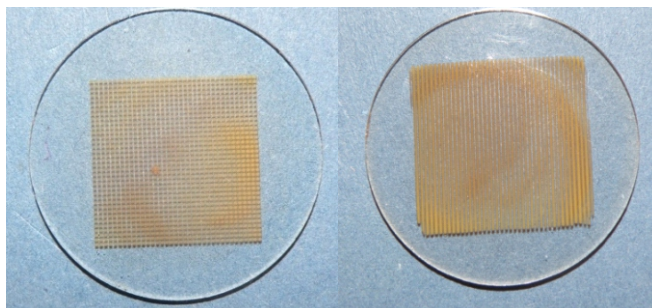


Fig.6: (c). Glass Discs after UV-Exposure, HT (0.2 mm holes and 0.2 mm line pattern).

Fig.2(a) & (b) showed Marotta plots for calculation of the activation energy for unexposed and UV-exposed glasses, respectively. Activation energy of crystallization for unexposed and exposed glasses were found to be 289kJmol⁻¹ and

276kJmol⁻¹. This reduction in activation energy after UV-exposure is due to the formation of silver nanoclusters, which provide heterogeneous nucleating sites for early growth of main phase.

Conversion of Ce³⁺ to Ce⁴⁺ state and Ag⁺ into Ag⁰ metallic state occurred after UV exposure.

Spectra in Fig.3 shows a broad band at around 305nm indicative of Ce³⁺ in base glass whereas in case of UV exposed sample the reduced peak intensity indicates conversion of Ce³⁺ to Ce⁴⁺ ions.

Fig.4 represents UV-Vis absorption spectra of nucleated samples which showed a broad band centered at around 430nm which confirms formation of Ag nanoclusters. These nanoclusters provide the heterogeneous nucleation sites for early growth of metasilicate phase in exposed sample, as compared to unexposed samples and helped for patterning in the glass.

X-ray diffraction patterns of annealed base glass, heat treated unexposed and heat treated UV- exposed samples are shown in Fig.5. XRD pattern of glass sample confirms its amorphous nature (broad hump in the region of 2θ≈20-30°). It also showed Lithium metasilicate phase (Li₂SiO₃) formation in exposed glass while no phase formation occurred in base glass/unexposed glass on subjecting to the optimized heat treatment. Early crystallization of this phase in glass after UV exposure is responsible for selective crystallization of glass, facilitating patterning/micro structuring.

Exposed and heat treated glasses were etched in dil. HF acid with varying concentration up to 10%. As the solubility of glass ceramic is more in the acid, it etched out from glass matrix leaving the matrix intact and thus desired pattern can be formed on the glass surface. Etching rate for metasilicate phase was found to be ~6μm/min. Etching ratio of glass ceramic to glass was found at around 10:1 in 10%HF.

Micropatterning of LAS glass ceramics

Micropatterning of different scales up to micron level were carried out using metal masking. Patterns with lines and holes up to size of 200μ could be prepared successfully with existing facility. Few photographs of microstructuring on Lithium Alumino silicate glass doped with Cerium and Silver are shown in Fig.6.

Conclusion

Ag and Ce doped LAS glasses were prepared, UV exposed and heat treatment process were fine tuned for selective growth of Lithium metasilicate phase. Shift in peak crystallization temperature in UV exposed samples to lower side was observed from DTA data. Kinetic analysis showed reduction in activation energy of crystallization after UV exposure which also indicates that silver is providing heterogeneous nucleation sites for early growth of metasilicate phase. Absorption spectra shows formation of silver nano clusters in the UV exposed and nucleated samples. Lithium metasilicate (Li_2SiO_3) phase formation was confirmed by XRD in exposed and heat treated glass while base glass showed no crystalline phase. Etching ratio of glass ceramic to glass was found ~10:1. Microstructures of dimensions up to 200μ could be prepared in these glasses using photolithography.

Acknowledgements

Authors wish to thank Madangopal Krishnan, Former Director, Materials Group, BARC for the support and guidance, B. C. Maji, MMD for providing XRD facility and T. K. Devangan, PTDD for providing masking facility. We also thank V. M. Phalke, EmA&ID for providing technical help in mask fabrication. We also thankfully acknowledge A. Dixit for helping in glass preparation and R. S. Nair for helping in establishment of exposure facility.

References

- [1] Tao Wang, Jing Chen, Tianfeng Zhou and Lu Song, Fabricating Microstructures on Glass for Microfluidic Chips by Glass Molding Process, *Micromachines*, 2018, 9, 269. doi:10.3390/mi9060269.
- [2] R. Knitter, D. Gohring, P. Risthaus, J. Hauelt, Microfabrication of ceramic microreactors, *Microsystem Technologies*, 2001, 7, 85-90.
- [3] Fei He, Yang Liao, Jintian Lin, Jiangxin Song, Lingling Qiao, Ya Cheng, Koji Sugioka, Femtosecond Laser Fabrication of Monolithically Integrated Microfluidic Sensors in Glass, *Sensors*, 2014, 14, 19402-19440. doi:10.3390/s141019402.
- [4] Lucas A. Hof, Jana Abou Ziki, Micro-Hole Drilling on Glass Substrates - A Review, *Micromachines*, 2017, 8, 53. doi: 10.3390/mi8020053.
- [5] A. Freitag, D. Vogel, R. Scholz, T. R. Dietrich, Microfluidic Devices Made of Glass, *Journal of the Association for Laboratory Automation*, 2001, 6 (4), 45-49.
- [6] Khalid Hasan Tantawi, Emmanuel Waddel, John D. William, Structural and composition analysis of ApexTM and FoturanTM photodefinable glasses, *J Mater Science*, 2013, 48, 5316-5323.
- [7] J. M. Fernandez-Pradas, D. Serrano, S. Bosch, J. L. Morenza, P. Serra, 3D features of modified photostructurable glass-ceramic with infrared femto second laser pulses, *Applied Surface Science*, 2011, 257, 5219-522.

Reinforced SiC Composites

Development of Silicon Carbide Fibre through Pre ceramic Polymer route

J. N. Sharma*, P. K. Mollick, Ramani Venugopalan, Ashok K. Arya and Vivekanand Kain

Glass & Advanced Materials Division, Materials Group, Bhabha Atomic Research Centre, Mumbai 400085, INDIA



Melt-spun (green) fibre

ABSTRACT

Silicon carbide fibres derived from polycarbosilane (PCS), a precursor polymer to SiC, offer exceptional opportunities for fabrication of SiC fibre reinforced SiC matrix composites. These composites are proposed as high temperature nuclear materials due to their excellent high-temperature fracture, creep, corrosion and thermal shock resistance and safety advantages arising from low induced radioactivity. PCS was synthesized at kilogram scale by pressure pyrolysis of polydimethylsilane (PDMS) in a gas induction autoclave in the temperature and pressure range of 480-500 °C and 90-100 bar respectively. PDMS was synthesised from Wurtz-type reductive dehalogenation of dimethyldichlorosilane with molten sodium. PCS of different molecular weight fractions were obtained by fractional distillation. The molecular weight, structure, softening temperature, ceramic yield and properties of PCS were characterized by measurements of GPC, FT-IR, ¹H-NMR, TG-DTA-DSC, Raman and XRD. SiC ceramic fibre was obtained from PCS by melt spinning, cross-linking of melt-spun fibre by oxidative curing followed by heat treatment of cured-fibre in argon atmosphere up to a temperature of 1250 °C. XRD of SiC fibre indicated presence of β-SiC nanocrystallite as main phase and SEM showed a smooth surface with no visible defects.

KEYWORDS: Polydimethylsilane, Polycarbosilane, Melt spinning, Curing, Pyrolysis, Silicon carbide fibre

Introduction

SiC fibres offer high strength-to-weight ratios and exceptional thermal stability in harsh environmental conditions. Such fibres are one of the best candidates as reinforcement for high-performance ceramic matrix composites due to their high mechanical properties, oxidation and creep resistance at elevated temperatures[1-3]. The ceramic derived from polymer enabled significant technological breakthroughs in development of ceramic fibres, coatings and ceramics stable at ultrahigh temperatures (up to 2000 °C)[4]. Polymer precursors represent organo-silicon polymeric systems that provide ceramics with a tailored chemical compositions and a crystalline nanostructured organization when subjected to proper thermal treatment under an inert atmosphere. Yajima *et al.* first reported the pioneering work on preparation of SiC fibre from PCS precursor. PCS, a polymer having silicon and carbon atoms repeated alternately, was melt spun to obtain precursor fibre, then cross-linked to render the fibres infusible, and finally pyrolyzed under inert atmosphere to produce SiC fibre. The SiC fibre obtained was continuous, having β-SiC nano-crystallite structure, high tensile strength and young's modulus[5,6]. Nippon Carbon Company, Japan made the first commercial SiC fibres under the trade name Nicalon™. These fibres have excellent stability up to a temperature of 1200 °C, resistance to acid/base corrosion and oxidation, high tensile strength and Young's modulus of 2.5-3.2 GPa and 180-300 GPa respectively[7]. Nippon Carbon in collaboration with Japan Atomic Energy Research Institute, carried further modifications in fibre processing parameters and developed

SiC fibre which retained its high tensile strength and Young's modulus up to a temperature of 1800 °C. This remarkable heat resistance fibre was named as Hi-Nicalon[8]. SiC fibre is an outstanding reinforcement for various composites, because of their excellent compatibility with resins, metals and ceramics. The SiC fibre reinforced SiC composite (SiC_f/SiC) is a class of ceramic matrix composites in which a SiC fibre preform phase is imbedded in a SiC matrix phase[8]. SiC_f/SiC matrix composites are fabricated from fibre wound preforms or fibre fabric preforms through processes such as, chemical vapour infiltration (CVI process), preceramic polymer infiltration pyrolysis (PIP process), reaction sintering process and SiC nanoparticle slurry infiltration transient eutectic (NITE process)[9-12]. These composites can be engineered for specific stress, temperature, life and environmental conditions. NASA patented SiC_f/SiC composites, which can withstand adverse structural and environmental conditions for a very long time at temperatures up to 2500 °C[13]. Several fusion power reactor design studies have mentioned the use of SiC_f/SiC composites as structural material[14-15]. These composites offer significant benefits over metallic superalloys, monolithic ceramics, carbon fibre and oxide/non-oxide ceramic composites[16-17].

Worldwide, the development and availability of these composites have been restricted to a few countries only, which either have the technology to manufacture SiC fibre through the preceramic polymer route or have free access to it. The key challenges in the manufacturing technology of SiC fibre is the large scale production of PCS and PDMS, the melt spinning of PCS to continuous PCS fibre, curing of PCS fibres by oxidative activation or electron beam irradiation and pyrolysis of the

*Author for Correspondence: J. N. Sharma
E-mail: jnsharma@barc.gov.in

cured fibre to SiC fibre. In relevance to the DAE reactor programme, SiC_i/SiC matrix composites are the most promising material for Accident Tolerant Fuel Cladding and for high temperature structural applications, while the PCS itself is important for SiC coatings on various structural components of high temperature reactors. In defence and space sector, C_i/SiC and SiC_i/SiC composites are used as light weight-high temperature stable structural materials. Recently, DRDO approached us for their large scale requirements of PCS for fabrication of C_i/SiC components through hybrid process consisting of PIP, CVI & CVD for hypersonic applications.

In this article, the on-going work on development of continuous SiC fibre through large scale synthesis of PCS, melt spinning of PCS to green fibre, oxidative curing and pyrolysis of cured fibre to SiC fibre and their characterization are reported.

Preparation of PCS

Yajima method for synthesis of PCS using PDMS is followed. Details of synthesis are given as under.

Synthesis of PDMS

PDMS is composed of a Si-Si backbone structure with methyl substituents attached to the silicon atoms. It is synthesised by Wurtz-like reductive dehalogenation of dimethyl dichlorosilane with molten sodium. The synthesis was carried out in a 10 L round bottom flask fitted with mechanical stirrer, reflux condenser and addition funnel. 1 kg of sodium was added with 5 L of xylene and heated up to 110 °C under N₂ atmosphere, then added 2.45 L of dimethyldichlorosilane drop-wise by maintaining the temperature in the range of 110-120 °C. The reaction mixture was refluxed for 10-12 h. The product was separated after necessary work-up. PDMS obtained was 1 kg with a yield of 85%. It is a white powder and was found to be insoluble in almost all paraffinic and aromatic solvents. It was characterized by FTIR. IR spectra show absorptions at 2900, 1400 cm⁻¹ for C-H and 1250, 835,750, 690, 635 cm⁻¹ for Si-CH₃.

Synthesis of PCS

1 kg of PDMS was charged in a gas induction autoclave in argon atmosphere and raised the temperature to 480 °C at the rate of 200 °C/h. The temperature was maintained between 480-500 °C for 6-10 h. The autogenic pressure at this temperature was about 100 bar. After completion of reaction, the reaction mass was fractionated under vacuum to obtain different molecular weight fractions of PCS. Autoclave for synthesis and fractionation is shown in Fig.1.



Fig.1: Autoclave for synthesis of PCS.

The rearrangement polymerization reaction is written as:

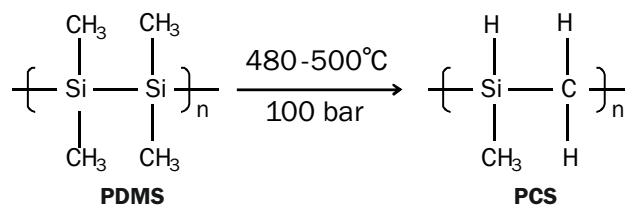


Fig. 2 &3: Liquid/gel and solid fractions of PCS.

Characterization of PCS

The formation of PCS is confirmed by presence of characteristic peaks, Si-H & Si-CH₂-Si by FTIR and ¹H-NMR (CDCl₃) measurements. IR absorptions, as shown in Fig.4, at 2098 cm⁻¹ contributed to Si-H, 1016 & 1356 cm⁻¹ to Si-CH₂-Si, and 600 to 920 cm⁻¹ to Si-CH₃. ¹H-NMR spectra (Fig.5) shows chemical shift at 4.26 for Si-H and 0.1695 for Si-CH₃.

Molecular weight distribution of PCS is measured by Gel Permeation Chromatography (GPC) using Agilent system, model: 1260 Infinity, fitted with refractive index detector. THF was used as eluent and polystyrene as calibration standard. PCS of number average molecular (M_n) in the range of 400 to 500 are low viscous liquid, M_n~500 to 700 are viscous liquid (gel) and M_n above 700-800 are solid. Melting points, M_n and weight average molecular weights (M_w) of solid PCS fractions are given in Table 1.

Ceramic yield of PCS is obtained by measurement of weight loss due to thermal decomposition using Mettler Toledo

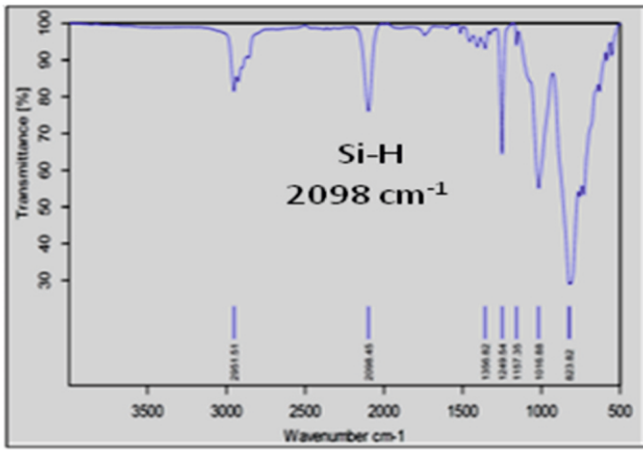


Fig.4: FT-IR spectra of PCS.

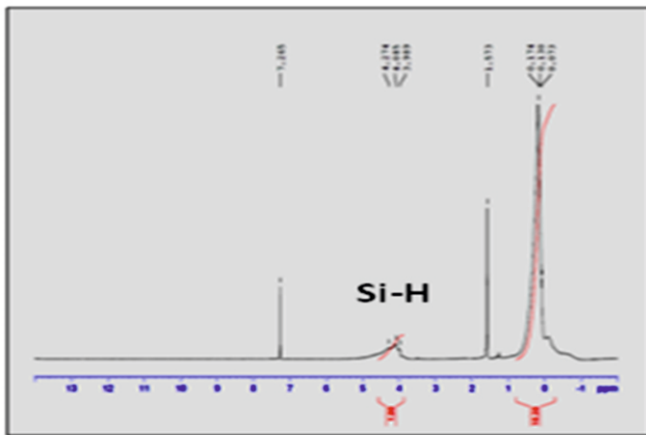


Fig.5: ¹H-NMR of PCS.

Table 1: Melting point and molecular weight information of PCS fractions.

| PCS fractions Melting points (°C) | M _n g/mol | M _w g/mol |
|--------------------------------------|-------------------------|-------------------------|
| <15 (liquid/gel) | 400-700 | 800-1020 |
| 118-124 | 1230 | 2279 |
| 135-141 | 1300 | 2619 |
| 148-154 | 1457 | 2914 |
| 174-184 | 1550 | 4693 |
| 237-250 | 1647 | 9000 |
| 285-290 | 1746 | 9650 |
| >350 | 1912 | 11059 |

TGA/DSC 3+ star system. PCS sample of 285-290 °C melting point fraction was heated up to a temperature of 1250 °C at a heating rate of 10 °C/min and argon flow rate of 40 cm³/min. Polymer to ceramic conversion is completed up to 1250 °C and ceramic yield obtained was about 75%.

SiC ceramic powder obtained on pyrolysis of PCS was analysed by XRD (Cu K α) and Raman spectroscopy. The XRD pattern shows formation of β -SiC crystallite as major phase (Fig.6). The peaks at $2\theta = 36^\circ, 60^\circ, 72^\circ$ corresponds to (111), (220), and (311) diffraction planes of face centered cubic β -SiC polymorph of SiC. The crystallite size of SiC was found to be 12 nm. Raman spectra (Fig.7) also shows cubic (3C) β -type crystal structure of SiC powder.

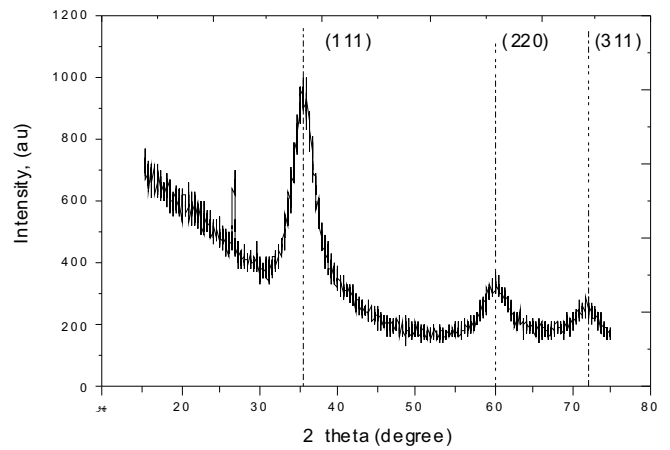


Fig.6: XRD pattern of SiC obtained on pyrolysis of PCS at 1250 °C in argon atmosphere.

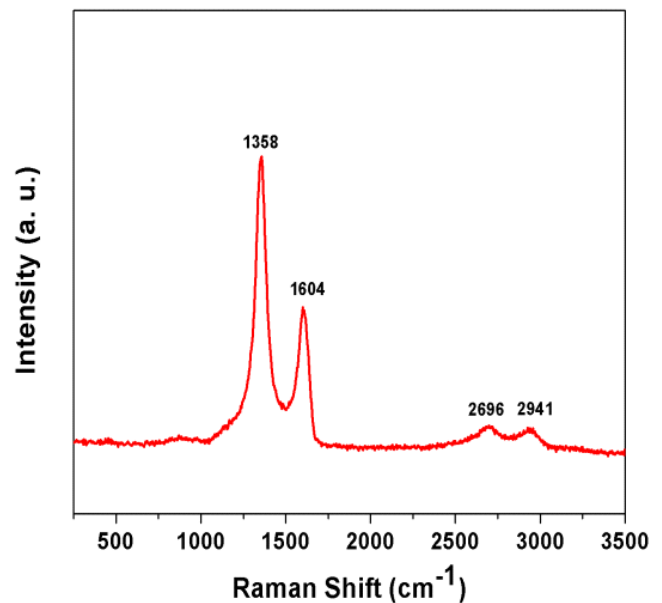


Fig.7: Raman spectra of SiC obtained on pyrolysis of PCS at 1250 °C in argon atmosphere.

Processing of PCS to SiC Fibre

It mainly consists of three steps: (a) Melt spinning of PCS to green fibre (b) Curing of PCS fibre by heating in an oxidising atmosphere to make it infusible (antimelt) fibre and (c) Pyrolysis of cured fibre in an inert atmosphere to obtain SiC fibre.

Melt Spinning of PCS

Solid PCS was converted to fibre by extruding the molten PCS under nitrogen pressure through a ten-hole spinneret of a melt spinning unit. For winding of fibre, a large diameter rotating bobbin was placed just below the spinneret. Prior to spinning, the PCS was heated just above its melt temperature under nitrogen gas pressure and kept for 1 h for obtaining uniform molten mass. The temperature was then reduced to near melting point and fibre spinning started by increasing the N₂ gas pressure and by adjusting the winding speed of bobbin. About 5 m continuous fibre without any surface defect was obtained. Image of the melt-spun fibre is shown in Fig.8. Different range of fibre diameters were produced by varying the spinneret orifice diameter, nitrogen pressure, winding speed and melt viscosity. Details of spinning conditions of a typical run are given in Table 2.

Table 2: Spinning parameters of PCS of melting point 237-250 °C.

| PCS | Spinning Temperature | Spinneret hole diameter | N ₂ pressure | Winding speed |
|--------------------------|----------------------|-------------------------|-------------------------|---------------|
| Melting point 237-250 °C | 270-280 °C | 0.2 mm | 5-7 bar | 300m/min |



Fig.8: ¹H-NMR of PCS.



Fig.9: Cured PCS fibres.

Oxidative Curing of Green Fibre

Curing step is necessary to make the green fibre infusible so that it retains the fibrous shape during pyrolysis. Here curing is carried by slow heating of fibre in a flow of dry air in an oven. The as-spun fibre was cut into a length of 20 cm and placed in an air-oven and heated at a rate of 0.5 °C/min up to a temperature of 200 °C. Curing results in surface oxidation of fibre forming a cross-linked structure which renders the green fibre infusible. Extent of curing is determined by the gel fraction of the cured fibre. Gel fraction is the insoluble portion during Soxhlet extraction of the cured fibre with xylene as eluent at 150 °C for 8 h. The gel fraction obtained in the present curing condition is about 70%. A gel fraction above 50% is sufficient to make fibre infusible and to retain the fibre shape on further heat treatment. Image of cured fibre is shown in Fig.9.

Pyrolysis of Cured Fibre

The cured PCS fibre was kept in an alumina boat and placed into a tubular furnace connected with a high purity argon gas cylinder and mass flow meter. The temperature of the furnace was raised to 1250 °C at a ramp rate of 5 °C/min and argon flow rate of 100 mL/min. The soaking time at set temperature was 1 h. The pyrolysis converted the yellowish

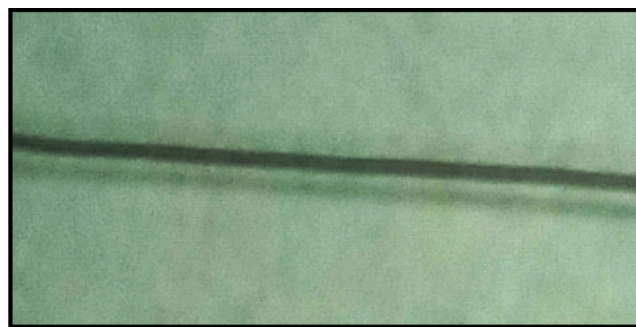


Fig.10: Typical SiC fibre of 10 cm length obtained on pyrolysis of cured fibre.

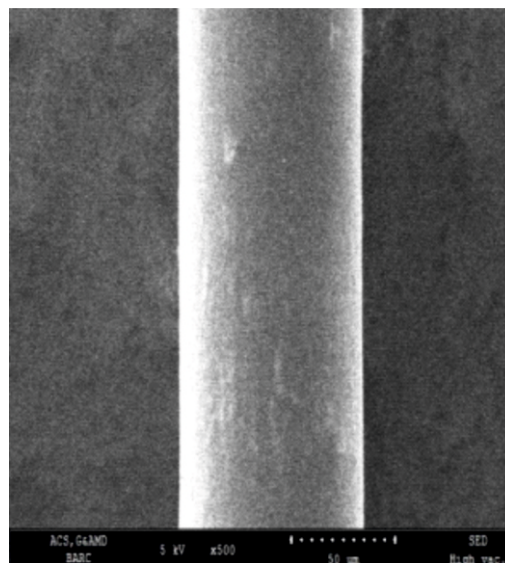


Fig.11: Micrograph of SiC fibre.

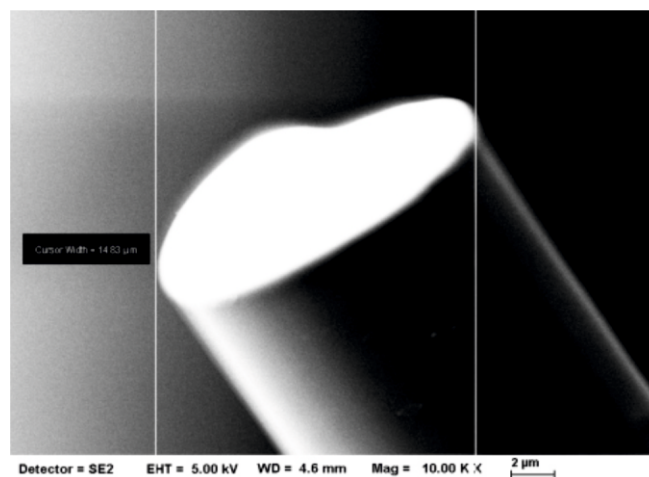


Fig.12: A SiC fibre of diameter 15 μ.

cured fibre to lustrous black SiC ceramic fibre (Fig.10). XRD of SiC fibre shows major phase as β-SiC with peaks at 2θ = 36°, 60°, 70° for (111), (220) and (311) diffraction lines. SEM image indicated a smooth surface with no visible surface defects (Fig.11). Diameter of fibres obtained was in the range of 14 to 16 μ (Fig.12). Measurement of mechanical properties of the fibres is in progress.

Conclusions

Kilogram scale synthesis of PDMS, PCS and fractionation of PCS to different molecular weight fractions and along with their characterizations has been well established. Processing

parameters for conversion of PCS to SiC fibre through, melt spinning of PCS to green fibre, oxidative thermal curing (cross-linking) of green fibre and finally pyrolysis of cured fibre to SiC fibre have been optimized. Here, it is to be noted that, technology for manufacture of continuous SiC fibre is associated with numerous challenges. Some of the difficulties encountered during the experiments are: (a) Spinning of continuous green fibre with uniform diameter and smooth surface, (b) Spinning of very low diameter ($< 20\mu$) continuous green fibre, (c) Control of oxygen content during thermal curing of green fibre, (d) Avoiding defects due to shrinkage of fibre during pyrolysis. All these challenges are being addressed methodically to realise the goal of making continuous SiC fibre and SiCf/ SiC composites.

References

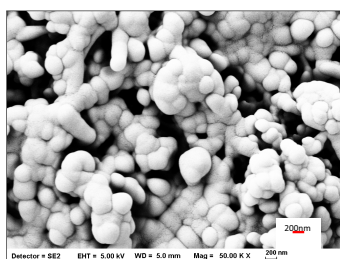
- [1] A. Kohyama, M. Singh, Hua-Tay Lin, Y. Katoh (Eds.), *Advanced SiC/SiC Ceramic Composites: Ceramics Transactions*, American Ceramic Society, 2002, 144.
- [2] Y. Katoh, S.M. Dong and A. Kohyama, Thermo-mechanical properties and microstructure of silicon carbide composites fabricated by nano-infiltrated transient eutectoid process, *Fusion Eng. Des.*, 2002, 61-62, 723-731.
- [3] A. Kohyama, Joon-Soo Park, Hun-Chea Jung, *Advanced SiC fibres and SiC/SiC composites toward industrialization*, *J. Nuclear Mater.*, 2011, 417 (1-3), 340-343.
- [4] Paolo Colombo, *Polymer-Derived Ceramics: 40 Years of Research and Innovation in Advanced Ceramics*, *J. Am. Ceram. Soc.*, 2010, 93(7), 1805-1837.
- [5] S. Yajima, Y. Hasegawa, J. Hayashi, M. Imura, Synthesis of continuous silicon carbide fibre with high tensile strength and high Young's modulus, Part 1: Synthesis of polycarbosilane as precursor, *J. Mater. Sci.*, 1978, 13, 2569-2576.
- [6] Y. Hasegawa, M. Imura, S. Yajima, Synthesis of continuous silicon carbide fibre, Part 2: Conversion of polycarbosilane fibre into silicon carbide fibres, *J. Mater. Sci.*, 1980, 15, 720-728.
- [7] Richard M. Laine, Florence Babonneau, *Pre-ceramic Polymer Routes to Silicon Carbide*, *Chem. Mater.*, 1993, 5, 260-279.
- [8] Toshikatsu Ishikawa, Recent development of the SiC fibre Nicalon and its composites, including properties of the SiC fibre Hi-Nicalon for ultra-high temperature, *Composites Science and Technology*, 1994, 51, 135-144.
- [9] W. Yang, H. Araki, A. Kohyama, S. Thaveethavorn, H. Suzuki, T. Noda, Fabrication in-situ SiC nanowires/SiC matrix composite by chemical vapour infiltration process, *Materials Letters*, 2004, 58, 25-32.
- [10] C.A. Nannetti, A. Ortona, D.A. de Pinto, and B. Riccardi, Manufacturing SiC-Fibre-Reinforced SiC Matrix Composites by Improved CVI/Slurry Infiltration/Polymer Impregnation and Pyrolysis. *Journal of the American Ceramic Society*, 2004, 87, 1205-1209.
- [11] Kazuya Shimoda, Akira Kohyama, Tatsuya Hinoki, High mechanical performance SiC/SiC composites by NITE process with tailoring of appropriate fabrication temperature to fibre volume fraction, *Composite Science and Technology*, 2009, 69, 10, 1623-1628.
- [12] William B. Hillig, Melt Infiltration Approach to Ceramic Matrix Composites. *Journal of the American Ceramic Society*, 1988, 71, 2, 96-99.
- [13] <https://technology.nasa.gov/patent/LEW-TOPS-25>
- [14] R.H. Jones, L. Giancarli, A. Hasegawa, Y. Katoh, A. Kohyama, B. Riccardi, L.L. Snead, W.J. Weber, Promise and challenges of SiCf/SiC composites for fusion energy applications, *Journal of Nuclear Materials*, 2002, 307-311, 1057-1072.
- [15] T. Noda, Advanced SiC-SiC Composites for Nuclear Application. In: Y.R. Mahajan, R. Johnson (eds) *Handbook of Advanced Ceramics and Composites*, Springer, Cham., [https://doi.org/10.1007/978-3-030-16347-1_20\(2020\)](https://doi.org/10.1007/978-3-030-16347-1_20(2020)).
- [16] J. Lamon, Chemical vapour infiltrated SiC/SiC composites (CVI SiC/SiC), *Handbook of Ceramic Composites*, 2005, Springer.
- [17] Masaki Kotani, Akira Kohyama, Yutai Katoh, Development of SiC/SiC composites by PIP an combination with RS, *Journal of nuclear Materials*, 2001, 289, 37-41.

Carbon fibre coated with SiC

Synthesis of Silicon Carbide Particulate and Fibre by Reaction-Conversion Method

Abhijit Ghosh*, Rohini Garg, A.K. Gulnar, Ashok K. Arya

Glass and Advanced Materials Division, Bhabha Atomic Research Centre, Mumbai 400085, INDIA



FE-SEM micrographs of SiC powder

ABSTRACT

A programme has been initiated to synthesize fully converted silicon carbide (SiC) powder and fully/ partially converted SiC fibre from the carbon particulate and fibre respectively. By reacting silicon monoxide with carbon (reaction conversion method) at temperature ~150°C, ultrafine SiC powder was prepared. Yield of the process was more than 80%. SiC produced by this method mimicked the original size and shape of the initial carbon powder. Fully converted SiC fibre and SiC coated Carbon fibre (partially converted) was also produced by this method. Indeed this method was optimized and successfully used to prepare reel to reel SiC coated carbon fibre in 500 meter length.

KEYWORDS: Silicon carbide (SiC), Carbon fibre, Composite

Introduction

Silicon carbide (SiC) based non-oxide ceramics in different forms found a wide range of applications - from conventional low-tech fields like abrasive and heat management (kiln furniture, heating elements etc.) to highly sophisticated applications such as in modern jet engines and electronic wafers. Indeed, in the structural ceramic field, SiC is one of the most promising non-oxide materials owing to its high thermal conductivity, superior oxidation resistance, low thermal expansion coefficient, excellent wear and corrosion resistance, high mechanical strength even at elevated temperature, low creep, high stiffness and chemical inertness[1]. Moreover, adequate radiation tolerance of SiC[2] makes it a potential candidate as a refractory nuclear material. This journey began with the earlier developmental effort for tri-layered isotropic micro-encapsulated fuel for a high-temperature gas-cooled reactor[3]. However, the major drawback of monolithic SiC is its brittleness, which makes this material unreliable, especially in accidental conditions. A composite of SiC particulate(p) with SiC fibre(f) provides the solution from such uncertainty due to its damage tolerance and highly predictable failure properties. In the aftermath of the nuclear accident in Fukushima, Japan, in 2011, the renewed interest in SiC(f)-SiC(p) composite as accident tolerant fuel (ATF) rod material gained interest[4]. Two major components needed to develop ATF clad are SiC fibre and ultrafine SiC powder. One of the most cost-effective and straightforward processes for producing continuous SiC fibre is the direct conversion of readily available carbon (C) fibre to SiC fibre[5-7]. In this, 'C' reacts with silicon monoxide (SiO) to form SiC. The gas-solid reaction is given below:



SiC has been synthesized by the above mentioned (Eq.1) gas-solid reaction [8-11]. Same reaction can also provide a coating of SiC on the C-fibre. Such type of fibre is deemed superior to the uncoated C fibre due to the former's better

chemical and physical compatibility with metal and ceramic matrices and excellent oxidation resistance property[12-14].

To realize the accident tolerant fuel cladding concept, a programme on the indigenous development of SiC fibre has been initiated recently. In this, the first step was to form fully converted SiC fibre. Besides, an attempt was also made to prepare SiC coated carbon fibre in continuous mode. In addition, the above-mentioned direct reaction, which we termed as reaction-conversion method, has also been used to prepare ultrafine SiC powder.

Experimental Procedure

A mixture of silicon (Si) and silicon dioxide (SiO₂) in a 1:1 molar ratio was used to generate SiO gas. The mixture was compacted at a pressure of 150 MPa and placed on an alumina boat. Both powder synthesis and fibre making were carried out in protective argon (Ar) gas environment. At elevated temperature, SiO reacted with C to form SiC. After several trial-and-error runs, the reaction temperature was fixed at 150°C. A schematic of the experimental set-up for powder and fibre synthesis has been shown in Fig.1(a and b).

The phase evolution was studied by X-ray diffraction (XRD) and Raman-scattering technique. The microstructure of the synthesized fibre was observed under a scanning electron microscope (SEM). Elemental mapping was carried out using the SEM-EDS technique.

Results and Discussion

Conversion of 'C' to SiC was carried out in static and continuous mode in protective Ar gas environment. Well dispersed ultrafine mixed-phase silicon carbide powder, which will be used for developing SiC-based structural components for the nuclear reactor has also been synthesized by this method. Initially, the time and temperature of the reaction were optimised for the synthesis of the powder. It was observed that with an increase in reaction time, the content of un-reacted 'C' decreased, and the amount of SiC increased. In the present study, it was found out that the synthesized SiC was a mixture

*Author for Correspondence: Abhijit Ghosh
E-mail: aghosh@barc.gov.in

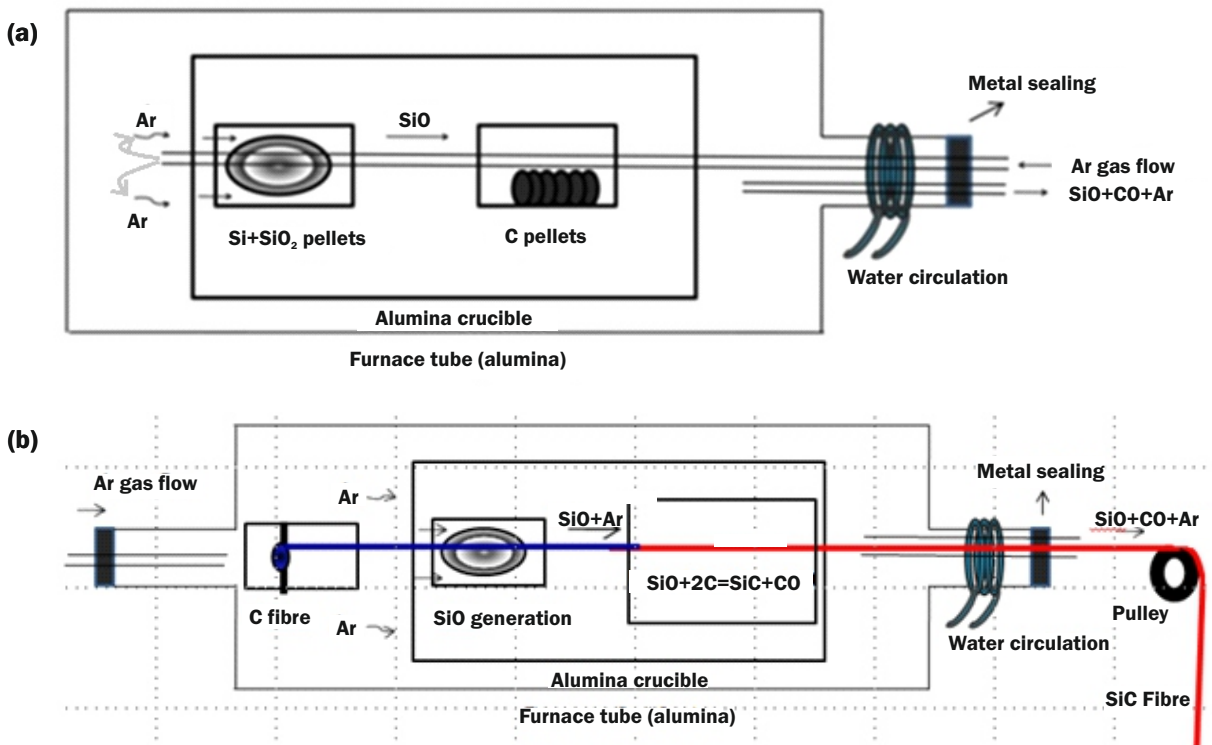


Fig.1: Schematic of reaction set-up for SiC synthesis by gas solid reaction (a) for powder synthesis and (b) 20m long fibre drawing.

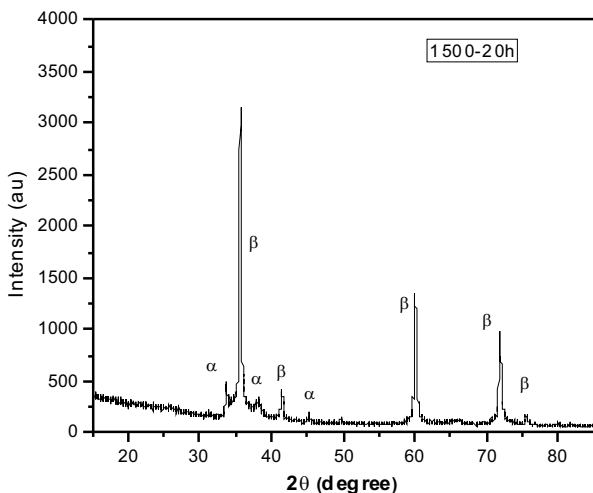


Fig.2: XRD patterns for converted C pellets obtained after 20h holding at 1500°C.

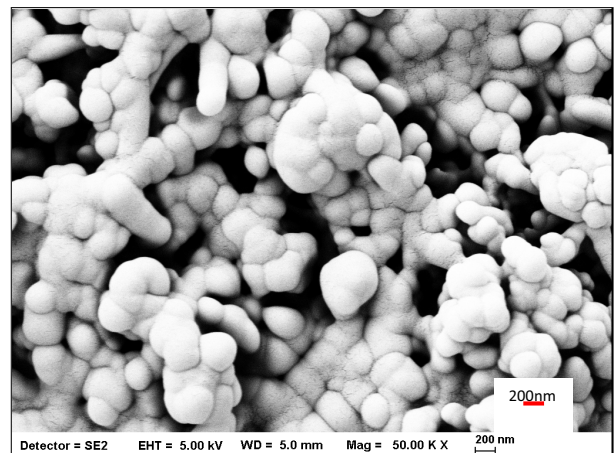


Fig.3: FE-SEM micrographs of SiC powder synthesized by reaction-conversion method.

of alpha-SiC (2H-SiC, H stands for hexagonal) and β-SiC (3C-SiC, C stands for cubic). More than 85% yield was observed for a reaction duration of 10 h. The flow rate of the carrier gas directly influenced the formation of SiC polytype. The amount of 2H-SiC in the end product was more (>10%) when the reaction was carried out at a higher flow rate of Ar gas. In the Fig.2, an X-ray diffractogram of SiC obtained after 20 hours of reaction at higher Ar gas flow rate has been shown. XRD result reveals the presence of 3C-SiC as a major phase along with a small fraction of 2H-SiC. Our observation is contradictory to the result reported by Frolova *et al*[15], who claimed formation of a mixture of 3C and 6H SiC as the gas-solid reaction product. Most importantly, the reported amount of 6H in the reaction product was significant (>30%)[15]. In the present investigation, the characteristic reflection for 6H was absent both in the X-ray diffractogram and Raman spectroscopy data. Surprisingly, the characteristic XRD peak of 6H-SiC was absent

in the x-ray diffractogram reported in the work by Frolova *et al*[15]. We have further confirmed the presence of 2H-SiC in the reaction product from the Raman study (result was not included here).

The micrographic feature shown in Fig.3 reveals the formation of very fine powder (individual particle in size range of 50-250 nm). Particles were present both as a single entity as well as in agglomerated form. Broadened nature of 2H-SiC peak corroborates this finding. The size of the agglomerate was found to be ~ 500 nm. Most interestingly, the synthesised powder mimicked the shape and size of the starting carbon powder. Particle size distribution of the ground powder (result was not included here) showed a narrow size distribution and the average size was ~ 300 nm (particle size distribution by laser scattering method measure agglomerate size).

Reel to reel synthesis of composite SiC fibre (core-

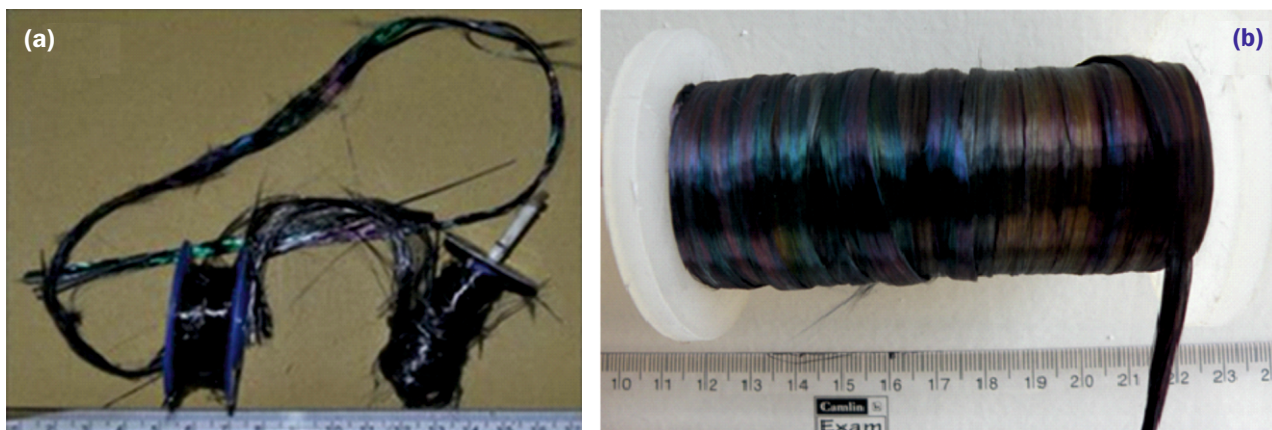


Fig.4: Reel to reel produced SiC fibre. (a) almost fully converted SiC fibre (5 m length), (b) SiC coated carbon fibre (>20 m length).

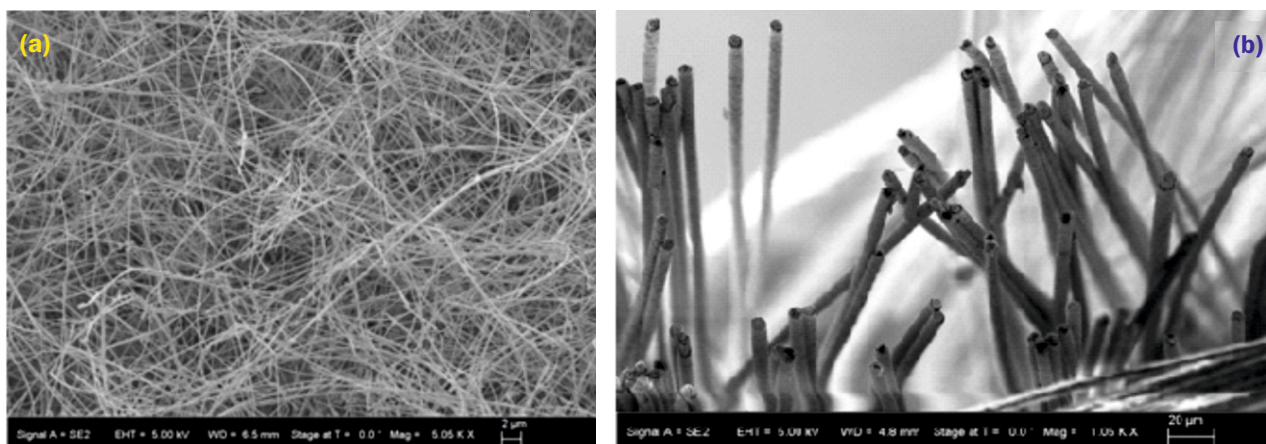


Fig.5: FE-SEM micrographs of fully converted (a) β -SiC fibre and (b) a mixture of fully and partially converted hollow core SiC fibre consisting of β and 2H-SiC phases. Diameter of the original carbon fibre (~6-7 micrometer) remained same even after conversion.

carbon with SiC periphery) in different length, starting from 5m to 500m was successfully carried out in semi-automatic mode (Fig.4). The fibre, unlike powder had different colour shades-rainbow, green, bluish, purple, and black. Upon observation under SEM, it was found out that the thickness of SiC was almost constant irrespective of different colour obtained. Hence thickness of in situ formed SiC didn't decide the colour of the fibre. The phase composition in the fibre was uniform. Hence, polytype of SiC was not the deciding factor. Most probably, the thin SiO₂ layer formed on the outer surface of the fibre was responsible for providing different colour shades [6]. This is to be noted that when the experiment was carried out in static mode, the fibre had shown usual SiC colour (greyish). Like powder, the major phase present in the fibre was β -SiC. The x-ray diffractogram also confirmed the presence of hexagonal polytype of SiC in the fibre. In addition, by optimising reaction temperature and duration of reaction along with gas flow rate, fully converted SiC fibre was made. However, fully converted fibre was more brittle than partially converted fibre (as observed). Fibre synthesis was also carried out in batch. In this, fully converted chopped fibre was produced. Micrographs of different types of SiC fibre produced in-house are shown in Fig.5. Depending on the reaction temperature and gas flow rate, the morphology of the fibre varied. Fig. 5(a) shows the formation of almost fully converted β -SiC fibre when gas flow rate was slow (amount of unreacted carbon at the core was negligible). Whereas a mixture of 2H and 3C-SiC was obtained when the gas flow rate was relatively faster. In the second case (5(b)), the resultant fibre had a hollow core. SiO reacting with

carbon formed the SiC at the surface of the C-fibre. At the latter stage, C diffused out through the barrier layer to react with the SiO to form SiC. This caused formation of hollow core. The 2D woven-mat of C has also been successfully converted to SiC coated 2D C-mat by this method. This mat was used to prepare SiC-SiC composite.

Conclusions

Reaction conversion is useful in converting carbon to SiC. This method was successfully applied to synthesize ultrafine SiC powder from C-black. Morphology, i.e. size and shape of the starting powder was retained in the final product. Yield of the process was more than 80%. Reaction conversion can be used either as a batch process or in continuous mode. Batch mode has the potential to fully convert carbon fibre into SiC. In continuous mode, nearly 500m long SiC coated C fibre, where the average thickness of the SiC was ~ 250 nm was prepared successfully.

References

- [1] M. Pierre, Surf. Sci. Reports, 2022, 48, 1–51.
- [2] B. Riccardi, L. Giancarli, A. Hasegawa, Y. Katoh, A. Kohyama, R.H. Jones and L.L. Snead, Journal of Nuclear Materials, 2004, 329-33, 56-65.
- [3] R.J. Price, Journal of Nuclear Materials, 1969, 33, 17-22.
- [4] Website: <https://www.iaea.org/OurWork/ST/NE/NEFW/TechnicalAreas/NFC/documents/TWGFPT/2015/Presentations/%2>

812%29ATF update and TM.pdf

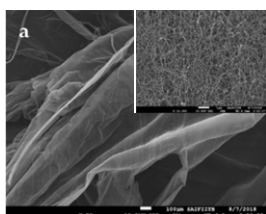
- [5] Z. Ryu, J. Zheng, M. Wang and B. Zhang, Carbon, 2002, 40 (5), 715-720.
- [6] K.M. McHugh, J.E. Garnier and G.W. Griffith, Proceedings of the ASME 2011 Small Modular Reactor Symposium SMR2011, 2011, September 28-30, Washington D.C., USA P-1-5.
- [7] H. He, F. Yang, Y. Ge, L. Ran, K. Peng and M. Yi, Mater. Res. Express, 2019, 6, 085603.
- [8] M. J. Ledoux, S. Hantzer, C. P. Huu, J. Guille and M. P. Desaneaux, J. Catal., 1988, 114 176.
- [9] K. Okada, H. Kato and K. Nakajima, J. Am. Ceram. Soc., 1994, 77, 1691.
- [10] E. Vogli, J. Mukerji, C. Hoffman, R. Kladny, H. Sieber, and P. Greil, J. Am. Ceram. Soc., 2001, 84, 1236.
- [11] Y. Morisada and Y. Miyamoto, Mater. Sci. Engg. A, 2004, 381, 57.
- [12] I.H. Kim, W. Lee, C.W. Lee, S.H. Koand J.M. Jang, Surf. Interface Anal., 2010, 42, 743-747.
- [13] L.A. Tkachenko, A.Y. Shaulov and A.A. Berlin, Inorg. Mater., 2012, 48, 213-221.
- [14] X. Yang, L. Ying and C. Feng, Compos. B Eng., 2015, 79, 204-208.
- [15] M.G. Frolova, D.D. Titov, A.S. Lysenkov, K.S. Kravchuk, E.I. Istomina, P.V. Istomin, K.A. Kim and Y. F. Kargin, Ceramic International, 2020, 46, 18101-05.

Novel Avenue for Bio-sensing

Carbon Nanotube Aerogel: Synthesis and Applications

Kinshuk Dasgupta*, Rajath Alexander, Amit Kaushal, P. T. Rao, S. A. Thakur, Jyoti Prakash

Glass and Advanced Materials Division, Bhabha Atomic Research Centre, Mumbai 400085, INDIA



SEM image of Carbon nanotube wool. Inset a large network of isotropically oriented nanotubes

ABSTRACT

Translating the nano-scale properties of individual carbon nanotube (CNT) into a macro-scale is of immense importance for practical utilization of its exotic properties and has been a technological challenge since its discovery. However, carbon nanotube aerogel (CNT aerogel), a self-standing structure of 3-D network of long CNTs, produced by floating catalyst chemical vapour deposition (FC-CVD), could give some hope of retaining large amount of exotic properties of CNTs in macro-scale. In this article our efforts towards synthesis of CNT aerogel have been described. The CNT aerogel has been characterized in detail and further utilized as flexible capacitors, filters for virus and bacteria and in bio-sensing.

KEYWORDS: Carbon nanotube, Chemical vapour deposition, Microstructure, Sensor

Introduction

Carbon nanotube (CNT) has been one of the highly researched materials amongst the carbon allotropes due to its extraordinary strength (>10 GPa), elastic modulus (~1 TPa), electrical conductivity (equivalent to copper) and thermal conductivity (equivalent to diamond). Despite its promising properties, the impact of this material has been limited when it comes to practical mainstream applications. This issue is mainly attributed to the loss of its outstanding properties when scaled-up to macro dimensions. For many years the properties of the CNT were confined to its nano dimension. The initial attempt to scale-up carbon nanotubes into a macro-structure was realized by Bando *et al.*[2], who made CNT film/ sheets by filtration technique producing Bucky-paper. Even though Bucky-paper was self-standing, a significant loss in properties was witnessed by the researchers[3,4]. Another macrostructure of CNT has become attractive amongst the researchers, named, carbon nanotube aerogel (CNT aerogel)[5]. CNT aerogel is a self-assembled 3D structure of long CNTs that was first envisaged by Li *et al.*[6] using floating catalyst chemical vapor deposition (FC-CVD) from which CNT fiber was drawn by direct spinning. This method was able to retain some of the significant properties of CNTs at macro-scale. CNT fiber produced from CNT aerogel spinning was able to get a strength of 5 GPa and electrical conductivity of 5.6 S/cm² [7].

This promising capability of transfer of properties of the CNT into the macro-scale has put it back in the spotlight for practical applications. Some of the established applications of CNT aerogel synthesized through FC-CVD are structural composites, electromagnetic shielding, water purification, ballistics, etc [7,8]. Even though several researchers are working on the production of CNT aerogel

through FC-CVD, till now the process mechanism is not very well understood. In this article, the synthesis and applications of CNT aerogel by our group have been discussed.

Synthesis of CNT Aerogel

The synthesis of CNT aerogel was carried out in a horizontal tubular resistance furnace developed in-house (schematic is given in Fig.1). Ethanol (purity ≥ 99.9%, Hayman Ltd, England) was used as the carbon source, ferrocene (purity ≥ 99%, Sigma Aldrich) was used as the catalyst and thiophene (purity ≥ 99%, Sigma Aldrich) was used as the promoter. Hydrogen and argon gases (purity > 99.9%, Six Sigma Gases India Pvt.Ltd) were used as the carrier gases and they provided an inert atmosphere.

Liquid feed (ferrocene and thiophene mixed in ethanol) was pumped to the preheater zone maintained at 200 °C and was allowed to be carried in the main furnace with a carrier flow (mixture of argon and hydrogen) of 1-3 lpm. Reaction took place in the main furnace maintained at a high temperature (1100-1300 °C). CNT aerogel was produced through catalytic cracking of carbon precursor in presence of catalyst. CNT produced in the form of spinnable sock along with other gaseous product was continuously drawn in a harvest box. Snapshot during CNT aerogel formation inside the furnace is shown in Fig.2a. Depending on the requirement, the product

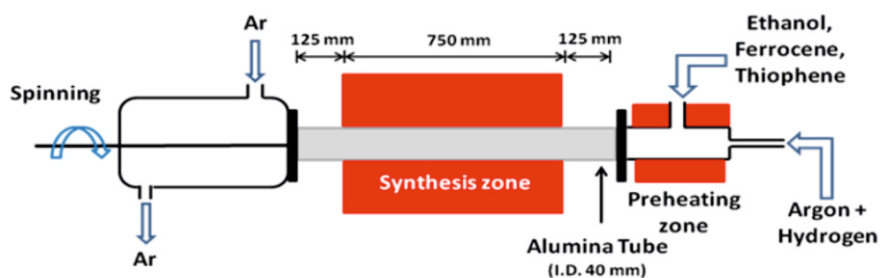


Fig.1: Schematic of the experimental setup for synthesis of CNT aerogel.

*Author for Correspondence: Kinshuk Dasgupta
E-mail: kdg@barc.gov.in

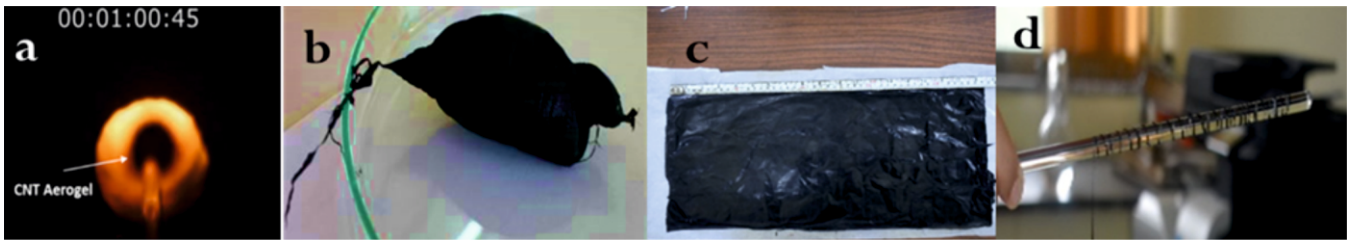


Fig.2: (a) Snapshot of CNT aerogel formation (b) CNT wool (c) CNT sheet (d) CNT fibre.

could be further collected in the form of wool (Fig.2b), sheet (Fig.2c) or fibre (Fig.2d) by varying the process parameters.

Computational Fluid Dynamics

The computational of fluid dynamics (CFD) was carried out using COMSOL Multiphysics software. Weakly compressive fluid flow condition coupled with heat transfer was utilized for determining the flow behavior. Theoretically calculated Reynolds number as per given flow conditions is in the range of 10-30. Hence, a 3-D, steady-state, non-isothermal laminar flow model was used for study. The governing equations utilized in the computation are given in Eqs. (1-4):

$$-\frac{d\rho}{dt} + \nabla \cdot (\rho u) = 0 \tag{1}$$

$$\rho \frac{du}{dt} + \rho u \cdot \nabla u = -\nabla \cdot p + \nabla \cdot (u(\nabla u + (\nabla u)^T) - \frac{2}{3} \mu (\nabla \cdot u) I) + \rho g \tag{2}$$

$$\rho C_p u \cdot \nabla T + \nabla \cdot q_h = Q_h \tag{3}$$

$$q_h = -k \nabla T \tag{4}$$

Where,

ρ =Density (kg/m³), μ =Dynamic viscosity (Pa·s), u =Velocity vector (m/s), p =Pressure (Pa), g =Gravitation acceleration (m²/s), C_p =Specific heat capacity at constant pressure (J/ (kg·K)), T =Absolute temperature (K), q_h =Heat flux vector (W/m²), k =thermal conductivity (W/(m·K)) Q_h =heat sources (W/m³).

The reactor was operated at atmospheric pressure condition and at elevated temperature for which the constant wall temperature was used as the boundary condition for heat transfer. The open boundary condition was used at the end of the harvest box (outlet to the computation domain). The boundary conditions at the inlet (flow and temperature) are specified in the previous section (synthesis of CNT aerogel).

Discretization was carried out using physics controlled meshing option available in COMSOL Multiphysics where 1056648 domain elements, 57574 boundary elements, and 2238 edge elements were used for the entire domain (reactor tube and harvest box). Selection of meshing was decided by grid independence test performed over wide range of meshing conditions.

The CFD model in this work has been used to predict the flow field inside the reactor. Fig.3 shows the velocity profile of the gas phase as predicted by the CFD simulation. It can be observed that the aerogel formation takes place at the upper half of the furnace tube. This is due to the backflow of the gas from the harvest box into the furnace tube through the bottom half of the furnace tube. The backflow occurs as a result of the low carrier flow rate utilized to maintain laminar flow to prevent flow instability. The rotation of the collection rod ensured that the collected CNT aerogel was symmetrical in shape and the collection was continuous. Detailed CFD analysis can be found in another BARC newsletter article[9].

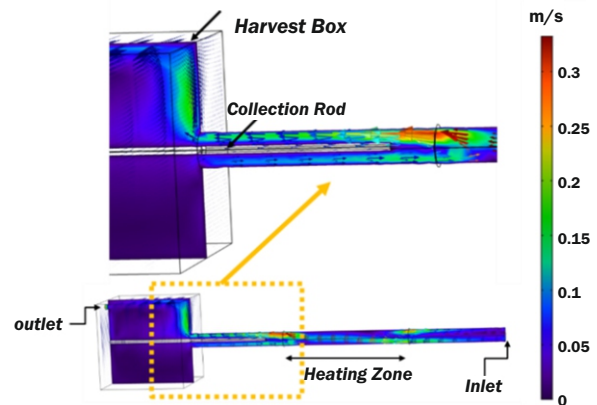


Fig.3: Velocity profile of the gas phase predicted by CFD.

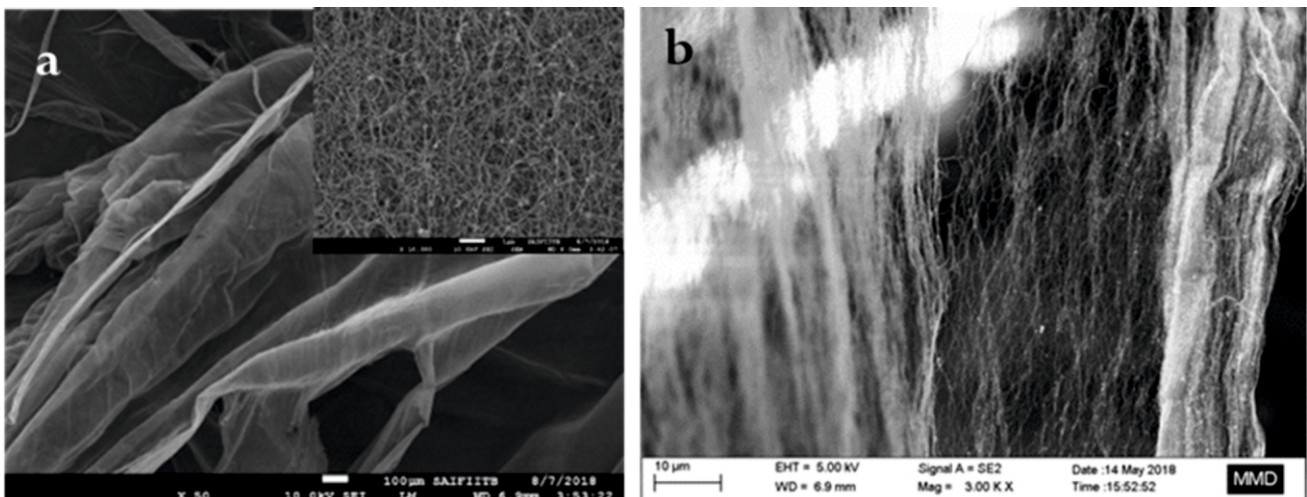


Fig.4: SEM images of (a) CNT wool and (b) CNT sheet.

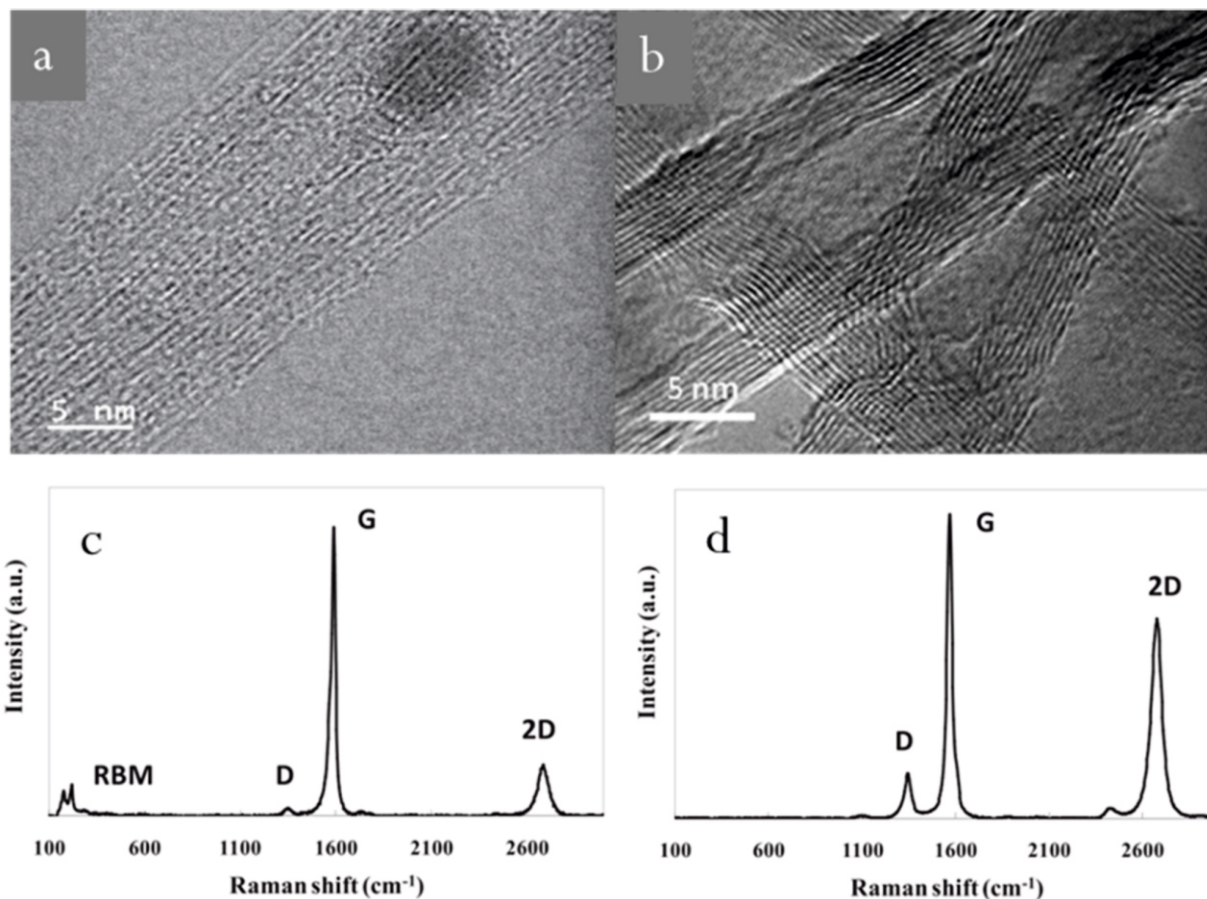


Fig.5: (a) TEM image of SWCNT bundles (b) TEM image of MWCNT (c) Raman spectrum of SWCNT (d) Raman spectra of MWCNT.

Microstructural Characterization

Typical scanning electron micrograph (SEM) of a CNT wool is shown in Fig.4(a). The inset image depicts a large network of isotropically oriented CNTs. However, in the CNT sheet the CNTs are relatively aligned, as shown in Fig.4(b).

Depending on the processing conditions the CNTs may be either single-walled (Fig.5a) or multi-walled (Fig.5b), which can be understood from the transmission electron micrographs (TEM). It can also be understood from the Raman spectra[10]. Single-walled CNT produces RBM peak along with sharp G peak, prominent 2D peak and negligible D peak (Fig.5c). The RBM peak is missing and the D peak is prominent in the case of multi-walled CNT (Fig.5d).

Application as a Flexible Capacitor

CNT aerogel derived films were cut into circular shapes (diameter =2.5 cm). Copper strips were connected to the CNT

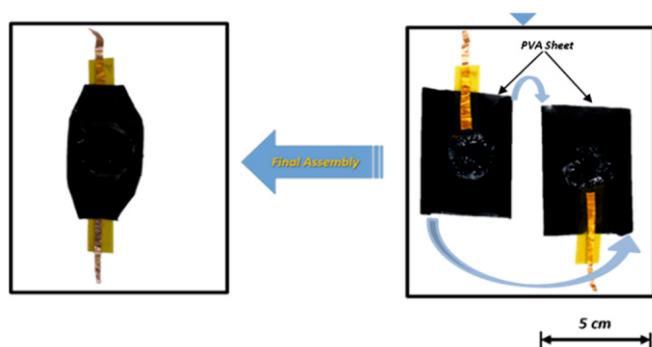


Fig.6: Preparation of a flexible capacitor.

films using silver paste. The copper strips were insulated using polyimide and epoxy layer. The solid-state electrolyte was prepared from polyvinyl alcohol (PVA: Sigma Aldrich) and KOH. Both the electrodes were covered with PVC sheets from backside. The two CNT aerogel circular films were placed over each other in such a way that a symmetrical capacitor was formed. The gist is given in Fig.6.

The effect of bending on the flexible capacitor is shown in Fig.7. Very low (less than 1%) change in capacitance was observed even after a full 180° bend.

Application as a Filter against Virus

Filters have been prepared from the CNT wool (Fig.8a) for trapping nanoparticles, virus and bacteria. The average pore-size of the CNT-wool is below 100 nm. The efficacy of CNT-wool based filter was tested against bacteriophage P1, which is a virus that infects bacteria. The phage P1 has a large icosahedral head of approximately 55–85 nm diameter attached to a characteristic long tail of 200–300nm. CNT wool filters were autoclaved (121°C and 15 Psi, 15 min) for sterilization and then used for checking filtration efficiency for P1 phage using the millipore filter assembly using standard procedure. The CNT wool filter could trap the bacteriophage with an efficiency comparable to a commercial N95 mask. The image of the trapped virus in the filter is shown in Fig.8b.

Application in Bio-sensing

An ultrasensitive label-free biosensor has been prepared from CNT aerogel, which is capable of detecting DNA hybridization very rapidly[11]. The multi-directional CNT embedding into the CNT aerogel electrode demonstrated linear ohmic and near isotropic electrical properties, therefore

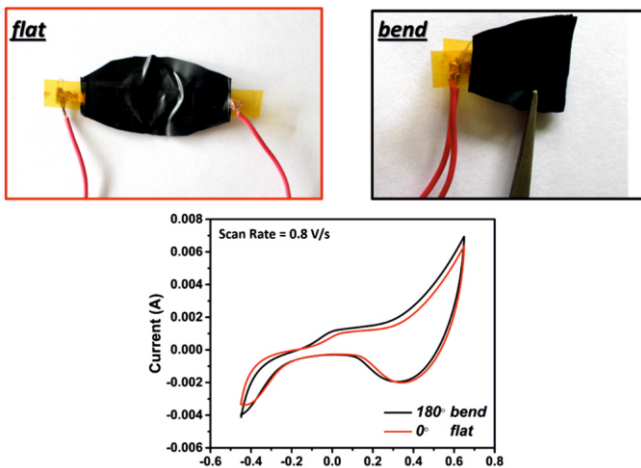


Fig.7: Variation of CV with bending of the flexible capacitor at a scan rate of 0.8 V/s.

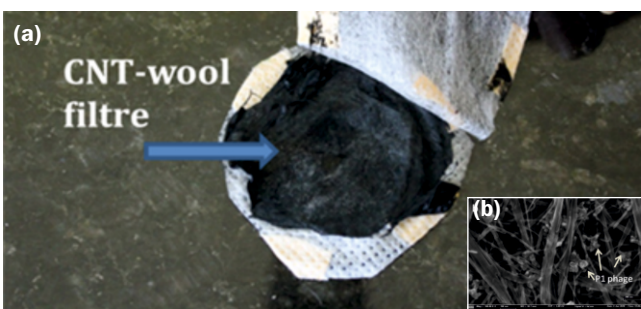


Fig.8: (a) Filter made from CNT wool (b) SEM image (inset) showing the P1 phage trapped in the filter.

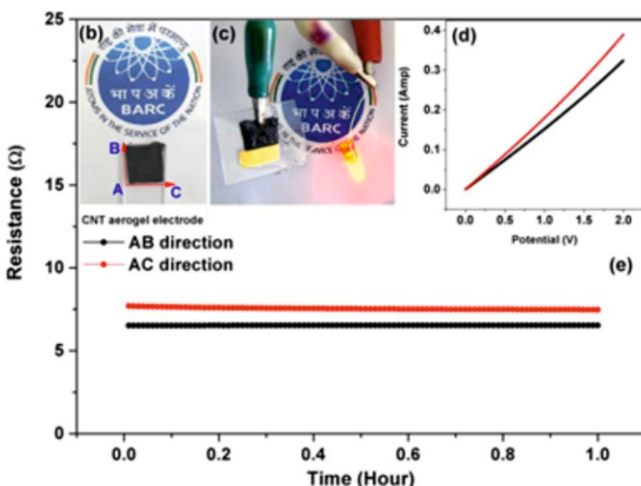
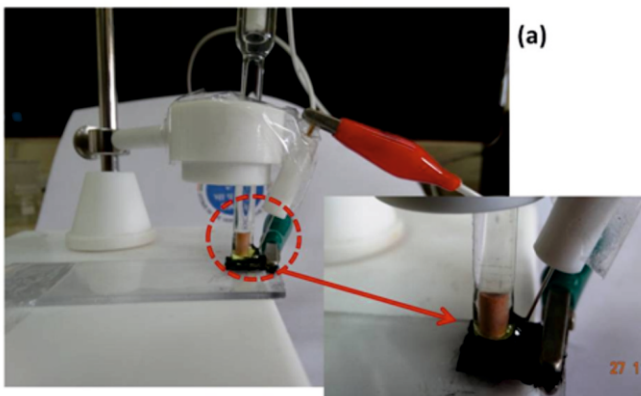


Fig.9: (a) Electrochemical impedance system for bio sensing and (b) CNT aerogel electrode (c) conductivity test (d) IV curve (e) chronoamperometry test of CNT aerogel electrode.

providing ultra-high sensitivity and specificity toward bio molecules (Fig.9(a-e)).

Using this device, the target DNA hybridization was detected by a quantifiable change in the electrochemical impedance, with a distinct response to the single-stranded probe alone or double-stranded target-probe complex. The target DNA was specifically detected with limit of detection (LoD) of 1 pM with a turnaround time of less than 20 minute (Fig.10(a-c)). Moreover, this system is able to differentiate between the closely related target sequences by the distinct impedance response rendering it highly specific. The detection mechanism of CNT aerogel electrode works on the principle of π - π interactions between negatively charged single stranded DNA and CNT.

Fig.10(a) The detailed sequence of the probe and target DNA oligonucleotides; Agarose gel electrophoresis showing the fluorescent bands corresponding to the perfect match (PM)-dsDNA and mismatch (MM)-dsDNA and Nyquist plot of all bio-samples in (b) hybridization buffer (c) stringent hybridization buffer (with 8% formamide). This is the first study in the literature, where fabricated standalone bare CNT electrode without any substrate support, coupled with electrochemical impedance spectroscopy, has been used for the detection of DNA hybridization. Altogether, the results show that our system is fast, sensitive and specific for label free rapid direct DNA detection, promising a novel avenue for bio-sensing.

Conclusion

CNT aerogel is an exotic material where long CNTs are self-assembled to form a self-standing 3-D structure. This material has been produced by FC-CVD process and shaped into wool, sheet and fibre forms. The flow and the temperature profiles of the reactor have been simulated using COMSOL Multiphysics. The CNT aerogel has been characterized by electron microscopy and Raman spectroscopy. The aerogels have been used to make (1) flexible energy storage devices, (2) filters for trapping viruses and (3) bio-sensors with low LoD and rapid detection time. This wide range of applications is possible by tuning the structures and the properties of the CNTs in the aerogel.

References

- [1] K. Dasgupta, J. B. Joshi and S. Banerjee., Fluidized bed synthesis of carbon nanotubes - A review, Chemical Engineering Journal, 2011, 171, 841-869.
- [2] S. Bandow, A.M. Rao, K.A. Williams, A. Thess, R.E. Smalley, P.C. Eklund, Purification of Single-Wall Carbon Nanotubes by Microfiltration, The Journal of Physical Chemistry B, 1997, 101, 8839-8842.
- [3] J.Y. Oh, S.J. Yang, J.Y. Park, T. Kim, K. Lee, Y.S. Kim, H.N. Han, C.R. Park, Easy Preparation of Self-Assembled High-Density Buckypaper with Enhanced Mechanical Properties, Nano Letters, 2015, 15, 190-197.
- [4] Z. Li, J. Xu, J.P. O'Byrne, L. Chen, K. Wang, M.A. Morris, J.D. Holmes, Freestanding bucky paper with high strength from multi-wall carbon nanotubes, Materials Chemistry and Physics, 2012, 135, 921-927.
- [5] M.D. Yadav, K. Dasgupta, Kinetics of Carbon Nanotube Aerogel Synthesis using Floating Catalyst Chemical Vapor Deposition, Industrial and Engineering Chemistry Research, 2021, 60, 2187-2196.
- [6] Y.-L. Li, I.A. Kinloch, A.H. Windle, Direct Spinning of Carbon Nanotube Fibers from Chemical Vapor Deposition Synthesis, Science, 2004, 304, 276.

- [7] F. Smail, A. Boies, A. Windle, Direct spinning of CNT fibres: Past, present and future scale up, *Carbon*, 2019, 152, 218-232.
- [8] M.D. Yadav, K. Dasgupta, A.W. Patwardhan, J.B. Joshi, High Performance Fibers from Carbon Nanotubes: Synthesis, Characterization, and Applications in Composites—A Review, *Industrial & Engineering Chemistry Research*, 2017, 56, 12407-12437.
- [9] A. Kaushal, R. Alexander, P.T. Rao, J. Prakash, K. Dasgupta, Computational Fluid Dynamics Study for Synthesis of Carbon Nanotube Aerogel by Chemical Vapour Deposition, Nov-Dec., 2021, *BARC Newsletter*, 379, 22-28.
- [10] R. Alexander, J. Prakash, A. Kaushal, K. Dasgupta, Confocal Raman Spectroscopy of Carbon Nanomaterials, *Physics News*, 2020, 50(4), 28-31.
- [11] J. Prakash, A. Dey, S. Uppal, R. Alexander, A. Kaushal, H.S. Misra, K. Dasgupta, Label-free rapid electrochemical detection of DNA hybridization using ultrasensitive standalone CNT aerogel biosensor, *Biosensors and Bioelectronics*, 2021, 191, 113480.

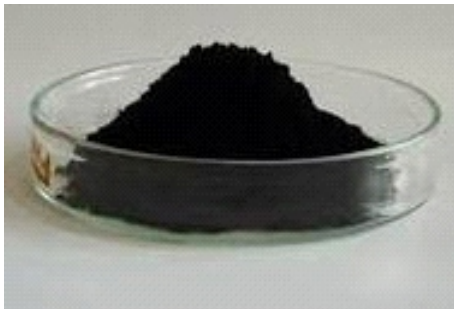
Minimizing Carbon Footprint

Nanocomposite of Cement and Graphene Oxide: Impact on Strength Properties and Carbon Footprint

P. T. Rao¹, Jyoti Prakash¹, M. J. Shinde², Rajath Alexander¹, S. A. Thakur¹, Kinshuk Dasgupta^{1*}

¹Glass and Advanced Material Division, Bhabha Atomic Research Centre, Mumbai 400085, INDIA

²Civil Engineering Division, Bhabha Atomic Research Centre, Mumbai 400085, INDIA



Graphene oxide used in preparation
M30 concrete

ABSTRACT

In the present now, need for the high performance of cement-based materials and the call for energy conservation and environmental protection has attracted immense scientific attention. Graphene oxide based nanomaterial is promising candidate by virtue of large specific surface area, excellent physical properties. This paper explores the key role played by graphene oxide (GO) in the cement concrete at different concentrations of 0.025, 0.05, 0.075 weight% GO of cement respectively. Compressive strength results have proved, a small quantity of GO is good enough to obtain substantial increase in strength properties of concrete. The usage of tiny quantity of GO offers a silver lining to reduce the carbon foot print associated with cement consumption. Graphene oxide based nanocomposite cement has potentially important role to play to achieve India's ambitious target to reach net-zero emissions by 2070 declared at COP 26 (26th UN Climate Change Conference of the Parties (COP26) at Glasgow, United Kingdom.

KEYWORDS: Graphene Oxide (GO), Carbon nanotube (CNT), Cement hydration, Cement hydration products

Introduction

Cement is an extensively used construction material due to the low cost and high compressive strength. The principal hydration products of cement are made up of nanocrystalline regions with the atomic structure resembling tobermorite and/or jennite[1]. This provides an opportunity to apply nano-materials and nano-technology in cement-based materials to modify their structures at the nano-scale and finally improve their macro-scale properties. The large specific surface area of the nano-materials can provide nucleation sites for hydration products. Moreover, the nano-materials can occupy the pores within cement matrix to provide a dense microstructure. Out of different options, carbon based nano-materials have gained importance to be incorporated in cement matrix due to their low density, high strength and high corrosion resistance. Carbon nanotube (CNT), a one-dimensional tubular structure with high aspect ratio, has unique crack-bridging effect to slowdown the crack propagation within cement composites[2]. Graphene oxide (GO) is a derivative of graphene[3], which can be viewed as a layer of graphene with grafted oxygen functional groups. The active functional groups promote chemical or physical interactions with cement, which can improve the interfacial bonding with the host materials.

Why Graphene Oxide (GO)? Why not Carbon Nanotube (CNT) for Cement Composite?

Many researchers found that the addition of CNTs to cement composite resulted in negligible change in strength or even a reduction in strength of the composite in some cases[4,5]. The explanation is by and large associated to the poor dispersion of CNTs and weak bonding between the CNTs and the cement matrix. Due to strong vander Waal's attractive

forces between particles, CNTs tend to form agglomerates or bundles which may become defect sites in the composites. The lack of interfacial areas between CNTs and the cement matrix reduces CNT's reinforcing efficiency, even though CNTs exhibit excellent mechanical properties. On the other hand GO being functionalized with oxygen, can easily make bonds with cement matrix[6]. The greater exposed surface area of graphene oxide sheets generates more potential sites for advantageous chemical or physical interactions, which in turn improve bonding between graphene sheets and host cement material.

Potential of Graphene Oxide to Reduce Carbon Footprint

Studies have shown on addition of relatively small amounts of graphene oxide enhances the strength of standard concrete; appreciably less cement could be needed to realize corresponding structural performance, therefore, reducing the carbon footprint. The additional strength might also reduce the need for steel reinforcement to enable further reductions in CO₂ emissions. University of Cambridge study indicates that if the addition of graphene oxide results in a 5% reduction of the Portland cement, the effect on global warming could reduce by 21%[7] another study from the University of Exeter, estimated that 125g of graphene oxide can decrease the total volume of cement down to 148kg per cubic metre of concrete (>50 wt% reduction of cement required for the original strength). With reference to environmental perspective, that would translate to total decrease of 446 kg/tonne emissions of CO₂[8].

Graphene oxide addition into construction materials does come with its own implications to the carbon footprint. Product Carbon Footprint (PCF) calculations consider the entire life cycle of the product. This means looking into energy requirements of the raw materials that make up graphene, how it is manufactured, transported, used and disposed of.

*Author for Correspondence: Kinshuk Dasgupta
E-mail: kdg@barc.gov.in

Understanding the PCF of graphene will help manufacturers to understand the impact of their product, and enable process optimisations such that climate neutral products can be offered, and strong carbon reduction targets can be set[9]. In most cases, electricity use is the largest contributor to CO₂ emission-switching to decarbonised energy sources will naturally reduce the carbon footprint of the production methods and any resulting products[10]. For high volume construction applications there will ultimately need to be a trade off between cost of graphene oxide production, quality of graphene oxide and contribution to CO₂.

India’s ambitious target to achieve net-zero emissions, removing as much carbon dioxide from the atmosphere as is produced by 2070 has been declared at COP 26 at Glasgow, United Kingdom[11]. India’s overall cement production accounted for 294.4million tonnes (MT) in FY21 and 329million tonnes (MT) in FY20[12]. Due to the increasing demand in various sectors such as housing, commercial construction and industrial construction, cement industry is expected to reach 550-600 million tonnes per annum (MTPA) by the year 2025[12]. Graphene oxide based concrete has potentially important role to play to achieve COP 26 target.

Synthesis of Graphene Oxide

The synthesis method utilizes highly oxidative ingredients for graphite exfoliation. This route follows a fixed stoichiometry of reactants. The synthesis route is called improved Hummers method[13], a 9:1 mixture of concentrated H₂SO₄ /H₃PO₄ (360:40 ml) is added to a mixture of graphite flakes (3 g). The mixture was stirred continuously with magnetic stirrer. Then KMnO₄ (18 g) is added to acidic slurry, producing a slight exothermic 35–40 °C reaction. The reaction mixture is then heated to 50 °C and stirred for 8 h. The reaction mixture is cooled to room temperature and poured onto ice (~400 ml) with 30% H₂O₂ (5 ml). The slurry is centrifuged (4000 rpm for 4 h), and the supernatant liquid is decanted until decanted water shows neutral pH. The remaining solid material is dried in oven for 12 hours ensuring complete moisture removal. The obtained GO lumps were crushed via mortar pestle and sieved through mesh to obtain as GO fine powder.

Table 1: Design mix concrete (M30) ingredients.

| Ingredients | Quantity (kg) |
|-------------------------|---------------|
| Cement | 25 |
| Coarse aggregate (20mm) | 34.26 |
| Fine aggregate (10mm) | 28 |
| Crushed sand | 45 |
| Admixture | 0.25 |
| Water | 10 |
| Water to Cement ratio | 0.39 |

Table 2: Weight % of GO added to M30 concrete mix.

| Weight % of GO in concrete mix |
|--------------------------------|
| 0.025% of cement |
| 0.05% of cement |
| 0.075% of cement |

Preparation of GO-Concrete

Design mix concrete (M30) was used to prepare GO based concrete by employing ingredients as listed in Table 1. GO was added to concrete mix via ultrasonication through water component of M30 concrete in following percentages as illustrated in Table 2. Fig.1 shows GO-Concrete nanocomposite preparation flowsheet. All the raw materials including fine aggregate (Fig.2a), coarse aggregate (Fig.2b), crushed sand (Fig.2c), and graphene (Fig.2d). These raw materials are homogeneously mixed using motorised concrete mixer as

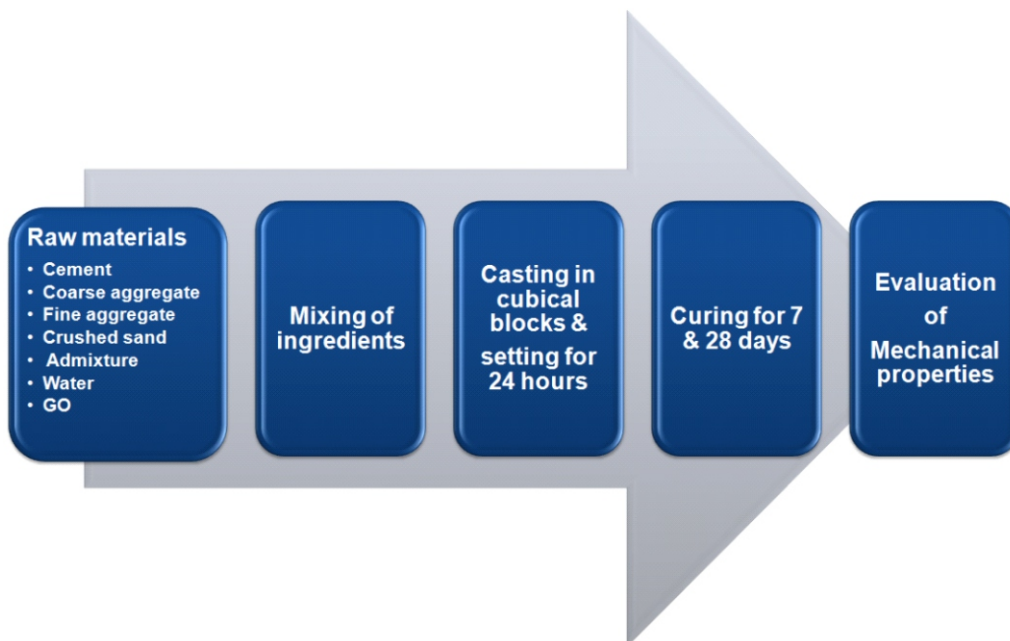


Fig.1: Flow sheet for preparation of GO-Concrete nanocomposite.



Fig.2: a) fine aggregate, b) coarse aggregate, c) crushed sand, and d) Graphene oxide used in preparation M30 concrete.



Fig.3: a) Motorized concrete mixer, b) Concrete moulds, c) Test specimen concrete cubes (15 X 15 X 15cm), d) Compressive strength testing unit.

depicted in Fig.3a. The Fig.3b reveals casting moulds to obtain concrete cubes (Fig.3c.) of size (15 X 15 X 15 cm), these concrete blocks are cured by immersing in water for 7 and 28 days respectively and are eventually used to evaluate the compressive strength using testing unit as shown in Fig.3d.

Results and Discussion

Cement strength is based on reactions between H_2O and the several successive cementitious phases that occur during hydration. Hydration is what causes cement to set and then harden; degree of hardening is function of time and relates to amount of hydration products. Hydration kinetics plays an

important role on the microstructural development and the final properties of hardened cement composites. Cement is a mixture of solid phases that can react with water to produce complex products, including CH, C-S-H gels and ettringite (Aft) as shown in Table 3[14]. The degree of hardening, hydrations kinetics of concrete is indicative of gain in compressive strength. Small amount of GO is making sizable gain in compressive strength properties as illustrated in Fig.4. GO nanosheets act as the nucleation sites for hydration products to speed up cement hydration as portrayed in Fig.5. The highest compressive strength is observed at 0.05 weight% of GO concentration (Fig.4), at 0.025GO concentration the compressive strength is lowered probably due inadequate nucleation sites for cement hydration products, leading to porous microstructure. However, at 0.075GO concentration, agglomeration of GO occurs thereby GO nanosheets are not participating as the nucleation sites for hydration products to speed up cement hydration kinetics.

The surface of GO has many oxygen functional groups main included of -OH, -COOH and -SO₃H as shown in Fig.5. The C₃S, C₂S and C₃A attach with functional groups preferentially and form the enlargement points of the hydration products[15]. The growth points and growth pattern of the hydration products are both controlled by GO, which is called a template effect[15]. Scanning electron microscopy (SEM) analysis further corroborates function of GO in enhancing concrete strength properties. Interconnect between the layers of concrete (Fig.6a) is almost non-existent due to zero GO concentration resulting in lower compressive strength. At 0.025% GO concentration, initiation of inter layer bonding is observed (Fig.6b), at 0.05% GO concentration, enhanced inter layer bonding is observed (Fig.6c) confirming the role of GO nanosheets acting as the nucleation sites promoting the growth of hydration products to increase strength properties. When GO concentration exceeds certain threshold value,

Table 3: Abbreviated cementitious compounds.

| Compound | Abbreviated formula | Actual formula |
|---|---------------------|--|
| Calcium Hydroxide | CH | 2(Ca).OH |
| Calcium Silicate Hydrate | C-S-H | CaO.SiO ₂ .H ₂ O |
| Tri - Calcium Aluminate | C ₃ A | 3CaO.Al ₂ O ₃ |
| Di - Calcium Silicate | C ₂ S | 2CaO.SiO ₂ |
| Tri - Calcium Silicate | C ₃ S | 3CaO.SiO ₂ |
| Calcium Tri Sulfoaluminate hydrate (Ettringite) | AFt | Ca ₆ Al ₂ (SO ₄) ₃ (OH) ₁₂ .26H ₂ O |

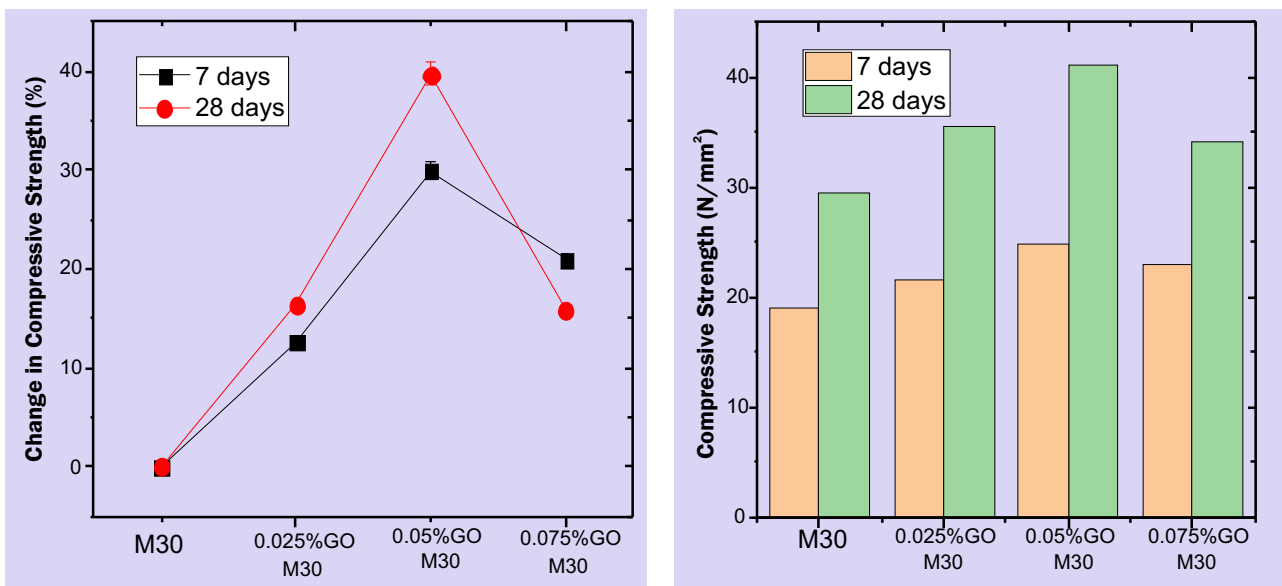
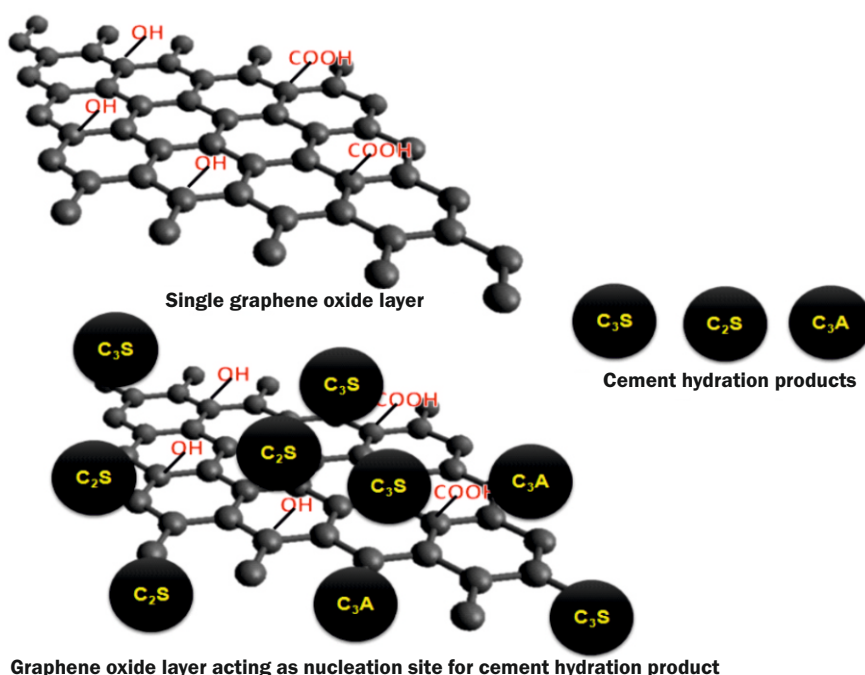


Fig.4: Compressive strength of concrete without GO and GO-Concrete at 0.025, 0.050, and 0.075 weight% GO, respectively.



Graphene oxide layer acting as nucleation site for cement hydration product

Fig.5: Schematic illustrating the role of GO acting as nucleation sites to cement hydration products.

agglomeration of GO occurs favouring random structure as indicated in Fig.6d, hence GO no longer act as seeding sites for cement densification.

Conclusion

The key role played by graphene oxide (GO) in the cement concrete has been investigated at different concentrations of GO. Compressive strength results have improved, a small quantity of GO is good enough to obtain substantial increase in strength properties of concrete. The usage of tiny quantity of GO offers a silver lining to reduce the carbon foot print associated with cement consumption. Graphene oxide based concrete has potentially important role to play to achieve India's ambitious target to reach net-zero emissions by 2070 declared at COP 26 in Glasgow and mitigate environmental concerns.

Acknowledgement

Authors acknowledge Poonam Suradkar and R.B. Fatania for their assistance in synthesis of graphene oxide.

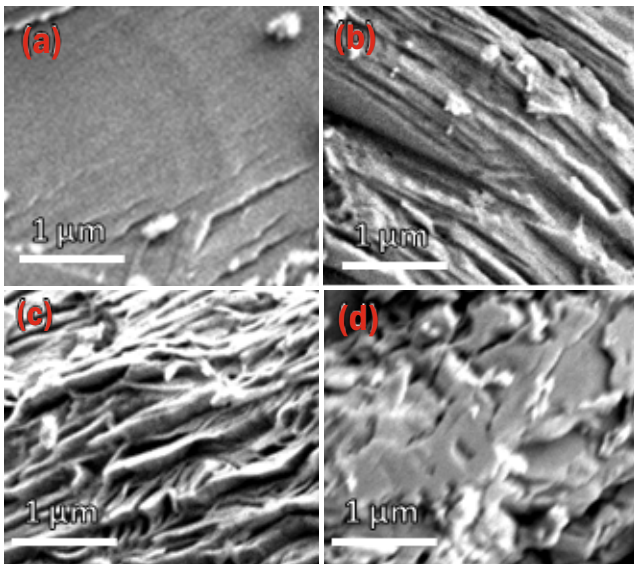


Fig.6: (a) SEM image of plain M30 concrete without GO, (b) GO-Concrete at 0.025 weight% GO, (c) GO-Concrete at 0.05 weight% GO and (d) GO-Concrete at 0.075 weight% GO.

References

- [1] J.E. Rossen, B. Lothenbach, K.L. Scrivener, Composition of C-S-H in pastes with increasing levels of silica fume addition, *Cem. Concr. Res.*, 2015, 75, 14–22.
- [2] S. Parveen, S. Rana, R. Figueiro, M.C. Paiva, Microstructure and mechanical properties of carbon nanotube reinforced cementitious composites developed using a novel dispersion technique, *Cem. Concr. Res.*, 2015, 73, 215–227.
- [3] Y.W. Zhu, S. Murali, W.W. Cai, X.S. Li, J.W. Suk, J.R. Potts, et al., Graphene and graphene oxide: synthesis, properties and applications, *Adv. Mater.*, 2010, 22(46), 3906–3924.
- [4] Cwirzen A. Controlling physical properties of cementitious matrixes by nanomaterials. *Adv Mat Res.*, 2010, 123–125, 639–42.
- [5] Cwirzen A, Habermehl-Cwirzen K, Nasibulin AG, Kaupinen EI, Mudimela PR, Penttala V. SEM/AFM studies of cementitious binder modified by MWCNT and nano-sized Fe needles. *Mater Charact.*, 2009, 60(7), 735–40
- [6] Lambert T.N., Chavez C.A., Hernandez-Sanchez B, Lu P, Bell N.S., Ambrosini A, et al, Synthesis and characterization of titania-graphene nanocomposites, *J Phys Chem., C*, 2009, 113(46), 19812–23.
- [7] I. Papanikolaou, N. Arena, and A. Al-Tabbaa, Graphene Nanoplatelet Reinforced Concrete for Self-Sensing Structures – A Lifecycle Assessment Perspective, *J. Clean. Prod.*, 2019, 240, 118202.
- [8] D. Dimov, I. Amit, O. Gorrie, M. D. Barnes, N. J. Townsend, A. I. S. Neves, F. Withers, S. Russo, and M. F. Craciun, Ultrahigh Performance Nanoengineered Graphene – Concrete Composites for Multifunctional Applications, *Adv. Funct. Mater.*, 2018, 28, 1705183.
- [9] D. Beloin-Saint-Pierre and R. Hischer, Towards a More Environmentally Sustainable Production of Graphene-Based Materials, *Int. J. Life Cycle Assess.*, 2021, 26, 327.
- [10] How to Make Graphene Greener. <https://graphene-flagship.eu/graphene/news/how-to-make-graphenegreener/>
- [11] Leading the climate charge: India sets hard targets at COP26. <https://www.business-standard.com › ... › News>
- [12] Indian Cement Industry Analysis of IBEF. <https://www.ibef.org>
- [13] Daniela C. Marcano, Dmitry V. Kosynkin, Jacob M. Berlin, Alexander Sinitskii, Zhengzong Sun, Alexander Slesarev, Lawrence B. Alemany, Wei Lu, and James M. Tour* Improved Synthesis of Graphene Oxide, *ACS Nano* 2010, 4(8), 4806–4814.
- [14] Zhu Pan, Li He, Ling Qiu, Asghar Habibnejad Korayem, Gang Li, Jun Wu Zhu, Frank Collins, Dan Li, Wen Hui Duan, Ming Chien Wang, Mechanical properties and microstructure of a graphene oxide–cement composite, *Cement & Concrete Composites*, 2015, 58, 140–147.
- [15] Shenghua Lv, Yujuan Ma, Chaochao Qiu, Ting Sun, Jingjing Liu, Qingfang Zhou, Effect of graphene oxide nanosheets on microstructure and mechanical properties of cement composites, *Construction and Building Materials*, 2013, 49, 121–127.

This page is intentionally left blank

Radiation chemical studies of Ionic Liquids & Deep Eutectic Solvents

■ Synthesis of IV-VI Semiconductor Nanomaterials

Dr. Laboni Das

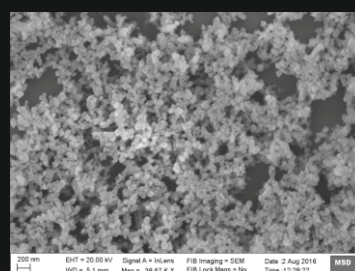
The Deep Eutectic Solvents (DESs) and Room Temperature Ionic Liquids (RTILs) are amongst the emerging exotic solvents being considered as potential alternatives to the conventional hazardous volatile organic solvents (VOCs).

In true spirit of “energy and environment sustainability” the aim of this thesis has been to explore how much and to what extent these solvents can act as a potential replacement of VOCs for utility in the back end cycle of nuclear energy program (reprocessing and waste management) as well as in other energy related applications wherein these solvents are susceptible to strong oxidizing or reducing conditions. DESs and RTILs can be better suited for such applications only under the condition that their radiation stability is understood properly. However, high cost of production and purification limits overall acceptance and applications of RTILs to a certain extent, which led to the emergence of DESs, which are relatively cost-effective, non-toxic, biodegradable with facile waste-free synthesis procedure requiring no post-synthetic purification in contrast to the RTILs.

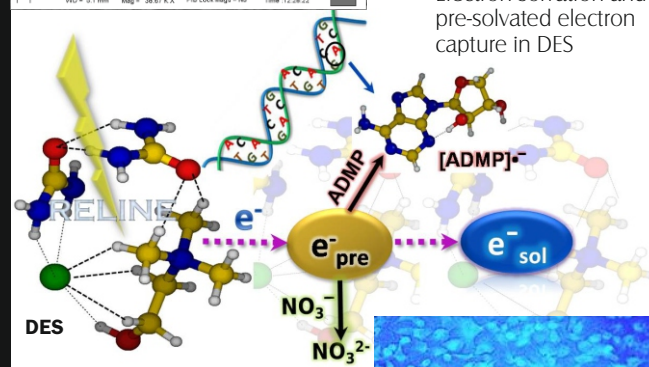
Some of the primary questions that the thesis addresses convincingly are; what are the transient species that would be generated within these two new solvents upon exposure to ionizing radiation? How and to what extent these transient species would affect the performance of these solvents? Is it possible to predict a radiation and chemically stable DES by computational methods for use in radiation related applications? How effectively these solvents can be used as host matrix and stabilizing medium for the synthesis of nanomaterials by radiation assisted technology?

The doctoral thesis has identified and characterized the new transient species; dicyanamide dimer radical anion $(DCA)_2^{\cdot-}$ within ionic liquid $Pyrr_{13} DCA$, which remains stable in the medium for hundreds of microseconds and is strongly oxidizing in nature. The results obtained in this particular work conclusively indicate that the case of $Pyrr_{13} DCA$ is unique; as in this medium both the solvated electrons (strongly reducing) and the long-lived oxidizing species $(DCA)_2^{\cdot-}$ are produced simultaneously and both can mediate the radiation chemistry in this medium, which warrants special attention in its energy related applications. The primary reducing species, i.e. the pre-solvated electron was observed for the first time in DESs in nanosecond timescale; and could be efficiently captured using DNA base adenosine. These results are important considering the research related to reductive DNA damage.

Additionally, a new redox and radiation stable DES composed of 1:2 molar ratio of choline acetate and malonic acid has been comprehended through computational and experimental techniques. Application of a particular solvent in the emerging field of semiconductor nanomaterials synthesis makes it versatile. In this context, both RTIL and DES have been successfully utilized as stabilizing media in nanomaterial synthesis with defined morphology and properties. For nanomaterial synthesis, novelty of radiation chemical method over other contemporary techniques has been highlighted. Photo luminescent tin oxide nanoparticles could be synthesized via radiation chemical technique in the DES reline,

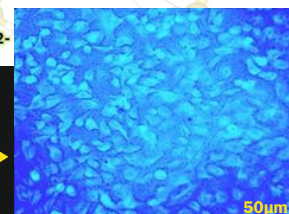


FESEM images of mesoporous SnSe nanoparticles synthesized via e-beam irradiation in $[EMIM][EtSO_4]$



Electron solvation and pre-solvated electron capture in DES

Human lung epithelial carcinoma (A549) cells treated with photoluminescent SnO_2 NPs showed bright blue fluorescence upon excitation using UV filter



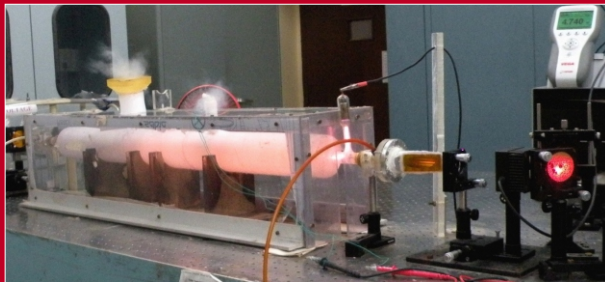
which were found to be non-toxic with suitable application in cell imaging. Further, in the RTIL $[EMIM][EtSO_4]$, mesoporous SnSe with high porosity could be synthesized via electron beam irradiation, shows potential applications in sensing, catalysis and photovoltaics.

(The Ph.D. dissertation was supervised by Dr. Soumyakanti Adhikari, Head, Scientific Information Resource Division, BARC)



Dr. Laboni Das, Scientific Officer/E in Radiation and Photochemistry Division of BARC, works in the field of Radiation Chemistry and Nanomaterials. Her research interests include radiation chemical studies of exotic solvents (e.g. deep eutectic solvents, room temperature ionic liquids) and their application in radiation assisted synthesis of semiconductor nanomaterials. She has 10 publications in peer reviewed reputed international journals and 15 conference papers. Dr. Das is a recipient of Homi Bhabha Gold medal from OCS 56th batch (Chemistry discipline).

Experimental setup of the CO laser system



CO laser emission spectra in 5 μm region from the gas discharge for 90% output couplers



A Novel CO Laser

Lasing action in 5 μm region occurring from CO molecules formed inherently in a CO₂-N₂-He gas discharge lead to applications in spectroscopy & material processing

M.B. Sai Prasad, Tatsat Dwivedi,
Ayan Ghosh, J Padma Nilaya*

CO₂ laser is the most powerful coherent source providing discretely tunable emission over the 9-11 μm region of the electromagnetic spectrum. Discovered in 1964, it is one of the most well researched lasers and has found its way into countless research papers published worldwide[1]. The laser dynamics is therefore well understood and active research is now confined to its applications in various disciplines. However, one aspect of CO₂ laser that has hitherto remained experimentally unexplored is its emission spectrum when the gain cell is subjected to LN₂ cooled conditions (77 K), understandably, owing to the freezing of the CO₂ gas at such low temperatures. We have reported for the first time[2], the operation of a free running CW-CO₂ laser when its gain cell is subjected to LN₂ temperature. Of particular interest is the observation of rich multi-line emission spectrum spanning over 4.95 μm to 5.49 μm. These findings are very significant, as they establish, for the first time, the laser emission in 5 μm region originating from CO molecules that are formed inherently in CO₂ laser discharge (comprising CO₂-N₂-He) due to electron impact dissociation. This has rendered the utilization of highly toxic extraneous CO gas source for obtaining lasing in the 5 μm region redundant. In another study, the laser was characterized to know the constituents of the gain medium, in particular, the CO concentration (active species). In the absence of the knowledge of the lasing medium a priori, FTIR based analysis of the exhaust of the flowing type CO laser enabled us to characterize the change in the lasing mixture composition as a function of coolant temperature[3]. Laser power exceeding 15 W was obtained in 10 μm region (CO₂ laser output) and ~10W of 5 μm (CO power), indicating ~60% conversion efficiency[3] under these operating conditions. In another work reported in the literature, it has been demonstrated that a 20 W CO laser cutting of polyethylene has about the same effect as that of a 150 W CO₂ laser[4]. Further optimisation of this laser is being carried out. Potential applications include molecular spectroscopy and material processing.

[1] The CO₂ laser; W J Witteman, Springer series in optical sciences, Springer-Verlag (1987).

[2] Cryogenically cooled CW electric discharge CO laser operated with CO₂ laser mixture; M. B. Sai Prasad, Tatsat Dwivedi, J. P. Nilaya*, Shailesh Kumar and D. J. Biswas, Laser Physics, 2018, 28 (12), 125002.

[3] Experimental estimation of CO concentration in LN₂ cooled CW-CO laser operating with CO₂ laser gas mixture; Tatsat Dwivedi, Ayan Ghosh, M. B. Sai Prasad and J. P. Nilaya*, Laser Physics Letters, 2022, 19 (9), 095001.

[4] [www.photonics.com/Articles/New CO laser technology offers processing benefits/a57681](http://www.photonics.com/Articles/New_CO_laser_technology_offers_processing_benefits/a57681).

The authors are from Laser & Plasma Technology Division. Authors acknowledge Head, Laser & Plasma Technology Division and Director of Beam Technology Development Group, BARC for their support and encouragement in this developmental activity.

*Author for Correspondence: J. Padma Nilaya
E-mail: jpnilaya@barc.gov.in

राजभाषा *in* BARC

Participants
attending

various competitions > 200

training programs > 100

workshops > 100

Staff

> 2300
quite proficient in Hindi

> 6900
with working knowledge in Hindi

glimpses of hindi pratyogita & hindi diwas-2022



The data presented above is for one-year period September 2021-22.



PARMANU JYOTI

A novel school-outreach initiative, aligned with the Scientific Social Responsibility, where the young scientists reach out to the students in remote areas. Mooted by the Department of Atomic Energy, it aims to inspire the next generation and spread awareness about the contributions of atomic energy to nation-building



On the lines of Corporate Social Responsibility, the concept of **Scientific Social Responsibility** needs to be introduced to connect our leading institutions to all stakeholders, including schools & colleges...

Prime Minister's CLARION CALL *Scientific Social Responsibility and a Global Commitment on Zero-Emission*



A NOVEL APPROACH *Taking Atomic Energy to the Next Gen with Minimum Lecture, Maximum Interaction*



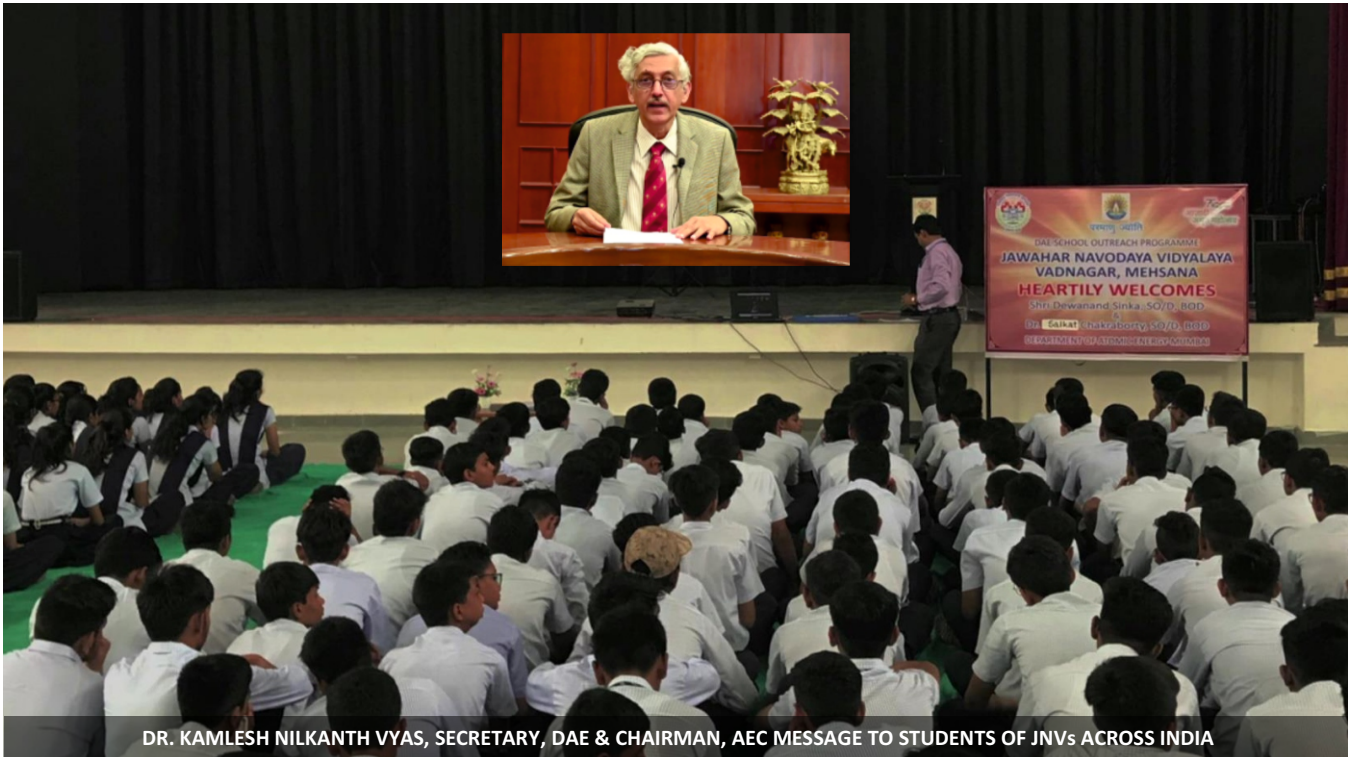
SCIENTISTS AS PARMANU MITRA *Young scientists from BARC as the Ambassadors of Atomic Energy*



THE POWER OF INFORMAL BONDING *Effective Engagement with Students, Overnight Stay at Schools*



2-WAY EXCHANGE *Gaining awareness Students' Aspirations, Spreading Awareness DAE Societal Technologies*



DR. KAMLESH NILKANTH VYAS, SECRETARY, DAE & CHAIRMAN, AEC MESSAGE TO STUDENTS OF JNVs ACROSS INDIA

CALL TO ACTION Encouraging Next Generation to Engage with Parmanu Mitra as Elder Brothers and Sisters



JNV AMRELI, GUJARAT



JNV KARGIL, LADAKH



JNV KABIRDHAM, CHHATTISGARH



JNV CHOULDARI, SOUTH ANDAMAN, A & N ISLANDS

PILOT PHASE Jawahar Navodaya Vidyalayas across India



STANDARDIZATION FOR SCIENCE OUTREACH *Inspiring the Young Minds, Scouting for the Latent Talent*

परमाणु ज्योति

50000+ STUDENTS
100+ SCHOOLS
80+ SCIENTISTS
34 STATES & UTs
4 MONTHS
1 MISSION

#BackToSchool

PAN-INDIA COVERAGE *Concurrent Execution at Multiple Locations for Effective Management*



*What we learn with pleasure
we never forget*

This page is intentionally left blank

This page is intentionally left blank



Edited & Published by
Scientific Information Resource Division
Bhabha Atomic Research Centre, Trombay, Mumbai-400 085, India
BARC Newsletter is also available at URL:<http://www.barc.gov.in>

